Simulations of electrode & solid electrolyte materials

de Klerk, Niek

DOI
10.4233/uuid:48e17e42-5335-41b3-838a-0586523e5b78

Publication date
2019

Document Version
Final published version

Simulations of electrode & solid electrolyte materials

Niek J. J. de Klerk

Simulations of electrode & solid electrolyte materials

Proefschrift

ter verkrijging van de graad van doctor
aan de Technische Universiteit Delft,
op gezag van de Rector Magnificus prof. dr. ir. T.H.J.J. van der Hagen,
voorzitter van het College voor Promoties,
in het openbaar te verdedigen op donderdag 31 januari 2019 om 15:00 uur

door

Nicolaas Jacobus Johannus de Klerk

Doctorandus in de Scheikunde,
Radboud Universiteit Nijmegen,
geboren te State College, Pennsylvania, Verenigde Staten van Amerika.

Dit proefschrift is goedgekeurd door de promotoren.

Samenstelling promotiecommissie:

Rector Magnificus,	voorzitter
Prof. dr. ir. M. Wagemaker,	Technische Universiteit Delft, promotor
Prof. dr. E.H. Brück,	Technische Universiteit Delft, promotor
Onafhankelijke leden:	
Prof. dr. F.M. Mulder	Technische Universiteit Delft
Prof. dr. C. Masquelier	Université de Picardie Jules Verne
Prof. dr. M. Huijben	Universiteit Twente
Dr. H.L.M. Meekes	Radboud Universiteit Nijmegen
Dr. ir. M.H.F. Sluiter	Technische Universiteit Delft
Prof. dr. B. Dam	Technische Universiteit Delft, reservelid

Keywords: Simulations, solid electrolytes, space-charge layers, molecular dynamics, phase-field modelling, batteries

Printed by: Ipskamp Printing

Front & Back: Abstract representation of a battery.

Tiger got to hunt,
Bird got to fly;
Man got to sit and wonder, 'Why, why why?'

Tiger got to sleep,
Bird got to land;
Man got to tell himself he understand.

the Books of Bokonon

Contents

1

Introduction

1

When we take a shower, make coffee, drive a car, use a computer, travel by train, or use a phone; all the time we use some sort of energy. Without sources of energy modern life would be impossible, and with the further development of the world the amount of energy used by humans continues to increase [1]. Currently, almost all the energy used in the world is generated by fossil fuels, which has led to a large increase in CO_2-concentration in the earth's atmosphere. The high CO_2-concentration causes an enhanced greenhouse effect, leading to an increase in global temperature, rising sea levels, and changing weather patterns all over the world [2]. In the coming century the combination of these effects will considerably change the environment, plants, and animals among which we live.
In order to prevent these changes (as much as possible) the Paris climate agreement has been made. The aim of this agreement is to limit the temperature increase to 1.5°C above pre-industrial levels [2], which, hopefully, is enough to keep the climate changes due to the greenhouse effect manageable. Ultimately, this will require the world to produce all the energy from sources which do not cause CO_2-emissions. This can be done by harvesting energy from processes powered by the earth (geothermal power), moon (tidal power), sun (biomass, solar-, wind- and hydro-power), supernovas (which form the heavy nuclei required for nuclear fission), or by using the same energy source as stars (nuclear fusion).
Currently the global energy use is approximately 17 terawatt ($15*10^{17}$ Watt-hour per year), and shifting the energy production of the entire world to renewable sources will require a huge effort. But considering that 17 terawatt is less than 0.02% of the amount of energy the earth receives from solar radiation [3], and considering that other processes can also be used to produce energy, this is definitely possible.

1.1. The need for batteries

Changing to sustainable energy will require a lot of changes. The way of generating electricity must change; but the fuels used to power cars, trucks and other mobile applications must also be replaced. And simply generating all the required electricity is not necessarily enough. The fluctuating nature of many sustainable energy sources throughout the day and year [3], in combination with the variable demand of electricity, will also make storage of the produced energy a necessity.
For day-night cycles and grid balancing, devices which can react quickly to a change in supply and demand are needed, for which capacitors and batteries are a good option [4]. The large scale energy storage necessary to cope with the seasonal changes in supply and demand is not feasible using current battery technology, because of the high price per kWh of current batteries [3]. Cheaper options for energy storage, which are also easily scalable, are therefore necessary. The development of very cheap batteries might solve this problem, but converting electricity to a liquid fuel will probably be a better solution [5].
For mobile applications different considerations play a role, and other properties are required for such an energy storage device. The most important requirements are a high volumetric and gravimetric (weight) energy density; otherwise the energy source will be too large or too heavy, making it impossible to carry it around, and thus ill-suited for mobile applications. Different energy storage technologies are being developed for

mobile applications, such as bio-fuels, hydrogen fuel cells, batteries, and capacitors. Which of these technologies is the best will depend on the application, location, price, and how each of the technologies will develop in the future.

Currently, of the above mentioned energy storage technologies batteries are most widely used. They are used for powering almost all small mobile devices, such as cell phones and laptops. At the same time the use of batteries in transport applications is growing rapidly [6], and the first aeroplanes powered by batteries are being developed [7].

All the different applications mentioned will put distinct demands on a battery. For large-scale storage the price of batteries (Wh/€) will be most important, while small electronic devices require small batteries (Wh/L), for transport applications weight (Wh/kg) will be an important factor, and car-owners demand batteries which can charge quickly. While factors such as safety, efficiency and life-time will also play a role in deciding which battery is best suited for a certain application.

The many different applications for batteries have led to a large range of materials

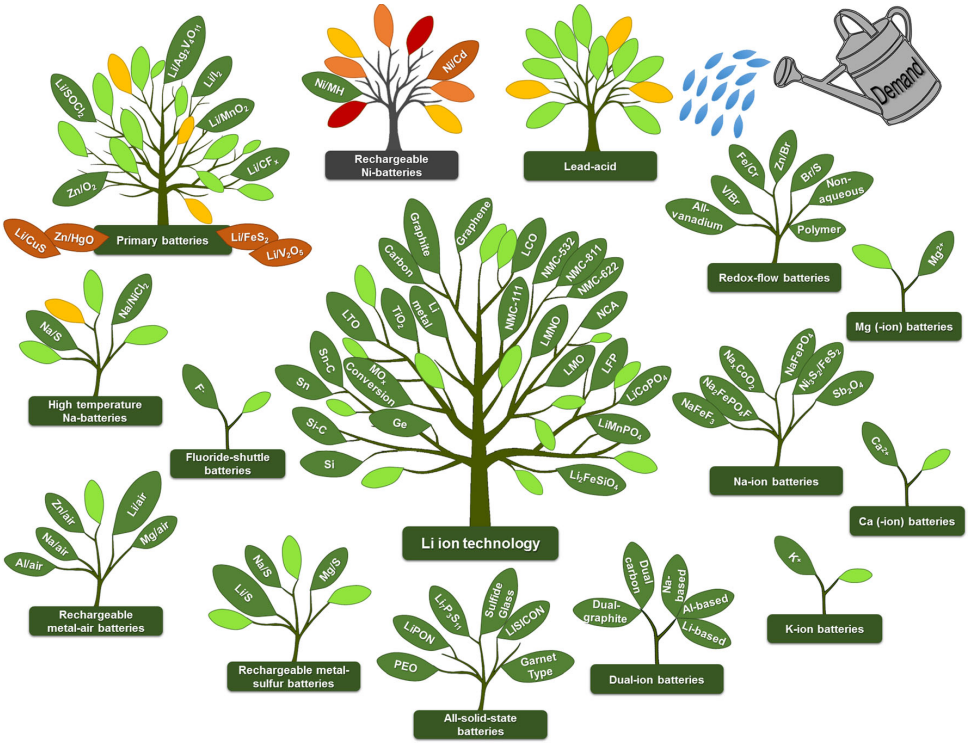

Figure 1.1: Battery chemistries currently being developed [6].

and types of batteries being investigated, most of which are shown in Figure 1.1. Each type of battery and material has its own advantages and disadvantages, making them suitable for different kinds of applications.

The range of demands on batteries means that there will not be a single type of battery which can cater to all the different requirements, so it is likely that in the future several different types of batteries will be used alongside each other. Predicting which battery type will be successful is nearly impossible, as all have their merits, and future success will strongly depend on the further development of each type. However, we can be sure that some of the batteries shown in Figure 1.1 will find widespread application, while others might never leave the research stage.
But before looking at future developments, first let's have a look at the history and working principles of batteries.

1.2. History of batteries

In the year 1800 Allessandro Volta reported on a device which could generate a constant flow of electricity [8], which became known as the voltaic pile. This invention was the first electrical battery. It consisted of a copper and zinc plate, between which an acidic solution was placed [6]. Placing an acidic solution between the metal plates was the essential step which lead to Volta's breakthrough, since this allowed zinc and hydrogen ions to move from the zinc plate to the copper plate. This enabled the electrochemical reaction in this battery, which involves the dissolving of zinc-ions, and the formation of hydrogen gas or copper oxide.[1] The movement of ions between the electrodes allows for the transfer of electrons through an external circuit, or in other words, electricity!
Scientists were enthusiastic about Volta's invention since it was the first device capable of delivering a constant flow of electricity. Many experiments which were impossible before now became possible, and the knowledge about electricity and related phenomena quickly increased during the 19th century [9]. Around 1830 this led to the invention of several electric motors and generators [10], which in 1835 made the construction of the first electric vehicle possible, although on model scale, by professor Stratingh in the Dutch city of Groningen [10].
The large interest in the battery invented by Volta caused improvements to be made quickly, by using different materials and improved designs. In 1854 an important type of rechargeable battery was invented by Wilhelm Josef Sinsteden [6]: the lead-acid battery. A few years later an improved design by Gaston Raimond Planté lead to the first commercially viable lead-acid battery [6], which has been widely used since then. Over the next century hundreds of combinations of materials were tested for batteries [11]. The most successful combinations were Ni-Fe, Ni-Cd, Zn-MnO_2 and nickel-metal hydride (Ni-MH), each having their own advantages and drawbacks.
A big step forward in battery technology was made when the Li-ion battery was commercially introduced by Sony in 1991 [6]. The high voltage of Li-ions allowed for an energy density of 200 Wh/L at the cell level, which is twice as high as lead-acid batteries [12]. The higher energy densities made it possible to power mobile electronic devices using a battery, thus enabling the development of mobile phones, laptops, etc.

[1] Although Volta's invention did what he intended, it was unknown to him that an electrochemical reaction was occurring in the device he made, or even that the movement of ions was happening. Volta believed that the electricity was generated by the contact tension at the interface of the two metals [8], but this theory was proven wrong years later.

In turn, the widespread use of these devices gave a strong incentive to further improve Li-ion batteries, and the energy density at the cell level has increased to nearly 700 Wh/L in current batteries [6].
With the advent of electric vehicles, the incentive to improve Li-ion batteries will grow further, considering that electric cars typically have a battery pack of tens of kilowatt hours, which is equal to a couple of thousand mobile phone batteries. Currently, the amount of Li-ion batteries used for the production of electric vehicles is already equal to the amount of Li-ion batteries used for electronic devices [6], even though electric vehicles are still a rare sight on the road. When electric cars, buses, and trucks become more common the amount of required batteries will increase rapidly.
To enable the storage of electrochemical energy required for these applications studying the fundamental aspects of materials and energy is necessary. Via a thorough investigation of the fundamental aspects, the problems facing current battery technology can be understood, and ideas can be developed to make further improvements.

1.3. Working principles of batteries

Batteries store electrical energy via a chemical reaction, and by reversing the chemical reaction the stored electrical energy can be used to power electrical devices.[2] As shown schematically in Figure 1.2, this is done by transporting a certain atomic species, lithium in Li-ion batteries, between two materials. The flow of atoms from

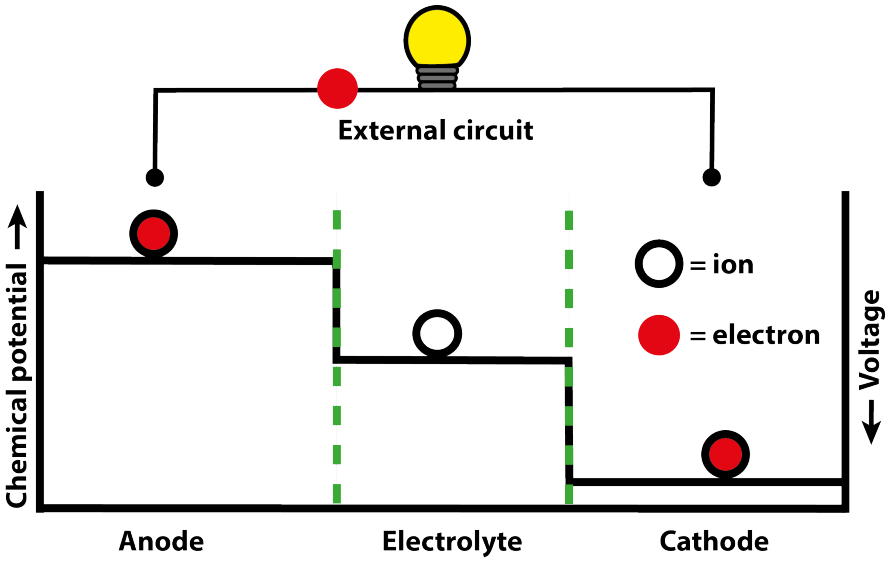

Figure 1.2: Schematic picture of a battery.

[2] Capacitors work in a similar manner as batteries, but the ions and electrons are stored at the surface of a material, while in batteries the ions and electrons chemically react with a material. Storing the ions and electrons at the surface of a material has the benefits of short charging times and a high power output, but the downsides are a lower voltage and lower energy density.

one material to another is caused by the difference in chemical potential, which is a measure for the 'eagerness' of atoms to be in a certain place.[3]
In a charged battery the ions and electrons are in the material with the highest chemical potential (lowest voltage), commonly known as the anode material, but they would rather be in the material with the lower chemical potential (higher voltage), which is commonly referred to as the cathode material. When the two materials are in contact with each other, the ions and electrons will flow towards the material with the lower chemical potential, similar to water flowing downhill. This reaction will occur spontaneously, so making a direct contact between the two electrode materials is equal to creating a short circuit, and does not give electric power which can be used to light a bulb, for example.
To make a battery work, a third material is therefore necessary: the electrolyte. The electrolyte allows ions to flow through it, but blocks the flow of electrons. By placing an electrolyte between the two electrodes the electrons must go through the external circuit to make the chemical reaction happen, enabling use of the electron's energy to power electrical devices or light a bulb, as shown schematically in Figure 1.2.
The amount of energy, which can be stored in a battery, is determined by the difference in chemical potential, and the amount of electrons which can be transferred from the anode to the cathode. The difference in chemical potential determines how much energy can be extracted from each electron, measured in Volts, which depends on the combination of materials used for the anode and the cathode. The amount of electrons being transferred defines the capacity of the battery, and is typically reported in milliampere hours per gram (mAh/g).
When the chemical potential of the two electrodes is equal, the flow of electrons and ions will stop. For primary (non-rechargeable) batteries this is the end of the story. Secondary batteries, more commonly known as rechargeable batteries, can be recharged. This is done by applying an electrical force using an external circuit,[4] which pushes the ions and electrons towards the anode material.

Unfortunately, the battery described so far is an idealisation. In reality, a difference in chemical potential is not necessarily enough to make atoms move from the anode to the cathode. This is caused by several hurdles which the atoms have to overcome when moving between the electrodes.
In order to leave the anode, the atom first has to move towards the surface of the anode material, then separate into an ion and an electron, after which the electron needs to reach the current collector connected to the external circuit, and the ion has to move through the electrolyte. On the other electrode, all these steps need to be traversed in reverse to make the battery work correctly.
When the battery is charged and the electrical circuit is closed, all these steps will occur spontaneously, lowering the chemical potential as thermodynamic principles dictate. But spontaneous does not mean instantaneous. If the atoms could move infinitely

[3] The thermodynamic definition of the chemical potential of an atomic species is: the rate of change of the free energy of a system as a function of the number of atoms added to a system.
[4] At least until photo-rechargeable batteries [13] have overcome the challenges currently associated with them.

fast such a naive picture would be correct. But each of the hurdles described above slows an atom down. This is because on the atomic scale the chemical potential is not flat, as shown schematically in Figure 1.3, energy barriers need to be overcome during each step. Around room temperature the activation energy necessary to cross these

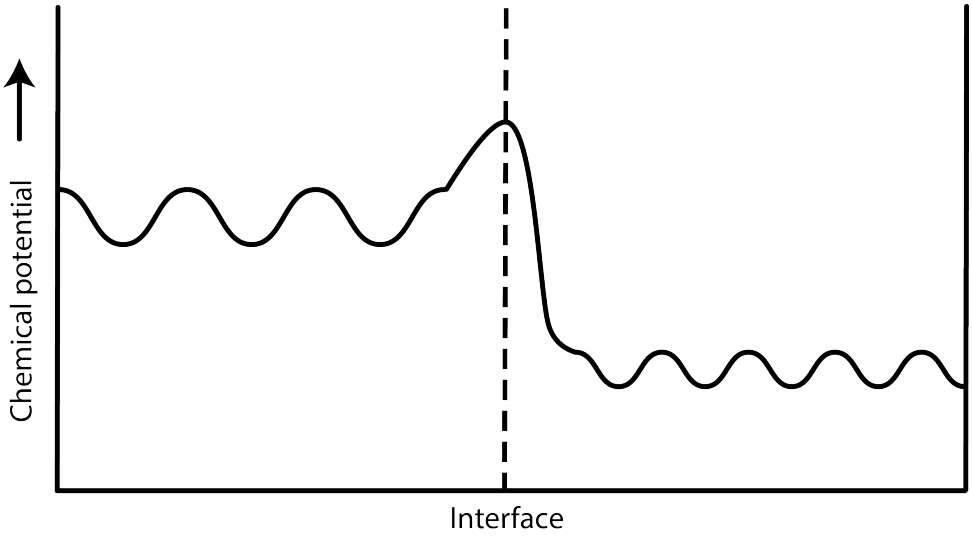

Figure 1.3: Schematic picture of the energy landscape on the atomic scale around the electrode-electrolyte interface.

barriers is, usually, higher than the kinetic energy of the average atom, so the crossing of a barrier is a relatively rare event. Luckily, an atom typically attempts to cross a barrier roughly 10^{13} times a second [14], so within one second it is still likely that an atom crosses many barriers. However, the finite speed of atoms can limit the amount of ions which can be transported through a battery within a certain time, leading to kinetic limitations in a battery, which must be taken into account when determining how fast a battery can be (dis)charged.

The number of ions being transported through the battery can be controlled via the electronic current drawn from the battery. At low currents the spontaneous movements of ions might be enough to supply the amount of current demanded, and the resistance of the battery will be negligible. When demanding higher currents this will not be the case, and an extra force will be required to overcome the resistance caused by all the energy barriers. This extra force is known as the overpotential, and leads to a lower output voltage of the battery, thus lowering the power output of a battery.

Each process in a battery contributes to the total overvoltage, so many different battery properties can affect its performance [15–17]. Material properties such as the particle size, electronic and ionic conductivity of the used materials, as well as electrode properties like the porosity (the amount of 'empty' space) and tortuosity (a measure for the average curvature of the diffusion paths), and external factors such as temperature and

the applied C-rate.[5]

The perfect battery?
To see how to make the perfect battery let's consider the properties of a perfect battery: small, lightweight, with a high capacity and long cycle-life, consisting of cheap and abundantly available materials, able to charge fast, and very safe. Clearly, this is a long list of demands, and whether it is possible to make a battery which satisfies all these criteria simultaneously is doubtful.
For example, how can a small, fast charging battery with a high capacity be made? A fast charging battery can be made using several approaches: thin electrodes can be used, the porosity of the electrodes can be made high, or electrode particles can be nano-sized. All of these three approaches allow for fast ionic diffusion through the battery, making fast charging possible. But, all these approaches also reduce the volumetric capacity of the battery, and the same amount of power will thus require a larger battery. By using approaches opposite to the ones mentioned above, a battery with a high volumetric capacity can be constructed, but this one can not be charged quickly.
In practice compromises thus have to be made between the different demands, after which a battery can be designed with the most suitable properties. The 'best' battery can then be made, which is 'perfect' for the chosen application.

To make the optimal battery a lot of research is being performed. New battery materials are being discovered [18–21], while known ones are being improved through nano-sizing [22–25], doping [26–28] and improved synthesis procedures [29, 30]. At the same time, *in situ* methods are being developed [31] to study the complex interplay between the different processes occuring in a battery, allowing for a better understanding and improved battery designs [32].
Complementary to experiments, computational studies are playing an increasingly important role in battery research. Using simulations, a large amount of possible battery designs can be compared [33], making optimisation efforts more focused. Computational studies can also be used to easily sample a broad range of possibly interesting materials [34, 35] to determine which ones are most promising. Furthermore, computational studies lead to insights into atomic scale processes [36, 37] which are difficult to investigate experimentally. Using models to investigate batteries and materials thus enables a better understanding and allows more focused experimental efforts.
Several models have been developed to simulate an entire battery [38–41], which make it possible to study the complex interplay between processes in a battery. Using a battery model, the processes limiting a battery's performance can be determined, showing which improvements will be most successful, or enabling battery management systems to prevent the circumstances under which problems might occur.
Unfortunately, the battery models presented in literature use one or more parameters

[5] The C-rate is used to describe the amount of time in which a battery is completely (dis)charged. It is defined as the reciprocal of the number of hours it takes to (dis)charge the full capacity of a battery, thus C/5 equals a complete (dis)charge in 5 hours, 1C in one hour, and 2C in half an hour.

which are fitted to experimental data. Since it is questionable whether values of fitted parameters have a physical meaning, or just fit a particular set of experiments,[6] using a model with fitted parameters to predict battery behaviour is therefore questionable [16]. When modelling a battery which is similar to those of the fitted experiments under similar conditions, the model will probably give satisfactory results. But under different conditions, or with different battery properties, the results become unreliable [16]. To be sure that the model is correct under the modelled conditions, the fitted parameters must be redetermined, which will require new experiments. However, this undermines the ultimate goal of a model, namely predicting the outcomes of (possible) experiments.

Since a battery's behaviour can be described using thermodynamic principles, it should be possible to construct a model without fitted parameters, if all relevant effects are properly taken into account. To determine whether this assumption is correct, in Chapter 2 a model is developed in which all parameters depend on material properties, thus removing the need for fitted parameters.

The material chosen for the thermodynamic model was TiO_2-anatase, a material which has been well studied for over 20 years. The large amount of literature available on TiO_2-anatase made all the necessary parameters available in literature, and gave ample experimental results for comparison between the model and experiments. This example shows that fitted parameters are not necessary when making a battery model, thus improving the reliability of battery models.

1.4. All-solid-state batteries

One of the many kinds of batteries currently being investigated are all-solid-state batteries (ASSB's). In comparison to conventional batteries, the main difference of ASSB's is that the liquid electrolyte is replaced by a solid electrolyte. In this way the most volatile component of a battery is removed, thus significantly increasing battery safety [43–45]. When a battery consists entirely of solid state materials, the packaging of a battery can also be simplified, as shown in Figure 1.4. As a consequence, less packaging is required for the same amount of active material, and ASSB's are therefore expected to have a higher volumetric energy density than current batteries [43, 46]. Besides increased safety and energy density ASSB's are also expected to have the benefits of a longer cycle life [45, 47, 48], more flexibility in designs [44], and higher voltages through the use of high voltage electrode materials and Li-metal anodes [45, 46].

The increased volumetric energy density and safety of ASSB's are especially interesting for mobile applications and electric cars. Toyota plans to use ASSB's in electric cars in 2022 [49], and although this may be a bit optimistic, the promises of ASSB's are also seen by several other big companies and car manufacturers who have invested

[6] When using a large number of fitted parameters their physical meaning will become increasingly questionable, and the likelihood that it is just a set of random parameter values which fits the given experimental results will increase. For example, the shape of an elephant can be fitted using just four complex numbers, and by adding a fifth a wiggling trunk can be added [42]. Clearly, the parameters fitting an elephantine shape do not have any physical meaning, but why would this be different for other parameters fitted to a certain line/shape?

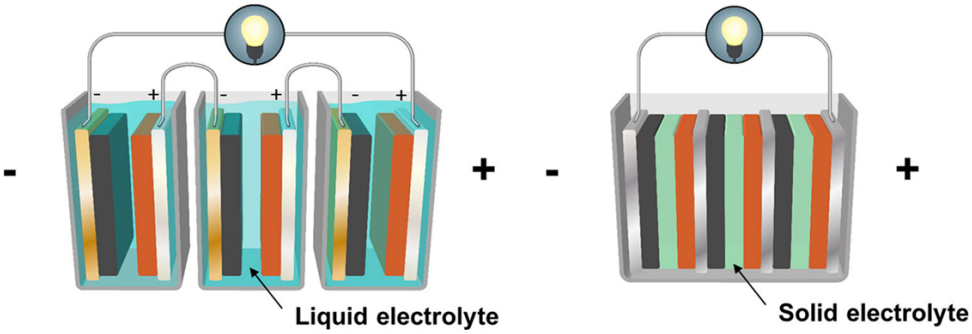

Figure 1.4: Comparison between batterie cells using liquid and solid electrolyte [6].

in ASSB start-ups [46].
However, currently the performance of ASSB's is poorer than those of batteries using liquid electrolytes, especially at 'high' C-rates [50]. For many years the poor high rate behaviour was attributed to the low ionic conductivity of solid state electrolytes (SSE's). However, in recent years a range of SSE's with ionic conductivities comparable to liquid electrolytes have been discovered [43, 45, 50]. High-rate behaviour comparable to liquid electrolyte batteries might thus be expected of ASSB's, but this is not yet the case [48, 51]. Several phenomena have been blamed for the difference in performance between solid and liquid electrolytes: low contact area at the electrode-solid electrolyte interface, (electro)chemical reactions at the interface, and space-charge layers.
One important difference between the two types of electrolyte is that liquid electrolytes will automatically wet the entire surface of electrode particles, which is not the case for solid electrolytes. This means that in ASSB's the amount of contact area between the electrode and electrolyte is significantly lower, causing larger interface resistances. Fortunately, several approaches show promise to overcome this problem. Nano-sizing the electrode and electrolyte material can reduce the interface resistance by an order of magnitude [51], but applying pressure to the ASSB also increases performance [52], as well as coating electrode particles with a solid electrolyte [53].
A problem which both solid and liquid electrolytes face is (in)stability at the electrode-electrolyte interfaces. To have a stable interface at both electrodes, the electrolyte must be stable in combination with both electrode materials, even when large voltage differences are present and the ion concentration changes. A property which few of the currently known solid electrolytes have [35, 54]. Instability at the interfaces will lead to the formation of solid electrolyte interphases (SEI). Although the formation of decomposition products is not ideal, SEI layers are not necessarily bad [35], as long as this layer has a low electronic conductivity in combination with a reasonable ionic conductivity.
Since the interface stability depends on the materials which can be formed, the stability of an electrolyte depends on the electrode material it is in contact with [35, 54] and the electrode voltage [55]. To further complicate matters, the kinetics of the decompo-

sition reactions must also be taken into account to predict which materials will form in the interphase [55]. However, in liquid electrolytes the stability at the electrode interfaces also used to be a problem, but this has been overcome [56]. Given the large amount of research on electrode-solid electrolyte interfaces, this problem is also likely to be overcome.

In literature there is consensus that the two phenomena discussed above play an important role in the interfacial problems currently facing ASSB's. A third phenomenon occurring at the electrode-solid electrolyte interface is the creation of a space-charge layer. Space-charge layers are caused by the large difference in chemical potential over the interface, in combination with the (practically) immobile electrons in the solid electrolyte. This causes ions to transfer over the interface, while the electrons cannot, leading to an electric field over the interface and changes in the ion concentration.

But whether space-charge layers play a role in ASSB performance is still under debate. Some reports on space-charge layers suggest that they are several micrometres in thickness [57, 58], which would cause a large interface resistance, and measures to prevent them would be required. On the other hand, there are also reports that the space-charge layer is only a few nanometres thick [59, 60], making it unlikely that they would give a significant contribution to the interface resistance.

To determine whether space-charge layers play an important or negligible role in ASSB's, in Chapter 3 a thermodynamic model has been made, which is applied to several electrode-solid electrolyte combinations. The thickness of the space-charge layers on the electrode-solid electrolytes interfaces was determined, and the resistance over the space-charge layer is calculated to asses their impact on ASSB performance.

1.5. Solid state electrolytes

To further develop ASSB's solid electrolytes (SSE) with suitable properties are of prime importance. As shown in Figure 1.5, nowadays several classes of solid electrolyte materials are known that show ionic conductivities in the order of 10^{-3} Siemens/cm (S/cm) at room temperature [45, 50], which is comparable to ionic conductivities in currently used liquid electrolytes. However, for successful ASSB's the SSE's must also meet several requirements related to fabrication, environmental friendliness, and economic viability of the ASSB. Since the ideal SSE has not been discovered yet, research in this area remains important.

Unfortunately, recently it has been shown that there is a correlation between high ionic mobility and low electrochemical stability [61], which implies that creating a very stable, highly conductive SSE will be difficult. But luckily, a solid electrolyte can also be successful if its decomposition products are stable, have a reasonable ionic conductivity and a low electronic conductivity [35], similar to the functioning of solid-electrolyte interphase (SEI) layers at electrodes in liquid electrolytes. It is essential to improve understanding of which properties of SSE's govern high ionic conductivity, otherwise research will be grasping in the dark.

It is clear that an essential feature for fast ion diffusion is an energy landscape which is as flat as possible, preferably in combination with a high ion concentration, which gives a material with high ionic conductivity. But how such a material can be obtained

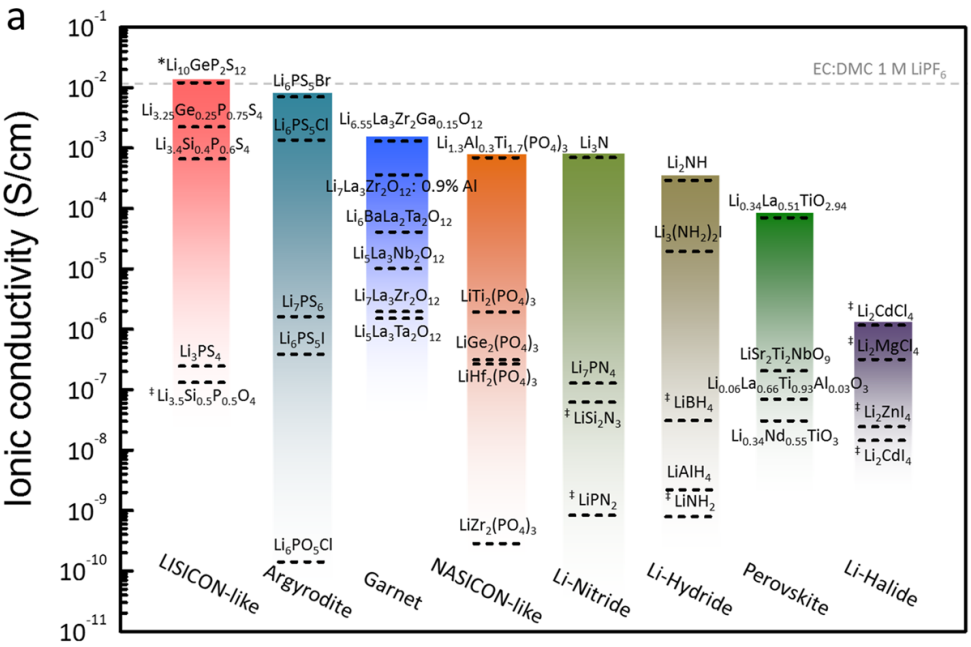

Figure 1.5: Li-ion conductivities of materials from several classes of solid state electrolytes [45].

remains vague. Over the years many material properties have been proposed as predictors for high ionic diffusivity, such as low-energy phonons [62], the polarisability of the rigid lattice [63], lattice volume [45], the percentage of empty Li-sites [64], and many others.
Although most of these predictors have their merits, and have increased the understanding of factors impacting high ionic conductivity, they are certainly not perfect. In the argyrodites [65] for example, crystalline Li_6PS_5Cl and Li_6PS_5Br show Li-ion conductivities of $7^{*}10^{-4}$ S/cm, while a value of $5^{*}10^{-7}$ S/cm is measured for crystalline Li_6PS_5I. A thousandfold difference, even though the crystal structures of these materials are practically similar, iodine has a higher polarisability and larger volume than the other two, the phonon properties are comparable [66], and the percentage of empty Li-sites is equal. The processes causing high ionic conductivity are thus not completely understood yet, and further studies into the mechanisms remain necessary.

Since ionic conduction is caused by processes on the atomic scale, atomistic simulations are a perfect tool for understanding ionic diffusion, and what causes the orders of magnitude difference in conductivity within a class of SSE's. Furthermore, atomic scale simulations allow great control over the structure of the studied materials, and easy manipulation of the structure. This makes studying a range of structures computationally much easier than experimentally, and new structures can easily be made to verify a hypothesis on how to improve a material.

A complicating factor when studying diffusion in SSE's is the high concentration of diffusing atoms, in β-Li_3PS_4 for example it is 31 mol/L (or equivalently: 19 Li-ions/nm^3). With so many atoms moving around in close proximity, complex interactions and diffusion behaviour are to be expected. And it has been shown that diffusion can involve collective jumps [67] or lattice vibrations [64], both of which are caused by the interactions between atoms.

To study diffusion in SSE's molecular dynamics (MD) simulations are therefore an ideal tool, because all possible motions of atoms, and interactions between them, are naturally included. A prerequisite for studying atomic motion is that the atomic motion under study occurs on the time-scale and temperature which is simulated. Luckily for MD simulations, in typical solid electrolytes the ionic diffusion is fast and the ion concentration is high. Usually MD simulations of short time-scales (approximately 100 picoseconds) and small systems (approximately 1 nm^3) at 'moderate' temperatures (300-700 K) thus suffice to obtain useful information about ionic diffusion in SSE's.

The short times and small size of the simulations allow the use of density functional theory (DFT) to calculate the forces between atoms. This has the advantage that the electronic structure of the material is taken into account, giving more reliable results than methods which do not calculate the electronic structure.

In Chapter 4 the sodium ion solid electrolyte Na_3PS_4 is investigated using DFT MD simulations. Analysis of MD simulations gives an understanding of the origin of fast Na-diffusion in the cubic and tetragonal phase, based on which possible ways of improving the Na-conductivity are investigated.

The large differences in Li ion conductivity of the argyrodite solid electrolytes is investigated in Chapter 5. The diffusion paths in the different structures are visualised, clearly revealing the origin of the large differences in Li-ion conductivity. Possibilities for further improving the argyrodite solid electrolytes are then explored based on these results.

The analysis method developed for MD simulations in Chapters 4 and 5 is further expanded upon in Chapter 6. The presented method is generally applicable to the analysis of MD-simulations of solid electrolytes, and it can be used to obtain activation energies, attempt frequencies, diffusion paths and several other properties related to ionic diffusion. As an example, Li-ion conductivity in β-Li_3PS_4 is investigated. This example shows how the analysis method can be applied to gain a better understanding of ionic diffusion in SSE's, and how this can lead to improvement of the material.

References

[1] A.E. Kontorovich, M.I. Epov, and L.V. Eder. Long-term and medium-term scenarios and factors in world energy perspectives for the 21st century. *Russ. Geol. Geophys.*, 55(5-6):534–543, 2014. doi: 10.1016/j.rgg.2014.05.002.

[2] J. Rogelj, M. den Elzen, N. Hohne, T. Fransen, H. Fekete, H. Winkler, R. Schaeffer, F. Sha, K. Riahi, and M. Meinshausen. Paris agreement climate proposals need a boost to keep warming well below 2 degrees C. *Nature*, 534(7609):631–639, 2016. doi: 10.1038/nature18307.

[3] F.M. Mulder. Implications of diurnal and seasonal variations in renewable energy generation for large scale energy storage. *J. Renew. Sustain. Ener.*, 6(3):033105, 2014. doi: 10.1063/1.4874845.

[4] B. Dunn, H. Kamath, and J.M. Tarascon. Electrical energy storage for the grid: a battery of choices. *Science*, 334(6058):928–935, 2011. doi: 10.1126/science.1212741.

[5] F.M. Mulder, B.M.H. Weninger, J. Middelkoop, F.G.B. Ooms, and H. Schreuders. Efficient electricity storage with a battolyser, an integrated Ni-Fe battery and electrolyser. *Energy Environ. Sci.*, 10(3):756–764, 2017. doi: 10.1039/c6ee02923j.

[6] T. Placke, R. Kloepsch, S. Dühnen, and M. Winter. Lithium ion, lithium metal, and alternative rechargeable battery technologies: the odyssey for high energy density. *J. Solid State Electrochem.*, 21(7):1939–1964, 2017. doi: 10.1007/s10008-017-3610-7.

[7] https://edition.cnn.com/travel/article/electric-aircraft/index.html, 2017 (accessed July 4, 2018).

[8] A. Volta. On the electricity excited by the mere contact of conducting substances of different kinds. *Philos. T. R. Soc. Lond.*, 90(0):403–431, 1800. doi: 10.1098/rstl.1800.0018.

[9] K. Funke. Solid state ionics: from Michael Faraday to green energy - the European dimension. *Sci. Technol. Adv. Mat.*, 14(4):043502, 2013. doi: 10.1088/1468-6996/14/4/043502.

[10] M. Doppelbauer. The invention of the electric motor 1800-1854, https://www.eti.kit.edu/english/1376.php, (accessed July 4, 2018).

[11] M. Armand and J.M. Tarascon. Building better batteries. *Nature*, 451(7179):652–657, 2008. doi: 10.1038/451652a.

[12] J.M. Tarascon and M. Armand. Issues and challenges facing rechargeable lithium batteries. *Nature*, 414(6861):359–367, 2001. doi: 10.1038/35104644.

[13] S. Ahmad, C. George, D.J. Beesley, J.J. Baumberg, and M. de Volder. Photo-rechargeable organo-halide perovskite batteries. *Nano Lett.*, 18(3):1856–1862, 2018. doi: 10.1021/acs.nanolett.7b05153.

[14] A. Van der Ven, G. Ceder, M. Asta, and P.D. Tepesch. First-principles theory of ionic diffusion with nondilute carriers. *Phys. Rev. B*, 64(18):184307, 2001. doi: 10.1103/PhysRevB.64.184307.

[15] D. Deng. Li-ion batteries: basics, progress, and challenges. *Energy Sci. Eng.*, 3(5):385–418, 2015. doi: 10.1002/ese3.95.

[16] A.A. Franco. Multiscale modelling and numerical simulation of rechargeable lithium ion batteries: concepts, methods and challenges. *RSC Adv.*, 3(32):13027–13058, 2013. doi: 10.1039/c3ra23502e.

[17] X. Zhang, T.W. Verhallen, F. Labohm, and M. Wagemaker. Direct observation of Li-ion transport in electrodes under nonequilibrium conditions using neutron depth profiling. *Adv. Energy Mater.*, 5(15), 2015. doi: 10.1002/aenm.201500498.

[18] V.S. Kandagal, M.D. Bharadwaj, and U.V. Waghmare. Theoretical prediction of a highly conducting solid electrolyte for sodium batteries: $Na_{10}GeP_2S_{12}$. *J. Mater. Chem. A*, 3(24):12992–12999, 2015. doi: 10.1039/c5ta01616a.

[19] Z. Zhang, E. Ramos, F. Lalère, A. Assoud, K. Kaup, P. Hartman, and L.F. Nazar. $Na_{11}Sn_2PS_{12}$: a new solid state sodium superionic conductor. *Energy Environ. Sci.*, 11(1):87–93, 2018. doi: 10.1039/c7ee03083e.

[20] H. Wang, Y. Chen, Z.D. Hood, G. Sahu, A.S. Pandian, J.K. Keum, K. An, and C. Liang. An air-stable Na_3SbS_4 superionic conductor prepared by a rapid and economic synthetic procedure. *Angew. Chem.*, 55(30):8551–8555, 2016. doi: 10.1002/anie.201601546.

[21] T.J. Udovic, M. Matsuo, A. Unemoto, N. Verdal, V. Stavila, A.V. Skripov, J.J. Rush, H. Takamura, and S.I. Orimo. Sodium superionic conduction in $Na_2B_{12}H_{12}$. *Chem. Commun.*, 50(28):3750–3752, 2014. doi: 10.1039/c3cc49805k.

[22] V. Gentili, S. Brutti, L.J. Hardwick, A.R. Armstrong, S. Panero, and P.G. Bruce. Lithium insertion into anatase nanotubes. *Chem. Mater.*, 24(22):4468–4476, 2012. doi: 10.1021/cm302912f.

[23] Y. Li, S. Meyer, J. Lim, S.C. Lee, W.E. Gent, S. Marchesini, H. Krishnan, T. Tyliszczak, D. Shapiro, A.L. Kilcoyne, and W.C. Chueh. Effects of particle size, electronic connectivity, and incoherent nanoscale domains on the sequence of lithiation in $LiFePO_4$ porous electrodes. *Adv. Mater.*, 27(42):6591–6597, 2015. doi: 10.1002/adma.201502276.

[24] Z. Liu, W. Fu, E.A. Payzant, X. Yu, Z. Wu, N.J. Dudney, J. Kiggans, K. Hong, A.J. Rondinone, and C. Liang. Anomalous high ionic conductivity of nanoporous β-Li_3PS_4. *J. Am. Chem. Soc.*, 135(3):975–978, 2013. doi: 10.1021/ja3110895.

[25] X. Yang, Y. Yang, H. Hou, Y. Zhang, L. Fang, J. Chen, and X. Ji. Size-tunable single-crystalline anatase TiO_2 cubes as anode materials for lithium ion batteries. *J. Phys. Chem. C*, 119(8):3923–3930, 2015. doi: 10.1021/jp512289g.

[26] I.H. Chu, C.S. Kompella, H. Nguyen, Z. Zhu, S. Hy, Z. Deng, Y.S. Meng, and S.P. Ong. Room-temperature all-solid-state rechargeable sodium-ion batteries with a Cl-doped Na_3PS_4 superionic conductor. *Sci. Rep.*, 6:33733, 2016. doi: 10.1038/srep33733.

[27] Z. Deng, B. Radhakrishnan, and S.P. Ong. Rational composition optimization of the lithium-rich $Li_3OCl_{1-x}Br_x$ anti-perovskite superionic conductors. *Chem. Mater.*, 27(10):3749–3755, 2015. doi: 10.1021/acs.chemmater.5b00988.

[28] Y. Ren, J. Li, and J. Yu. Enhanced electrochemical performance of TiO_2 by Ti^{3+} doping using a facile solvothermal method as anode materials for lithium-ion batteries. *Electrochim. Acta*, 138:41–47, 2014. doi: 10.1016/j.electacta.2014.06.068.

[29] C. Yu, L. van Eijck, S. Ganapathy, and M. Wagemaker. Synthesis, structure and electrochemical performance of the argyrodite Li_6PS_5Cl solid electrolyte for Li-ion solid state batteries. *Electrochim. Acta*, 215:93–99, 2016. doi: 10.1016/j.electacta.2016.08.081.

[30] J.Y. Shin, J.H. Joo, D. Samuelis, and J. Maier. Oxygen-deficient $TiO_{2-\delta}$ nanoparticles via hydrogen reduction for high rate capability lithium batteries. *Chem. Mater.*, 24(3):543–551, 2012. doi: 10.1021/cm2031009.

[31] P.P.R.M.L. Harks, F.M. Mulder, and P.H.L. Notten. *In situ* methods for Li-ion battery research: a review of recent developments. *J. Power Sources*, 288:92–105, 2015. doi: 10.1016/j.jpowsour.2015.04.084.

[32] Z. Liu, T.W. Verhallen, D.P. Singh, H. Wang, M. Wagemaker, and S. Barnett. Relating the 3D electrode morphology to Li-ion battery performance; a case for $LiFePO_4$. *J. Power Sources*, 324:358–367, 2016. doi: 10.1016/j.jpowsour.2016.05.097.

[33] A. Vasileiadis, N.J.J. de Klerk, R.B. Smith, S. Ganapathy, P.P.R.M.L. Harks, M.Z. Bazant, and M. Wagemaker. Toward optimal performance and in-depth understanding of spinel $Li_4Ti_5O_{12}$ electrodes through phase field modeling. *Adv. Funct. Mater.*, 28(16):1705992, 2018. doi: 10.1002/adfm.201705992.

[34] S.P. Ong, Y. Mo, W.D. Richards, L. Miara, H.S. Lee, and G. Ceder. Phase stability, electrochemical stability and ionic conductivity of the $Li_{10\pm1}MP_2X_{12}$(M = Ge, Si, Sn, Al or P, and X = O, S or Se) family of superionic conductors. *Energy Environ. Sci.*, 6(1):148–156, 2013. doi: 10.1039/c2ee23355j.

[35] Y. Zhu, X. He, and Y. Mo. Origin of outstanding stability in the lithium solid electrolyte materials: Insights from thermodynamic analyses based on first-principles calculations. *ACS Appl. Mater. Interfaces*, 7(42):23685–23693, 2015. doi: 10.1021/acsami.5b07517.

[36] N. Adelstein and B.C. Wood. Role of dynamically frustrated bond disorder in a Li^+ superionic solid electrolyte. *Chem. Mater.*, 28(20):7218–7231, 2016. doi: 10.1021/acs.chemmater.6b00790.

[37] S. Ganapathy, A. Vasileiadis, J.R. Heringa, and M. Wagemaker. The fine line between a two-phase and solid-solution phase transformation and highly mobile phase interfaces in spinel $Li_{4+x}Ti_5O_{12}$. *Adv. Energy Mater.*, page 1601781, 2016. doi: 10.1002/aenm.201601781.

[38] M.Z. Bazant. Theory of chemical kinetics and charge transfer based on nonequilibrium thermodynamics. *Accounts Chem. Res.*, 46(5):1144–1160, 2013. doi: 10.1021/ar300145c.

[39] M. Landstorfer, S. Funken, and T. Jacob. An advanced model framework for solid electrolyte intercalation batteries. *Phys. Chem. Chem. Phys.*, 13(28):12817–12825, 2011. doi: 10.1039/c0cp02473b.

[40] A. Salvadori, D. Grazioli, and M.G.D. Geers. Governing equations for a two-scale analysis of Li-ion battery cells. *Int. J. Solids Struct.*, 59:90–109, 2015. doi: 10.1016/j.ijsolstr.2015.01.014.

[41] P.H.L. Notten and D.L. Danilov. Battery modeling: a versatile tool to design advanced battery management systems. *Adv. Chem. Eng. Science*, 04(01):62–72, 2014. doi: 10.4236/aces.2014.41009.

[42] J. Mayer, K. Khairy, and J. Howard. Drawing an elephant with four complex parameters. *Am. J. Phys.*, 78(6):648–649, 2010. doi: 10.1119/1.3254017.

[43] K. Takada. Progress and prospective of solid-state lithium batteries. *Acta Mater.*, 61(3):759–770, 2013. doi: 10.1016/j.actamat.2012.10.034.

[44] M. Tatsumisago and A. Hayashi. Sulfide glass-ceramic electrolytes for all-solid-state lithium and sodium batteries. *Int. J. Appl. Glass Sci.*, 5(3):226–235, 2014. doi: 10.1111/ijag.12084.

[45] J.C. Bachman, S. Muy, A. Grimaud, H.H. Chang, N. Pour, S.F. Lux, O. Paschos, F. Maglia, S. Lupart, P. Lamp, L. Giordano, and Y. Shao-Horn. Inorganic solid-state electrolytes for lithium batteries: mechanisms and properties governing ion conduction. *Chem. Rev.*, 116(1):140–162, 2016. doi: 10.1021/acs.chemrev.5b00563.

[46] A.C. Luntz, J. Voss, and K. Reuter. Interfacial challenges in solid-state Li ion batteries. *J. Phys. Chem. Lett.*, 6(22):4599–4604, 2015. doi: 10.1021/acs.jpclett.5b02352.

[47] J. Li, C. Ma, M. Chi, C. Liang, and N.J. Dudney. Solid electrolyte: the key for high-voltage lithium batteries. *Adv. Energy Mater.*, 5(4):1401408, 2015. doi: 10.1002/aenm.201401408.

[48] K. Takada. Solid electrolytes and solid-state batteries. *AIP Conf. Proc.*, 1765: 020008, 2016. doi: 10.1063/1.4961900.

[49] https://insideevs.com/toyota-says-itll-launch-solid-state-battery-evs-2022/, 2018 (accessed June 18, 2018).

[50] B.V. Lotsch and J. Maier. Relevance of solid electrolytes for lithium-based batteries: a realistic view. *J. Electroceram.*, 38(2-4):128–141, 2017. doi: 10.1007/s10832-017-0091-0.

[51] C. Yu, S. Ganapathy, E.R.H. van Eck, H. Wang, S. Basak, Z. Li, and M. Wagemaker. Accessing the bottleneck in all-solid state batteries, lithium-ion transport over the solid-electrolyte-electrode interface. *Nat. Commun.*, 8(1):1086, 2017. doi: 10.1038/s41467-017-01187-y.

[52] H.K. Tian and Y. Qi. Simulation of the effect of contact area loss in all-solid-state Li-ion batteries. *J. Electrochem. Soc.*, 164(11):E3512–E3521, 2017. doi: 10.1149/2.0481711jes.

[53] Y. Ito, S. Yamakawa, A. Hayashi, and M. Tatsumisago. Effects of the microstructure of solid-electrolyte-coated $LiCoO_2$ on its discharge properties in all-solid-state lithium batteries. *J. Mater. Chem. A*, 5(21):10658–10668, 2017. doi: 10.1039/c7ta01227f.

[54] W.D. Richards, L.J. Miara, Y. Wang, J.C. Kim, and G. Ceder. Interface stability in solid-state batteries. *Chem. Mater.*, 28(1):266–273, 2016. doi: 10.1021/acs.chemmater.5b04082.

[55] Y. Tian, T. Shi, W.D. Richards, J. Li, J.C. Kim, S.H. Bo, and G. Ceder. Compatibility issues between electrodes and electrolytes in solid-state batteries. *Ener. Env. Science*, 10(5):1150–1166, 2017. doi: 10.1039/c7ee00534b.

[56] Q. Zhang, J. Pan, P. Lu, Z. Liu, M.W. Verbrugge, B.W. Sheldon, Y.T. Cheng, Y. Qi, and X. Xiao. Synergetic effects of inorganic components in solid electrolyte interphase on high cycle efficiency of lithium ion batteries. *Nano Lett.*, 16(3):2011–2016, 2016. doi: 10.1021/acs.nanolett.5b05283.

[57] K. Yamamoto, Y. Iriyama, T. Asaka, T. Hirayama, H. Fujita, C.A. Fisher, K. Nonaka, Y. Sugita, and Z. Ogumi. Dynamic visualization of the electric potential in an all-solid-state rechargeable lithium battery. *Angew. Chem.*, 49(26):4414–4417, 2010. doi: 10.1002/anie.200907319.

[58] H. Masuda, N. Ishida, Y. Ogata, D. Ito, and D. Fujita. Internal potential mapping of charged solid-state-lithium ion batteries using *in situ* Kelvin probe force microscopy. *Nanoscale*, 9(2):893–898, 2017. doi: 10.1039/c6nr07971g.

[59] Y. Aizawa, K. Yamamoto, T. Sato, H. Murata, R. Yoshida, C.A.J. Fisher, T. Kato, Y. Iriyama, and T. Hirayama. *In situ* electron holography of electric potentials inside a solid-state electrolyte: effect of electric-field leakage. *Ultramicroscopy*, 178:20–26, 2017. doi: 10.1016/j.ultramic.2016.07.015.

[60] K. Takada, N. Ohta, L. Zhang, X. Xu, B.T. Hang, T. Ohnishi, M. Osada, and T. Sasaki. Interfacial phenomena in solid-state lithium battery with sulfide solid electrolyte. *Solid State Ionics*, 225:594–597, 2012. doi: 10.1016/j.ssi.2012.01.009.

[61] S. Muy, J.C. Bachman, L. Giordano, H.H. Chang, D.L. Abernathy, D. Bansal, O. Delaire, S. Hori, R. Kanno, F. Maglia, S. Lupart, P. Lamp, and Y. Shao-Horn. Tuning mobility and stability of lithium ion conductors based on lattice dynamics. *Energy Environ. Sci.*, 11(4):850–859, 2018. doi: 10.1039/c7ee03364h.

[62] K. Wakamura. Roles of phonon amplitude and low-energy optical phonons on superionic conduction. *Phys. Rev. B*, 56(18):11593–11599, 1997. doi: 10.1103/PhysRevB.56.11593.

[63] T. Krauskopf, C. Pompe, M.A. Kraft, and W.G. Zeier. Influence of lattice dynamics on Na^+ transport in the solid electrolyte $Na_3PS_{4-x}Se_x$. *Chem. Mater.*, 29(20): 8859–8869, 2017. doi: 10.1021/acs.chemmater.7b03474.

[64] G.K. Phani Dathar, J. Balachandran, P.R.C. Kent, A.J. Rondinone, and P. Ganesh. Li-ion site disorder driven superionic conductivity in solid electrolytes: a first-principles investigation of β-Li_3PS_4. *J. Mater. Chem. A*, 5(3):1153–1159, 2017. doi: 10.1039/c6ta07713g.

[65] P.R. Rayavarapu, N. Sharma, V.K. Peterson, and S. Adams. Variation in structure and Li^+-ion migration in argyrodite-type Li_6PS_5X (X = Cl, Br, I) solid electrolytes. *J. Solid State Electrochem.*, 16(5):1807–1813, 2011. doi: 10.1007/s10008-011-1572-8.

[66] M.A. Kraft, S.P. Culver, M. Calderon, F. Bocher, T. Krauskopf, A. Senyshyn, C. Dietrich, A. Zevalkink, J. Janek, and W.G. Zeier. Influence of lattice polarizability on the ionic conductivity in the lithium superionic argyrodites Li_6PS_5X (X = Cl, Br, I). *J. Am. Chem. Soc.*, 139(31):10909–10918, 2017. doi: 10.1021/jacs.7b06327.

[67] A. Vasileiadis and M. Wagemaker. Thermodynamics and kinetics of Na-ion insertion into hollandite-TiO_2 and O3-layered $NaTiO_2$: an unexpected link between two promising anode materials for Na-ion batteries. *Chem. Mater.*, 29(3):1076–1088, 2017. doi: 10.1021/acs.chemmater.6b03928.

2

Explaining key properties of lithiation in TiO_2-anatase Li-ion battery electrodes using phase-field modelling

This chapter has been published as: Niek J.J. de Klerk, Alexandros Vasileiadis, Raymond B. Smith, Martin Z. Bazant and Marnix Wagemaker, Explaining key properties of lithiation in TiO_2-anatase Li-ion battery electrodes using phase-field modelling; Physical Review Materials **1** (2), 025404 (2017), doi: 10.1103/PhysRevMaterials.1.025404

The improvement of Li-ion battery performance requires development of models that capture the essential physics and chemistry in Li-ion battery electrode materials. Phase-field modelling has recently been shown to have this ability, providing new opportunities to gain understanding of these complex systems. In this paper a novel electrochemical phase-field model is presented that captures the thermodynamic and kinetic properties of lithium-insertion in TiO_2-anatase, a well-known and intensively studied Li-ion battery electrode material. Using a linear combination of two regular solution models the two phase transitions during lithiation are described as lithiation of two separate lattices with different physical properties.
Previous elaborate experimental work on lithiated anatase TiO_2 provides all parameters necessary for the phase-field simulations, giving the opportunity to gain fundamental insight in the lithiation of anatase and validate this phase-field model. The phase-field model captures the essential experimentally observed phenomena, rationalising the impact of C-rate, particle size, surface area, and the memory effect on the performance of anatase as a Li-ion battery electrode. Thereby a comprehensive physical picture of the lithiation of anatase TiO_2 is provided.
The results of the simulations demonstrate that the performance of anatase is limited by poor Li-ion diffusion in the Li_1TiO_2 phase at the surface of the particles. Unlike other electrode materials, the kinetic limitations of individual anatase particles limit the performance of full electrodes. Hence, rather than improving the ionic and electronic network in electrodes, improving the performance of anatase TiO_2 electrodes requires preventing the formation of a blocking Li_1TiO_2 phase at the surface of particles.
Additionally, the qualitative agreement of the phase-field model, containing only parameters from literature, with a broad spectrum of experiments demonstrates the capabilities of phase-field models for understanding Li-ion electrode materials, and its promise for guiding the design of electrodes through a thorough understanding of material properties and their interactions.

2.1. Introduction

High energy densities realised by Li-ion batteries have enabled mobile applications scaling from mobile phones, tablets, and laptops, up to electrical vehicles. The application of batteries in electric vehicles in particular has driven the demand for faster and more efficient electricity storage. Different mechanisms may limit battery performance [1–3]: the electronic wiring in the electrodes, ionic transport through the electrolyte, the charge transfer reaction, and the solid state transport process. Which of these mechanisms is limiting depends on the applied current and the morphology of the electrodes [3].
To understand the complex interplay of the processes in batteries and to enable improved battery design, various models have been developed [4–10]. Using these models it is possible to design better battery management systems [4], decrease charging times [5], estimate the effect of side-reactions on performance [6], and study what limits the performance of a battery [7].
The challenge for models describing batteries is taking into account microscopic processes, such as phase transitions and interfaces, in combination with macroscopic phe-

nomena such as many particle effects [11] and charge transport. The non-equilibrium conditions in complete electrodes will lead to macroscopic gradients in diffusing species, and the associated potential gradients can change phase-transition kinetics, as has been demonstrated for $LiFePO_4$ [11]. Even when a model is obtained which reasonably describes the processes, it often involves a number of unknown physical parameters, which require fitting to experimental data. Although this may result in an appropriate model for conditions similar to those of the fitted experimental data, extrapolation to other operating conditions is uncertain [2], making accurate model validation under different conditions vital.

The introduction of phase-field modelling to the battery field [9, 12–14] has enabled accurate prediction of the phase transitions both in individual electrode particles and multi-particle systems [11] representing entire electrodes. This is computationally feasible because the phase-interface is taken implicitly into account [9], making it unnecessary to evaluate the phase transition kinetics in every position in an electrode particle.

Using phase-field models for $LiFePO_4$ the observed decreasing miscibility and spinodal gap in nano-particles [15] has been explained [13, 16], the observed transition from a first order phase transition to a solid solution reaction at high overpotentials [17, 18] has been predicted, and the transition from particle-by-particle to a concurrent mechanism was predicted [11] consistent with observations [19]. Recently a three-dimensional phase-field model has been presented for $LiFePO_4$ [16], and crack formation and the effects this causes have also been incorporated [20].

The phase-field method has also been used to describe the lithiation of graphite electrodes [21, 22], requiring the introduction of two first-order phase-transformations, which is relatively straight forward in a phase-field model, resulting in good agreement with experiments [21].

These results demonstrate the success of phase-field modelling of battery electrodes, and anatase TiO_2 is another ideal candidate for applying phase-field modelling. It has been extensively studied for more than two decades, in which all parameters required for the phase-field model have been measured experimentally. This will allow comparison of a parameter free phase-field model towards a broad range of experimental results available in literature.

Anatase TiO_2 is an attractive Li-ion battery electrode material, based on its cheap and abundant elements, high theoretical capacity of 335 mAh/g, small volume expansion during lithiation [23], and good electronic conductivity [24]. The TiO_2-anatase lattice consists of stacked one dimensional zigzag chains of TiO_6 octahedra sharing distorted edges, as shown in Figure 2.1. This stacking leads to empty zigzag channels with octahedral and tetrahedral interstitial sites that can accommodate lithium.

A typical voltage profile for lithiation of anatase is shown in Figure 2.1. At low Li-concentrations a solid solution is formed (region A), the length of which depends on the particle size [25–27]. Past the solid solution limit, phase separation occurs, reflected by the plateau in region B, where half of the octahedral sites are filled to form the Li-titanate phase ($Li_{0.5}TiO_2$). This is followed by a pseudo-plateau (region C) during which the remaining octahedral sites are filled, forming Li_1TiO_2. Even though this phase transition usually does not show a voltage plateau, it is reported to occur via a

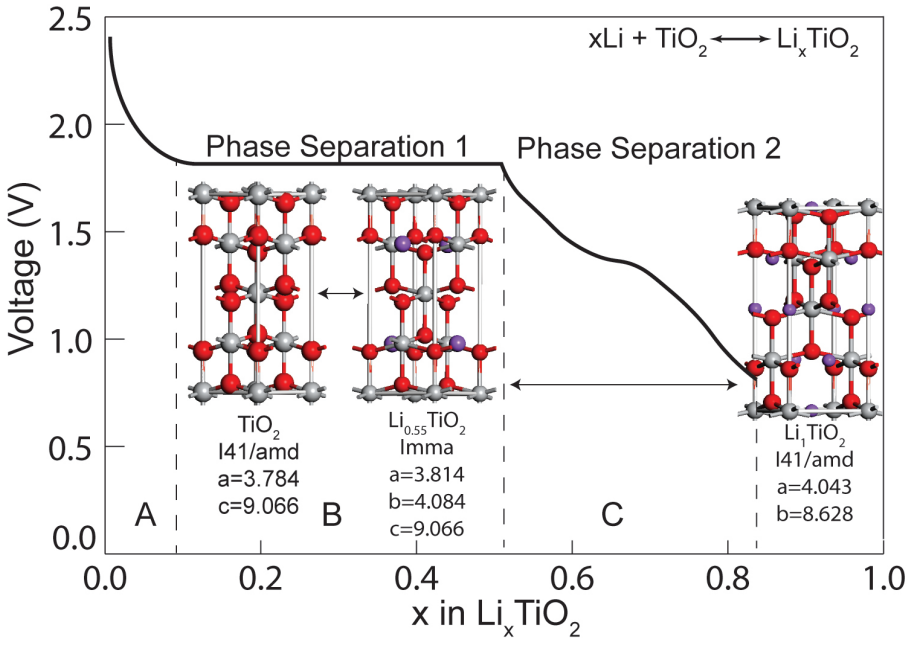

Figure 2.1: The crystal structure [23] and typical voltage profile of anatase during lithiation.

phase separation mechanism [26, 28].

In bulk anatase roughly 0.6 lithium per formula unit is reversibly inserted in most experiments [26, 27], leading to capacities of approximately 200 mAh/g. However, many parameters have been shown to affect the capacity drastically, including the preparation method [29], removing water from the anatase crystals before assembling the battery [30], the atmosphere during annealing [31], the morphology of the crystals [32], and the cut-off potential used during cycling [33]. However, the most decisive factor appears to be the particle size [26, 27, 34, 35]. By nano-sizing anatase particles the Li_1TiO_2-phase can be obtained at room temperature, realising the theoretical capacity of 335 mAh/g [23, 34].

For bulk samples complete lithiation via electrochemical experiments has been reported, but only when kinetic restrictions were removed, either by lithiating at 120°C [36, 37], or by allowing the anatase electrode to equilibrate during galvanostatic intermittent titration technique (GITT) measurements [25, 27]. Computational results also indicate that full lithiation is energetically favourable [28, 38], and attribute the fact that experimentally only small particles can fully lithiate to the slow Li-diffusion in the lithium rich phase (Li_xTiO_2, x >0.5) [38, 39], which has also been measured by NMR spectroscopy [40]. It has been suggested that the slow Li-diffusion makes the Li_1TiO_2-layer act as a blocking layer, preventing further lithiation [40].

Despite the large amount of research regarding anatase, a comprehensive explanation for its complex behaviour during lithiation is absent. In the present study, a phase-

field model free of fitted parameters for the lithiation of anatase TiO_2 is presented, based on microscopic parameters from the literature, describing both first-order phase-transitions.
The phase-field model for anatase consistently explains the experimentally observed phenomena, improving the understanding of TiO_2-anatase during Li-intercalation, and shedding light on the limitations and possibilities for anatase as an electrode material. Considering that this is achieved with a model that only contains parameters from the literature, this provides important validation for the physical foundation of phase-field modelling, especially considering the complex behaviour of anatase during lithiation. Furthermore, our work strengthens the background of simulating materials that undergo multiple phase transitions during lithiation, which poses a considerable challenge for conventional computational models.

2.2. PHASE-FIELD MODEL FOR ANATASE

In this section the phase-field model for lithiation in anatase-TiO_2 is presented. For a thorough background on phase-field modelling the reader is referred to several comprehensive publications [9, 41]. The most important macroscopic output variable for phase-field modelling of batteries is the measured cell voltage (V_{cell}) given by:

$$V_{\text{cell}} = -\frac{\Delta\mu}{e} + \eta_{\text{cell}} \tag{2.1}$$

where $\Delta\mu$ is the change in chemical potential, e the electron charge, and η_{cell} is the total cell overpotential.
The change in chemical potential is the difference in free energy of lithium at the solid-electrolyte interfaces of the anode and cathode material. For the simulated Li-metal/anatase system $\Delta\mu$ is the change in free energy for the reaction:

$$x\,\text{Li} + \text{TiO}_2 \longleftrightarrow \text{Li}_x\text{TiO}_2 \tag{2.2}$$

Li-metal is defined as the reference electrode, and consequently its chemical potential is defined as zero. Furthermore, the overpotential of the Li-metal electrode is assumed to be zero, which appears to be a good approximation given the small overpotentials experimentally observed for Li-metal electrodes [42]. These simplifications lead to a phase-field model in which only the lithiation of anatase needs to be taken into account to describe V_{cell}.
The two first-order phase-transitions occurring upon lithiation of anatase can be considered as two independent chemical reactions, since (locally) the two reactions cannot occur simultaneously, and can therefore be described by two independent lattices having their own free energy functional. The first lattice represents the reaction:

$$\text{TiO}_2 + 0.5\,\text{Li}^+ + 0.5\,\text{e}^- \longleftrightarrow \text{Li}_{0.5}\text{TiO}_2$$

and the second lattice represents the reaction:

$$\text{Li}_{0.5}\text{TiO}_2 + 0.5\,\text{Li}^+ + 0.5\,\text{e}^- \longleftrightarrow \text{Li}_1\text{TiO}_2$$

Similar to the phase-field model for graphite [43] this requires the introduction of two parameters (c_1 and c_2) that describe the Li-concentration in the first and second lattice, respectively. In both lattices the Gibbs free energy ($g(\tilde{c}_i)$) is described by a Cahn-Hilliard regular solution model [9]:

$$g(\tilde{c}_i) = k_B T\,(\tilde{c}_i \ln(\tilde{c}_i) + (1-\tilde{c}_i)\ln(1-\tilde{c}_i)) + \Omega_i \tilde{c}_i (1-\tilde{c}_i) + \frac{1}{2}\frac{\kappa_i}{c_{max}}|\nabla \tilde{c}_i|^2 + \tilde{c}_i \mu_i^{\Theta} \tag{2.3}$$

where k_B is Boltzmann's constant, T the temperature in Kelvin, $\tilde{c}_i$ the normalised concentration in lattice i ($\tilde{c}_i = \frac{c_i}{c_{max}}$), Ω_i the enthalpy of mixing, μ_i^{Θ} the reference potential versus. Li/Li^+, and κ_i the gradient penalty parameter.
The first term in Equation 2.3 describes the entropy change upon adding Li-ions ($\tilde{c}_i$) and removing Li-vacancies ($1-\tilde{c}_i$). The enthalpy of mixing (Ω_i) describes the interactions between Li-atoms in an intercalation material. Positive values for Ω_i correspond to attractive forces between Li-atoms, favouring phase separation into the end member phase (a Li-rich and a Li-poor phase). The κ_i-term represents the energy penalty for the existence of concentration gradients when phase-separation occurs, with larger values for κ_i leading to a wider interface region between Li-rich and Li-poor phases.
Large entropy and κ_i-terms in Equation 2.3 promote solid solution behaviour, while a large Ω_i-term will promote phase-separation. Which term dominates, and thus determines the phase-behaviour of a material, not only depends on the values of the parameters, but also on C-rate, temperature, and particle size [3, 17, 44, 45].
The diffusional chemical potential (μ_i) of lithium in anatase is given by the variational derivative of the free energy with respect to concentration [41]:

$$\mu_i = \frac{\partial g_i}{\partial \tilde{c}_i} - \nabla \cdot \frac{\partial g_i}{\partial \nabla \tilde{c}_i} \tag{2.4}$$

Using Equation 2.3 this gives:

$$\mu_i = k_B T \ln\left(\frac{\tilde{c}_i}{1-\tilde{c}_i}\right) + \Omega(1-2\tilde{c}_i) - \frac{\kappa_i}{c_{max}}\nabla^2 \tilde{c}_i + \mu_i^{\Theta} \tag{2.5}$$

From the diffusional chemical potential the flux of lithium (F_i) through the particle can be determined based on the gradient of the diffusional chemical potential ($\nabla\mu_i$) [9]:

$$F_i = -M_i c_i \nabla \mu_i = -\frac{D_i c_{max} \tilde{c}_i}{k_B T}\nabla \mu_i \tag{2.6}$$

where M_i is the mobility and D_i is the tracer diffusivity.
It is known that the lithium diffusion in TiO_2 anatase is dependent on the lithium concentration, but the effect of the Li-concentration on Li-diffusion is unclear. Papers with calculations show contradicting results, with some reporting a large [38] or small [46] increase in activation energy for Li-diffusion with increasing Li-concentration, while others show a large [47] or small [39] decrease in activation energy at higher Li-contents. Experiments by Sussman et al. [48] show a decrease in Li-diffusivity with increasing Li-content, although the magnitude of this effect strongly depends on the

synthesis procedure.
The simplest approximation for the tracer diffusivity on a lattice is proportional to the vacancy concentration, $D_i \sim (1-c_i)$, in order to account for site exclusion [9, 14] and for thermodynamic consistency with binary species mixing [49], but we find that this model is not able to reproduce the general features of the experimental voltage profiles. On the other hand, ab initio calculations predict a much stronger concentration dependence, where the chemical diffusivity drops by many orders of magnitude between the TiO_2-, $Li_{0.5}TiO_2$- and Li_1TiO_2-phases [38], thus indicating stronger cooperative diffusion barriers. As a first approximation of such effects, we introduce a simple power-law correction:

$$D_i = D_i^* \frac{(1-\tilde{c}_i)}{\tilde{c}_i} \tag{2.7}$$

where D_i^* is the reference tracer diffusivity in lattice i at $c_i = 0.5$. Despite the unphysical divergence at $c_i = 0$, the diffusivity effectively saturates at realistic values in our phase-field simulations, since the regular solution model only allows small, but finite, concentrations. Combining Equations 2.6 and 2.7, the flux of lithium is given by:

$$F_i = -\frac{D_i^* c_{\max}(1-\tilde{c}_i)}{k_B T} \nabla \mu_i \tag{2.8}$$

which is simply proportional to the vacancy concentration. The implied chemical diffusivity $D_i^{\text{chem}} = D_i^* \left(\frac{(1-\tilde{c}_i)}{\tilde{c}_i} - 2\Omega_i (1-\tilde{c}_i)^2 \right)$, is negative in the spinodal regions of thermodynamic instability, while capturing the strongly decreasing trend across the solid solution phases [38], similar to the experiments of Sussman et al. [48]. We find that this model is also capable of providing a good fit of the experimental voltage profiles. Using Equation 2.5 and 2.8 the behaviour of lithium inside anatase particles can be described, but to determine the battery voltage and influx of lithium the charge-transfer reaction at the electrode-electrolyte interface must also be described. This can be done using the Butler-Volmer equation [41]:

$$I_i = \frac{k_0 n e (a_O a_e^{\eta})^{1-\alpha} a_{R,i}^{\alpha}}{\gamma_i^{\ddagger}} \left(\exp\left(-\frac{\alpha e \eta_{\text{eff},i}}{k_B T} \right) - \exp\left(\frac{(1-\alpha) e \eta_{\text{eff},i}}{k_B T} \right) \right) \tag{2.9}$$

where I_i is the current density in lattice i, k_0 the reaction rate constant per surface area of the particle, α the reaction symmetry factor (assumed to be 0.5), n the number of electrons participating in the reaction (one in this case), and e the electronic charge. The charge-transfer overpotential ($\eta_{\text{eff},i}$) is defined as: $e\eta_{\text{eff},i} = \mu_{R,i} - \mu_O$, where $\mu_{R,i}$ (the chemical potential of the reduced state of Li) is obtained from Equation 2.5, μ_O (the chemical potential of the oxidised state of Li) depends on the Li-concentration in the electrolyte (c_{lyte}) and is approximated using a dilute electrolyte model as: $\mu_O = k_B T ln(c_{\text{lyte}})$. The activity of the oxidised state (a_O) is equal to c_{lyte}, the activity of the electrons a_e is taken to be unity, thus assuming that the Fermi level is unaffected by the changing lithium concentration [9]. The activity of the reduced state ($a_{R,i}$) depends on the diffusional chemical potential (μ_i) of lithium inside the particle: $a_{R,i} = \exp\left(\frac{\mu_i - \mu^{\ominus}}{k_B T} \right)$, and the activity of the transition state ($\gamma_i^{\ddagger}$) depends on the concentration of lithium-vacancies [44]: $\gamma_i^{\ddagger} = \frac{1}{1-\tilde{c}_i}$. During constant current simulations the

applied current ($I_{\text{applied}} = (I_1 + I_2) * \text{Area}$) is known, thus $\eta_{\text{eff},i}$ can be calculated.
The charge-transfer overpotential given by Equation 2.9 describes the thermodynamic driving force for a lithium-ion to enter/leave the electrode particle. All the terms in Equation 2.9 depend on the diffusional chemical potential or concentration of lithium, i.e. the size of the charge-transfer overpotential is determined by the Li-concentration of the electrode and electrolyte near the electrode-electrolyte interface. Using the equations given above, the diffusional chemical potential of Li in the particles (Equation 2.5), the Li-flow through the particle (Equation 2.8), and the Li-flow into the anatase particles (Equation 2.9) can be described. Using the appropriate set of boundary conditions this set of equations can be solved [50], ultimately giving the cell voltage (Equation 2.1), and the Li-concentration inside the anatase particles.
In contrast to the graphite phase-field model [21, 22], which directly couples the two phase transitions, the anatase model consists of two independent lattices. The reason for this are the very different physical properties of the first and second phase transition in anatase, while in graphite the only difference between the two phase transitions (relevant to the phase-field model) is the voltage. To describe the two phase transitions in anatase different parameters are necessary, which can be implemented by introducing two independent lattices with different physical properties, schematically shown in Figure 2.2. At the start of the lithiation process the first phase transition will occur due to its higher intercalation potential, filling the first lattice with Li-ions. When the first lattice fills the charge-transfer overpotential will increase (lowering the voltage), because it gradually becomes harder to add more Li-ions. When the intercalation potential of the second lattice is reached lithiation of the second lattice becomes favourable, and the second phase transition will start. There are no interaction terms between the two lattices, since the effect the first lattice has on the second is already incorporated by the different parameters that are used. In Table 2.1 all parameters and their values from literature are listed, as well as what each one is based on.

Normally, several physical parameters necessary for phase-field modelling are not available, either experimentally or computationally, and are therefore fitted by optimising the phase-field model towards experimental voltage profiles. Intensive research towards lithiation of anatase TiO_2 during the last decades makes it possible to quantify all parameters necessary for the present phase-field model. Thus providing a unique opportunity to validate a phase-field model, using only parameters from the literature, with micro- and macroscopic observations.
The reference potentials μ_1^Θ and μ_2^Θ are based on literature data which are closest to equilibrium conditions at room temperature. μ_1^Θ is based on GITT measurements [25, 27] performed at room temperature, but for the second phase transition equilibrium is not even reached during the reported GITT measurements. Therefore the value for μ_2^Θ is taken from experiments performed at 120°C, in which the second plateau indicates that equilibrium was reached [36, 37].
For anatase electrodes electrochemical experiments have reported diffusivities in the first lattice between $5 * 10^{-10}$ and $4 * 10^{-20}$ cm^2/sec [48, 51–53, 56–59], and changes of 2 orders of magnitude during charging have been reported [48]. Furthermore, calculations on Li-diffusion in anatase also show strongly differing results [38, 39, 46, 47], and NMR experiments indicate that diffusion over the interface between the anatase and

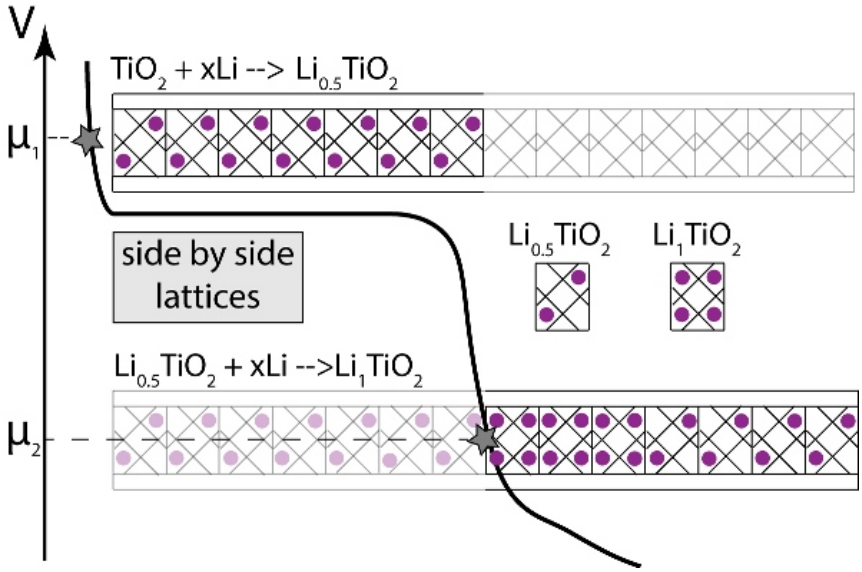

Figure 2.2: Schematic representation of the two lattice phase-field model for lithiation in anatase TiO_2.

Parameter	Value	Units	Based on
μ_1^Θ	1.82	V	GITT experiments [25, 27]
μ_2^Θ	1.56	V	Electrochemical experiments at 120°C [36, 37]
D_1^*	$1 * 10^{-16}$	cm^2/sec	Electrochemical experiments [51–53]
D_2^*	$1 * 10^{-17}$	cm^2/sec	Force-field molecular dynamics simulations [39]
Ω_1	$0.6 * 10^{-20}$	J/Li	DFT calculations [28, 38]
Ω_2	$1.6 * 10^{-20}$	J/Li	DFT calculations [28, 38]
κ_1	$5.3 * 10^{-8}$	J/m	Phase diagram (see text) [26]
κ_2	$0.8 * 10^{-8}$	J/m	Phase diagram (see text) [26]
c_{max}	$1.419 * 10^{28}$	Li/m^3	Neutron diffraction [54]
k_0	0.049	A/m^2	NMR experiments [55], see Supporting Information

Table 2.1: Values for the model parameters and on what information they are based.

Li-titanate phases [60, 61] is the limiting step. For the second lattice no experimental value for the diffusivity has been reported, but NMR experiments [40] and calculations [38, 39] have shown that it is smaller than in the first lattice .

Given the large range of values in the literature for Li-diffusion in TiO_2 anatase several values from the literature were used for testing, after which the simulated voltage profiles were compared to experimental ones. The best agreement with experiments was obtained using a value of $1*10^{-16}$ cm^2/sec for D_1^*, which has been reported by several experimental studies [51–53]. For D_2^* a value of $1*10^{-17}$ cm^2/sec gave the best results, which is obtained from molecular dynamics simulations [39].

Since it is impossible to experimentally measure the enthalpy of mixing the values for Ω_1 and Ω_2 are based on DFT calculations [28, 38], the values were determined by the difference between the convex hull and the configurational energies. Values of κ_1 and κ_2 are based on the particle size at which two phase coexistence inside a particle no longer occurs [26]. This means that for the radial 1D-model presented here the interface width (λ_i) corresponds to half of the particle size [15], which gives interface widths of 25 and 6 nm for lattice 1 and 2, respectively. Using these interface widths κ_i can be calculated using [9]:

$$\kappa_i = \lambda_i^2 c_{\max} \Omega_i \tag{2.10}$$

The maximum Li-concentration ($c_{\max}$) is calculated based on the four Li-sites per unit cell upon complete lithiation and the volume [54] of the unit cell of $Li_{0.5}TiO_2$ divided over the two lattices. There is a small volume change (3%) upon lithiation from TiO_2 to $Li_{0.5}TiO_2$, but given that the volume differs by just 0.1% between $Li_{0.5}TiO_2$ and Li_1TiO_2, the volume of $Li_{0.5}TiO_2$ is the best approximation over the range of possible Li-concentrations.

The equilibrium charge transfer constant (k_0) is typically not known because it is very hard to experimentally distinguish the Li reaction between electrolyte and electrode from other processes occurring simultaneously. However, using NMR this has been shown to be possible by Ganapathy et al. [55], reporting k_0 for the $Li_{0.5}TiO_2$ phase, which is at present assumed to be representative for both lattices. Please note that physically the second phase transformation can only occur after the first phase transformation has happened (locally), and although this is not formally implemented in the model the 0.26 V lower insertion potential satisfies this condition during the simulations. To keep the model simple all properties of anatase were assumed to be isotropic, a reasonable assumption given the 3D-diffusion pathway [39] and small changes in lattice parameters upon lithiation [23]. During lithiation of anatase TiO_2 the interfaces with the Li-rich phase are predicted to occur along strain invariant planes [38]. For this reason it was assumed that the role of strain and of stress assisted diffusion can be neglected in the present 1D-simulations.

The simulations were performed using a modified version of the publicly available MPET code [62], in which the coupled differential equations are solved using the DAE tools package [63]. A 1D-model along the radial direction of the particles is used for the simulations, and unless stated otherwise simulations were performed on a single particle with a radius of 20 nm., a C-rate of 0.5C, a temperature of 298 K, and a cut-off voltage of 1 V vs. Li/Li^+. For the single particle simulations the Li-concentration in the electrolyte was assumed to be constant, in multi-particle simulations the dilute

electrolyte model as implemented in the MPET code [41] was used to describe the Li-concentration in the electrolyte.

2.3. Results

The results of the phase-field model for lithiation of anatase TiO_2 are compared to a broad spectrum of experimental results available in literature. The aim here is qualitative validation of the phase-field model and understanding of the physical processes that determine the performance of anatase electrodes. A qualitative validation rather than a quantitative validation is motivated by the many experimental parameters that affect the performance of anatase electrodes, resulting in a wide distribution of performances, even for equivalent electrochemical conditions [29].

2.3.1. Impact of lithiation rate

Similar to other electrode materials the (dis)charge rate, expressed in the C-rate (a 2C rate corresponds to (dis)charge of the full theoretical battery capacity in 1/2 hour, 1C in 1 hour, 0.5C in 2 hours, etc.) has a large impact on the voltage profile of anatase electrodes. Typically the capacity drops by approximately 25% when going from cycling at 0.5C to 1C [59], and at higher C-rates a significant drop of the plateau voltage is detected [64].

The drop in capacity and voltage with increasing lithiation rate are both consistently reflected in the simulated voltage profiles for a single anatase particle with a radius of 20 nm shown in Figure 2.3a. At 5C the simulation leads to a maximum composition of $Li_{0.45}TiO_2$, increasing to $Li_{0.7}TiO_2$ at 0.5C, and at 0.01C the anatase particle is almost completely lithiated. With increasing lithiation rate the increasing charge-transfer overpotential results in a voltage drop in Figure 2.3a, driven by limited Li transport away from the surface. The significant decrease in voltage upon increasing the current from 0.01C to 0.1C indicates poor Li-ion kinetics in anatase, in particular considering the small particle radius of 20 nm. Generally, 0.1C results in close to equilibrium conditions in most nano-structured electrode materials, whereas in anatase TiO_2 Li-ion kinetics still restricts the capacity at this rate.

The large voltage drop at high C-rates for the second voltage plateau indicates that the formation of the Li_1TiO_2 phase limits the charge transport away from the surface, thus increasing the charge-transfer overpotential. An estimate for the time it takes a Li-ion to reach the center of the particle can be obtained by calculating the characteristic diffusion time [65], t_D, defined as:

$$t_D = \frac{R^2}{D} \tag{2.11}$$

where R is the particle radius and D the diffusion constant. For a particle with a radius of 20 nm, the characteristic time for diffusion in the $Li_{0.5}TiO_2$ and Li_1TiO_2 are approximately $4 * 10^4$ and $4 * 10^5$ seconds, respectively. For the first voltage plateau, the phase transition towards $Li_{0.5}TiO_2$, this roughly corresponds to 0.1C. Therefore, at this rate the entire voltage plateau associated with the first phase transition should be observed, consistent with Figure 2.3a.

For the second voltage plateau, the phase transition towards Li_1TiO_2, the characteristic

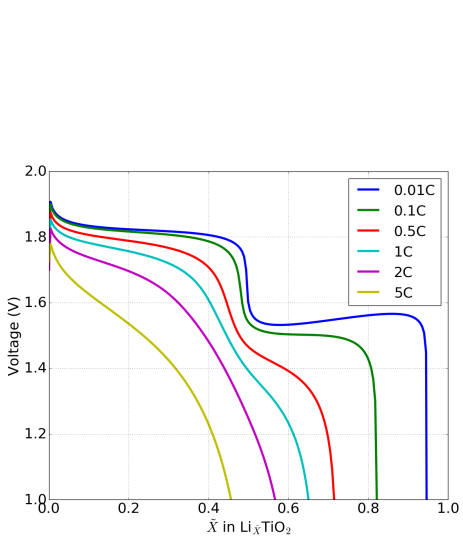

(a)

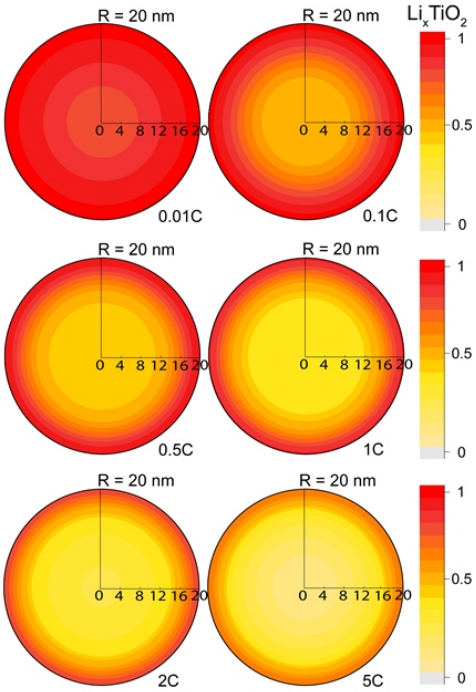

(b)

Figure 2.3: (a) Voltages profiles versus average concentration ($\tilde{X}$) and (b) final concentration profiles in the particle at different C-rates.

time roughly corresponds to 0.01C, consistently reflected by the complete appearance of the second voltage plateau at this C-rate in Figure 2.3a. At time-scales shorter than t_D the lithium ions are unable to reach the centre of the particle within the given time, i.e. kinetic limitations will restrict the capacity and decrease the cell voltage, as visible at higher C-rates in Figure 2.3a. This is confirmed by the Li-ion concentration profiles shown in Figure 2.3b, in which at 0.01C most of the particle is transformed to the Li_1TiO_2-phase. At 0.5C only a thin layer at the surface approaches the maximum composition Li_1TiO_2, and the inner 10 nm is only transformed to the $Li_{0.5}TiO_2$-phase. At 5C this effect is augmented, with a large part of the particle having a Li-concentration below $x = 0.5$, and only near the surface the Li-concentration exceeds $x = 0.5$.
For experimental electrochemical lithiation at room temperature only the onset of the second voltage plateau is observed, as consistently predicted by the simulation at 0.5C in Figure 2.3a. Raising the temperature to 120 °C will significantly enhance Li-diffusion, largely lifting the diffusional limitations of the second lattice, resulting in a clear experimental observation of the second voltage plateau at 120 °C [36, 37]. The simulation at a very slow lithiation rate, 0.01C, predicts that particles with a 20 nm. radius can also be fully lithiated at room temperature. Although no experimental evidence showing this appears present (to the best of our knowledge), GITT measurements on particles with a diameter of 130 nm have been shown to reach full lithiation [25].
As shown in Figure 2.4 the increasing voltage at 0.01C is caused by simulating only a single particle, and repeating the same simulation with 10 particles gives a flat voltage profile. For a single particle the voltage follows the spinodal potential, giving an upwards slope in the voltage profile [66]. The difference is caused by the fact that a single particle will always follow the spinodal line, which is inherently unstable [44], but a single particle cannot depart from the spinodal line. When multiple particles are present interparticle phase-separation can occur, which smooths the voltage curve [21, 66].

In order to gain understanding of the rate limiting kinetic mechanism in anatase TiO_2 electrodes, multi-particle simulations were performed. A 50 μm porous electrode was separated into five volumes connected in series reflecting different depths inside the electrode, and each volume contained five particles with a 20(±2) nm radius. The chosen rate is 2C, since at this rate the performance of the material already results in a significant decrease in the capacity and voltage, as shown in Figure 2.3. The results of the multi-particle simulations in Figure 2.5 demonstrate that the lithiation process proceeds concurrently at any given depth of the electrode. All particles are transforming simultaneously, which implies that the Li-ion diffusion in a single anatase grain is rate limiting, even when the particles are nano sized. In an actual electrode the consequence is that all grains are actively participating in delivering the current, thus electrode performance can be improved significantly by increasing the Li-diffusivity in the anatase lattice. For comparison, in the simulation shown in Figure 2.5 the typical diffusion time (t_D) through the electrolyte is 10 seconds (using an ambipolar diffusivity of $2.5 * 10^{-6}$ cm^2/sec), three orders of magnitude below the t_D inside the particles.
Furthermore, Singh et al. [24] have shown that TiO_2 anatase without electron conducting additives has excellent cycling behaviour. Thus electrode performance of TiO_2

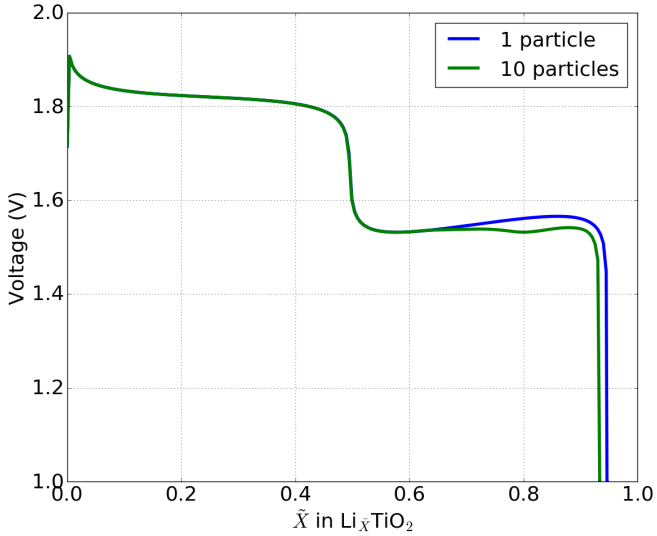

Figure 2.4: Voltage profiles for simulations with 1 and 10 particles at 0.01C.

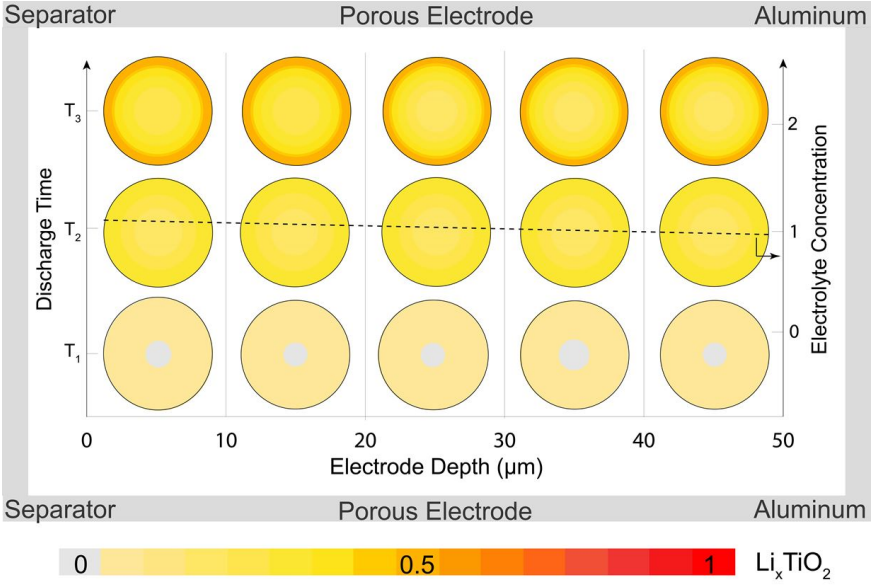

Figure 2.5: Li-ion concentration profiles in the electrolyte and in electrode particles at different electrode depths at different times during 2C discharge. The filling fraction in the displayed particles is the average of that in the simulated particles in each volume.

anatase can primarily be improved by increasing the Li-diffusivity in the anatase lattice, and only slightly by enhancing the ionic and electronic wiring. This behaviour differs from other electrode materials, such as $LiFePO_4$, $Li_4Ti_5O_{12}$, and $LiCoO_2$, where it has been shown that for full electrodes the ionic and electronic wiring dominate the internal resistance from small to large (dis)charge rates [67–71].
Interestingly, in $LiFePO_4$ the increasing overpotential when increasing the C-rate widens the interface between the coexisting phases, at some critical rate leading to a solid-solution reaction as predicted by phase-field modelling [44] and observed experimentally [17–19]. In anatase TiO_2 the phase interface also widens when increasing the C-rate; however, even at large C-rates the Li_1TiO_2 phase forms at the particle surface, because of the poor Li-ion diffusivity. Thus the model predicts that anatase TiO_2 will undergo phase separation regardless of the imposed current.

2.3.2. Impact of Li-diffusion coefficient

The impact of the C-rate on the capacity and voltage for anatase TiO_2 electrodes reveals that the Li-ion diffusivity in the anatase lattice is the key limiting factor. Experimentally the Li-diffusivity has been increased by annealing in argon [31], by hydrogen treatment [56], and by Ti^{3+} doping [72], which all increase the amount of oxygen vacancies in TiO_2. Impedance measurements have shown that this can increase the Li-diffusivity by one order of magnitude [56]. To capture the effects of a higher Li-diffusivity, simulations were performed at 0.5C and 2C, where the Li-diffusion in both lattices is increased by a factor of 2, 5 and 10 compared to the values given in Table 2.1.
As should be anticipated, this results in larger capacities and higher voltages with increasing diffusivity, as shown in Figure 2.6, consistent with experimental observations [31, 56, 72]. For the lithium concentrations in the particle the higher diffusivity results in an extension of the Li_1TiO_2 phase from the surface into the particle. At 0.5C the inside of the particle transforms completely to the $Li_{0.5}TiO_2$ phase, even for the original diffusivity. Transformation of the inside of the particle to the $Li_{0.5}TiO_2$ phase at 2C does not occur when using the original diffusivity. To achieve this transformation at 2C the diffusivity must be increased by a factor of at least 5. These results confirm that increasing the diffusivity is a promising way to increase the capacity of anatase electrodes, especially when aiming at high (dis)charge rates.

2.3.3. Impact of surface area

The simulations shown in Figure 2.3 and 2.6 predict large charge-transfer overpotentials during the lithiation of anatase particles. These large overpotentials are caused by a high Li-concentration near the surface of anatase particles, making it hard for Li-ions to enter into the anatase particles. A reduction in the surface Li-concentration can be achieved by increasing the surface area, which will lead to smaller charge-transfer overpotentials. An additional advantage is that a larger surface areas also lowers the current density, which further decreases the charge-transfer overpotential. This leads to larger capacities, as has been demonstrated by various experimental studies on high surface area anatase particles [73–75]. To capture the surface area effect simulations were performed on a spherical and a cylindrical particle (infinitely

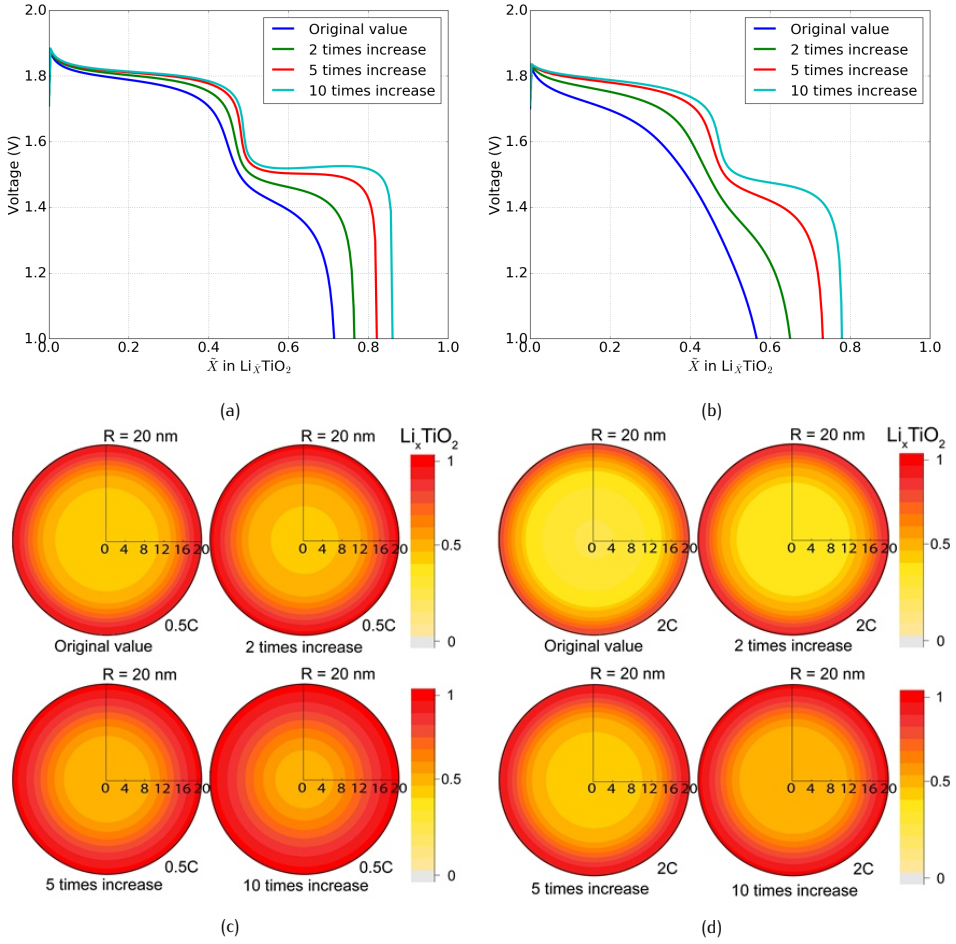

Figure 2.6: Voltage profiles versus average concentration ($\bar{X}$) for different increases in diffusivity at (a) 0.5C, and (b) 2C, and final concentration profiles inside the particles at (c) 0.5C and (d) 2C.

long, i.e. neglecting the top and bottom surface of the cylinder). The spherical particle has a surface to volume ratio of $\frac{3}{R}$, whereas the cylindrical particle has a smaller surface to volume ratio of $\frac{2}{R}$.

The concentration profiles in Figure 2.7b show that when the cut-off voltage is reached

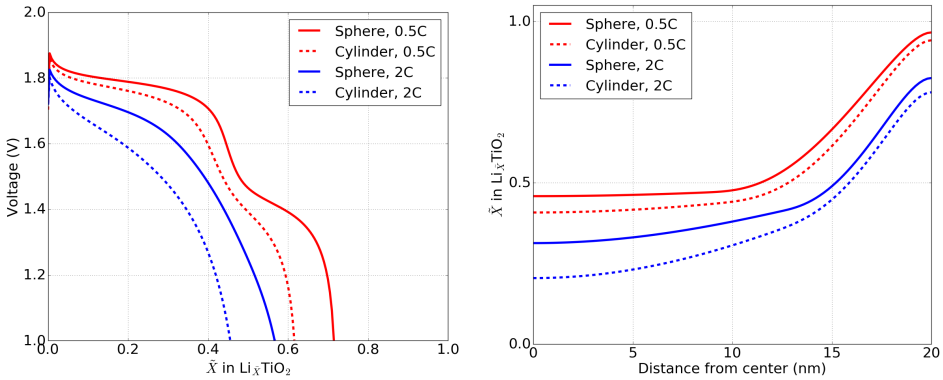

(a) (b)

Figure 2.7: (a) Voltage profiles versus average concentration ($\tilde{X}$) and (b) final concentration profiles of a spherical and a cylindrical particle at 0.5C and 2C.

the Li-concentration near the surface is comparable in the spherical and cylindrical particle. However, the larger surface area of the spherical particle allows for a larger Li-ion flux into the anatase TiO_2 particle, resulting in a final Li-fraction approximately 20% larger compared to the cylindrical particle. As shown in Figure 2.7a, at 0.5C relatively small differences for the first voltage plateau are predicted, the difference in capacity being primarily caused by the second phase transition. This is because the slower diffusion in the second phase leads to high Li-concentrations near the surface more quickly, and thus high charge-transfer overpotentials at an earlier stage. Increasing the C-rate to 2C significantly augments this effect, raising the difference in charge-transfer overpotential between the spherical and cylindrical particle, although the decrease in final Li-composition is similar when compared to 0.5C.

Experimentally similar observations are reported upon increasing the surface area [73–75]. However, higher surface areas are usually achieved by reducing the particle size [73, 74], which has a similar impact on the voltage profiles, as shown in Figure 2.8 and discussed below, making it hard to distinguish between the effects of nano-sizing and particle shape.

2.3.4. Impact of particle size

When Li-ion diffusion limits the electrode performance, decreasing the diffusion distance through the electrode material by particle size reduction is a well-established strategy to reach improved rate performance. Smaller particles increase the surface to volume ratio, which has been shown to be beneficial in the prior section. Additionally, particle size reduction has been shown to change the thermodynamics by increasing

the solubility limits, which in small particles can even lead to suppression of phase separation, as shown for anatase TiO_2 [26, 76] and $LiFePO_4$ [13, 15].
A solid solution reaction can be expected to enhance Li-ion kinetics, in anatase specifically by suppressing the phase transition towards Li_1TiO_2 at the particle surface, thereby promoting Li-ion transport and resulting in higher voltages and larger capacities at high C-rates. Indeed for anatase TiO_2 particle size reduction has been shown to improve performance drastically, for instance resulting in complete lithiation of 7 nm particles at C/20 [23], whereas large particles cannot practically be lithiated to compositions exceeding $Li_{0.6}TiO_2$ [26, 34]. Consistently, phase-field simulations for different particle sizes, shown in Figure 2.8, predict that decreasing the particle size diminishes kinetic limitations, resulting in nearly complete lithiation of 5 nm radius particles at 0.5C.
Experimentally it has been reported that only the first few nanometres near the sur-

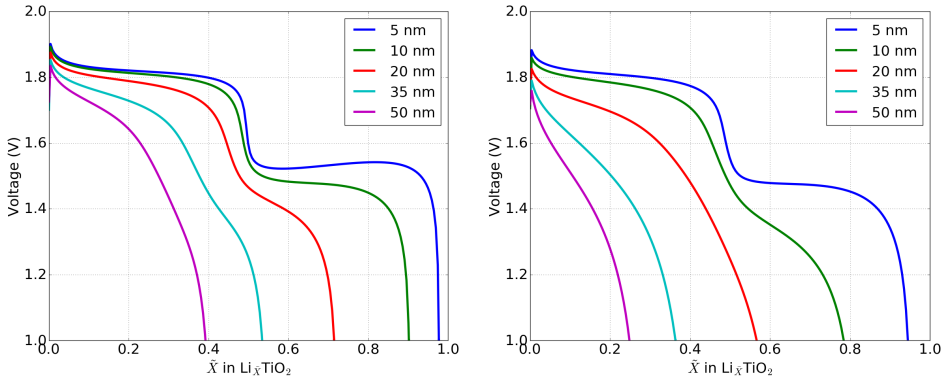

Figure 2.8: Voltage profiles versus average concentration ($\tilde{X}$) for particles with different radii at (a) 0.5C and (b) 2C.

face transform to the Li_1TiO_2 phase [26, 40, 77], explaining why only nano-particles are able to reach the theoretical Li_1TiO_2 composition [23, 26]. This is fully supported by the predicted concentration profiles in Figure 2.9. At 0.5C and 2C particles with a 5 nm radius transform completely to the Li_1TiO_2 phase, while in bigger particles only the first few nanometres at the surface transform to the Li_1TiO_2 phase. As a consequence decreasing the particle size increases the capacity, in particular because of the increasing utilization of the second phase transition.

Increasing the C-rate makes these effects more pronounced. For example, the final Li-composition of a 50 nm radius particle decreases from $Li_{0.39}TiO_2$ to $Li_{0.25}TiO_2$ when increasing the rate from 0.5C to 2C, while it only drops from $Li_{0.98}TiO_2$ to $Li_{0.94}TiO_2$ in a 5 nm particle. In the first place improved performance upon particle size reduction can be understood through the trivial effect of reducing the diffusion distance. The phase-field simulations also demonstrate that the non-trivial size effect, the destabilization of the first order phase transition, plays a crucial role in the enhanced performance of the smaller particles. As shown in Figure 2.11 the thickness of the Li_1TiO_2-layer

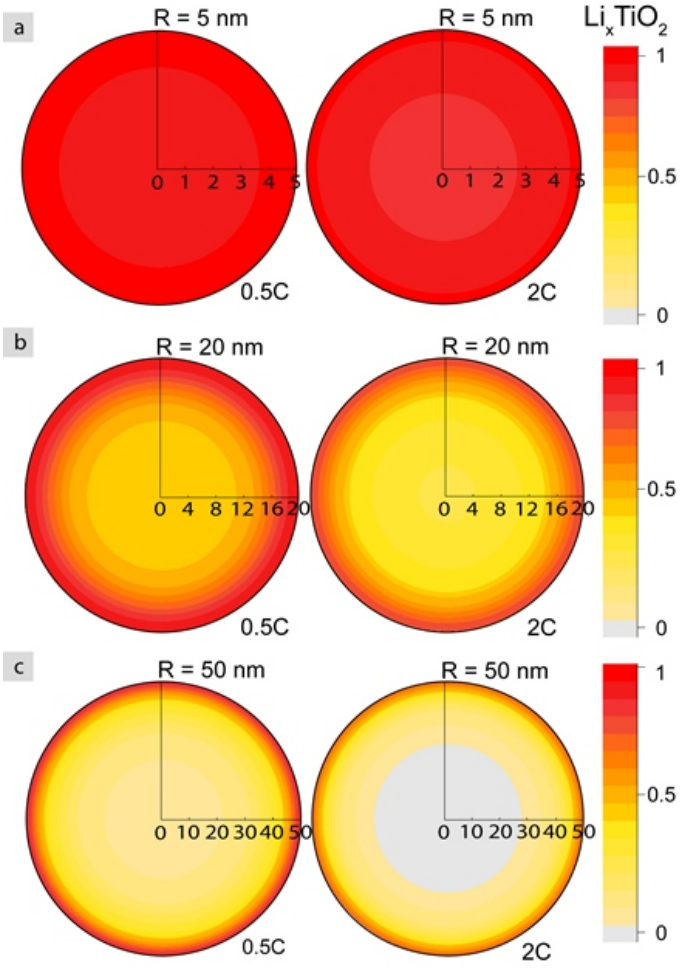

Figure 2.9: Final concentration profiles at the end of a simulation at 0.5C and 2C for particles with a radius of (a) 5 nm, (b) 20 nm, and (c) 50 nm.

depends on particle size, with smaller particles having thicker Li_1TiO_2-layers. When the particle size approaches the width of the interface between the coexisting phases, phase separation is suppressed as previously shown for $LiFePO_4$ [13, 15].
For the TiO_2-$Li_{0.5}TiO_2$ and $Li_{0.5}TiO_2$-Li_1TiO_2 transitions the interface widths are approximately 40 nm and 5 nm, respectively [26], directly related to the gradient penalty (κ). This explains the evolution of the Li-ion concentration throughout the 5 and 50 nm particles shown for 0.5C in Figure 2.10. The 5 nm particle completely lithiates through a solid solution reaction in which both phase transitions are suppressed due to the small particle size. In the 50 nm particle the first transformation from TiO_2 to $Li_{0.5}TiO_2$ is largely suppressed because it approaches the interface width of approximately 40 nm. However, at this particle size the second transition from $Li_{0.5}TiO_2$ to Li_1TiO_2 is not suppressed.

The consequence of the particle size induced solid solution behaviour is that the for-

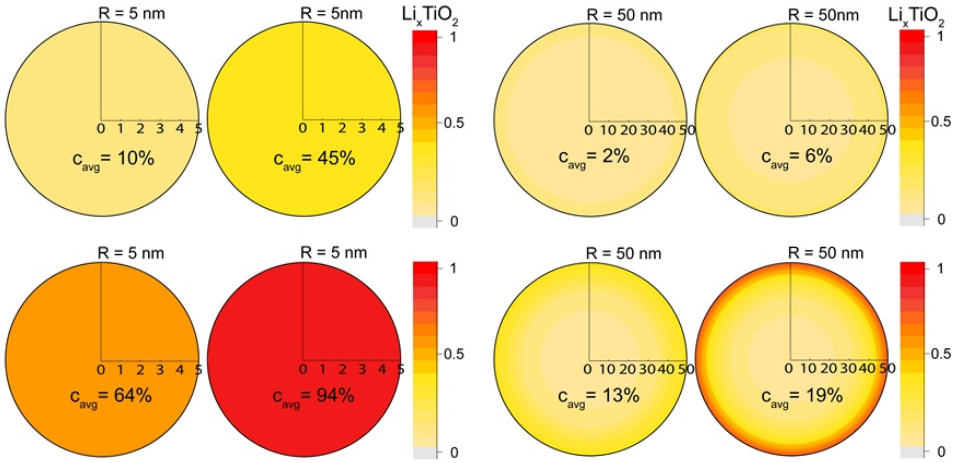

Figure 2.10: Concentration profiles during a 0.5C simulation at different lithiation stages for particles with a radius of (a) 5 nm and (b) 50 nm.

mation of the blocking Li_1TiO_2 phase at the particle surface is prevented, as observed in Figure 2.9, resulting in higher voltages and larger capacities for small particles. In larger particles phase separation will occur, and Li-concentrations near the surface will approach Li_1TiO_2. The poor Li-diffusivity in the Li_1TiO_2 phase prevents moving of the phase boundary away from the surface, and the Li_1TiO_2 surface layer will block further lithiation of the particle.
To show how this affects battery capacity, the final capacity vs. C-rate and final thickness of the Li_1TiO_2-layer vs. C-rate are shown for different particle sizes in Figure 2.11. Figure 2.11 shows that the thickness of the blocking Li_1TiO_2 layer strongly depends on the particle size and C-rate, and that this is strongly correlated with the final capacity. As shown in Figure 2.11 to obtain high capacities small particles or low C-rates are required, otherwise the layer of Li_1TiO_2 forming at the surface will

block Li-intercalation.

To obtain a general prediction of the maximum obtainable capacity as a function of

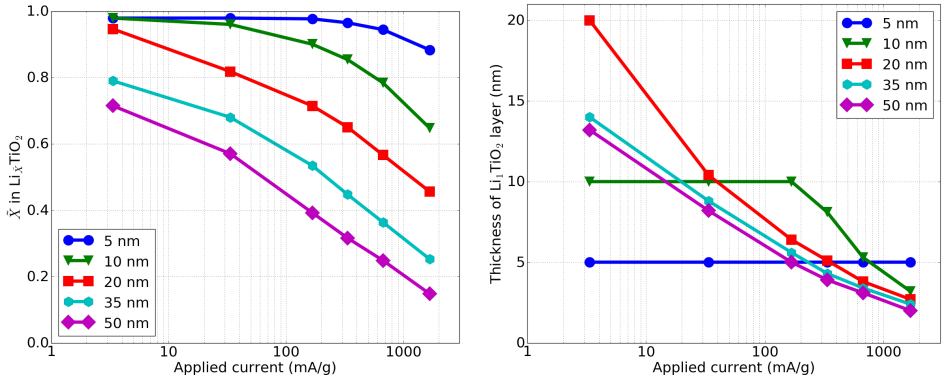

Figure 2.11: For different particle sizes and C-rates the (a) final Li-concentrations and (b) final thickness of the Li_1TiO_2 layer (defined as the depth at which $Li_{0.6}TiO_2$ occurs), the lines are a guide to the eye.

applied current the concept of Sand's time [78] could be used. However, to incorporate the non-linear Li-flux through the anatase particles, which also depends on the particle size, modifications to the formulation of Sand's time are necessary. For small particles the simulations show good agreement with experiments, but for large particles (>35 nm.) the simulated maximum particle composition is significantly smaller than $Li_{0.6}TiO_2$ at moderate C-rates (>0.5C), underestimating experimental observations [26, 34].

We propose two arguments for this. First, in experiments the surface area is larger compared to that of spherical particles assumed in the simulations. As a consequence the present simulations underestimate the amount of Li_1TiO_2 formed, explaining the smaller capacities predicted. Second, although the phase-field calculations predict the extended solubility limits, the subsequently enhanced Li-ion diffusivity is not implemented. Implementing this would require a diffusion term which depends on the local Li-concentration and the gradient of the Li-concentration, which requires further research outside of the scope of this study. Therefore the Li-ion diffusivity in particles where the solubility limits are significantly affected will be underestimated. This will be relevant for particle sizes comparable to the interface width, where in particular the larger interface width of the first phase transition enhances the Li-ion solubility limits. Thus explaining why for particles larger than 35 nm the present phase-field calculations underestimate the capacities as compared to experiments.

2.4. Discussion

As summarised in Figure 2.12, the second phase transformation towards the Li_1TiO_2 phase at the surface of anatase TiO_2 particles is primarily responsible for the performance of anatase as Li-ion battery electrode. During lithiation TiO_2-anatase is

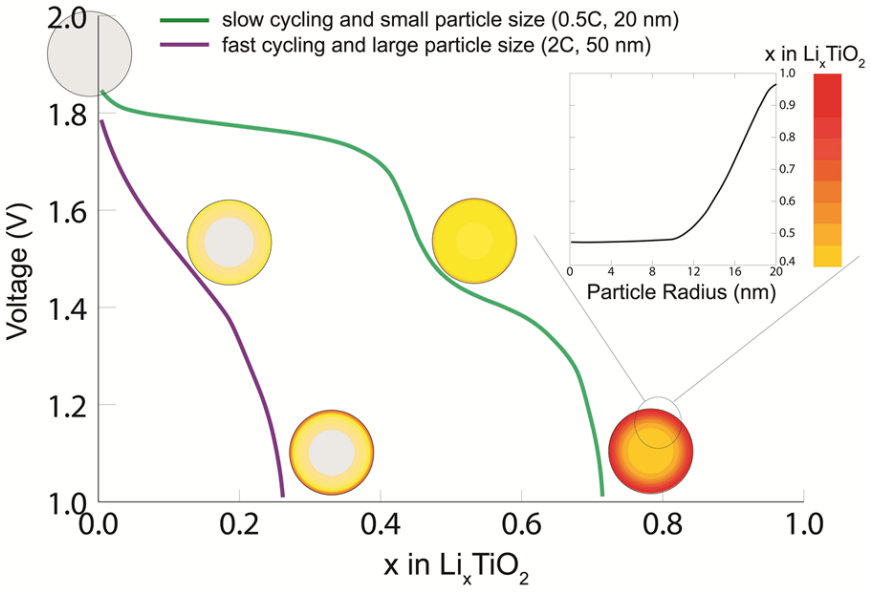

Figure 2.12: Overview of Li-intercalation in anatase.

transformed to $Li_{0.5}TiO_2$, and this is followed by the formation of a thin layer of Li_1TiO_2 at the particle surface. Because the Li-diffusion is poor in the Li_1TiO_2-layer, the thickness of this layer primarily depends on the applied C-rate, as shown in Figure 2.11.

When applying small C-rates the entire anatase particle is able to transform to the Li_1TiO_2-phase, electrochemically represented by a second voltage plateau. At moderate C-rates only the onset of the second plateau will occur, as consistently predicted by the present phase-field simulations. For large C-rates and/or large anatase particles the lower voltage will drive the formation of a thin layer of the Li_1TiO_2 phase. The slow Li transport through this layer prevents transformation of the complete particle towards the Li_1TiO_2 phase. This is the origin of the observed large charge-transfer overpotentials, causing a shortening of the first voltage plateau, followed by a sloped tail in the voltage profile, thus rationalising the decreasing capacities with increasing lithiation rates and increasing particle size.

The strongly concentration dependent Li-diffusion provides an explanation of the memory effect observed for anatase electrodes [75], which presents itself through an decrease in the voltage in the charge-cycle (lithiation) following upon an incomplete charge/discharge cycle. The memory effect is caused by particles that are not completely delithiated before they are lithiating again, and thus more regions with poor diffusivity will remain in comparison to a complete charge/discharge cycle. In the memory-cycle the regions with poor diffusion will increase the charge-transfer overpotential in comparison to completely delithiated particles, explaining the observed

memory effect. The phase-field simulations show that the charge-transfer overpotential strongly depends on the applied C-rate and the surface to volume ratio, explaining the experimental observations [75] of a larger memory effect at high C-rates and with smaller surface to volume ratios.
The blocking mechanism through the Li_1TiO_2 phase formation at the surface of anatase particles, as predicted by the present simulations, indicates that the single grain lithiation limits the rate performance of complete electrodes. This is explicitly demonstrated by the multi-particle phase-field simulation, where all particles transform concurrently. All grains are active, implying that the electrode is unable to provide a higher current due to the single particle limitations. This is unlike other electrode materials, such as $LiFePO_4$, $Li_4Ti_5O_{12}$, and $LiCoO_2$, in which ionic and electronic wiring dominate the internal resistance [67–71]. The phase-field model predicts that the applied overpotential is unable to induce solid solution behaviour through widening of the phase interface regions, which has been shown for $LiFePO_4$ [17], because at high overpotentials a layer of Li_1TiO_2 phase will form at the surface, after which the poor Li-ion diffusivity in this phase consumes the applied overpotential.

2.5. Conclusions

The present phase-field model with parameters from literature is able to qualitatively explain practically all experimental phenomena observed during lithiation of anatase electrodes. This includes the impact of particle size, C-rate, Li-ion diffusivity, surface area, and the observed memory effect. The kinetic restrictions of the Li_1TiO_2 phase forming at the surface of anatase particles is the origin of the performance restrictions, and prevents fast transformation of anatase particles, even under high current. The simulations reveal that the transformation of single anatase particles limits the performance of the complete electrode, rather than the ionic and electronic wiring that appears to be rate limiting for other electrode materials.
This demonstrates that the limitation of anatase can only be addressed if the formation of a blocking Li_1TiO_2 layer can be suppressed. This can be achieved by particle size reduction, where the reduction of the Li-ion diffusion distance as well as the suppression of the phase transitions enhances the Li-ion transport, increasing the capacity at high C-rates. A second strategy is to improve the Li-ion diffusivity in the anatase TiO_2 lattice by doping. The simulations give detailed insight on the impact of both approaches, providing a rational strategy towards improved performance.
Thus, a comprehensive model for lithiation of anatase TiO_2 has been presented. The good agreement with literature provides deep insight into the lithiation mechanism of anatase, and validation of the physical description of the phase-field model. This further motivates developing phase-field models for electrode materials, which will provide fundamental understanding of the limitations of battery materials, necessary for the formulation of strategies towards improved battery materials, design, and performance.

References

[1] D. Deng. Li-ion batteries: basics, progress, and challenges. *Energy Sci. Eng.*, 3 (5):385–418, 2015. doi: 10.1002/ese3.95.

[2] A.A. Franco. Multiscale modelling and numerical simulation of rechargeable lithium ion batteries: concepts, methods and challenges. *RSC Adv.*, 3(32):13027–13058, 2013. doi: 10.1039/c3ra23502e.

[3] X. Zhang, T.W. Verhallen, F. Labohm, and M. Wagemaker. Direct observation of Li-ion transport in electrodes under nonequilibrium conditions using neutron depth profiling. *Adv. Energy Mater.*, 5(15), 2015. doi: 10.1002/aenm.201500498.

[4] P.H.L. Notten and D.L. Danilov. Battery modeling: a versatile tool to design advanced battery management systems. *Adv. Chem. Eng. Science*, 04(01):62–72, 2014. doi: 10.4236/aces.2014.41009.

[5] T.T. Vo, X. Chen, W. Shen, and A. Kapoor. New charging strategy for lithium-ion batteries based on the integration of Taguchi method and state of charge estimation. *J. Power Sources*, 273:413–422, 2015. doi: 10.1016/j.jpowsour.2014.09.108.

[6] V.A. Sethuraman, V. Srinivasan, and J. Newman. Analysis of electrochemical lithiation and delithiation kinetics in silicon. *J. Electrochem. Soc.*, 160(2):A394–A403, 2012. doi: 10.1149/2.008303jes.

[7] M. Landstorfer, S. Funken, and T. Jacob. An advanced model framework for solid electrolyte intercalation batteries. *Phys. Chem. Chem. Phys.*, 13(28):12817–12825, 2011. doi: 10.1039/c0cp02473b.

[8] S. Dargaville and T.W. Farrell. A comparison of mathematical models for phase-change in high-rate $LiFePO_4$ cathodes. *Electrochim. Acta*, 111:474–490, 2013. doi: 10.1016/j.electacta.2013.08.014.

[9] M.Z. Bazant. Theory of chemical kinetics and charge transfer based on nonequilibrium thermodynamics. *Accounts Chem. Res.*, 46(5):1144–1160, 2013. doi: 10.1021/ar300145c.

[10] A. Salvadori, D. Grazioli, and M.G.D. Geers. Governing equations for a two-scale analysis of Li-ion battery cells. *Int. J. Solids Struct.*, 59:90–109, 2015. doi: 10.1016/j.ijsolstr.2015.01.014.

[11] Y. Li, F. El Gabaly, T.R. Ferguson, R.B. Smith, N.C. Bartelt, J.D. Sugar, K.R. Fenton, D.A. Cogswell, A.L.D. Kilcoyne, T. Tyliszczak, M.Z. Bazant, and W.C. Chueh. Current-induced transition from particle-by-particle to concurrent intercalation in phase-separating battery electrodes. *Nat. Mater.*, 13(12):1149–1156, 2014. doi: 10.1038/nmat4084.

[12] G.K. Singh, G. Ceder, and M.Z. Bazant. Intercalation dynamics in rechargeable battery materials: general theory and phase-transformation waves in $LiFePO_4$. *Electrochim. Acta*, 53(26):7599–7613, 2008. doi: 10.1016/j.electacta.2008.03.083.

[13] D. Burch and M.Z. Bazant. Size-dependent spinodal and miscibility gaps for intercalation in nanoparticles. *Nano Lett.*, 9(11):3795–3800, 2009. doi: 10.1021/nl9019787.

[14] T.R. Ferguson and M.Z. Bazant. Nonequilibrium thermodynamics of porous electrodes. *J. Electrochem. Soc.*, 159(12):A1967–A1985, 2012. doi: 10.1149/2.048212jes.

[15] M. Wagemaker, D.P. Singh, W.J.H. Borghols, U. Lafont, L. Haverkate, V.K. Peterson, and F.M. Mulder. Dynamic solubility limits in nanosized olivine $LiFePO_4$. *J. Am. Chem. Soc.*, 133(26):10222–10228, 2011. doi: 10.1021/ja2026213.

[16] M.J. Welland, D. Karpeyev, D.T. O'Connor, and O. Heinonen. Miscibility gap closure, interface morphology, and phase microstructure of 3D Li_xFePO_4 nanoparticles from surface wetting and coherency strain. *ACS Nano*, 9(10):9757–9771, 2015. doi: 10.1021/acsnano.5b02555.

[17] X. Zhang, M. van Hulzen, D.P. Singh, A. Brownrigg, J.P. Wright, N.H. van Dijk, and M. Wagemaker. Rate-induced solubility and suppression of the first-order phase transition in olivine $LiFePO_4$. *Nano Lett.*, 14(5):2279–2285, 2014. doi: 10.1021/nl404285y.

[18] H. Liu, F.C. Strobridge, O.J. Borkiewicz, K.M. Wiaderek, K.W. Chapman, P.J. Chupas, and C.P. Grey. Capturing metastable structures during high-rate cycling of $LiFePO_4$ nanoparticle electrodes. *Science*, 344(6191):1252817, 2014. doi: 10.1126/science.1252817.

[19] X. Zhang, M. van Hulzen, D.P. Singh, A. Brownrigg, J.P. Wright, N.H. van Dijk, and M. Wagemaker. Direct view on the phase evolution in individual $LiFePO_4$ nanoparticles during Li-ion battery cycling. *Nat. Commun.*, 6:8333, 2015. doi: 10.1038/ncomms9333.

[20] D.T. O'Connor, M.J. Welland, W. Kam Liu, and P.W. Voorhees. Phase transformation and fracture in single Li_xFePO_4 cathode particles: a phase-field approach to Li-ion intercalation and fracture. *Modell. Simul. Mater. Sci. Eng.*, 24(3):035020, 2016. doi: 10.1088/0965-0393/24/3/035020.

[21] T.R. Ferguson and M.Z. Bazant. Phase transformation dynamics in porous battery electrodes. *Electrochim. Acta*, 146:89–97, 2014. doi: 10.1016/j.electacta.2014.08.083.

[22] Y. Guo, R.B. Smith, Z. Yu, D.K. Efetov, J. Wang, P. Kim, M.Z. Bazant, and L.E. Brus. Li intercalation into graphite: direct optical imaging and Cahn-Hilliard reaction dynamics. *J. Phys. Chem. Lett.*, 7(11):2151–2156, 2016. doi: 10.1021/acs.jpclett.6b00625.

[23] U. Lafont, D. Carta, G. Mountjoy, A.V. Chadwick, and E.M. Kelder. *In situ* structural changes upon electrochemical lithium insertion in nanosized anatase TiO_2. *J. Phys. Chem. C*, 114(2):1372–1378, 2010. doi: 10.1021/jp908786t.

[24] D.P. Singh, A. George, R.V. Kumar, J. E. ten Elshof, and M. Wagemaker. Nanostructured TiO_2 anatase micropatterned three-dimensional electrodes for high-performance Li-ion batteries. *J. Phys. Chem. C*, 117(39):19809–19815, 2013. doi: 10.1021/jp3118659.

[25] K. Shen, H. Chen, F. Klaver, F.M. Mulder, and M. Wagemaker. Impact of particle size on the non-equilibrium phase transition of lithium-inserted anatase TiO_2. *Chem. Mater.*, 26(4):1608–1615, 2014. doi: 10.1021/cm4037346.

[26] M. Wagemaker, W.J.H. Borghols, and F.M. Mulder. Large impact of particle size on insertion reactions: a case for anatase Li_xTiO_2. *J. Am. Chem. Soc.*, 129(14): 4323–4327, 2007. doi: 10.1021/ja067733p.

[27] G. Sudant, E. Baudrin, D. Larcher, and J.M. Tarascon. Electrochemical lithium reactivity with nanotextured anatase-type TiO_2. *J. Mater. Chem.*, 15(12):1263–1269, 2005. doi: 10.1039/b416176a.

[28] B.J. Morgan and G.W. Watson. Role of lithium ordering in the Li_xTiO_2 anatase → titanate phase transition. *J. Phys. Chem. Lett.*, 2(14):1657–1661, 2011. doi: 10.1021/jz200718e.

[29] M. Søndergaard, Y. Shen, A. Mamakhel, M. Marinaro, M. Wohlfahrt-Mehrens, K. Wonsyld, S. Dahl, and B.B. Iversen. TiO_2 nanoparticles for Li-ion battery anodes: mitigation of growth and irreversible capacity using LiOH and NaOH. *Chem. Mater.*, 27(1):119–126, 2015. doi: 10.1021/cm503479h.

[30] E. Madej, F. La Mantia, B. Mei, S. Klink, M. Muhler, W. Schuhmann, and E. Ventosa. Reliable benchmark material for anatase TiO_2 in Li-ion batteries: on the role of dehydration of commercial TiO_2. *J. Power Sources*, 266:155–161, 2014. doi: 10.1016/j.jpowsour.2014.05.018.

[31] Y. Wang, S. Liu, K. Huang, D. Fang, and S. Zhuang. Electrochemical properties of freestanding TiO_2 nanotube membranes annealed in Ar for lithium anode material. *J. Solid State Electrochem.*, 16(2):723–729, 2011. doi: 10.1007/s10008-011-1417-5.

[32] C.H. Sun, X.H. Yang, J.S. Chen, Z. Li, X.W. Lou, C. Li, S.C. Smith, G.Q. Lu, and H.G. Yang. Higher charge/discharge rates of lithium-ions across engineered TiO_2 surfaces leads to enhanced battery performance. *Chem. Commun.*, 46(33):6129–6131, 2010. doi: 10.1039/c0cc00832j.

[33] E. Madej, E. Ventosa, S. Klink, W. Schuhmann, and F. La Mantia. Aging effects of anatase TiO_2 nanoparticles in Li-ion batteries. *Phys. Chem. Chem. Phys.*, 16 (17):7939–7945, 2014. doi: 10.1039/c4cp00630e.

[34] V. Gentili, S. Brutti, L.J. Hardwick, A.R. Armstrong, S. Panero, and P.G. Bruce. Lithium insertion into anatase nanotubes. *Chem. Mater.*, 24(22):4468–4476, 2012. doi: 10.1021/cm302912f.

[35] A.K. Rai, L.T. Anh, J. Gim, V. Mathew, J. Kang, B.J. Paul, J. Song, and J. Kim. Simple synthesis and particle size effects of TiO_2 nanoparticle anodes for rechargeable lithium ion batteries. *Electrochim. Acta*, 90:112–118, 2013. doi: 10.1016/j.electacta.2012.11.104.

[36] B. Zachau-Christiansen, K. West, T. Jacobsen, and S. Atlung. Lithium insertion in different TiO_2 modifications. *Solid State Ionics*, 28(0):1176–1182, 1988. doi: 10.1016/0167-2738(88)90352-9.

[37] W.J. Macklin and R.J. Neat. Performance of titanium dioxide-based cathodes in a lithium polymer electrolyte cell. *Solid State Ionics*, 53:694–700, 1992. doi: 10.1016/0167-2738(92)90449-y.

[38] A.A. Belak, Y. Wang, and A. Van der Ven. Kinetics of anatase electrodes: the role of ordering, anisotropy, and shape memory effects. *Chem. Mater.*, 24(15): 2894–2898, 2012. doi: 10.1021/cm300881t.

[39] H. Yildirim, J. Greeley, and S.K.R.S. Sankaranarayanan. Effect of concentration on the energetics and dynamics of Li ion transport in anatase and amorphous TiO_2. *J. Phys. Chem. C*, 115(31):15661–15673, 2011. doi: 10.1021/jp202514j.

[40] W.J.H. Borghols, D. Lützenkirchen-Hecht, U. Haake, E.R.H. van Eck, F.M. Mulder, and M. Wagemaker. The electronic structure and ionic diffusion of nanoscale $LiTiO_2$ anatase. *Phys. Chem. Chem. Phys.*, 11(27):5742–5748, 2009. doi: 10.1039/b823142g.

[41] R.B. Smith and M.Z. Bazant. Multiphase porous electrode theory. *J. Electrochem. Soc.*, 164(11):E3291–E3310, 2017. doi: 10.1149/2.0171711jes.

[42] N. Munichandraiah, L.G. Scanlon, R.A. Marsh, B. Kumar, and A.K. Sircar. Determination of the exchange current density of the $Li^+ + e^- \leftrightarrow Li$ reaction in polymer electrolytes by galvanostatic linear polarization of symmetrical cells. *J. Electroanal. Chem.*, 379(1-2):495–499, 1994. doi: 10.1016/0022-0728(94)87174-4.

[43] R.B. Smith, E. Khoo, and M.Z. Bazant. Intercalation kinetics in multiphase-layered materials. *J. Phys. Chem. C*, 121(23):12505–12523, 2017. doi: 10.1021/acs.jpcc.7b00185.

[44] P. Bai, D.A. Cogswell, and M.Z. Bazant. Suppression of phase separation in $LiFePO_4$ nanoparticles during battery discharge. *Nano Lett.*, 11(11):4890–4896, 2011. doi: 10.1021/nl202764f.

[45] W.J. Borghols, M. Wagemaker, U. Lafont, E.M. Kelder, and F.M. Mulder. Size effects in the $Li_{4+x}Ti_5O_{12}$ spinel. *J. Am. Chem. Soc.*, 131(49):17786–17792, 2009. doi: 10.1021/ja902423e.

[46] S. Lunell, A. Stashans, L. Ojamäe, H. Lindström, and A. Hagfeldt. Li and Na diffusion in TiO_2 from quantum chemical theory versus electrochemical experiment. *J. Am. Chem. Soc.*, 119(31):7374–7380, 1997. doi: 10.1021/ja9708629.

[47] F. Tielens, M. Calatayud, A. Beltran, C. Minot, and J. Andres. Lithium insertion and mobility in the TiO_2-anatase/titanate structure: a periodic DFT study. *J. Electroanal. Chem.*, 581(2):216–223, 2005. doi: 10.1016/j.jelechem.2005.04.009.

[48] M.J. Sussman, A. Yasin, and G.P. Demopoulos. On the complex interplay of crystallinity and surface area effects on Li-ion intercalation and pseudocapacitive storage properties of nanocrystalline anatase. *J. Power Sources*, 272:58–67, 2014. doi: 10.1016/j.jpowsour.2014.08.050.

[49] E.B. Nauman and D.Q. He. Nonlinear diffusion and phase separation. *Chem. Eng. Sci.*, 56(6):1999–2018, 2001. doi: 10.1016/s0009-2509(01)00005-7.

[50] Y. Zeng and M.Z. Bazant. Phase separation dynamics in isotropic ion-intercalation particles. *SIAM J. Appl. Math.*, 74(4):980–1004, 2014. doi: 10.1137/130937548.

[51] J. Wang, J. Polleux, J. Lim, and B. Dunn. Pseudocapacitive contributions to electrochemical energy storage in TiO_2 (anatase) nanoparticles. *J. Phys. Chem. C*, 111(40):14925–14931, 2007. doi: 10.1021/jp074464w.

[52] S.H. Kim and S.Y. Choi. Fabrication of Cu-coated TiO_2 nanotubes and enhanced electrochemical performance of lithium ion batteries. *J. Electroanal. Chem.*, 744: 45–52, 2015. doi: 10.1016/j.jelechem.2015.03.007.

[53] H. Lindstrom, S. Sodergren, A. Solbrand, H. Rensmo, J. Hjelm, A. Hagfeldt, and S.E. Lindquist. Li^+ ion insertion in TiO_2 (anatase). 2. Voltammetry on nanoporous films. *J. Phys. Chem. B*, 101(39):7717–7722, 1997. doi: 10.1021/jp970490q.

[54] M. Wagemaker, G.J. Kearley, A.A. van Well, H. Mutka, and F.M. Mulder. Multiple Li positions inside oxygen octahedra in lithiated TiO_2 anatase. *J. Am. Chem. Soc.*, 125(3):840–848, 2003. doi: 10.1021/ja028165q.

[55] S. Ganapathy, E.R.H. van Eck, A.P. Kentgens, F.M. Mulder, and M. Wagemaker. Equilibrium lithium-ion transport between nanocrystalline lithium-inserted anatase TiO_2 and the electrolyte. *Chemistry*, 17(52):14811–14816, 2011. doi: 10.1002/chem.201101431.

[56] J.Y. Shin, J.H. Joo, D. Samuelis, and J. Maier. Oxygen-deficient $TiO_{2-\delta}$ nanoparticles via hydrogen reduction for high rate capability lithium batteries. *Chem. Mater.*, 24(3):543–551, 2012. doi: 10.1021/cm2031009.

[57] L. Kavan. Lithium insertion into TiO_2 (anatase): electrochemistry, Raman spectroscopy, and isotope labeling. *J. Solid State Electr.*, 18(8):2297–2306, 2014. doi: 10.1007/s10008-014-2435-x.

[58] Z. Wang, J. Sha, E. Liu, C. He, C. Shi, J. Li, and N. Zhao. A large ultrathin anatase TiO_2 nanosheet/reduced graphene oxide composite with enhanced lithium storage capability. *J. Mater. Chem. A*, 2(23):8893, 2014. doi: 10.1039/c4ta00574k.

[59] X. Yang, Y. Yang, H. Hou, Y. Zhang, L. Fang, J. Chen, and X. Ji. Size-tunable single-crystalline anatase TiO_2 cubes as anode materials for lithium ion batteries. *J. Phys. Chem. C*, 119(8):3923–3930, 2015. doi: 10.1021/jp512289g.

[60] M. Wagemaker, R. van de Krol, A.P.M. Kentgens, A.A. van Well, and F.M. Mulder. Two phase morphology limits lithium diffusion in TiO_2 (anatase): a ^{7}Li MAS NMR study. *J. Am. Chem. Soc.*, 123(46):11454–11461, 2001. doi: 10.1021/ja0161148.

[61] M. Wagemaker, A.P.M. Kentgens, and F.M. Mulder. Equilibrium lithium transport between nanocrystalline phases in intercalated TiO_2 anatase. *Nature*, 418(6896): 397–399, 2002. doi: 10.1038/nature00901.

[62] R.B. Smith. MPET code. *https://bitbucket.org/bazantgroup/mpet*, 2017.

[63] D.D. Nikolić. DAE Tools: equation-based object-oriented modelling, simulation and optimisation software. *PeerJ Comp. Science*, 2:e54, 2016. doi: 10.7717/peerj-cs.54.

[64] M.G. Kim, H. Kim, and J. Cho. V_2O_5-coated TiO_2 nanorod electrodes. *J. Electrochem. Soc.*, 157(7):A802, 2010. doi: 10.1149/1.3425619.

[65] P.G. Bruce, B. Scrosati, and J.M. Tarascon. Nanomaterials for rechargeable lithium batteries. *Angew. Chem. Int. Ed. Engl.*, 47(16):2930–2946, 2008. doi: 10.1002/anie.200702505.

[66] B. Orvananos, H.C. Yu, A. Abdellahi, R. Malik, C.P. Grey, G. Ceder, and K. Thornton. Kinetics of nanoparticle interactions in battery electrodes. *J. Electrochem. Soc.*, 162(6):A965–A973, 2015. doi: 10.1149/2.0481506jes.

[67] Z. Liu, T.W. Verhallen, D.P. Singh, H. Wang, M. Wagemaker, and S. Barnett. Relating the 3D electrode morphology to Li-ion battery performance; a case for $LiFePO_4$. *J. Power Sources*, 324:358–367, 2016. doi: 10.1016/j.jpowsour.2016.05.097.

[68] F.C. Strobridge, B. Orvananos, M. Croft, H.C. Yu, R. Robert, H. Liu, Z. Zhong, T. Connolley, M. Drakopoulos, K. Thornton, and C.P. Grey. Mapping the inhomogeneous electrochemical reaction through porous $LiFePO_4$-electrodes in a standard coin cell battery. *Chem. Mater.*, 27(7):2374–2386, 2015. doi: 10.1021/cm504317a.

[69] Y. Li, S. Meyer, J. Lim, S.C. Lee, W.E. Gent, S. Marchesini, H. Krishnan, T. Tyliszczak, D. Shapiro, A.L. Kilcoyne, and W.C. Chueh. Effects of particle size, electronic connectivity, and incoherent nanoscale domains on the sequence of lithiation in $LiFePO_4$ porous electrodes. *Adv. Mater.*, 27(42):6591–6597, 2015. doi: 10.1002/adma.201502276.

[70] D.P. Singh, F.M. Mulder, and M. Wagemaker. Templated spinel $Li_4Ti_5O_{12}$ Li-ion battery electrodes combining high rates with high energy density. *Electrochem. Commun.*, 35:124–127, 2013. doi: 10.1016/j.elecom.2013.08.014.

[71] C. Kim, N.S. Norberg, C.T. Alexander, R. Kostecki, and J. Cabana. Mechanism of phase propagation during lithiation in carbon-free $Li_4Ti_5O_{12}$ battery electrodes. *Adv. Funct. Mater.*, 23(9):1214–1222, 2013. doi: 10.1002/adfm.201201684.

[72] Y. Ren, J. Li, and J. Yu. Enhanced electrochemical performance of TiO_2 by Ti^{3+} doping using a facile solvothermal method as anode materials for lithium-ion batteries. *Electrochim. Acta*, 138:41–47, 2014. doi: 10.1016/j.electacta.2014.06.068.

[73] J.Y. Shin, D. Samuelis, and J. Maier. Sustained lithium-storage performance of hierarchical, nanoporous anatase TiO_2 at high rates: emphasis on interfacial storage phenomena. *Adv. Funct. Mater.*, 21(18):3464–3472, 2011. doi: 10.1002/adfm.201002527.

[74] E. Madej, S. Klink, W. Schuhmann, E. Ventosa, and F. La Mantia. Effect of the specific surface area on thermodynamic and kinetic properties of nanoparticle anatase TiO_2 in lithium-ion batteries. *J. Power Sources*, 297:140–148, 2015. doi: 10.1016/j.jpowsour.2015.07.079.

[75] E. Madej, F. La Mantia, W. Schuhmann, and E. Ventosa. Impact of the specific surface area on the memory effect in Li-ion batteries: the case of anatase TiO_2. *Adv. Energy Mater.*, 4(17):1400829, 2014. doi: 10.1002/aenm.201400829.

[76] M. Wagemaker, F.M. Mulder, and A. Van der Ven. The role of surface and interface energy on phase stability of nanosized insertion compounds. *Adv. Mater.*, 21(25-26):2703–2709, 2009. doi: 10.1002/adma.200803038.

[77] M. Wagemaker, D. Lüenkirchen-Hecht, A.A. van Well, and R. Frahm. Atomic and electronic bulk versus surface structure: lithium intercalation in anatase TiO_2. *J. Phys. Chem. B*, 108(33):12456–12464, 2004. doi: 10.1021/jp048567f.

[78] P. Bai, J. Li, F.R. Brushett, and M.Z. Bazant. Transition of lithium growth mechanisms in liquid electrolytes. *Energy Environ. Sci.*, 9(10):3221–3229, 2016. doi: 10.1039/c6ee01674j.

[79] C.L. Olson, J. Nelson, and M.S. Islam. Defect chemistry, surface structures, and lithium insertion in anatase TiO_2. *J. Phys. Chem. B*, 110(20):9995–10001, 2006. doi: 10.1021/jp057261l.

Supporting Information

The charge transfer coefficient (k_0) used for the simulations is based on the diffusion coefficient between anatase $Li_{0.5}TiO_2$ and electrolyte as measured by NMR experiments [55]. The measured diffusion coefficient is between $1^{*}10^{-12}$ and $5^{*}10^{-12}$ cm^2/sec at room temperature, depending on the electrolyte.

The diffusivity can be related to jump rates using the Einstein-Smulochowski relation: $D = \frac{\tau a^2}{2d}$. Assuming a diffusion distance (a) equal to the particle size of 40 nm., and 1 dimensional diffusion (d) perpendicular to the surface, leads to a Li-jump frequency (τ) between 0.125 and 0.625 sec^{-1}. Combining this with the Li-density of $2.45^{*}10^{18}$ Li/m^2 for $Li_{0.5}TiO_2$ at (101)-surfaces, which are the most stable facets of anatase crystals [79], this gives a charge transfer between $0.31^{*}10^{18}$ and $1.53^{*}10^{18}$ Li sec^{-1} m^{-2}, which is equal to 0.049 and 0.245 A/m^2, respectively.

To be on the safe side the lower value of 0.049 A/m^2 is chosen for the simulations. However, as shown in Figure 2.13 the difference between the voltage profiles for k_0-values of 0.049 and 0.245 is negligible. In the first plateau there is a tiny difference in voltage that is below 0.01 V, and during the second phase transformation no differences are visible.

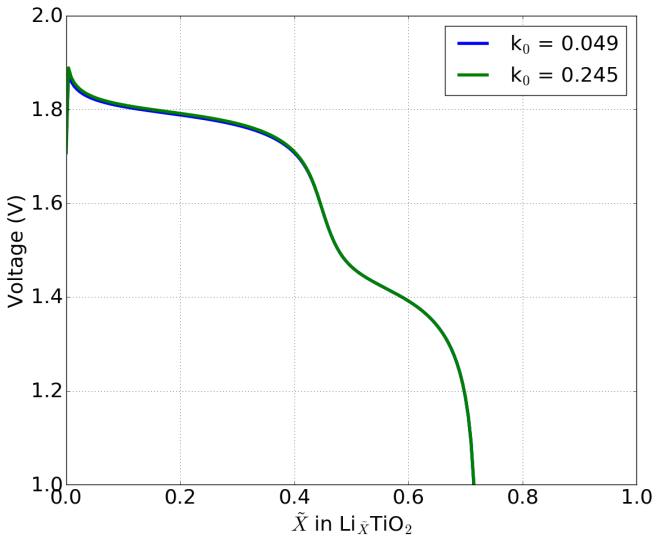

Figure 2.13: Voltage profiles with high (0.245 A/m^2) and low (0.049 A/m^2) values for the charge transfer coefficient at 0.5C.

3

Space-charge layers in all-solid-state batteries; important or negligible?

This chapter has been published as: Niek J.J. de Klerk and Marnix Wagemaker, Space-charge layers in all-solid-state batteries; important or negligible?; ACS Applied Energy Materials, **1** (7), 5609-5618 (2018) doi: 10.1021/acsaem.8b01141

All-solid state batteries have the promise to increase the safety of Li-ion batteries. A prerequisite for high performance all-solid-state batteries is a high Li-ion conductivity through the solid electrolyte. In recent decades several solid electrolytes have been developed which have an ionic conductivity comparable to that of common liquid electrolytes. However, fast charging and discharging of all-solid-state batteries remains challenging. This is generally attributed to poor kinetics over the electrode-solid electrolyte interface, either due to poorly conducting decomposition products, small contact areas, or space-charge layers.
To understand and quantify the role of space-charge layers in all-solid-state batteries a simple model is presented which allows to asses the interface capacitance and resistance caused by the space-charge layer. The model is applied to LCO ($LiCoO_2$) and graphite electrodes in contact with an LLZO ($Li_7La_3Zr_2O_{12}$) and LATP ($Li_{1.2}Al_{0.2}Ti_{1.8}(PO_4)_3$) solid electrolyte at several voltages. The predictions demonstrate that the space-charge layer for typical electrode-electrolyte combinations is about a nanometre in thickness, and the consequential resistance for Li-ion transport through the space-charge layer is negligible, except when layers completely depleted of Li-ions are formed in the solid electrolyte. This suggests that space-charge layers have a negligible impact on the performance of all-solid-state batteries.

3.1. Introduction

Batteries are becoming increasingly important in modern society by enabling mobile electronic applications, such as smart-phones, laptops and electric cars. For transport applications batteries are the most sustainable alternative for replacing fossil fuels [1], but there are concerns whether the safety and energy density of current battery technology is sufficient. All-solid-state batteries (ASSB's) are expected to overcome these concerns [2, 3], and even promise to have higher energy densities on the cell level, lower self-discharge rates and significantly improved safety.
For many years the low ionic conductivity of solid state electrolytes was the main concern for the development of ASSB's, but in recent years many solid state electrolytes with ionic conductivities comparable to those of liquid electrolytes have been discovered [2]. Although the ionic conductivity of solid state electrolytes is comparable to their liquid counterparts nowadays, ASSB's typically show low capacities at high (dis)charge rates [4, 5], which is attributed to the electrode-electrolyte interface. Possible causes for the poor ionic diffusion over the electrode-electrolyte interface are suggested to be [6]: a small effective contact area for charge transfer, poorly conducting interphases caused by chemical and electrochemical decomposition, and space-charge effects, which change the conductivity by redistributing the ions near the interface. Ways of increasing the contact area and its effects are being investigated [4, 7, 8], and research towards thermodynamic (in)stabilities has resulted in better understanding [8–11]. In comparison, relatively little is known about space-charge effects, and as a consequence the importance of space-charge layers in ASSB's remains unclear.
Space-charge layers in ASSB's have been suggested to be several micrometers in thickness [12, 13], which would cause a large interface resistance. However, recent NMR results on Li-ion kinetics show interface resistances of only a few Ω cm^2 over pristine electrode-electrolyte interfaces [4], in thin film batteries interface resistances

below 10 Ω cm^2 have been reported [14]. Both of which seem incompatible with reports on micrometre thick space-charge layers. Reports indicating that the thickness of the space-charge layer is on the nanometre scale [15, 16] seem more compatible with these results, since such a thickness is unlikely to lead to an interface resistance that has a noticeable effect on the performance of ASSB's.
Furthermore, it is being debated if space-charge layers play a role in the beneficial effects of coatings at the electrode-solid electrolyte interface [16–18]. Some authors claim that coating layers reduce the space-charge effect at the interface due to a higher permittivity (dielectric constant) of the material used for the coating [16, 19–21]. This is expected to lead to thinner space-charge layers at the electrode-solid electrolyte interface, thus decreasing the interface resistance. Other authors suggest that coatings increase ASSB performance by preventing decomposition of the electrode and electrolyte at the interface. In this case the coating allows Li-ion diffusion, but blocks the diffusion of other atomic species over the interface, thus preventing chemical reactions between the electrode and the solid electrolyte [22–24].
Since several effects simultaneously play a role at the electrode-electrolyte interface, experimental studies on space-charge effects are challenging. Modelling the space-charge layer is therefore an important approach to gain a better understanding of its effects, and models to calculate the lithium concentrations and potentials in solid electrolytes have been developed [25, 26]. These models indicate that the space-charge layer is about a nanometre in thickness, and that the Li-concentration near the interface can change by 100% in comparison to the bulk concentration. However, these models neglect the Coulomb interactions between charged Li-defects, which are created in the space-charge layer when the Li-ions migrate towards the material with the higher voltage. In AgI the interaction energy between defects is reported to be 0.68 eV [27], which represents a significant contribution to the total energy of the material at high defect concentrations. It has been reported that the Coulomb interaction starts to have an impact at a defect concentration of 0.1% already [28], and the validity of the previous models should therefore be evaluated to comprehend the impact in all-solid-state batteries.
In the next section a model for space-charges is presented which takes the Coulomb interaction between defects into account. The model is used to predict the space-charge at the interface of LCO and graphite electrodes in contact with an LLZO and LATP solid electrolyte at several voltages. Because space-charges are driven by the voltage difference between two materials, which changes during cycling, the space-charges are also determined at different electrode voltages. Using the model the thickness of the space-charge layer at the electrode-electrolyte interfaces is determined, and in addition how much interface resistance this causes. Knowledge of the interface resistance triggered by the space-charge layers provides valuable understanding of its contribution to the internal resistance of ASSB's.
The model is available as supplemental information to the published article in the form of Matlab-code in combination with a short manual. Interested readers can apply the model to the combination of materials they are interested in, provided that the material properties required for the model are known.

3.2. Space-charges

Space-charges have been studied for many years and in numerous materials. They can have beneficial effects, such as increased ionic diffusion in solid-solid dispersions [29–32] and in SEI-layers of liquid electrolytes [33]. But space-charge layers have also been suggested to have detrimental effects on battery performance by increasing the resistance [16, 17, 34, 35].

A space-charge layer is formed when two materials with different chemical potentials are brought in contact with each other, and the atoms *or* electrons are unable to migrate to establish local charge neutrality. Near the interface the atoms and electrons are driven towards the material with the lowest chemical potential (highest voltage). But if only one charged species, either electrons or ions, is able to migrate this will create a region in which charge builds up, the so-called space-charge layer.

The insulating nature of solid electrolytes means that the electrons are (practically) unable to conduct, so the amount of electrons transferring over the interface will be negligible. On the other hand, the ionic conduction is several orders of magnitude higher in the solid electrolyte. The potential difference, of several volts, between the electrolyte and electrode will thus drive the mobile ions near the electrolyte-electrode interface towards the material with the lowest chemical potential. This process stops when equilibrium is reached, meaning that the electrochemical potential is constant, which implicates that the attractive chemical potential is balanced by the repulsive electric field build up by accumulation of charge.

The thickness of the space-charge layer and the deviation of the ion concentration from the bulk equilibrium concentration is determined by the properties of the materials which are in contact, including the electric permittivity, ion concentration, and the potential difference between the materials. For a thorough thermodynamic description of the space-charge effect we refer the reader to the work of Maier and co-workers [36–38].

Whether the space-charge layer is beneficial or detrimental for ionic conductivity depends on the diffusion mechanism in the solid electrolyte. When Li-vacancies increase the Li-conductivity the space-charge layer is beneficial for Li-conduction over the cathode-solid electrolyte interface [31], although the magnitude of the effect depends on the cathode material and the cathode voltage. Detrimental effects of space-charges are observed when an increase in Li-vacancies reduces the Li-conduction in the solid electrolyte [35]. Note that space-charges occur under open-circuit conditions, i.e. there is no charge transfer between the anode and cathode. The formation of the space-charge layer thus starts at the moment an electrode and solid electrolyte make contact with each other.

3.2.1. Electrochemical potential

To describe the behaviour of ions in a battery material the electrochemical potential ($\bar{\mu}$) is used, which consists of the chemical potential (μ) and the electric potential (φ) [39]:

$$\bar{\mu} = \mu + ze\varphi \tag{3.1}$$

where z is the ionic charge, and e the elementary charge. In equilibrium the electrochemical potential throughout the material is constant [37, 39]:

$$\frac{\partial}{\partial x}\bar{\mu}_j = 0 \tag{3.2}$$

where x is the distance from the interface. By combining equations 3.1 and 3.2 the change in electric potential can be linked to the change in the chemical potential:

$$\Delta\mu_j(x) = -z_j e\Delta\varphi(x) \tag{3.3}$$

Since the chemical potential depends on the ion concentration, this equation makes it possible to determine the ion concentration as a function of the electric potential.

3.2.2. Chemical potential

To describe the chemical potential the solid solution model is used at present, similar to previous models of solid electrolytes [25, 26] and electrodes [40]. The Coulomb interactions between charged defects are taken account for as proposed by Maier and co-workers [28, 41], which is required in particular at high defect concentrations. This results in the following relation between the chemical potential and the ion concentration [27]:

$$\mu(\tilde{c}) = \Omega(1-2(\tilde{c}_0+\tilde{c}_d)) + kT\ln\left(\frac{\tilde{c}_0+\tilde{c}_d}{1-(\tilde{c}_0+\tilde{c}_d)}\right) - J\sqrt[3]{|\tilde{c}_d|} \tag{3.4}$$

where $\tilde{c}$ is the normalised ion concentration (c/c_{max}), $\tilde{c}_0$ is the normalised bulk ion concentration (c_0/c_{max}), $\tilde{c}_d$ is the normalised ionic defect concentration (negative values for vacancies, positive values for interstitials), Ω is the solid solution parameter, J is the strength of the Coulomb interaction between defects, k is Boltzmann's constant, and T is the temperature in Kelvin.

The strength of the Coulomb interaction can be estimated by the Madelung constants and Madelung energy of a material [27]. Unfortunately, for many materials the Madelung constants and energies are not reported in the literature. However, it has been shown that the Madelung constant of a material is closely related to its voltage [42, 43]. Therefore the Madelung constants are replaced by the voltages of the material phases which are filled with ions (V_f) and emptied of ions (V_e). The interaction energy between defects is then obtained using [27]:

$$J = \frac{4}{3}\frac{E_M}{\epsilon}\frac{V_e}{V_f} \tag{3.5}$$

where E_M is the Madelung energy per Li-equivalent of the structure, and ϵ is the relative permittivity of the material.

3.2.3. Potential drop

To determine the concentration profile near the surface and the thickness of the interface layer the potential as a function of the distance must be determined, which requires solving the Poisson equation. Since the electric potential is linked to the

chemical potential and ion concentration via Equations 3.3 and 3.4, the electric potential can be calculated at different ion concentrations (c_i). By doing this for a range of concentrations the change in distance (Δx) from the bulk with changing concentration can be determined numerically [44]:

$$\Delta x = \frac{\epsilon}{c_{i-1} + \frac{\Delta c}{3}} \left(-E_{i-1} \pm \sqrt{E_{i-1}^2 - \frac{2}{\epsilon} \Delta\varphi \left(c_{i-1} + \frac{\Delta c}{3} \right)} \right) \tag{3.6}$$

where c_i is the total ion concentration ($c_0 + c_d$) at step i, Δc the concentration difference between step i and $i-1$, and E_i the electric field at step i. The electric field E_i is calculated by [44]:

$$E_i = -\sqrt{\frac{2kT}{\epsilon} \left(\Delta c - \frac{c_0}{kT} \varphi \right)} \tag{3.7}$$

Summation over Equation 3.6 results in the concentration (and electric potential) as a function of distance from the bulk. In combination with the boundary conditions presented in the next section this enables determination of the thickness of the space-charge layer at the electrode-solid electrolyte interface.

3.2.4. Boundary conditions

To determine what happens when two materials are in contact specific boundary conditions are applied. The first boundary condition is that the created space-charge layer must obey the law of mass conservation. Hence, the number of ions entering one material must be equal to the number of ions that leave the other material:

$$\int_{x=0}^{bulk} c_d^{lyte} dx = -\int_{x=0}^{bulk} c_d^{trode} dx \tag{3.8}$$

where c_d^{lyte} is the defect concentration in the electrolyte, and c_d^{trode} is the defect concentration in the electrode (c_d has a negative value for vacancies and a positive value for interstitials).

Furthermore, the total voltage difference over the interface region must be equal to the voltage difference between the bulk phases of the two materials. This provides the second boundary condition, which states that the total voltage difference over the interface (ΔV_{tot}) must be equal to the combined potential change in the interface region of the electrode (ΔV_{trode}) and electrolyte (ΔV_{lyte}):

$$\Delta V_{tot} = \Delta V_{lyte} + \Delta V_{trode} \tag{3.9}$$

Using the equations and boundary conditions described a 1D-model of the space-charge layer is obtained, under the assumptions that only the ions are mobile, the two materials are chemically stable towards each other, and the presence of a perfect interface contact.

3.2.5. Space-charge resistance and capacitance

To determine the effect of the space-charge layer on the performance of ASSB's the resistance and capacitance of the space-charge layer are calculated. The capacitance

(C) is determined by the number of Li-ions transferred towards the high voltage side divided by the change in voltage of these Li-ions:

$$C = \int_{x=0}^{bulk} \frac{c_d(x)}{\Delta V_{tot} - \Delta\varphi(x)} dx \tag{3.10}$$

To determine the resistance caused by the space-charge layer the large changes in Li-concentration must be taken into account, since this leads to large changes in the lithium diffusivity [45, 46]. In LCO [46] the Li-diffusivity (D) shows a minimum at a fractional Li-concentration ($\tilde{c}$) of 0.5, the concentration dependence is thus approximated by:

$$D = D^*|\tilde{c} - 0.5| + D_{min} \tag{3.11}$$

where D^* is the tracer diffusivity, and D_{min} is the minimal diffusivity, which is introduced to avoid infinitely small values near $\tilde{c} = 0.5$.
The Li-diffusivity in graphite [45] shows two minima, around $\tilde{c} = \frac{1}{3}$ and $\tilde{c} = \frac{2}{3}$, the concentration dependence is thus approximated by:

$$D = D^*|\tilde{c} - \frac{1}{3}||\tilde{c} - \frac{2}{3}| + D_{min} \tag{3.12}$$

For the solid electrolytes the concentration dependence of the lithium diffusivity is not reported over a wide concentration range in literature, but a reasonable assumption is that a 50% site-occupancy displays the highest lithium diffusivity [47]. Therefore, the lattice diffusion model [40], showing a maximum diffusivity at $\tilde{c} = 0.5$, is applied for the solid electrolytes:

$$D = D^*\tilde{c}(1 - \tilde{c})) \tag{3.13}$$

The conductivity (σ) of a material can then be calculated using the Nernst-Einstein relation:

$$\sigma = \frac{e^2 z^2}{kT} cD \tag{3.14}$$

where c is the total Li-concentration. The conductivity in the space-charge layer changes with concentration, so the resistance in the space-charge layer (R_{sc}) is obtained by:

$$R_{sc} A = \int_{x=0}^{bulk} \frac{l}{\sigma(x)} dx \tag{3.15}$$

where l is the distance through which diffusion occurs, A the surface area, and $\sigma(x)$ the conductivity at x. To determine the effect of the space-charge layer the resistance which would be caused by the same diffusion distance in the bulk material (R_{bulk}) is subtracted from the resistance in the space-charge layer (R_{sc}), resulting in the additional resistance (R) in the all-solid-state battery caused by the space-charge layer:

$$R = R_{sc} - R_{bulk} \tag{3.16}$$

3.3. Results

Using the model described in the previous section the space-charge layers occurring at the interfaces of a high voltage $LiCoO_2$ electrode (LCO) and a low voltage graphite electrode in contact with the solid electrolytes $Li_7La_3Zr_2O_{12}$ (LLZO) and $Li_{1.2}Al_{0.2}Ti_{1.8}(PO_4)_3$ (LATP) are calculated. The material properties used for the simulations are provided in Table 3.1, for all the calculations a temperature of 300 Kelvin was used.

The voltage of LLZO has been determined by measuring the open circuit potential of

Property	LCO	graphite	LATP	LLZO
c_{max} (Li/nm^3)	31.6 [48]	16.93 [48]	13.06 [49]	54.97 [50]
c_0 (Li/nm^3)	variable	variable	5.37 [49]	25.65 [50]
Voltage (vs. Li/Li$^+$)	3.8 to 4.4 [51]	0.1 to 0.2 [40]	2.5 [52]	2.85 [53]
ϵ (relative to ϵ_0)	12.9 [54]	11 [55]	15 [56]	60 [57, 58]
Ω (eV)	0.026 [59]	0.088 [40]	0.0	0.0
E_M (eV/Li)	7.0† [60]	4.5 [61]	10.6‡	10.6† [62]
D^* (cm^2/sec)	2*10^{-10} [46]	1*10^{-8} [45]	3*10^{-9} [63]	4*10^{-9} [26]
D_{min} (cm^2/sec)	1*10^{-12} [46]	1*10^{-11} [45]	-	-

Table 3.1: Material properties used in the space-charge model. †Formation enthalpy instead of Madelung energy. ‡Formation enthalpy of LLZO (see text).

an LLZO electrode versus lithium metal [53]. To determine the Coulomb interaction in equation 3.5 for the solid electrolytes it was assumed that $V_e = V_f$. A value of 0.0 was chosen for the Ω-parameter based on a previous model for solid electrolytes [26]. To determine the Coulomb interaction between defects the Madelung energy is required, but in literature the Madelung energy is only reported for lithiated graphite. For LCO and LLZO the formation enthalpy is used as an approximation to the Madelung energy, which appears to be a reasonable appropriximation since the Madelung energy is the largest contributor to the formation enthalpy in ionic crystals [43, 64]. In the case of LATP the Madelung energy and the formation enthalpy are unavailable, and therefore the formation enthalpy of LLZO was used as an approximation, making it possible to compare the effects of the other material properties of the two solid electrolytes.
With the parameters shown in Table 3.1 the Coulomb interaction between defects (J) results in 0.84, 1.09, 0.94 and 0.24 eV for LCO, graphite, LATP and LLZO, respectively.

3.3.1. Interfaces of cathode and solid-electrolyte materials

At the positive electrode lithium ions near the interface of the cathode and electrolyte material are driven towards the cathode material by its larger voltage (lower chemical potential), thus reducing the lithium concentration in the solid electrolyte. At higher applied voltages during charging the driving force for Li-ions to move from the solid electrolyte to the cathode material increases, and the declining Li-concentration upon

charging will facilitate accommodation of the extra Li-ions in the cathode material. For the LCO-LLZO interface this increases the spatial extend of the space-charge layer with increasing potential of the LCO, as shown in Figure 3.1. At an LCO potential of

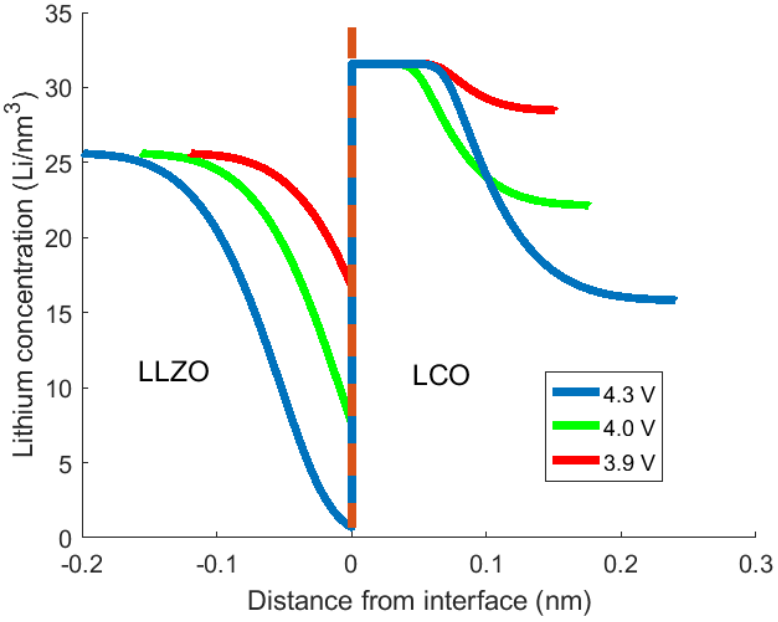

Figure 3.1: Lithium concentration at the LLZO-LCO interface at different voltages (vs. Li/Li^+) of LCO: blue = 4.3 V ($Li_{0.5}CoO_2$), green = 4.0 V ($Li_{0.7}CoO_2$), red = 3.9 V ($Li_{0.9}CoO_2$). Where the lines end the bulk lithium concentration is reached.

3.9 V the space-charge region is approximately 0.25 nm wide, but at 4.3 V the space-charge region has almost doubled in thickness. The effect on the Li-concentration at the LLZO interface is even more dramatic, at 3.9 V the Li-concentration drops by 35%, while at 4.3 V it decreases by more as 95 %.

As shown in Figure 3.2 the effect of space-charges on the Li-concentration are significantly smaller at the LCO-LATP interface. Although with a thickness of 0.3 to 0.5 nm the size of the space-charge region is comparable to that at the LCO-LLZO interface, the amount of Li-ions inserted in the LCO is much smaller. The smaller change in Li-concentration in LCO at the LATP interface compared to LCO at the interface of LLZO is caused by the stronger Coulomb interaction between defects in LATP, a consequence of the lower relative permittivity of LATP. This makes it energetically more expensive to remove lithium-ions from LATP, and therefore less lithium ions migrate towards the LCO to compensate for the difference in chemical potential. Although less Li-ions move over the LCO-LATP interface, the lower bulk Li-concentration in LATP means that a larger percentage of Li-ions is removed, over 60% at 3.9 V and 100% at 4.3 V.

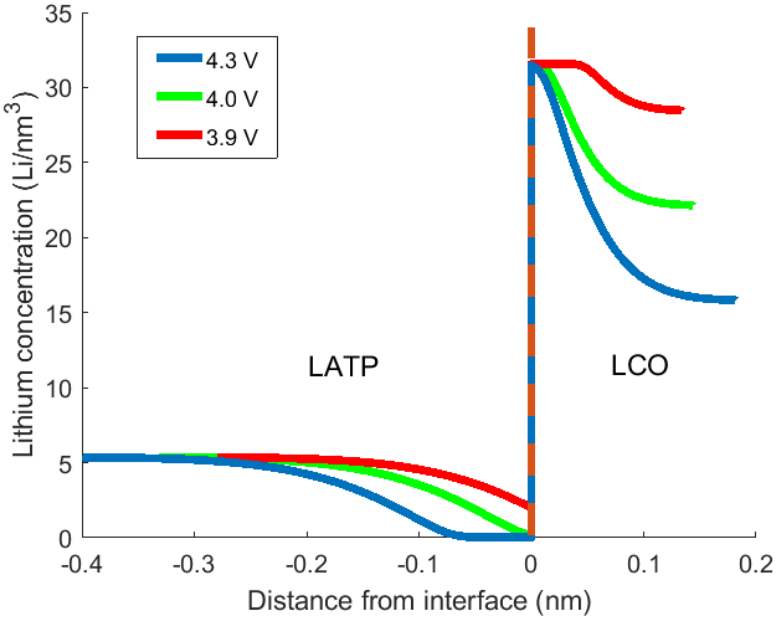

Figure 3.2: Lithium concentration at the LATP-LCO interface at different voltages of LCO: blue = 4.3 V ($Li_{0.5}CoO_2$), green = 4.0 V ($Li_{0.7}CoO_2$), red = 3.9 V ($Li_{0.9}CoO_2$). Where the lines end the bulk lithium concentration is reached.

The differences in capacitance of the LCO-LLZO and LCO-LATP interfaces shown in Table 3.2 reflect the differences in migrated Li-ions. With increasing voltage more Li-ions move into the LCO, thus increasing the capacitance of the space-charge layer. At the LCO-LATP interface this leads to a capacitance of 4 to 11 $\mu F/cm^2$, while the

	LATP		LLZO	
	Capacitance ($\mu F/cm^2$)	Resistance (Ω cm^2)	Capacitance ($\mu F/cm^2$)	Resistance (Ω cm^2)
3.9 V	4	$5*10^{-4}$	12	$-3*10^{-5}$
4.0 V	8	$2*10^{-2}$	29	$-2*10^{-4}$
4.3 V	11	17	49	$3*10^{-3}$

Table 3.2: Space-charge layer capacitance and resistance at the LCO-solid electrolyte interfaces.

capacitance at the LLZO interface is between 12 and 49 $\mu F/cm^2$. The calculated capacitances at the interfaces of the LCO and solid electrolytes are comparable to the capacitance reported at the interface of LCO in contact with a liquid electrolyte [65]. Landstorfer et al. have calculated a capacitance of 370.81 $\mu F/cm^2$ at the interface of LLZO with an unspecified cathode material, which is significantly larger compared to the results presented here. This large value can be explained by the fact that the Coulomb interaction was not taken into account and a larger maximum Li-concentration in LLZO was assumed, which both contribute to a higher capacitance.
Based on the present model an increasing potential leads to a rising Li-conductivity in LCO, because of an increased Li-concentration and an increased Li-diffusivity. In both solid electrolytes the Li-conductivity decreases, because of a lower Li-concentration and a decreasing Li-diffusivity. At the LCO-LLZO interface the increase in Li-conductivity through LCO is larger than the decrease in Li-conductivity through the LLZO at 3.9 and 4.0 V, and consequentially the space-charge layer decreases the resistance for Li-ion transport over the interface. When increasing the LCO voltage to 4.3 V the LLZO becomes almost depleted of Li-ions, which leads to an increased resistance over the interface, as shown in Table 3.2.
At the LCO-LATP interface the removal of Li-ions from LATP causes larger problems, reflected in the orders of magnitude rise in interface resistance upon increasing the voltage. At 3.9 V the resistance is small, but at 4.0 V the Li-concentration drops significantly, raising the resistance by two orders of magnitude. At 4.3 V a Li-depleted layer of 1 Ångström is formed, in which the Li-conductivity is negligible, and as a result a further increase in the space-charge resistance is observed. However, the resistance of 17 Ω cm^2 reported in Table 3.2 is doubtful, because it quadratically depends on the lower limit of the Li-concentration allowed in the model via Equations 3.13 and 3.14, which is (arbitrarily) set at 0.015 Li/nm^3.[1] Currently, it is unknown which value is realistic for the lower limit for the Li-concentration in LATP, and it could be that

[1] Defining a lower limit for the Li-concentration is necessary because a Li-concentration of zero would cause the resistance to reach an infinite value, which seems unrealistic over distances below a few Ångström.

a value of 0.15 Li/nm^3 is a more realistic limit, which would reduce the space-charge resistance to 0.3 Ω cm^2, but determining the lower limit of the Li-concentration will require a thorough experimental investigation. In addition, the depletion of Li-ions at the interface may induce local structural changes that have additional consequences on the resistance, not taken into account here.
However, this example does show an advantage of solid electrolytes with high Li-ion concentration, such as LLZO. Although more Li-ions are removed from LLZO than from LATP, the high Li-concentration prevents the formation of a layer depleted of Li-ions, thus leading to a smaller interface resistance due to the space-charge layer.

3.3.2. Interfaces of anode and solid-electrolyte materials

At the negative electrode Li-ions near the interface of the electrolyte and the anode material are driven towards the higher Li-voltage (lower chemical potential) of the solid electrolyte. When graphite is in contact with LLZO this leads to a space-charge region in graphite where lithium is completely depleted, while there is a significant increase of Li-ions in the LLZO, as shown in Figure 3.3.

The thickness of the space-charge layer strongly depends on the voltage applied to

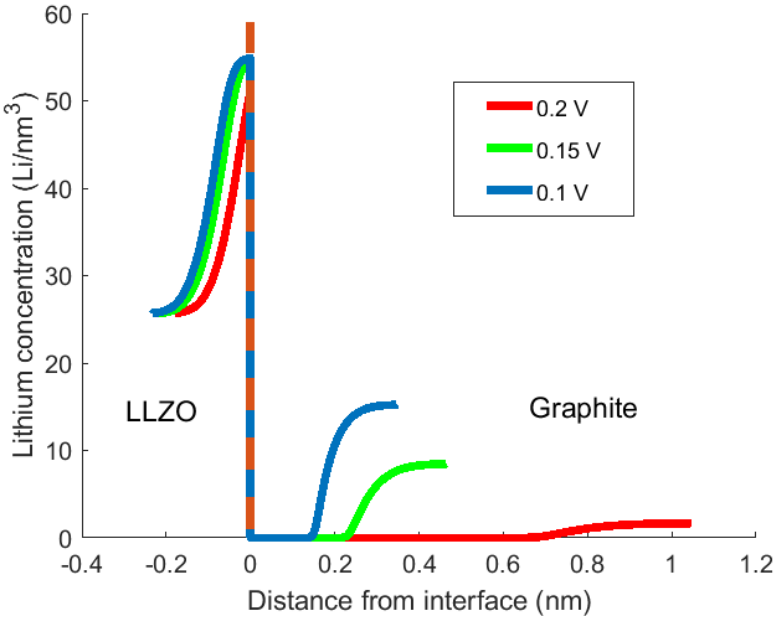

Figure 3.3: Lithium concentration at the LLZO-graphite interface at different voltages for graphite: blue = 0.1 V ($Li_{0.9}C_6$), green = 0.15 V ($Li_{0.5}C_6$), red = 0.2 V ($Li_{0.1}C_6$). Where the lines end the bulk lithium concentration is reached.

the graphite, being approximately 0.4 nm at 0.1 V, increasing to approximately 1 nm. when graphite is at 0.2 V. Even though less Li-ions transfer towards the LLZO at 0.2 V

as compared to 0.1 V, a more extensive space-charge layer is formed due to the lower Li-concentration in the graphite bulk.
In Figure 3.4 it is shown that at the LATP-graphite interface the thickness of the space-charge layer is smaller compared to the LLZO-graphite interface. The lower maximum Li concentration in LATP in combination with its lower permittivity, compared to LLZO, makes it energetically more expensive to change the Li-concentration in LATP, leading to a smaller space-charge layer in the graphite.

The larger Coulomb interaction in LATP in combination with the small change

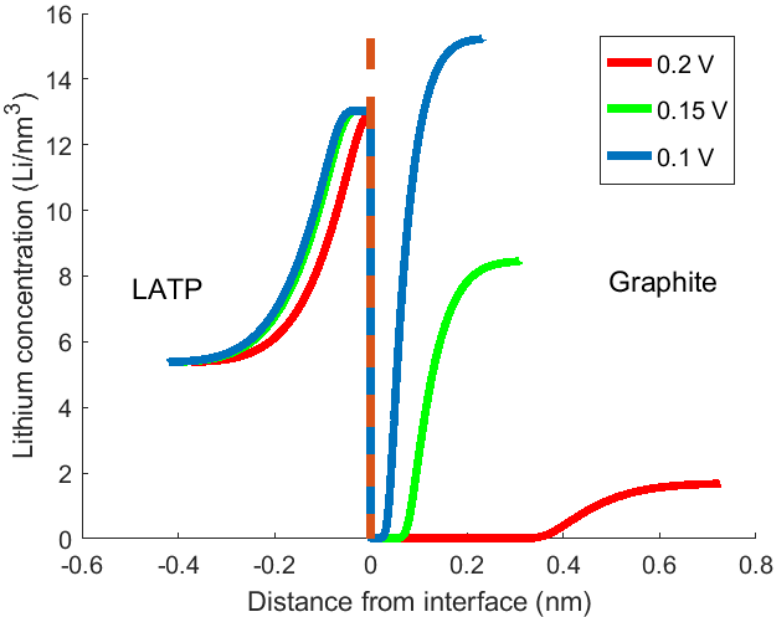

Figure 3.4: Lithium concentration at the LATP-graphite interface at different voltages for graphite: blue = 0.1 V ($Li_{0.9}C_6$), green = 0.15 V ($Li_{0.5}C_6$), red = 0.2 V ($Li_{0.1}C_6$). Where the lines end the bulk lithium concentration is reached.

in graphite voltage causes the amount of Li-ions transferring over the interface to be almost equal in all three cases, as demonstrated by the nearly overlapping Li-concentration profiles in the LATP in Figure 3.4. In the graphite the space-charge layer changes considerably with voltage, due to the large changes in bulk Li-concentration with voltage. When graphite is at 0.1 V the Li-concentration is large and Li-ions can easily be extracted, leading to a space-charge layer of 0.3 nm. At higher voltages the Li-concentration in graphite is much lower, and extraction of the same amount of Li-ions leads to a thicker space-charge layer, growing to 0.6 nm when the graphite is at 0.2 V.
In Table 3.3 the interface capacitances and resistances at the graphite interfaces are shown. In both cases the capacitance increases upon lowering the graphite voltage,

	LATP		LLZO	
	Capacitance (μF/cm^2)	Resistance ($*10^{-2}$ Ω cm^2)	Capacitance (μF/cm^2)	Resistance ($*10^{-2}$ Ω cm^2)
0.1 V	12	2	19	6
0.15 V	11	4	16	10
0.2 V	8	15	9	29

Table 3.3: Space-charge layer capacitance and resistance at the graphite-solid electrolyte interfaces.

because the voltage difference increases, it thus becomes more favourable for Li-ions to migrate towards the solid electrolyte.
In all the presented cases the interface resistance is in the order of 10^{-1} Ω cm^2, even though there is always a Li-depleted layer present in the graphite. Although the resistance shows a significant increase when thickness of the Li-depletion layer increases, in comparison to the Li-depleted layer at LATP-LLZO interface, it has a small effect. This can be explained by the high Li-diffusivity in graphite at low Li-concentrations (Equation 3.12), while the Li-diffusivity drops dramatically in the solid electrolytes at low Li-concentrations (Equation 3.13). As a result the formation of a layer depleted of Li-ions leads to a large interface resistance in LATP, while in graphite the interface resistance remains small. This shows that the resistance caused by space-charge layers strongly depends on the diffusion mechanism, as has been shown experimentally [31, 35].

3.3.3. Impact of Coulomb interaction

As discussed, the high defect concentrations in the space-charge layer of ASSB's implies that the Coulomb interaction between defects must be taken into account. To demonstrate the impact of the Coulomb interaction Li-concentration profiles with and without taking the Coulomb interaction into account are shown in Figure 3.5 for the LCO-LLZO interface at 4.3 V. Without the Coulomb interaction a steeper and larger change in lithium concentration is predicted, similar to the results of previous models [25, 26]. This results in a layer which is completely depleted of Li-ions in the solid electrolyte, a thicker space-charge layer in the LCO, and a larger region in which the maximum lithium concentration is reached.
By neglecting the Coulomb interaction between Li-defects the thickness of the interface layer is almost doubled. In comparison to the results with the Coulomb interaction in Table 3.2 the interface capacitance increases almost twofold to 90 μF/cm^2, and the interface resistance increases by two orders of magnitude to 2 Ω cm^2, caused by the low Li-conductivity in the LLZO layer depleted of lithium ions. Neglecting the Coulomb interaction thus has a significant impact on the space-charge layer and its properties, and this demonstrate that the Coulomb interactions between Li-defects cannot be neglected when describing space-charge layers and their effects in ASSB's.

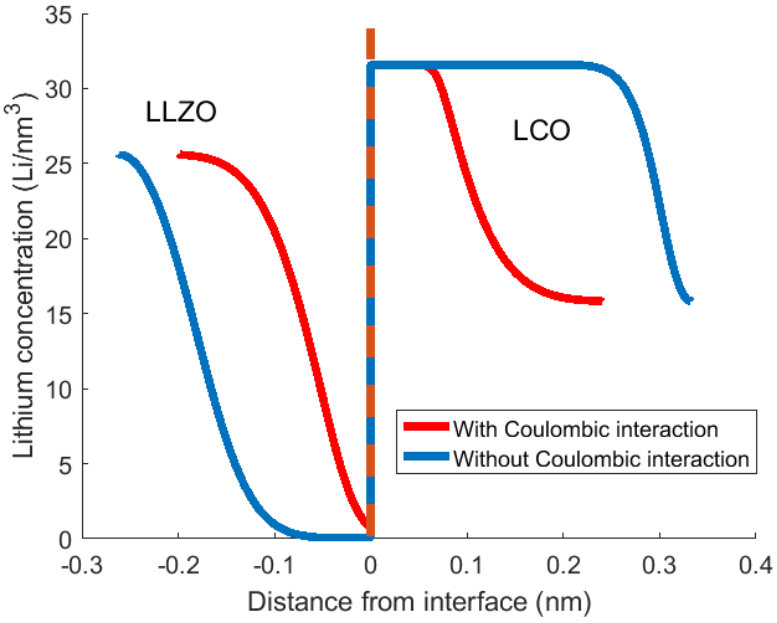

Figure 3.5: Lithium concentration at the LCO-LLZO interface at 4.3 V with and without Coulomb interactions. Where the lines end the bulk lithium concentration is reached.

3.4. Discussion

The presented space-charge model for electrode-solid electrolyte interfaces in ASSB's indicates that the space-charge layer has a thickness in the order of one nanometre, consistent with previous models [25, 26] and experiments [15, 16]. The resistance, capacitance, and thickness of the space-charge layer are shown to strongly depend on the electrode-solid electrolyte combination and electrode voltage. Taking the Coulomb interaction between defects into account is shown to have a significant effect. It severely reduces the amount of Li-defects formed in the space-charge layer, which in turn leads to a smaller interface capacitance. Comparing the calculations with and without the Coulomb interaction shows that it also has a large effect on the calculated interface resistance.

It should be realised that the current approach has a number of uncertainties. First of all, the Coulomb interaction energy term used here is based on the lattice energy of the crystal times the average distance between Li-defects, giving only a rough approximation of the interactions between charged defects. At high defect concentrations this approach might also break down when other effects, such as the transfer of electrons over the interface to reduce the Coulomb repulsion, might become more favourable as further increasing the ionic defect concentration.

Furthermore, a simple relation between ionic diffusion and ion concentration (Eq. 3.13) was used to calculate the resistance. As shown by Kozinsky et al. [66] the ionic conduction in a solid electrolyte can strongly vary with ion concentration, which influences the resistance over the space-charge layer. Implementing more complex equations to describe the ionic diffusion with changing ion concentration might therefore be necessary to improve the description of the space-charge resistance.

The space-charge model indicates that the Li-concentration in the solid electrolyte can change by 100% at the interface. With such large changes in Li-concentration it is unlikely that the solid electrolyte retains its original structure and properties. On the other hand, the model suggests that the changes in Li-concentration only occur in the first few atomic layers at the interface, whose structure may be stabilised by the underlying bulk crystal. In addition, the permittivity of the materials will depend on the Li-concentration, which has not been accounted for. Nevertheless, we believe that the presently used approximations allow a prediction that results in space-charge layer properties in the correct order of magnitude.

A comparison between experimental results [4, 14] and the model shows large differences in the interface resistance for most cases. Although the LCO-LATP interface at 4.3 V shows a similar interface resistance compared to experiments, in the other cases the differences are most likely caused by the approximation of a perfect and stable interface in the model, which is unlikely to hold for real interfaces.

At the moment electrode and solid electrolyte are brought into contact the high ionic conductivity will cause a transfer of ions over the interface within seconds. This is likely to cause a topotactic phase transition, for which indications have been found experimentally [11]. This will be the starting point of solid electrolyte decomposition, although it is unlikely that the phase formed via the topotactic transition is the thermodynamically most stable phase. More stable phases are likely to form [11], and even though their growth is kinetically limited [67] experiments have been able to observe

these phases grow within a day [68, 69]. Extrapolation of the decomposition rate for $Li_{10}GeP_2S_{12}$ (LGPS) shows an expected thickness of the decomposition layer of 370 nm after one year [68]. But this is without considering the effects of cycling the battery, which will lead to further growth of the decomposition layer [70]. In this decomposition layer different phases with differing potentials can occur, thus explaining experimental observations of potential drops at the interface spread out over roughly a micrometer [12, 13]. Especially considering the results of the model presented here, the potential drop over the decomposition layer seems to be a more plausible explanation of the experimental observations than a space-charge layer of a micrometre.

The current results also shed light on the effect of coatings at the electrode-electrolyte interfaces. Since the space-charge layers are on the scale of a nanometre it is unlikely that they improve battery performance by reducing space-charge effects, as has been suggested [16, 19–21], although space-charge layers can become smaller when applying coatings [71]. Instead, the prediction that space-charge layers are small in extend supports the suggestion that coatings improve the performance of ASSB's by preventing interface decomposition of the electrode and electrolyte [22–24], which underlines that creating a stable electrode-electrolyte interface is essential for creating high-rate ASSB's.

The formation of decomposition products on the electrode-electrolyte interface changes the properties of the materials on the interfaces, new phases might be formed, and the presented space-charge model breaks down. Incorporating the effects of the instability at the interfaces requires the determination of all the relevant parameters for the newly formed phases, which may be an important next step for modelling specific electrode-solid electrolyte interfaces when sufficient data is available.

The nanometre scale of space-charge layers implicates that these will only form when the electrode and solid electrolyte are in contact with each other on the atomic scale, which is essential for charge-transfer over the interface. The space-charge capacitance can thus be used as a measure for the amount of contact area between solid electrolyte and electrode on the atomic scale, which is an important parameter for increasing the performance for ASSB's.

Here we have shown results for a number of electrode and solid electrolyte combinations, but we have not studied the important class of sulphide solid electrolytes. Since the ion concentration, potential and dielectric constant are not vastly different between oxide and sulphide solid electrolytes, we expect space-charge layers in the order of a nanometre. But the effects caused by the space-charge layer could be quite different, for example if thick Li-depleted layers cause a large resistance over the space-charge layer. Applying the model to other electrode and solid electrolyte materials would therefore be an interesting path for future research.

3.5. Conclusion

The space-charge effect in all-solid-state-batteries is shown to lead to space-charge layers with a thickness in the nanometre regime, causing resistances below one $\Omega\ cm^2$ at the interfaces investigated, thus having a negligible effect on the performance of ASSB's. A significant increase to the interface resistance is only expected to occur when the solid electrolyte becomes completely depleted of Li-ions in the space-charge

layer.
These results suggest that space-charge layers do not stand in the way of high-rate all-solid-state batteries. Instead formation of poorly conducting decomposition products, as well as small contact areas are expected to induce the large interface resistances observed experimentally.
Furthermore, the Li-concentration in the space-charge layer can change by 100%, although it strongly depends on the combination of materials and the electrode voltage. Taking Coulomb interactions between charged defects into account is shown to have a large impact, and therefore appears to be essential for a correct description of space-charge layers and their effects in ASSB's.

References

[1] C. Bauer, J. Hofer, H.J. Althaus, A. Del Duce, and A. Simons. The environmental performance of current and future passenger vehicles: life cycle assessment based on a novel scenario analysis framework. *Appl. Energy*, 157:871–883, 2015. doi: 10.1016/j.apenergy.2015.01.019.

[2] B.V. Lotsch and J. Maier. Relevance of solid electrolytes for lithium-based batteries: a realistic view. *J. Electroceram.*, 38(2-4):128–141, 2017. doi: 10.1007/s10832-017-0091-0.

[3] T. Placke, R. Kloepsch, S. Dühnen, and M. Winter. Lithium ion, lithium metal, and alternative rechargeable battery technologies: the odyssey for high energy density. *J. Solid State Electrochem.*, 21(7):1939–1964, 2017. doi: 10.1007/s10008-017-3610-7.

[4] C. Yu, S. Ganapathy, E.R.H. van Eck, H. Wang, S. Basak, Z. Li, and M. Wagemaker. Accessing the bottleneck in all-solid state batteries, lithium-ion transport over the solid-electrolyte-electrode interface. *Nat. Commun.*, 8(1):1086, 2017. doi: 10.1038/s41467-017-01187-y.

[5] K. Takada. Solid electrolytes and solid-state batteries. *AIP Conf. Proc.*, 1765: 020008, 2016. doi: 10.1063/1.4961900.

[6] A.C. Luntz, J. Voss, and K. Reuter. Interfacial challenges in solid-state Li ion batteries. *J. Phys. Chem. Lett.*, 6(22):4599–4604, 2015. doi: 10.1021/acs.jpclett.5b02352.

[7] H.K. Tian and Y. Qi. Simulation of the effect of contact area loss in all-solid-state Li-ion batteries. *J. Electrochem. Soc.*, 164(11):E3512–E3521, 2017. doi: 10.1149/2.0481711jes.

[8] J.G. Kim, B. Son, S. Mukherjee, N. Schuppert, A. Bates, O. Kwon, M.J. Choi, H.Y. Chung, and S. Park. A review of lithium and non-lithium based solid state batteries. *J. Power Sources*, 282:299–322, 2015. doi: 10.1016/j.jpowsour.2015.02.054.

[9] Y. Zhu, X. He, and Y. Mo. Origin of outstanding stability in the lithium solid electrolyte materials: Insights from thermodynamic analyses based on first-principles calculations. *ACS Appl. Mater. Interfaces*, 7(42):23685–23693, 2015. doi: 10.1021/acsami.5b07517.

[10] J. Auvergniot, A. Cassel, J.B. Ledeuil, V. Viallet, V. Seznec, and R. Dedryvere. Interface stability of argyrodite Li_6PS_5Cl toward $LiCoO_2$, $LiNi_{1/3}Co_{1/3}Mn_{1/3}O_2$, and $LiMn_2O_4$ in bulk all-solid-state batteries. *Chem. Mater.*, 29(9):3883–3890, 2017. doi: 10.1021/acs.chemmater.6b04990.

[11] Y. Tian, T. Shi, W.D. Richards, J. Li, J.C. Kim, S.H. Bo, and G. Ceder. Compatibility issues between electrodes and electrolytes in solid-state batteries. *Ener. Env. Science*, 10(5):1150–1166, 2017. doi: 10.1039/c7ee00534b.

[12] K. Yamamoto, Y. Iriyama, T. Asaka, T. Hirayama, H. Fujita, C.A. Fisher, K. Nonaka, Y. Sugita, and Z. Ogumi. Dynamic visualization of the electric potential in an all-solid-state rechargeable lithium battery. *Angew. Chem.*, 49(26):4414–4417, 2010. doi: 10.1002/anie.200907319.

[13] H. Masuda, N. Ishida, Y. Ogata, D. Ito, and D. Fujita. Internal potential mapping of charged solid-state-lithium ion batteries using *in situ* Kelvin probe force microscopy. *Nanoscale*, 9(2):893–898, 2017. doi: 10.1039/c6nr07971g.

[14] M. Haruta, S. Shiraki, T. Suzuki, A. Kumatani, T. Ohsawa, Y. Takagi, R. Shimizu, and T. Hitosugi. Negligible negative space-charge layer effects at oxide-electrolyte/electrode interfaces of thin-film batteries. *Nano Lett.*, 15(3):1498–1502, 2015. doi: 10.1021/nl5035896.

[15] Y. Aizawa, K. Yamamoto, T. Sato, H. Murata, R. Yoshida, C.A.J. Fisher, T. Kato, Y. Iriyama, and T. Hirayama. *In situ* electron holography of electric potentials inside a solid-state electrolyte: effect of electric-field leakage. *Ultramicroscopy*, 178:20–26, 2017. doi: 10.1016/j.ultramic.2016.07.015.

[16] K. Takada, N. Ohta, L. Zhang, X. Xu, B.T. Hang, T. Ohnishi, M. Osada, and T. Sasaki. Interfacial phenomena in solid-state lithium battery with sulfide solid electrolyte. *Solid State Ionics*, 225:594–597, 2012. doi: 10.1016/j.ssi.2012.01.009.

[17] K. Takada. Progress and prospective of solid-state lithium batteries. *Acta Mater.*, 61(3):759–770, 2013. doi: 10.1016/j.actamat.2012.10.034.

[18] K. Takada, N. Ohta, and Y. Tateyama. Recent progress in interfacial nanoarchitectonics in solid-state batteries. *J. Inorg. Organomet. P.*, 25(2):205–213, 2014. doi: 10.1007/s10904-014-0127-8.

[19] T. Okumura, T. Nakatsutsumi, T. Ina, Y. Orikasa, H. Arai, T. Fukutsuka, Y. Iriyama, T. Uruga, H. Tanida, Y. Uchimoto, and Z. Ogumi. Depth-resolved X-ray absorption spectroscopic study on nanoscale observation of the electrode-solid electrolyte interface for all solid state lithium ion batteries. *J. Mater. Chem.*, 21(27):10051, 2011. doi: 10.1039/c0jm04366d.

[20] B. Wu, S. Wang, W.J. Evans Iv, D.Z. Deng, J. Yang, and J. Xiao. Interfacial behaviours between lithium ion conductors and electrode materials in various battery systems. *J. Mater. Chem. A*, 4(40):15266–15280, 2016. doi: 10.1039/c6ta05439k.

[21] C. Yada, C.E. Lee, D. Laughman, L. Hannah, H. Iba, and B.E. Hayden. A high-throughput approach developing lithium-niobium-tantalum oxides as electrolyte/cathode interlayers for high-voltage all-solid-state lithium batteries. *J. Electrochem. Soc.*, 162(4):A722–A726, 2015. doi: 10.1149/2.0661504jes.

[22] A. Sakuda, A. Hayashi, and M. Tatsumisago. Interfacial observation between $LiCoO_2$ electrode and Li_2S-P_2S_5 solid electrolytes of all-solid-state lithium secondary batteries using transmission electron microscopy. *Chem. Mater.*, 22(3): 949–956, 2010. doi: 10.1021/cm901819c.

[23] T. Ohtomo, A. Hayashi, M. Tatsumisago, Y. Tsuchida, S. Hama, and K. Kawamoto. All-solid-state lithium secondary batteries using the $75Li_2S$ - $25P_2S_5$ glass and the $70Li_2S$ - $30P_2S_5$ glass-ceramic as solid electrolytes. *J. Power Sources*, 233: 231–235, 2013. doi: 10.1016/j.jpowsour.2013.01.090.

[24] K. Takahashi, K. Hattori, T. Yamazaki, K. Takada, M. Matsuo, S. Orimo, H. Maekawa, and H. Takamura. All-solid-state lithium battery with $LiBH_4$ solid electrolyte. *J. Power Sources*, 226:61–64, 2013. doi: 10.1016/j.jpowsour.2012.10.079.

[25] S. Braun, C. Yada, and A. Latz. Thermodynamically consistent model for space-charge-layer formation in a solid electrolyte. *J. Phys. Chem. C*, 119(39):22281–22288, 2015. doi: 10.1021/acs.jpcc.5b02679.

[26] M. Landstorfer, S. Funken, and T. Jacob. An advanced model framework for solid electrolyte intercalation batteries. *Phys. Chem. Chem. Phys.*, 13(28):12817–12825, 2011. doi: 10.1039/c0cp02473b.

[27] F. Zimmer, P. Ballone, J. Maier, and M. Parrinello. Charge carrier interactions in ionic conductors: a classical molecular-dynamics and Monte Carlo study on AgI. *J. Chem. Phys.*, 112(14):6416–6423, 2000. doi: 10.1063/1.481205.

[28] J. Maier. Chemical potential of charge carriers in solids. *Z. Phys. Chem.*, 219 (1-2005):35–46, 2005. doi: 10.1524/zpch.219.1.35.55018.

[29] J. Maier. Enhancement of the ionic conductivity in solid-solid-dispersions by surface induced defects. *Berich. Bunsengesell.*, 88(11):1057–1062, 1984. doi: 10.1002/bbpc.198400007.

[30] J. Maier. Defect chemistry and conductivity effects in heterogeneous solid electrolytes. *J. Electrochem. Soc.*, 134(6):1524, 1987. doi: 10.1149/1.2100703.

[31] H. Yamada, K. Suzuki, Y. Oga, I. Saruwatari, and I. Moriguchi. Lithium depletion in the solid electrolyte adjacent to cathode materials. *ECS Transactions*, 50(1): 1–12, 2013. doi: 10.1149/05001.0001ecst.

[32] J. Maier. Nanoionics: ion transport and electrochemical storage in confined systems. *Nat. Mater.*, 4(11):805–815, 2005. doi: 10.1038/nmat1513.

[33] Q. Zhang, J. Pan, P. Lu, Z. Liu, M.W. Verbrugge, B.W. Sheldon, Y.T. Cheng, Y. Qi, and X. Xiao. Synergetic effects of inorganic components in solid electrolyte interphase on high cycle efficiency of lithium ion batteries. *Nano Lett.*, 16(3):2011–2016, 2016. doi: 10.1021/acs.nanolett.5b05283.

[34] B. Kumar, S. Nellutla, J.S. Thokchom, and C. Chen. Ionic conduction through heterogeneous solids: delineation of the blocking and space charge effects. *J. Power Sources*, 160(2):1329–1335, 2006. doi: 10.1016/j.jpowsour.2006.02.062.

[35] H. Yamada, K. Suzuki, K. Nishio, K. Takemoto, G. Isomichi, and I. Moriguchi. Interfacial phenomena between lithium ion conductors and cathodes. *Solid State Ionics*, 262:879–882, 2014. doi: 10.1016/j.ssi.2013.10.001.

[36] J. Maier. Ionic conduction in space charge regions. *Prog. Solid State Chem.*, 23 (3):171–263, 1995. doi: 10.1016/0079-6786(95)00004-e.

[37] S. Kim, J. Fleig, and J. Maier. Space charge conduction: simple analytical solutions for ionic and mixed conductors and application to nanocrystalline ceria. *Phys. Chem. Chem. Phys.*, 5(11):2268–2273, 2003. doi: 10.1039/b300170a.

[38] C.C. Chen and J. Maier. Space charge storage in composites: thermodynamics. *Phys. Chem. Chem. Phys.*, 19(9):6379–6396, 2017. doi: 10.1039/c6cp08134g.

[39] L.A. Haverkate, W.K. Chan, and F.M. Mulder. Large space-charge effects in a nanostructured proton conductor. *Adv. Funct. Mater.*, 20(23):4107–4116, 2010. doi: 10.1002/adfm.201000692.

[40] R.B. Smith, E. Khoo, and M.Z. Bazant. Intercalation kinetics in multiphase-layered materials. *J. Phys. Chem. C*, 121(23):12505–12523, 2017. doi: 10.1021/acs.jpcc.7b00185.

[41] N. Hainovsky and J. Maier. Simple phenomenological approach to premelting and sublattice melting in Frenkel disordered ionic crystals. *Phys. Rev. B*, 51(22):15789–15797, 1995. doi: 10.1103/PhysRevB.51.15789.

[42] K. Ragavendran, D. Vasudevan, A. Veluchamy, and B. Emmanuel. Computation of Madelung energies for ionic crystals of variable stoichiometries and mixed valencies and their application in lithium-ion battery voltage modeling. *J. Phys. Chem. B*, 108(43):16899–16903, 2004. doi: 10.1021/jp047174d.

[43] D. Sherwood, K. Ragavendran, and B. Emmanuel. Madelung-Buckingham model as applied to the prediction of voltage, crystal volume changes, and ordering phenomena in spinel-type cathodes for lithium batteries. *J. Phys. Chem. B*, 109 (26):12791–12794, 2005. doi: 10.1021/jp050854b.

[44] M.C. Gobel, G. Gregori, and J. Maier. Numerical calculations of space charge layer effects in nanocrystalline ceria. Part I: comparison with the analytical models and derivation of improved analytical solutions. *Phys. Chem. Chem. Phys.*, 16(21): 10214–10231, 2014. doi: 10.1039/c3cp54615b.

[45] M.D. Levi and D. Aurbach. Diffusion coefficients of lithium ions during intercalation into graphite derived from the simultaneous measurements and modeling of electrochemical impedance and potentiostatic intermittent titration characteristics of thin graphite electrodes. *J. Phys. Chem. B*, 101(23):4641–4647, 1997. doi: 10.1021/Jp9701911.

[46] M.D. Levi, G. Salitra, B. Markovsky, H. Teller, D. Aurbach, U. Heider, and L. Heider. Solid-state electrochemical kinetics of Li-ion intercalation into $Li_{1-x}CoO_2$: simultaneous application of electroanalytical techniques SSCV, PITT, and EIS. *J. Electrochem. Soc.*, 146(4):1279, 1999. doi: 10.1149/1.1391759.

[47] G.K. Phani Dathar, J. Balachandran, P.R.C. Kent, A.J. Rondinone, and P. Ganesh. Li-ion site disorder driven superionic conductivity in solid electrolytes: a first-principles investigation of β-Li_3PS_4. *J. Mater. Chem. A*, 5(3):1153–1159, 2017. doi: 10.1039/c6ta07713g.

[48] B. Vadlamani, K. An, M. Jagannathan, and K.S.R. Chandran. An *in situ* electrochemical cell for neutron diffraction studies of phase transitions in small volume electrodes of Li-ion batteries. *J. Electrochem. Soc.*, 161(10):A1731–A1741, 2014. doi: 10.1149/2.0951410jes.

[49] K. Arbi, M. Hoelzel, A. Kuhn, F. Garcia-Alvarado, and J. Sanz. Structural factors that enhance lithium mobility in fast-ion $Li_{1+x}Ti_{2-x}Al_x(PO_4)_3$ ($0 \leq x \leq 0.4$) conductors investigated by neutron diffraction in the temperature range 100-500 K. *Inorg. Chem.*, 52(16):9290–9296, 2013. doi: 10.1021/ic400577v.

[50] H. Buschmann, J. Dolle, S. Berendts, A. Kuhn, P. Bottke, M. Wilkening, P. Heitjans, A. Senyshyn, H. Ehrenberg, A. Lotnyk, V. Duppel, L. Kienle, and J. Janek. Structure and dynamics of the fast lithium ion conductor $Li_7La_3Zr_2O_{12}$. *Phys. Chem. Chem. Phys.*, 13(43):19378–19392, 2011. doi: 10.1039/c1cp22108f.

[51] Y.M. Choi, S.I. Pyun, J.S. Bae, and S.I. Moon. Effects of lithium content on the electrochemical lithium intercalation reaction into $LiNiO_2$ and $LiCoO_2$ electrodes. *J. Power Sources*, 56(1):25–30, 1995. doi: 10.1016/0378-7753(95)80004-z.

[52] K.S. Nanjundaswamy, A.K. Padhi, J.B. Goodenough, S. Okada, H. Ohtsuka, H. Arai, and J. Yamaki. Synthesis, redox potential evaluation and electrochemical characteristics of NASICON-related-3D framework compounds. *Solid State Ionics*, 92(1-2):1–10, 1996. doi: 10.1016/S0167-2738(96)00472-9.

[53] S. Lv, Z. Li, Z. Li, S. Ganapathy, E.R.H. van Eck, and M. Wagemaker. The garnet structure-ionic liquid composite electrolyte for Li-ion conducting paths interconnecting the double layers. *in preparation*.

[54] K.V. Rao and A. Smakula. Dielectric properties of cobalt oxide, nickel oxide, and their mixed crystals. *J. Appl. Phys.*, 36(6):2031–2038, 1965. doi: 10.1063/1.1714397.

[55] P. Delhaes, J.P. Manceau, and D. Guerard. Physical properties of first and second stage lithium graphite intercalation compounds. *Synth. Met.*, 2(3-4):277–284, 1980. doi: 10.1016/0379-6779(80)90057-0.

[56] T. Zangina, J. Hassan, K.A. Matori, R.S. Azis, U. Ahmadu, and A. See. Sintering behavior, AC conductivity and dielectric relaxation of $Li_{1.3}Ti_{1.7}Al_{0.3}(PO_4)_3$ NASICON compound. *Results Phys.*, 6:719–725, 2016. doi: 10.1016/j.rinp.2016.10.003.

[57] D. Rettenwander, A. Welzl, L. Cheng, J. Fleig, M. Musso, E. Suard, M.M. Doeff, G.J. Redhammer, and G. Amthauer. Synthesis, crystal chemistry, and electrochemical properties of $Li_{7-2x}La_3Zr_{2-x}Mo_xO_{12}$ (x = 0.1-0.4): stabilization of the cubic garnet polymorph via substitution of Zr^{4+} by Mo^{6+}. *Inorg. Chem.*, 54(21):10440–10449, 2015. doi: 10.1021/acs.inorgchem.5b01895.

[58] A. Wachter-Welzl, R. Wagner, D. Rettenwander, S. Taibl, G. Amthauer, and J. Fleig. Microelectrodes for local conductivity and degradation measurements on Al stabilized $Li_7La_3Zr_2O_{12}$ garnets. *J. Electroceram.*, 38(2-4):176–181, 2016. doi: 10.1007/s10832-016-0058-6.

[59] C. Wolverton and A. Zunger. First-principles prediction of vacancy order-disorder and intercalation battery voltages in Li_xCoO_2. *Phys. Rev. Lett.*, 81(3):606–609, 1998. doi: 10.1103/PhysRevLett.81.606.

[60] H. Yokokawa. Thermodynamic stability of sulfide electrolyte/oxide electrode interface in solid-state lithium batteries. *Solid State Ionics*, 285:126–135, 2016. doi: 10.1016/j.ssi.2015.05.010.

[61] R. Setton and J. Conard. Madelung energy and stability of the compound Li_7C_{24} prepared under pressure. *Mol. Cryst. Liq. Cryst. A*, 244(1):307–312, 1994. doi: 10.1080/10587259408050122.

[62] E.A. Il'ina, A.A. Raskovalov, and A.P. Safronov. The standard enthalpy of formation of superionic solid electrolyte $Li_7La_3Zr_2O_{12}$. *Thermochim. Acta*, 657:26–30, 2017. doi: 10.1016/j.tca.2017.09.019.

[63] V. Epp, Q. Ma, E.M. Hammer, F. Tietz, and M. Wilkening. Very fast bulk Li ion diffusivity in crystalline $Li_{1.5}Al_{0.5}Ti_{1.5}(PO_4)_3$ as seen using NMR relaxometry. *Phys. Chem. Chem. Phys.*, 17(48):32115–32121, 2015. doi: 10.1039/c5cp05337d.

[64] H.S.C. O'Neill and A. Navrotsky. Simple spinels: crystallographic parameters, cation radii, lattice energies, and cation distribution. *Am. Mineral.*, 68:181–194, 1983.

[65] M.G.S.R. Thomas, P.G. Bruce, and J.B. Goodenough. AC impedance analysis of polycrystalline insertion electrodes: application to $Li_{1-x}CoO_2$. *J. Electrochem. Soc.*, 132(7):1521, 1985. doi: 10.1149/1.2114158.

[66] B. Kozinsky, S.A. Akhade, P. Hirel, A. Hashibon, C. Elsasser, P. Mehta, A. Logeat, and U. Eisele. Effects of sublattice symmetry and frustration on ionic transport in garnet solid electrolytes. *Phys. Rev. Lett.*, 116(5):055901, 2016. doi: 10.1103/PhysRevLett.116.055901.

[67] Fudong Han, Yizhou Zhu, Xingfeng He, Yifei Mo, and Chunsheng Wang. Electrochemical stability of $Li_{10}GeP_2S_{12}$ and $Li_7La_3Zr_2O_{12}$ solid electrolytes. *Adv. Ener. Mater.*, 6(8):1501590, 2016. doi: 10.1002/aenm.201501590.

[68] S. Wenzel, S. Randau, T. Leichtweiss, D.A. Weber, J. Sann, W.G. Zeier, and J. Janek. Direct observation of the interfacial instability of the fast ionic conductor $Li_{10}GeP_2S_{12}$ at the lithium metal anode. *Chem. Mater.*, 28(7):2400–2407, 2016. doi: 10.1021/acs.chemmater.6b00610.

[69] S. Wenzel, S.J. Sedlmaier, C. Dietrich, W.G. Zeier, and J. Janek. Interfacial reactivity and interphase growth of argyrodite solid electrolytes at lithium metal electrodes. *Solid State Ionics*, 2017. doi: 10.1016/j.ssi.2017.07.005.

[70] F. Han, T. Gao, Y. Zhu, K. J. Gaskell, and C. Wang. A battery made from a single material. *Adv. Mater.*, 27(23):3473–3483, 2015. doi: 10.1002/adma.201500180.

[71] J. Haruyama, K. Sodeyama, L.Y. Han, K. Takada, and Y. Tateyama. Space-charge layer effect at interface between oxide cathode and sulfide electrolyte in all-solid-state lithium-ion battery. *Chem. Mater.*, 26(14):4248–4255, 2014. doi: 10.1021/cm5016959.

Supporting information

The Matlab code of the space-charge model, in combination with a short manual on how to apply the code, is available as supporting information to the published article.

4

Diffusion mechanism of the Na-ion solid electrolyte Na_3PS_4 and potential improvements of halogen doping

This chapter has been published as: Niek J.J. de Klerk and Marnix Wagemaker, Diffusion mechanism of the Na-ion solid electrolyte Na_3PS_4 and potential improvements of halogen doping; Chemistry of Materials **28** (9), 3122-3130 (2016), doi: 10.1021/acs.chemmater.6b00698

DFT MD-simulations were performed on cubic and tetragonal Na_3PS_4. The MD-simulations show that the Na-conductivity based on the predicted self-diffusion is high in both the cubic and tetragonal phase. Higher Na-ion conductivity in Na_3PS_4 can be obtained by introducing Na-ion vacancies. Just 2% vacancies results in a conductivity of 0.2 S/cm, which is an order of magnitude larger than the calculated conductivity of the stoichiometric compound.
MD-simulations of halogen doped cubic Na_3PS_4 suggest a practical route to introduce vacancies, where Br-doping is predicted to result in the highest bulk conductivity. Detailed investigation of the Na-ion transitions during the MD-simulation reveals the role of vacancies and phonons in the diffusion mechanism. Furthermore, the orders of magnitude difference between the MD-simulations and experiments suggest that macroscopic conductivity can be significantly increased by reducing the grain boundary resistance.

4.1. Introduction

Nowadays the application of Li-ion batteries is widespread, powering mobile phones, laptops and electric cars. With the current growth rate the world's lithium resources could be depleted within 65 years [1], not yet considering the potential use of Li-ion batteries for large-scale storage of renewable energy sources. Already decades ago the larger sodium abundance has motivated the development of materials for Na-ion batteries [2–5]. Especially for static large scale application, as required for the storage of renewable energy, the lower costs of Na-batteries may outweigh the lower energy density [2].
Both for Li-ion and Na-ion batteries the flammability of liquid electrolytes poses a safety risk, encouraging the development of solid electrolytes [6–9]. An additional advantage of solid electrolytes is a potentially higher percentage of active material in the battery increasing the specific energy density, the ability to develop versatile geometries [10], and stability in excess of 10000 cycles [11].
At present Na-ion solid state batteries, applied for static large scale storage, typically use β"-alumina as solid electrolyte operating at temperatures above 270°C [4]. For this material conductivities between 0.1 and 0.001 S/cm have been reported at room temperature [4]. However, the synthesis of β"-alumina requires temperatures above 1200°C, and even higher temperatures to lower the grain boundary resistance, making these systems inherently expensive.
Recently Udovic et al. [12] have reported on $Na_2B_{12}H_{12}$, which is synthesised more easily, resulting in conductivities in the order of 0.1 S/cm above 270°C, however, with a relatively low room temperature conductivity of 10^{-6} S/cm. Sulphur based Na-ion solid electrolytes offer promising room temperature conductivities [13], of which glass-ceramic Na_3PS_4 doped with Si currently has the highest reported conductivity reaching $7.4 * 10^{-4}$ S/cm at room temperature [14].
The tetragonal phase of Na_3PS_4 has been known as a sodium-conductor for more than 20 years [15]. But Na_3PS_4 has gained renewed attention since Hayashi et al. [13] synthesised a room temperature stable glass ceramic phase showing a Na-conductivity of $2 * 10^{-4}$ S/cm. Since then the highest reported conductivities for this material are $4.6 * 10^{-4}$ S/cm [16], and $7.4 * 10^{-4}$ S/cm with 6% Si-doping [14].

Although high conductivity is an important prerequisite for electrolyte materials, good electrolyte-electrolyte and electrode-electrolyte contacts are an additional prerequisite for efficient charge transport in solid state batteries. For Na_3PS_4 it has been shown that good electrode-electrolyte contact can be obtained using cold pressing [13], in contrast to β"-alumina that requires sintering at 1800°C to obtain good solid-solid contacts [13]. Yubuchi et al. demonstrated that Na_3PS_4 can be prepared via a liquid-phase reaction [17], which can lead to even better electrode-electrolyte contacts. The present work aims at revealing the diffusion mechanism in Na_3PS_4, based on which potential routes to increase the Na-ion conductivity are investigated by modelling the diffusion using density functional theory molecular dynamics (DFT MD) simulations. For both the cubic and tetragonal phases of Na_3PS_4 high bulk self-diffusion is predicted, in both phases uncovering a vacancy mediated Na-ion transport mechanism. The modelling indicates that increasing the amount of vacancies, for instance achieved by halogen doping, may further enhance the Na-ion conductivity of this promising Na-ion solid electrolyte material.

4.2. Methods

DFT-calculations were performed using the GGA approach with the PAW-PBE basis set of VASP [18] and a cut-off energy of 280 eV. For the minimisation of Na_3PS_4 a single unit cell was used, and a k-point mesh of 4x4x4. For the minimisation of the other compositions a 2x2x2 super cell was used, with a k-point mesh of 2x2x2. For all the MD-calculations a 2x2x2 super cell was used, and a k-point mesh of 1x1x1 was used to reduce calculation time. The time between MD-steps was 2 femtoseconds, and the total simulation time was between 40 and 100 picoseconds. The MD-simulations were performed in the NVT-ensemble, with velocity scaling at every time-step. In all cases an equilibration time of 2.5 picoseconds was applied, to allow the system to reach equilibrium during the MD-simulations.
Based on the MD-simulations the jump rates between the different crystallographic sites in the cubic crystals has been determined. To locate the crystallographic position of a Na-ion during the MD-simulation the distance of a Na-ion to crystallographic distinct Na1(6b) and Na2(12d) sites was calculated. If the distance between the Na-ion and a crystallographic position is smaller than 1/8 of the unit cell length (~ 0.875 Å), corresponding to half the distance between neighbouring Na1- and Na2-sites, the Na-ion is assigned to the crystallographic position. In this way the crystallographic position of each Na-ion during the MD-simulation is known, and any transition towards another site can be distinguished.

4.3. Results

For Na_3PS_4 two crystal phases are known, a tetragonal phase [15], and a cubic phase [19]. However, the differences between the two phases are small, the tetragonal phase being tetragonal distorted with respect to the cubic phase. The tetragonal phase of Na_3PS_4 crystallises in the space group $P\bar{4}2_1c$ (no. 114) with lattice parameters a = 6.9520 Å and c = 7.0757 Å [15], while the cubic phase of Na_3PS_4 crystallises in the space group $I\bar{4}3m$ (no. 217) with lattice parameter a = 6.9965 Å [19]. The largest

difference between the lattice parameters is 1.1%, and the volume difference is less as 0.2%. The only significant difference is in the positions of the Na-ions.
In the tetragonal cell the cubic Na1(6b)-site splits into two Na-ion sites Na(2a) and Na(4d), where the latter is shifted approximately 0.5 Å with respect to its position in the cubic phase. For the cubic phase Na2(12d)-site occupancy is reported [19], which are positioned between the Na1(6b)-sites, but present energy minimisations of this structure indicate that the Na2(12d)-sites are not stable.
For both phases conductivities in the order of 10^{-6} S/cm have been reported in case

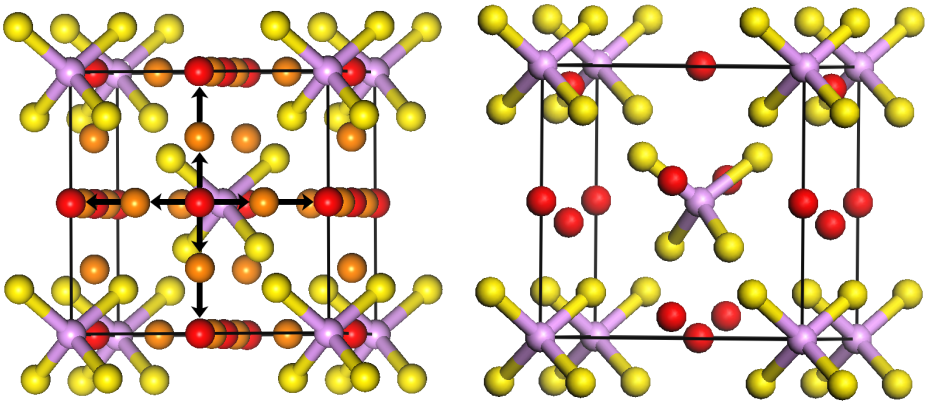

(a) (b)

Figure 4.1: (a) The unit cell of cubic Na_3PS_4, the P, S, Na1(6b)- and Na2(12d)-sites are represented by purple, yellow, red and orange, respectively, the proposed Na-pathway [19] is shown with arrows. (b) The unit cell of tetragonal Na_3PS_4, the P, S, and Na-sites are represented by purple, yellow, and red, respectively.

of poor inter-particle contacts [15, 17]. When the two phases are prepared in a similar way the two phases show similar conductivities [20]. Going from crystalline to glass-ceramic samples for the cubic phase results in a 30 times higher conductivity [19], which if applicable to the tetragonal phase should also make Na-conductivities in the order of 10^{-4} S/cm possible.
To test whether the small differences in crystal structure of the cubic and tetragonal phase have an influence on the Na-diffusivity MD-simulations where performed on both phases. As a starting point for the calculations on the cubic phase the crystal structure reported by Tanibata et al. [19] was used, shown in Figure 4.1a.
Relaxation of the reported structure, including a mixed Na1/Na2 occupancy [19], resulted in migration of the Na-ions on the Na2(12d)-sites towards the nearest vacant Na1(6b)-site. Apparently, at zero Kelvin in stoichiometric Na_3PS_4 Na-ion occupancy of the Na2-site is unstable in comparison to the Na1-site, therefore further energy minimisations were performed with all Na-ions occupying the Na1-sites.
For the tetragonal phase the crystal structure reported by Jansen et al. [15] was used as a starting point, shown in Figure 4.1b. After minimisation the energy of the tetragonal structure is 2 meV/atom lower compared to the energy of the cubic structure, in

close agreement to the value of 5 meV/atom recently reported [21]. The lower energy of the tetragonal phase is consistent with experiments that have shown that the tetragonal structure is the stable phase at low temperatures, and that the cubic phase is more stable at high temperatures [13].
The only significant difference between the two phases at the start of the MD-simulations is the 0.5 Å displacement from the center of each face of $\frac{2}{3}$ of the Na-ions in the tetragonal phase. The slightly different Na-positions do not lead to significant differences in the Na-ion distributions during the MD-simulations, as shown in Figure 4.2.
In Figures 4.2a and 4.2b the Na-ion distribution during a 100 ps. MD-simulation for stoichiometric Na_3PS_4 are shown, reflecting almost no Na-ion mobility between different Na1(6b)-sites at the time-scale of the MD-simulation. The Na-ions mostly vibrate around their original positions, and no transition paths between neighbouring Na-sites are observed.
Calculations on defect formation energies in the closely related compound Na_3PSe_4 have shown that the formation energy of Na-vacancies is two times lower than formation energies of other common defects [22]. This in combination with the small amount of impurities present in the starting compounds [14, 16] suggests that small amounts of Na-vacancies are present in Na_3PS_4, the impact of which will be investigated by introducing Na-vacancies in the MD-simulations.
When one Na-atom is removed from the 2x2x2 super cell, corresponding to a composition of $Na_{2.94}PS_4$, the Na-ion mobility increases drastically as demonstrated in Figures 4.2c and 4.2d. For both the cubic and tetragonal phases the $Na_{2.94}PS_4$ composition shows a broad Na-ion distribution around the Na1(6b)-sites, which are interconnected through the Na2(12d)-sites, consistent with the proposed pathway based on the Maximum Entropy Method applied to powder XRD data [19].
The effect of the vacancy concentration on Na-ion conductivity was studied by systematically varying the vacancy concentration as shown in Table 4.1. For all stoichiometries Na_xPS_4 with x <2.94 the super cell was optimised resulting in minor changes of the lattice parameters, all within 1% from the experimental value. For both phases the crystal structure became unstable during MD-simulations at the composition of $Na_{2.25}PS_4$, indicating the maximum vacancy concentration that can be achieved while keeping a stable crystal structure is less than 25%.

4.3.1. Diffusivity

From MD-simulations the tracer diffusivity (D^*) can be calculated using the definition for the tracer diffusion coefficient [23]:

$$D^* = \frac{1}{N2d} \sum_{i=1}^{N} \left(\frac{dr_i(t)}{dt} \right)^2 \tag{4.1}$$

where N is the total number of diffusing particles, d the dimensionality of the diffusion path (3 in this case), dt the simulation time, and $dr_i(t)$ the displacement of a single diffusing particle. By using the Nernst-Einstein equation the diffusivity can be related

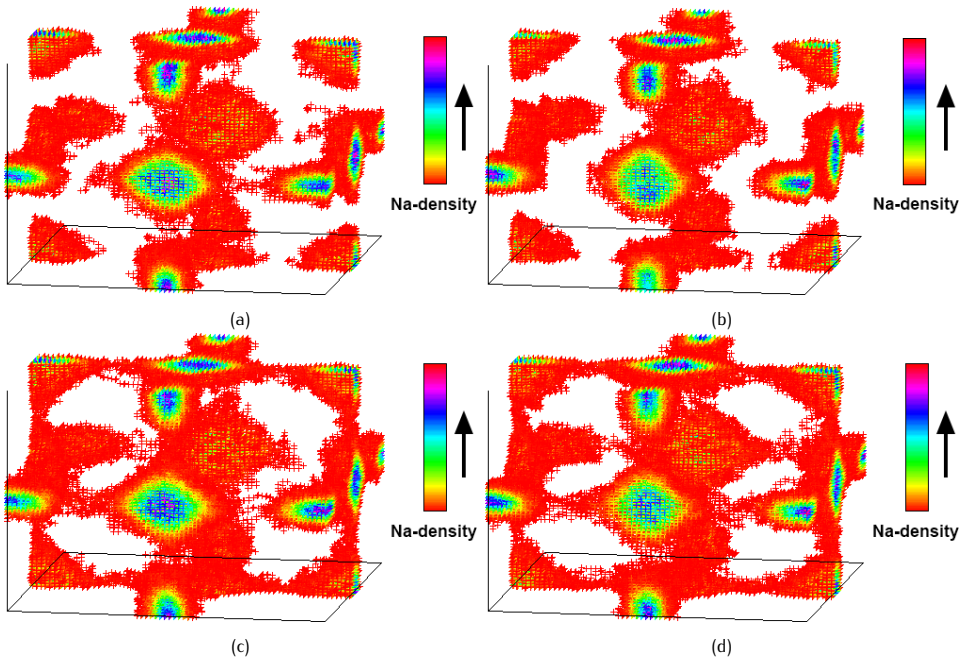

Figure 4.2: The Na-distribution during a 100 ps. MD-simulation at 525 K for (a) cubic Na_3PS_4, (b) tetragonal Na_3PS_4, (c) cubic $Na_{2.94}PS_4$, and (d) tetragonal $Na_{2.94}PS_4$.

to the conductivity (σ) [24]:

$$\sigma = \frac{ne^2z^2D}{kT} \tag{4.2}$$

where n is the particle density, e the elementary charge, z the ionic charge, D the diffusivity, k is Boltzmann's constant, and T the temperature in Kelvin.

Composition	Phase	D* ($*10^{-6}$ cm^2/sec)	σ^* (S/cm)
Na_3PS_4	cubic	0.3	0.02
	tetragonal	0.1	0.01
$Na_{2.94}PS_4$	cubic	3.3	0.20
	tetragonal	2.3	0.14
$Na_{2.88}PS_4$	cubic	5.0	0.30
	tetragonal	5.4	0.33
$Na_{2.75}PS_4$	cubic	5.0	0.29
	tetragonal	8.1	0.47
$Na_{2.50}PS_4$	cubic	8.0	0.42
	tetragonal	8.2	0.43

Table 4.1: Na-diffusivity and -conductivity for different compositions of Na_xPS_4 at 525 Kelvin based on the tracer diffusivity.

The results shown in Table 4.1 and Figure 4.3 show that introducing Na-vacancies has a large influence on the conductivity. This is illustrated by comparing the Na-densities for Na_3PS_4 and $Na_{2.94}PS_4$ in Figure 4.2 where a vacancy concentration of 2% ($Na_{2.94}PS_4$) shows to have a large impact on the Na-diffusion. This is reflected by the large increase in the MSD when vacancies are introduced, for the cubic (Figure 4.3a) as well as the tetragonal phase (Figure 4.3b).
Without vacancies the conductivity in the cubic and tetragonal phase are 0.02 and 0.01 S/cm, respectively, while a vacancy concentration of 2% ($Na_{2.94}PS_4$) results in an order of magnitude larger conductivity of 0.20 and 0.14 S/cm for the cubic and tetragonal phase, respectively. Further increasing the vacancy concentration to 17% ($Na_{2.50}PS_4$) raises the conductivity to 0.42 and 0.43 S/cm for the cubic and tetragonal phase, respectively.
For the glass ceramic cubic Na_3PS_4 experimental conductivities in the order of 10^{-4} S/cm have been reported [13, 14, 16, 25]. The results from the MD-simulations are two orders of magnitude higher in both phases. However, the experimentally measured macroscopic bulk conductivity includes diffusion over the grain boundaries and the electrode-electrolyte interface.
Recently Nose et al. have shown that improving the contact between Na_3PS_4 particles

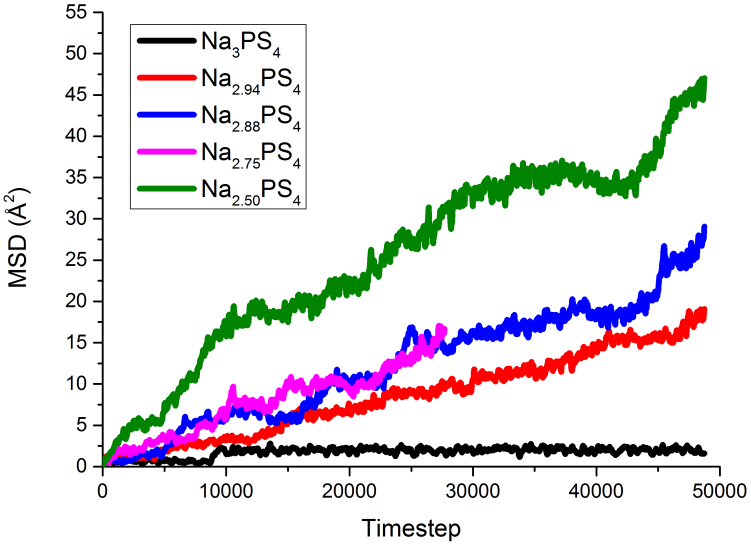

(a)

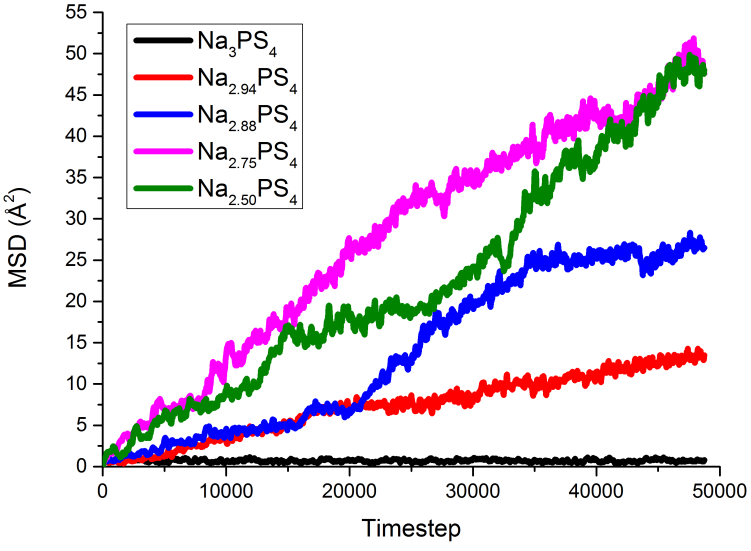

(b)

Figure 4.3: The MSD of Na during simulations with different compositions of Na_xPS_4 at 525 K in the (a) cubic and (b) tetragonal phase.

can increase the conductivity by a factor of 2 [26]. The 30 times increase in conductivity between crystalline and glass-ceramic samples [13] also indicates that diffusion over grain boundaries is more sluggish than bulk diffusion in Na_3PS_4. This indicates that the large differences between simulated and experimental conductivities are primarily caused by grain boundary and interface resistivity. This suggests that improving the contacts between Na_3PS_4 particles could significantly increase the performance of electrolytes of this material.
Although there are differences in the conductivities of the cubic and tetragonal phases, these are small and of the same order of magnitude as the error margin in the MD-calculations. The results shown in Figure 4.2 and in Table 4.1 predict that the cubic and tetragonal phases are equally good Na-ion conductors, and that the properties relevant to Na-diffusion are similar in both phases.
This was confirmed by comparison of the mean jump rates and activation energies of the two phases, shown in Table 4.2, the crystallographic sites of the cubic phase were used for both to be able to make a comparison between the jump rates. For brevity we will only describe the results for the cubic phase in the rest of this chapter.

Composition	Phase	mean Na1→Na1 jump rate (*10^{10} Hz)	mean Na1→Na2 jump rate (*10^{10} Hz)	Na1→Na1 ΔE_A (eV)
Na_3PS_4	cubic	0.09	41.56	0.28
	tetragonal	-†	42.95	-†
$Na_{2.94}PS_4$	cubic	1.57	50.10	0.16
	tetragonal	1.51	51.17	0.16
$Na_{2.88}PS_4$	cubic	3.28	60.60	0.13
	tetragonal	3.03	56.52	0.13
$Na_{2.75}PS_4$	cubic	5.83	63.27	0.11
	tetragonal	6.20	66.78	0.11
$Na_{2.50}PS_4$	cubic	7.97	79.38	0.10
	tetragonal	8.08	79.92	0.10

Table 4.2: Mean jump rates for the Na1→Na1-transition, mean jump rates for the Na1→Na2-transition, and the activation energy for Na1→Na1-transitions for different compositions of the cubic and tetragonal phase at 525 K. † In the simulation of tetragonal Na_3PS_4 no Na1-Na1 jumps occurred, thus the jump rate and activation energy could not be calculated.

4.3.2. Temperature dependence

The temperature dependence of the Na-ion diffusion was investigated by performing MD-simulations between 300 and 525 Kelvin for cubic $Na_{2.94}PS_4$ and $Na_{2.50}PS_4$. For $Na_{2.94}PS_4$ increasing the temperature showed to have a small effect, with the conductivity increasing from 0.17 S/cm at 300 K to 0.20 S/cm at 525 K. The effect of temperature is larger for $Na_{2.50}PS_4$, the conductivity went from 0.27 to 0.42 S/cm

when increasing the temperature from 300 to 525 K.
Because the lattice expansion with increasing temperature was not taken into account a MD-simulation with increased lattice parameters was also performed. The thermal volumetric expansion coefficient of Na_3PS_4 is unknown, however, for the related compound γ-Li_3PS_4 the volume expansion has been measured to be approximately 1.2% upon heating from 297 to 543 Kelvin [27]. Based on this we assume that the thermal volumetric lattice expansion of Na_3PS_4 is also small. Therefore MD-simulations were performed with 1% increased lattice parameters (3% volume expansion) for cubic $Na_{2.50}PS_4$ and $Na_{2.94}PS_4$ at 525 K.
The expanded lattice resulted in an increased conductivity, for $Na_{2.94}PS_4$ σ^* amounting 10% and for $Na_{2.50}PS_4$ σ^* amounting 17%. Clearly, the lattice expansion upon increasing temperature has a significant effect on the conductivity, also shown by the large effect of introducing bigger dopant atoms [21].

4.3.3. Detecting transitions

Using the method described in the Methods section jumps between distinct crystallographic Na-sites can be extracted from the MD-simulations. Using equation 4.3 the mean jump rate (τ) of the Na-ions can be determined:

$$\tau = \frac{J}{Nt} \tag{4.3}$$

where J is the number of jumps between Na-sites, N the number of Na-ions in the super cell, and t the total simulation time.
The mean jump rates for Na1→Na1-transitions and Na1→Na2-transitions are shown in Table 4.3. The most striking observation is the order of magnitude difference between the Na1→Na2 and Na1→Na1 mean jump rates, even when vacancies are present. This implies that in more than 90% of the cases a Na1→Na2 transition is followed by a backward Na2→Na1 transition, thus not contributing to (macroscopic) diffusion.
Transition state theory can be used to calculate the activation energy (ΔE_A) with [28]:

$$\Delta E_A = -kT\ln(\frac{\Gamma}{\nu_0}) \tag{4.4}$$

Where Γ is the hopping frequency and ν_0 is the attempt frequency. Since macroscopic diffusion is caused by the Na1→Na1 transitions the Na1→Na1 jump rate is used as the hopping frequency and the Na1→Na2 jump rate as the attempt frequency.
Although it is possible to determine the attempt frequency based on the lattice vibrations[29], this is not a trivial procedure, and typically it is assumed to be on the order of 10^{13} sec^{-1} [23]. With the method of detecting transitions used at present, estimating the attempt frequency is straightforward, assuming the position of the transition state is known and sufficiently separated from the starting state and final state. In this case the attempt frequency is 12 to 25 times smaller than the typically assumed 10^{13} sec^{-1}, where the latter would lead to severe overestimation of the activation energy.
Table 4.3 shows that the introduction of vacancies results in an increased mean jump rate for both transitions. However, upon introducing 2% vacancies the mean Na1→Na1 jump rate increases by a factor of 17, while the mean Na1→Na2 jump rate only increases by a factor of 1.2.

Composition	mean Na1→Na1 jump rate (*10^{10} sec^{-1})	mean Na1→Na2 jump rate (*10^{10} sec^{-1})	ΔE_A Na1→Na1 (eV)
Na_3PS_4	0.09	41.56	0.28
$Na_{2.94}PS_4$	1.57	50.10	0.16
$Na_{2.88}PS_4$	3.28	60.60	0.13
$Na_{2.75}PS_4$	5.83	63.27	0.11
$Na_{2.50}PS_4$	7.97	79.38	0.10

Table 4.3: Mean jump rates for the Na1→Na1-transition, mean jump rates for the Na1→Na2-transition, and the activation energy for Na1→Na1-transitions for different compositions of the cubic phase at 525 K.

This effect is reflected in the activation energies for Na1→Na1 transitions, which show a reduction of 0.12 eV on going from no vacancies (Na_3PS_4) to 2% vacancies ($Na_{2.94}PS_4$). By adding more vacancies the activation energy decreases further, although the effect per vacancy becomes smaller.
Experimentally activation energies between 0.20 and 0.28 eV have been reported, depending on the preparation procedure [14, 16], with more crystalline phases showing lower activation energies. The activation energies from the MD-simulations are very similar to the experimentally determined values, where the activation energy of Na_3PS_4 corresponds to the highest experimental value, and the activation energy based on 2% Na-vacancies is close to the lowest experimental activation energy.
Using the mean jump rates the diffusivity (D_J) can be calculated using the Einstein-Smoluchowski equation:

$$D_J = \frac{\tau a^2}{2d} \tag{4.5}$$

Where τ is the mean jump rate, a is the distance between the sites (3.5 Å between Na1(6b)-sites), and d is the number of dimensions of the diffusion pathway.
Since only the Na1→Na1-transitions contribute to macroscopic diffusion, the diffusivity is calculated based on the mean jump rate of this transition. Using Equation 4.2 the conductivity based on the mean jump rates (σ_J) can also be calculated.
When comparing the conductivities in Figure 4.4 significant differences are observed between the conductivities based on the tracer diffusivity and the mean jump rate. This can be explained by the back and forth transitions that contribute to the jump rates, thereby increasing the conductivity, whereas for the calculation of the tracer diffusivity these cancel out.
This can be quantified by the correlation factor (f), which is defined as $f = \frac{D^*}{D_J}$ [23]. For the vacancy rich compositions both diffusivity and conductivity are larger when calculated based on the jump rates, therefore $f<1$, indicating that in the presence of vacancies Na-ions often jump back and forth between Na1(6b)-sites.
Figure 4.4 suggests a relation between f and the vacancy concentration, however, we anticipate that this has no physical origin. At low vacancy concentrations on average the Na-ions perform only a few jumps during the simulations. Because the number of jumps is small, a jump to a previously visited site becomes less likely, and f will be

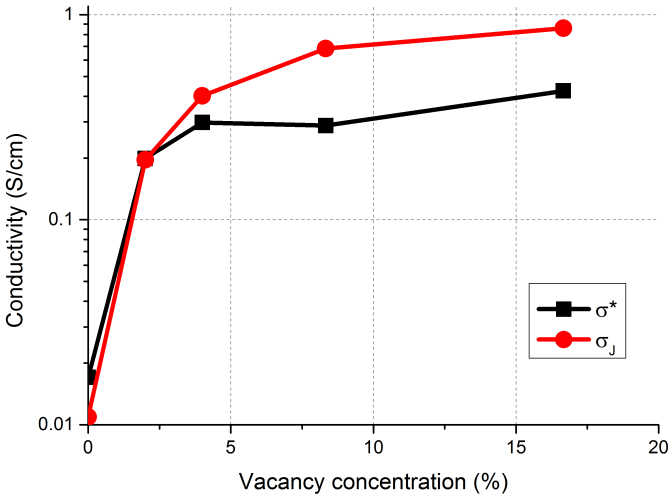

Figure 4.4: The conductivity, based on the tracer conductivity (σ^*) and on the mean Na1→Na1 jump rate (σ_J), versus vacancy concentration for the cubic phase at 525 K.

overestimated.
This effect is smaller at high vacancy concentrations since then more jumps occur, increasing the chance of back and forth jumps, explaining the dependence of f on the vacancy concentration. In order to obtain reliable values of f at low concentrations much more jumps should be sampled. This was not attempted here because of the significantly longer computational times this would require.

4.3.4. Metastability of the Na2-site

Tanibata et al. [19] report partial occupancies in the cubic phase, the Na2(12d)-site having an occupancy of 10% and the Na1(6b)-site having an occupancy of 80%, determined by refinement of room temperature X-ray diffraction data.
Because the multiplicity of the Na2(12d)-sites is twice that of the Na1(6b)-sites this implies that Na-ions on average spent 20% of their time on Na2-sites, and 80% of their time at Na1-sites. As mentioned earlier, relaxing a cubic structure with partial Na2-site occupancy towards its minimal energy results in migration of the Na-ions from the Na2-sites towards the Na1-sites, indicating that at zero Kelvin the Na2-site is unstable and thus unoccupied.
At room temperature therefore, the Na2-occupancies must be due to transitions between neighbouring Na1-sites connected via Na2-sites, as indicated by the electron density derived from the maximum entropy method [19] and the average Na-ion density from the present MD-simulations in Figures 4.2c and 4.2d.
The average Na2-site occupancies at finite temperatures can be extracted from the MD-simulations, the results of which are shown in Table 4.4. These indicate that an increasing number of vacancies, or equivalently a larger conductivity, induces a larger time spend on the Na2-site, consistent with the increasing Na1→Na2 jump rate in

Table 4.3.
The increased amount of time the Na-ions spend on the Na2-site does not imply that the Na2-site becomes stabilised by Na-vacancies. In Figure 4.2 it is visible that the Na-distribution around the Na1-sites broadens when Na-vacancies are introduced. At higher vacancy concentrations this effect becomes more pronounced, as shown in Figure 4.5. The increased Na2-occupancy can thus be ascribed to larger Na-vibrations

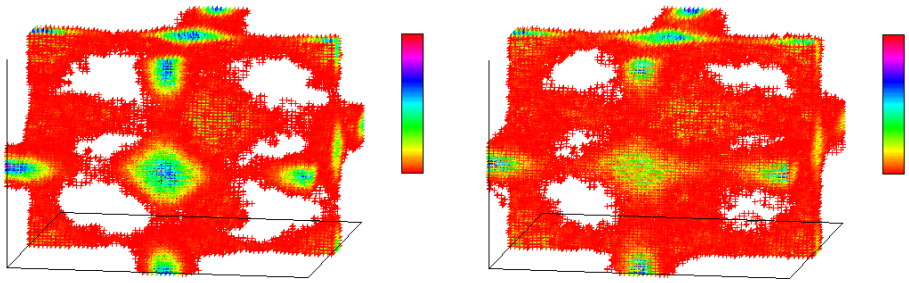

(a) (b)

Figure 4.5: Na-density plots from 100 ps. simulations at 525 K of cubic (a) $Na_{2.88}PS_4$, and (b) $Na_{2.50}PS_4$.

at the Na1-site, and a higher number of Na1→Na1-transitions.

The metastability of the Na2-site is confirmed by the MD-simulations at different

Composition	% of time at Na2-site
Na_3PS_4	3.0
$Na_{2.94}PS_4$	5.3
$Na_{2.88}PS_4$	8.1
$Na_{2.75}PS_4$	10.8
$Na_{2.50}PS_4$	16.4

Table 4.4: The percentages of time Na-ions spend at the Na2-site for different compositions of the cubic phase at 525 Kelvin.

temperatures for cubic $Na_{2.94}PS_4$ and $Na_{2.50}PS_4$, in which the percentage of time spent at the Na2-site increases with temperature. For $Na_{2.94}PS_4$ at 300 Kelvin the percentage of time spent at Na2-sites is 2.9%, increasing to 4.1%, 4.7% and 5.3% at 375, 450 and 525 K, respectively. The percentage of time at the Na2-site for $Na_{2.50}PS_4$ is 13.1%, 14.7%, 15.7%, and 16.4% at 300, 375, 450 and 525 K, respectively.
In Figure 4.6 the diffusion path of a single Na-ion is shown. The Na-ion vibrates around the Na1-sites most of the time, whereas in contrast the Na2-site is occupied very shortly during the transition. During the transitions between Na1-sites in Figure 4.6 the Na-ion passes through the Na2-site and no vibrations near the Na2-site are observed, further indicating that the Na2-site is not stable.

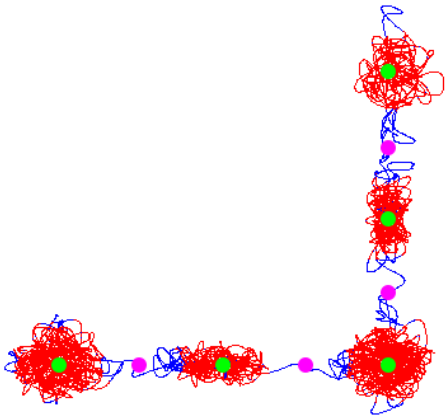

Figure 4.6: The diffusion path of a single Na-ion during the MD-simulation for cubic $Na_{2.94}PS_4$ at 525 K. The red and blue colors correspond to the atom residing at the Na1(6b)- and Na2(12d)-site, respectively, and green and pink dots correspond to the crystallographic Na1(6b)- and Na2(12d)-positions, respectively.

4.3.5. The transition mechanism

The rise in conductivity with increasing vacancy concentrations predicted by the MD-simulations indicates that diffusion proceeds through a vacancy mechanism. Note that a different mechanism seems to occur upon Si-doping ($Na_{3+3x}P_{1-x}S_4Si_x$ with x between 0 and 0.06) [14] which also leads to increased conductivities, due to interstitial Na-ions introduced upon Si-doping [21].
In contrast to the related Na_3PO_4 compound, where it has been reported that the Na-diffusion is mediated through the rotation of PO_4-groups (a paddle-wheel mechanism) [30, 31], the present MD-simulations do not display rotating PS_4-groups in Na_3PS_4. Table 4.3 illustrates the high frequency of Na1→Na2-transitions, but less than 10% leads to Na1→Na1-transitions, the latter being responsible for bulk conductivity.
To determine what is preventing Na1→Na1-transitions after a successful Na1→Na2-transition the conditions of three different cases are investigated:

I Successful transition to a neighbouring Na1-site (contributing to bulk conductivity).

II No Na1→Na1 transition because the neighbouring site is already occupied.

III No Na1→Na1 transition for another reason.

The relative occurrence of each of these cases at different temperatures is shown for cubic $Na_{2.50}PS_4$ in Table 4.5. As expected raising the temperature increases the relative amount of successful Na1→Na1 transitions (case I).
More surprisingly, it also shows an increase in failing transitions due to occupation of the destination Na1-site (case II), and a decrease in failing transitions for other

Temperature (K)	Case I (%)	Case II (%)	Case III (%)
300	6.8	50.6	42.6
375	8.5	57.3	34.3
450	10.5	62.2	27.3
525	10.2	69.7	20.1

Table 4.5: Percentages of case I, II and III at different temperatures for cubic $Na_{2.50}PS_4$.

reasons (case III). To investigate the mechanism behind this the radial distribution functions (RDF) for all the Na-atoms at the Na2-site were determined. By combining the RDF's of individual Na-atoms per case the average atomic surrounding of the Na-ions for each case can be determined by the RDF's.
Based on the differences between the RDF's of the three cases it is possible to deduce which atomic surroundings are responsible for successful and failing transitions, thus providing insight in the transition mechanism. Independent of the crystal structure, composition, and temperature all MD-simulations display similar RDF's, indicating that in all present MD-simulations a similar diffusion mechanism takes place. To analyse differences between the RDF's for the three cases the MD-simulation of cubic $Na_{2.88}PS_4$ at 525 K was used, resulting in Na-Na, Na-P and Na-S RDF's for each case as shown in Figure 4.7.

As a consequence of the higher occupancy of neighbouring Na-sites case II (no transition because the neighbouring Na-site is occupied) shows a slightly larger average Na-ion occupancy in the first 3.5 Å compared to the other two cases as shown in Figure 4.7a. There is no significant difference between the Na-distributions for case I and case III in the first few Ångstroms, illustrating that this is not the only parameter preventing Na1→Na1-transitions.
In Figure 4.7b the Na-S RDF is shown, displaying the most obvious differences between 3 and 4 Å. For successful transitions (case I) on average less S-atoms are located between 3 and 3.5 Å, which apparently shift to the range 3.5 to 4 Å, indicating a different atomic arrangement when a successful jump occurs.
The Na-P RDF in Figure 4.7c shows a clear difference around 4 Å, for case I a single P-peak is observed here, while for the other cases two peaks are visible. This indicates that a prerequisite for a successful transition is that the Na-ion is in the centre of the nearest P-atoms, i.e. it is exactly at the crystallographic Na2-position.
Concluding, the Na-P and Na-S RDF's show that when a successful transition occurs there are less P and S atoms in the first 3.5 Å . The extra free volume around the Na-ion enlarges the window through which the ion must hop for a successful Na1→Na1-transition, indicating that opening of this window is vital for macroscopic diffusion.
The better conductivity for expanded lattices can be explained by this effect. In the expanded lattice on average the windows will be larger which leads to the observed improved conductivity. The extra free volume has to be created by phonons within the crystal, which explains the changing ratio between case I and case III with increasing

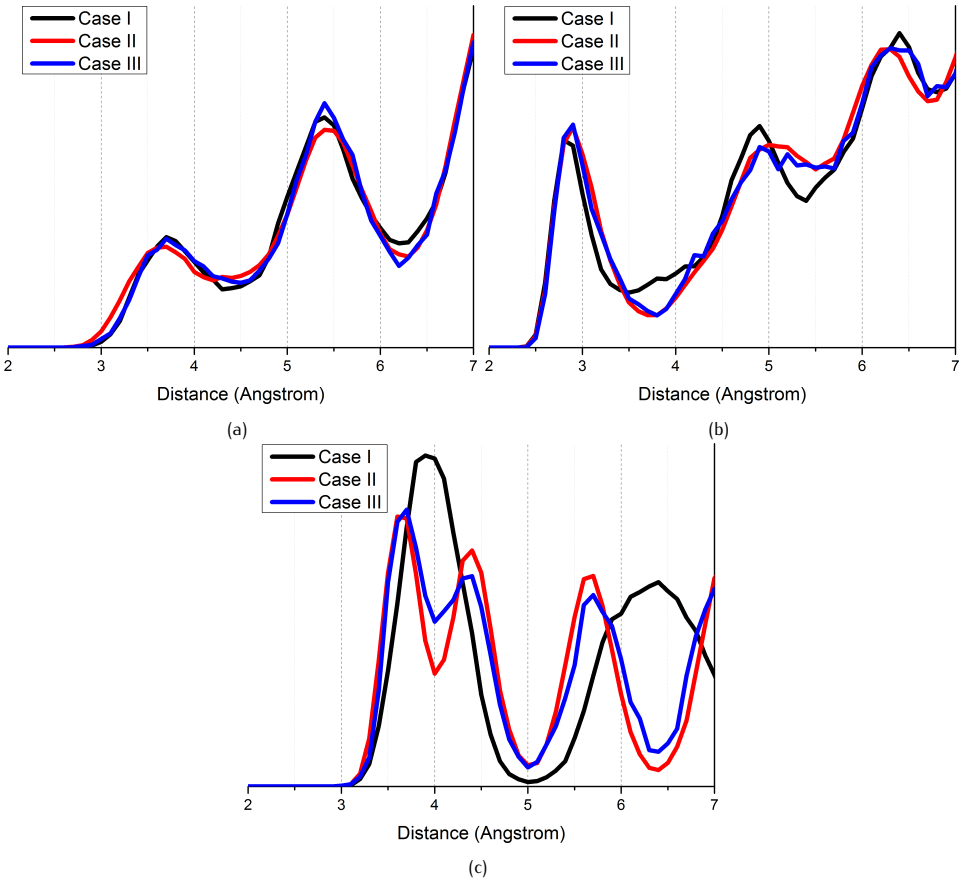

Figure 4.7: The (a) Na-Na, (b) Na-S and (c) Na-P RDF's between 2 and 7 Å for the three cases from the MD-simulation of cubic $Na_{2.88}PS_4$ at 525 K.

temperature. At higher temperatures more phonons are present, thus the window for a transition will be open more frequently, enhancing the Na1→Na1 transitions and hence the macroscopic diffusion.

4.3.6. Halogen doping in Na_3PS_4

The results from MD-simulations shown in Figure 4.4 indicate that introducing Na-vacancies into Na_3PS_4 will increase the bulk conductivity. In MD-simulations the vacancies can be introduced without charge compensation, however, in reality charge compensation is necessary when introducing vacancies.
A straightforward way to introduce vacancies in Na_3PS_4 would be by replacing S atoms with halogen atoms, a commonly used approach in Li-sulphide materials [32]. DFT calculations on Na-argyrodite solid electrolytes have shown that upon doping with halogens the materials remain stable [33], therefore we expect that doping with halogens is also possible for Na_3PS_4.
To simulate the impact of halogen doping a 2x2x2 super cell of the cubic phase was built, in which two S atoms were replaced with halogen atoms charge compensated by removing two Na-ions, resulting in the composition $Na_{2.88}PS_{3.88}X_{0.12}$ (X = F, Cl, Br, I), corresponding to 4% Na-vacancies via halogen doping.
Structural energy minimisations were performed for several configurations of Cl-atoms and Na-vacancies. To find the lowest energy configuration the Cl atoms were placed on nearest S-positions, as well as S-positions with the maximal distance within the 2x2x2 super cell. Na-vacancies were positioned next to the Cl-atoms and as far from the Cl-atoms as possible.
The resulting energies suggest that Cl-atoms prefer to be well distributed in the lattice, maximising their mutual distance, whereas Na-vacancies are preferably located next to the Cl-atoms. This lowest energy configuration was used as a starting point for relaxations of the other halogen dopants. After relaxation the cell parameters changed by less than 1% in all cases. MD-simulations for all halogen dopants were performed at 525 K, the resulting conductivities are compared to the cubic phase without charge compensation in Figure 4.8.

The conductivities with halogen doping are comparable to the values for cubic $Na_{2.88}PS_4$, and the Na-Na distribution changes only slightly. As shown in Figure 4.9 the Na-Na RDF shows very small changes between the different dopants. Other properties, such as the mean jump rates, activation energy, and the occupancy of the Na2-site, are also comparable to the MD-simulation for cubic $Na_{2.88}PS_4$. This indicates that doping with halogens has the same effect in the DFT-MD simulations as the vacancies without charge compensation, and it is concluded that doping with halogens may be a promising strategy to further improve the conductivity of Na_3PS_4.

That the conductivity rises when going from F- to Cl- to Br-doping indicates that a larger ionic radius of the dopant increases the conductivity of halogen-doped Na_3PS_4. However, the lower conductivity upon I-doping indicates that this trend does not continue beyond Br. To explain this the distribution functions for the different halogens are shown in Figure 4.10. The X-Na (X = F, Cl, Br, I) distributions in Figure 4.10a strongly depend on the halogen dopant. Upon increasing halogen ionic radius the first peak of the Na-distributions becomes more narrow, indicating that the Na-positions

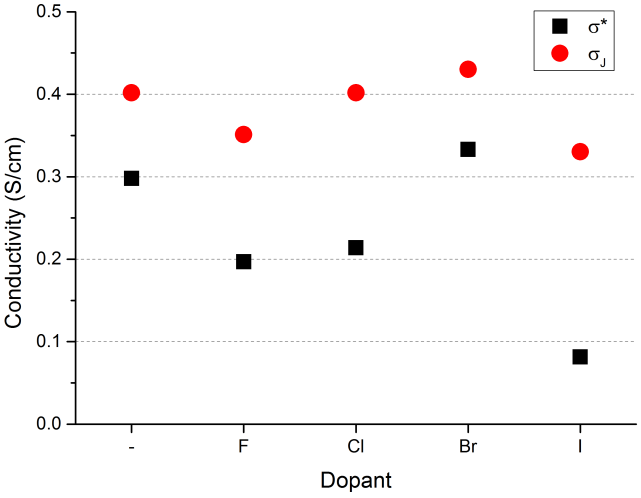

Figure 4.8: The conductivities for 4% Na-vacancy concentration without (-) and with halogen doping from MD-simulations of the cubic phase at 525 K based on the MSD (σ^*) and mean Na1→Na1 jump rates (σ_J).

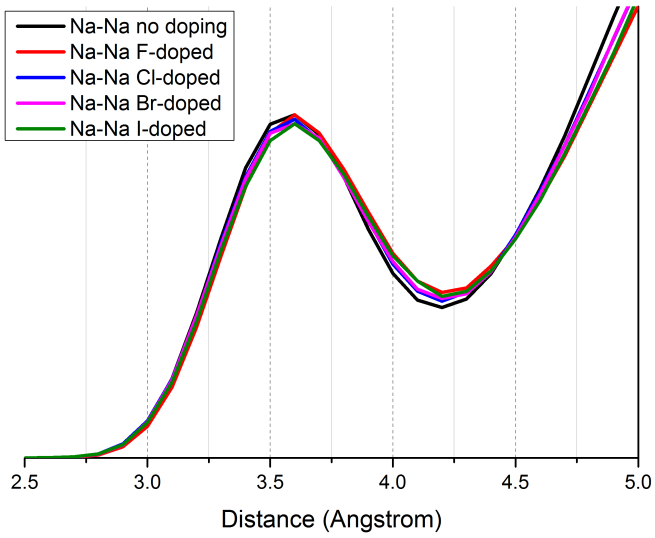

Figure 4.9: The Na-Na RDF from simulations at 525 K with different dopants.

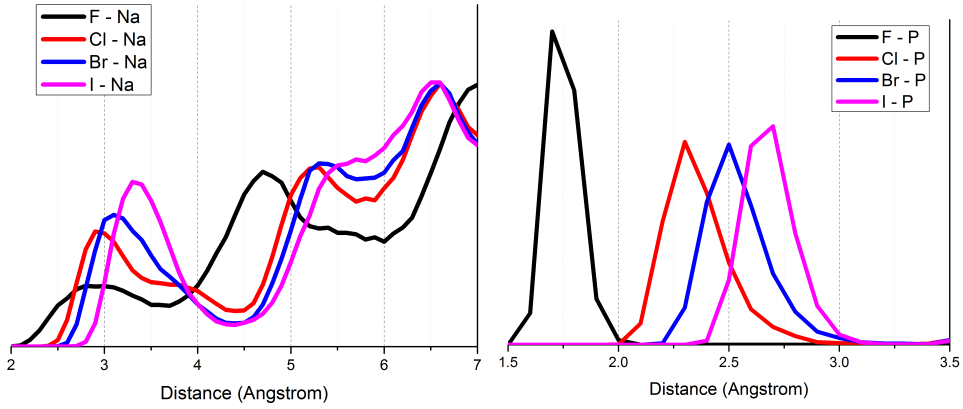

Figure 4.10: The (a) X-Na distribution between 2 and 7 Å, and (b) the X-P distribution between 1.5 and 3.5 Å from the MD-simulation of cubic $Na_{2.88}PS_{3.88}X_{0.12}$ (X = F, Cl, Br, I) at 525 K.

are better defined.
The larger ionic radius also has an effect on the window through which a transition to the neighbouring Na1(6b)-site occurs, as shown in the X-P distributions in Figure 4.10b. With larger ionic radius the X-P distance increases, making the window through which diffusion occurs smaller, and Na1-Na1 transitions less likely to occur. These two mechanisms have opposite effects as a function of halogen ionic radius, with an apparent optimum effect on diffusion for Br-doping. Thereby the MD-simulations indicate that Br-doping should lead to the highest vacancy induced conductivity in Na_3PS_4.

4.4. Conclusions

DFT MD-simulations indicate that higher Na-ion conductivity in Na_3PS_4 can be obtained by introducing Na-ion vacancies. Just 2% vacancies results in an order of magnitude larger conductivity (compared to the stoichiometric compound), reaching 0.20 S/cm, and a reduction in the activation energy from 0.28 eV to 0.16 eV.
MD-simulations of halogen doped cubic Na_3PS_4 suggest a practical route towards charge compensated vacancies to raise the conductivity of this material. A systematic variation of the halogen dopants indicates that all halogens can increase the conductivity by raising the Na-vacancy concentration, with Br-doping leading to the best results.
Not only vacancies appear vital for microscopic diffusion, the MD-simulations indicate that free volume also plays a role in the transition mechanism. A large free volume induced by phonons enhances the chance for Na-ions to make a successful transition towards a neighbouring site. The MD-simulations also show that Na-conductivity in the cubic and tetragonal phase are similar, thus both phases of Na_3PS_4 are predicted to be highly conductive solid electrolytes.
Furthermore, the orders of magnitude difference between the MD-simulations and ex-

periments suggest that the conductivity can be significantly increased by reducing the grain boundary resistance, which is most likely one of the major bottlenecks towards high performance solid state batteries. The Na2(12d)-site in the cubic phase, connecting the occupied Na1(6b)-sites, shows to be metastable, and upon increased Na-ion conductivity the time averaged Na2-site occupancy increases with increasing vacancy concentrations and/or higher temperatures due to an increase in Na1→Na1 transitions.
Thereby present DFT-MD simulations reveal the diffusion mechanism, and potential routes towards larger Na-ion conductivities in Na_3PS_4.

References

[1] C.X. Zu and H. Li. Thermodynamic analysis on energy densities of batteries. *Energy Environ. Science*, 4(8):2614–2624, 2011. doi: 10.1039/c0ee00777c.

[2] M.D. Slater, D. Kim, E. Lee, and C.S. Johnson. Sodium-ion batteries. *Adv. Funct. Mater.*, 23(8):947–958, 2013. doi: 10.1002/adfm.201200691.

[3] B.L. Ellis and L.F. Nazar. Sodium and sodium-ion energy storage batteries. *Curr. Opin. Solid State Mater. Sci.*, 16(4):168–177, 2012. doi: 10.1016/j.cossms.2012.04.002.

[4] X.C. Lu, G.G. Xia, J.P. Lemmon, and Z.G. Yang. Advanced materials for sodium-beta alumina batteries: status, challenges and perspectives. *J. Power Sources*, 195(9):2431–2442, 2010. doi: 10.1016/j.jpowsour.2009.11.120.

[5] J.L. Sudworth. The sodium/sulphur battery. *J. Power Sources*, 11(1):143–154, 1984. doi: 10.1016/0378-7753(84)80080-4.

[6] K. Takada. Progress and prospective of solid-state lithium batteries. *Acta Mater.*, 61(3):759–770, 2013. doi: 10.1016/j.actamat.2012.10.034.

[7] P. Knauth. Inorganic solid Li ion conductors: an overview. *Solid State Ionics*, 180(14-16):911–916, 2009. doi: 10.1016/j.ssi.2009.03.022.

[8] V. Thangadurai and W. Weppner. Recent progress in solid oxide and lithium ion conducting electrolytes research. *Ionics*, 12(1):81–92, 2006. doi: 10.1007/s11581-006-0013-7.

[9] N. Anantharamulu, K. Koteswara Rao, G. Rambabu, B. Vijaya Kumar, Velchuri Radha, and M. Vithal. A wide-ranging review on NASICON type materials. *J. Mater. Sci.*, 46(9):2821–2837, 2011. doi: 10.1007/s10853-011-5302-5.

[10] M. Tatsumisago and A. Hayashi. Sulfide glass-ceramic electrolytes for all-solid-state lithium and sodium batteries. *Int. J. Appl. Glass Sci.*, 5(3):226–235, 2014. doi: 10.1111/ijag.12084.

[11] J. Li, C. Ma, M. Chi, C. Liang, and N.J. Dudney. Solid electrolyte: the key for high-voltage lithium batteries. *Adv. Energy Mater.*, 5(4):1401408, 2015. doi: 10.1002/aenm.201401408.

[12] T.J. Udovic, M. Matsuo, A. Unemoto, N. Verdal, V. Stavila, A.V. Skripov, J.J. Rush, H. Takamura, and S.I. Orimo. Sodium superionic conduction in $Na_2B_{12}H_{12}$. *Chem. Commun.*, 50(28):3750–3752, 2014. doi: 10.1039/c3cc49805k.

[13] A. Hayashi, K. Noi, A. Sakuda, and M. Tatsumisago. Superionic glass-ceramic electrolytes for room-temperature rechargeable sodium batteries. *Nat. Commun.*, 3:856, 2012. doi: 10.1038/ncomms1843.

[14] N. Tanibata, K. Noi, A. Hayashi, and M. Tatsumisago. Preparation and characterization of highly sodium ion conducting Na_3PS_4-Na_4SiS_4 solid electrolytes. *RSC Adv.*, 4(33):17120–17123, 2014. doi: 10.1039/c4ra00996g.

[15] M. Jansen and U. Henseler. Synthesis, structure determination, and ionic conductivity of sodium tetrathiophosphate. *J. Solid State Chem.*, 99(1):110–119, 1992. doi: 10.1016/0022-4596(92)90295-7.

[16] A. Hayashi, K. Noi, N. Tanibata, M. Nagao, and M. Tatsumisago. High sodium ion conductivity of glass ceramic electrolytes with cubic Na_3PS_4. *J. Power Sources*, 258:420–423, 2014. doi: 10.1016/j.jpowsour.2014.02.054.

[17] S. Yubuchi, A. Hayashi, and M. Tatsumisago. Sodium-ion conducting Na_3PS_4 electrolyte synthesized via a liquid-phase process using *N*-methylformamide. *Chem. Lett.*, 44(7):884–886, 2015. doi: 10.1246/cl.150195.

[18] G. Kresse and J. Hafner. Ab initio molecular dynamics for liquid metals. *Phys. Rev. B*, 47(1):558–561, 1993. doi: 10.1103/PhysRevB.47.558.

[19] N. Tanibata, K. Noi, A. Hayashi, N. Kitamura, Y. Idemoto, and M. Tatsumisago. X-ray crystal structure analysis of sodium-ion conductivity in $94Na_3PS_4 \cdot 6Na_4SiS_4$ glass-ceramic electrolytes. *Chem. Electro. Chem*, 1(7):1130–1132, 2014. doi: 10.1002/celc.201402016.

[20] K. Noi, A. Hayashi, and M. Tatsumisago. Structure and properties of the Na_2S-P_2S_5 glasses and glass ceramics prepared by mechanical milling. *J. Power Sources*, 269:260–265, 2014. doi: 10.1016/j.jpowsour.2014.06.158.

[21] Z. Zhu, I.H. Chu, Z. Deng, and S.P. Ong. Role of Na^+ interstitials and dopants in enhancing the Na^+ conductivity of the cubic Na_3PS_4 superionic conductor. *Chem. Mater.*, 27(24):8318–8325, 2015. doi: 10.1021/acs.chemmater.5b03656.

[22] S.H. Bo, Y. Wang, J.C. Kim, W.D. Richards, and G. Ceder. Computational and experimental investigations of Na-ion conduction in cubic Na_3PSe_4. *Chem. Mater.*, 28(1):252–258, 2016. doi: 10.1021/acs.chemmater.5b04013.

[23] A. Van der Ven, G. Ceder, M. Asta, and P.D. Tepesch. First-principles theory of ionic diffusion with nondilute carriers. *Phys. Rev. B*, 64(18):184307, 2001. doi: 10.1103/PhysRevB.64.184307.

[24] R.J. Friauf. Correlation effects for diffusion in ionic crystals. *J. Appl. Phys.*, 33(1): 494–505, 1962. doi: 10.1063/1.1777148.

[25] H. Nagata and Y. Chikusa. An all-solid-state sodium-sulfur battery operating at room temperature using a high-sulfur-content positive composite electrode. *Chem. Lett.*, 43(8):1333–1334, 2014. doi: 10.1246/cl.140353.

[26] M. Nose, A. Kato, A. Sakuda, A. Hayashi, and M. Tatsumisago. Evaluation of mechanical properties of Na_2S-P_2S_5 sulfide glass electrolytes. *J. Mater. Chem. A*, 3(44):22061–22065, 2015. doi: 10.1039/c5ta05590c.

[27] K. Homma, M. Yonemura, T. Kobayashi, M. Nagao, M. Hirayama, and R. Kanno. Crystal structure and phase transitions of the lithium ionic conductor Li_3PS_4. *Solid State Ionics*, 182(1):53–58, 2011. doi: 10.1016/j.ssi.2010.10.001.

[28] G.H. Vineyard. Frequency factors and isotope effects in solid state rate processes. *J. Phys. Chem. Solids*, 3(1-2):121–127, 1957. doi: 10.1016/0022-3697(57)90059-8.

[29] K. Toyoura, Y. Koyama, A. Kuwabara, F. Oba, and I. Tanaka. First-principles approach to chemical diffusion of lithium atoms in a graphite intercalation compound. *Phys. Rev. B*, 78(21), 2008. doi: 10.1103/PhysRevB.78.214303.

[30] M. Jansen. Volumeneffekt oder drehtürmechanismus - schnelle alkalimetallionenleitung in festkörpern mit rotationsfehlgeordneten komplexen anionen. *Angew. Chem.*, 103(12):1574–1586, 1991. doi: 10.1002/ange.19911031205.

[31] D. Wilmer, K. Funke, M. Witschas, R.D. Banhatti, M. Jansen, G. Korus, J. Fitter, and R.E. Lechner. Anion reorientation in an ion conducting plastic crystal - coherent quasielastic neutron scattering from sodium ortho-phosphate. *Physica B*, 266(1-2):60–68, 1999. doi: 10.1016/s0921-4526(98)01494-x.

[32] R.P. Rao and S. Adams. Studies of lithium argyrodite solid electrolytes for all-solid-state batteries. *Phys. Status Solidi A*, 208(8):1804–1807, 2011. doi: 10.1002/pssa.201001117.

[33] H.M. Chen, M. Chen, and S. Adams. Stability and ionic mobility in argyrodite-related lithium-ion solid electrolytes. *Phys. Chem. Chem. Phys.*, 17(25):16494–16506, 2015. doi: 10.1039/c5cp01841b.

5

Diffusion mechanism of Li-argyrodite solid electrolytes for Li-ion batteries and prediction of optimised halogen doping: the effect of Li-vacancies, halogens, and halogen disorder

This chapter has been published as: Niek J.J. de Klerk, Irek Rosłoń and Marnix Wagemaker, Diffusion mechanism of Li-argyrodite solid electrolytes for Li-ion batteries and prediction of optimised halogen doping: the effect of Li-vacancies, halogens, and halogen disorder; Chemistry of Materials **28** (21), 7955-7963 (2016), doi: 10.1021/acs.chemmater.6b03630

Using DFT MD-simulations the origin of the Li-ion conductivity in argyrodite solid electrolytes is investigated. The simulations show that besides Li-ion vacancies in Li_6PS_5Cl and Li_6PS_5Br the influence of halogen atoms on their local surroundings also plays an important role in the Li-ion diffusion.
The orders of magnitude difference in Li-ion conductivity between Li_6PS_5Cl and Li_6PS_5I is caused by the distribution of the halogen ions over the available crystallographic sites. This suggests that altering the halogen distribution in Li-argyrodites during synthesis could increase the Li-ion conductivity of these materials. For Li_6PS_5Cl the simulations predict an optimal Cl-distribution of 1:3 over 4a- and 4c-sites, resulting in a Li-ion conductivity two times larger than the currently prepared materials.
Based on these results simulations were performed on $Li_5PS_4X_2$ (X = Cl, Br or I), which show Li-ion conductivities similar to Li_6PS_5Cl and Li_6PS_5Br, suggesting that the $Li_5PS_4X_2$ compounds are interesting new compositions for solid state electrolytes.

5.1. Introduction

5

Li-ion batteries are an important technology in the current society, powering laptops, mobile phones, electric cars, etc. However, the use of liquid electrolytes makes current batteries prone to dangerous thermal runaway reactions, igniting the battery [1]. To improve the safety, liquid electrolytes should be replaced by solid state electrolytes, of which several show Li-ion conductivities comparable to liquid electrolytes [2, 3]. Besides the improved safety, solid state electrolytes potentially have additional advantages such as an increased voltage stability window, increased energy density due to more efficient packing, and versatility in the battery geometry [2, 3].
Lithium argyrodites are a promising family of solid state electrolytes, characterized by the general composition Li_7PnCh_6, where Pn = P or As, and Ch = O, S or Se. By replacing part of the Ch-atoms with halogens (X) the composition Li_6PnCh_5X can be obtained [4], of which Li_6PS_5Cl and Li_6PS_5Br show Li-ion conductivities comparable to liquid electrolytes [5]. Although calculations indicate that the argyrodite structures are unstable [6] a large range of compositions has been synthesised. These include Li-argyrodites containing oxygen [7], arsenic [4], selenium [8], halogens [9], and combinations of these [4].
The highest room temperature Li-ion conductivities are reported for Li_6PS_5Cl and Li_6PS_5Br, reaching up to 10^{-3} S/cm [10–12]. However, the related Li_6PS_5I structure shows an orders of magnitude lower conductivity, attributed to the different ordering of I- and Cl-/Br-ions over 4a- and 4c-sites [11]. The Li-ion conductivity of Li_6PO_5Cl and Li_6PO_5Br has been reported to be around 10^{-9} S/cm [7], this is attributed to the 20% smaller lattice constants which drastically reduces the free volume for lithium ion diffusion. Besides a high conductivity the halogen-argyrodites also show excellent electrochemical stability from 0 to 7 V vs. Li/Li^+ [10], and a low electronic conductivity on the order of 10^{-10} S/cm [13].
Most argyrodites show a high temperature (HT) and a low temperature (LT) phase [14], but the temperature at which the phase transition occurs strongly depends on the composition [4, 15]. Without halogens the HT-phase occurs above 450 K, but halogens stabilise the HT-phase down to 170 K. Since the halogen containing argyrodites show the highest Li-ion conductivities we are primarily interested in the HT-phase. The

HT-phase crystallises in the cubic $F\bar{4}3m$ space group, responsible for the beneficial three dimensional diffusion pathway through the lattice. The excellent electrochemical and thermal stability, high conductivity, facile synthesis [10], the possibility of preparation from solution [16], and cheap starting materials make the halogen-argyrodites an excellent electrolyte candidate for solid state batteries.
Recently several groups have reported on solid state batteries using either Li_6PS_5Cl [12, 16–19] or Li_6PS_5Br [13, 20–22]. Batteries with coulombic efficiencies of 99% [17, 19, 22] and excellent stability upto 700 cycles [22] have been reported. Recently, solid state NMR measurements of the Li-exchange between argyrodite electrolytes and a Li_2S-cathode has shown that the electrode-electrolyte interface limits the power of these solid state batteries [18].
Despite the increasing amount of research on Li-argyrodites the diffusion mechanism is not yet fully understood. NMR measurements [23] and bond valence calculations [11] have shown that several different jump processes play a role, which together are responsible for the macroscopic Li-ion diffusion. Furthermore, neutron diffraction combined with conductivity measurements has shown that halogen disorder over the 4a- and 4c-sites has a large influence on the Li-ion conductivity [19], but the origin of the increased conductivity is unclear.
In the previous chapter on the Na-ion solid electrolyte Na_3PS_4 it was shown that a better understanding of the diffusion mechanism can give direction to the synthesis of better conducting materials. In this chapter we aim to do the same for the Li-argyrodites. The results of density functional theory (DFT) molecular dynamics (MD) simulations performed on a range of argyrodite structures are presented to provide understanding of the Li-ion diffusion in argyrodites. The MD-simulations rationalize the impact of Cl- and Br-doping on the Li-ion conductivity, the role of the halogen disorder is revealed, and guidelines to obtain better Li-ion conducting argyrodites are presented.

5.2. Methods

The DFT MD-simulations were performed with VASP [24], using the GGA approximation [25] and the PAW-PBE basis set [26] with a cut-off energy of 280 eV. Given the large unit cell size of 10 Ångstrom all the calculations were performed using one unit cell. During the minimisations a k-point mesh of 2x2x2 was used, which was reduced to 1x1x1 for the MD-simulations. The total simulation time of the MD-simulations was 100 ps., with 2 fs. time-steps, and 2.5 ps. initial equilibration time. Simulations were performed in the NVT ensemble, with temperature scaling after every 1000 time-steps. For all the compositions MD-simulations were performed at 300, 450 and 600 K.
As a starting point for the minimisations, structures from literature were used if available, otherwise the most similar structure was used. Obtaining the appropriate amount of Li-ions in the unit cell was done by removing one Li-ion from every 48h-site pair, since the small Li-Li distance of 1.9 Ångstrom makes it energetically unfavourable to occupy both 48h-sites in a pair simultaneously.
The jump rates were determined by monitoring which crystal sites each Li-ion visits during a MD-simulation, as described in a previous publication [27]. The crystal site-radius was chosen to be as large as possible without causing overlap between

neighbouring sites. This results in crystal site-radii of approximately 0.9 Ångstrom, the precise value depending on the unit cell size. Counting the number of jumps between sites (J) gives the mean jump rate (τ) using:

$$\tau = \frac{J}{Nt} \tag{5.1}$$

where N is the number of Li-ions, and t the simulation time. Based on the jump rate the activation energy (ΔE_A) can be calculated with [28]:

$$\Delta E_A = -kT\ln(\frac{\tau}{\nu_0}) \tag{5.2}$$

where k is Boltzmann's constant, T the temperature in Kelvin, and ν_0 the attempt frequency. The jump rate diffusivity (D_J) can be calculated using the Einstein-Smulochowski relation:

$$D_J = \frac{\tau a^2}{2d} \tag{5.3}$$

where a is the jump distance and d the number of diffusion dimensions (3 in this case). The diffusivity can also be calculated using the mean square displacement (MSD) of the Li-ions during a simulation, commonly known as the tracer diffusivity. The tracer diffusivity (D^*) is calculated using [29]:

$$D^* = \frac{1}{2dN}\sum_{i=1}^{N}\left(\frac{r_i(t)^2}{dt}\right) \tag{5.4}$$

where $r_i(t)$ is the displacement of a single Li-ion, and dt is the simulated time. Using the diffusivity (either D_J or D^*) the conductivity (σ) can be determined using the Nernst-Einstein relation [29]:

$$\sigma = \frac{ne^2z^2}{k_BT}D \tag{5.5}$$

where n is the diffusing particle density, e the elementary electron charge, and z the ionic charge. The conductivity calculated based on D^* and D_J will be referred to as σ^* and σ_J, respectively. To determine the uncertainty in the simulations the standard deviation for all the properties based on the jump rates has been calculated by dividing each simulation into ten parts. Assuming uncorrelated jump processes, no equilibration is necessary in between the different parts, thus avoiding an increase in the required simulation time.

5.3. Results & Discussion

Although several argyrodites are not stable at room temperature in the high temperature (HT) phase, including Li_7PS_6 and Li_7PSe_6, all simulations are performed on the HT-phase of each composition to gain understanding of the influence of the argyrodite composition on the Li-ion conductivity. The high-temperature Li_7PS_6-phase is shown in Figure 5.1, representing the cubic unit cell in the $F\bar{4}3m$ (no. 216) space-group where the unit cell parameters are close to 10 Ångstrom for all the experimentally

determined structures [4, 9, 15, 30].
The backbone is build up by PS_4-groups centred at 4b-sites, with the remaining sulphur occupying the 4a- and 4c-sites, and the Li-ions occupy 48h-sites surrounding the 4c-sites. Upon substitution of sulphur by halogens, the halogens occupy the 4a- or 4c-sites, whereas the sulphur in the PS_4-groups are not substituted [9]. The Li-ions are distributed over the available 48h-sites, of which approximately 50% are occupied [11]. The existence of pairs of 48h-sites separated by only 1.9 Ångstrom suggests that each pair of 48h-sites is occupied by just one Li-ion [11]. Twelve 48h-sites (6 pairs) surround each 4c-site, which appears as a cage-like Li-ion structure. Besides the 48h-site other crystallographic sites are also suggested to be suitable locations for Li-ions [4], but there is no crystallographic evidence that these sites are occupied.
Between the 48h-sites in the HT-argyrodite structure three different types of jumps

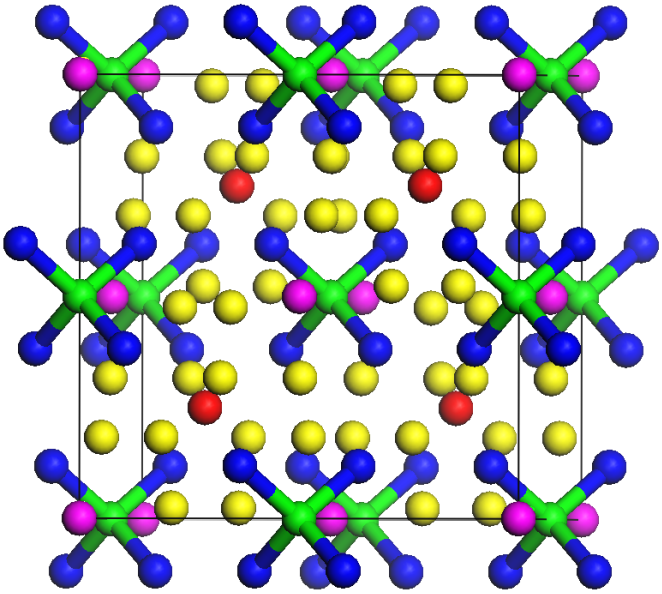

Figure 5.1: Crystal structure of HT-Li_7PS_6 [15]. Colours correspond to; yellow: Li-sites (48h), green: phosphorus, blue: bonded sulphur, pink: 4a-sites, red: 4c-sites

were identified during the MD-simulations. The first type is a jump between the paired 48h-sites over a distance of 1.9 Ångstrom, which we will refer to as a doublet-jump. The second type are the jumps within the cages between different 48h-pairs over a distance of 2.25 Ångstrom, which we will refer to as intracage jumps. The third type are the jumps interconnecting the 4 cages in each unit cell, for which the distance can vary, which will be referred to as intercage jumps. In order to have Li-ion diffusion pathways throughout the crystal these three jump-types must all occur, and the one with the smallest jump rate will limit the macroscopic diffusion.

5.3.1. Conductivities

The MD-simulations were performed on the HT-phases of the Li_7PS_6, Li_7PSe_6, Li_6PS_5Cl, Li_6PS_5Br and Li_6PS_5I argyrodite compositions to investigate the influence of S versus Se, and the influence of the halide dopants on the Li-ion conductivity. The conductivities from the simulations are shown in Figure 5.2, the jump rates and activation energies for the three types of jumps are shown in Table 5.1, 5.2, and 5.3 in the Supporting Information.

For all compositions the intercage jump rate has the lowest frequency, and is therefore used to determine the macroscopic conductivity. In the simulations of Li_6PS_5I and the simulations of Li_7PS_6 and Li_7PSe_6 at 300 K no intercage jumps occurred during the MD-simulations. Only local Li-ion jumps (doublet and intracage) are predicted to occur, and consequentially these compositions showed no macroscopic conductivity on the time-scale of the MD-simulations, as shown in Figure 5.2. The jump distance used to calculate the conductivity based on the intercage jump frequency, σ_J, is the distance between the centres of the cages, which equals 7.0 Ångstrom.

Because the other two jump frequencies are much larger than the intercage jump frequency, the average position of a Li-ion between two intercage jumps is the centre of the cage, and hence intercage jumps effectively take place between the centres of the cages. The MD-simulations predict Li_6PS_5Cl and Li_6PS_5Br to have the highest

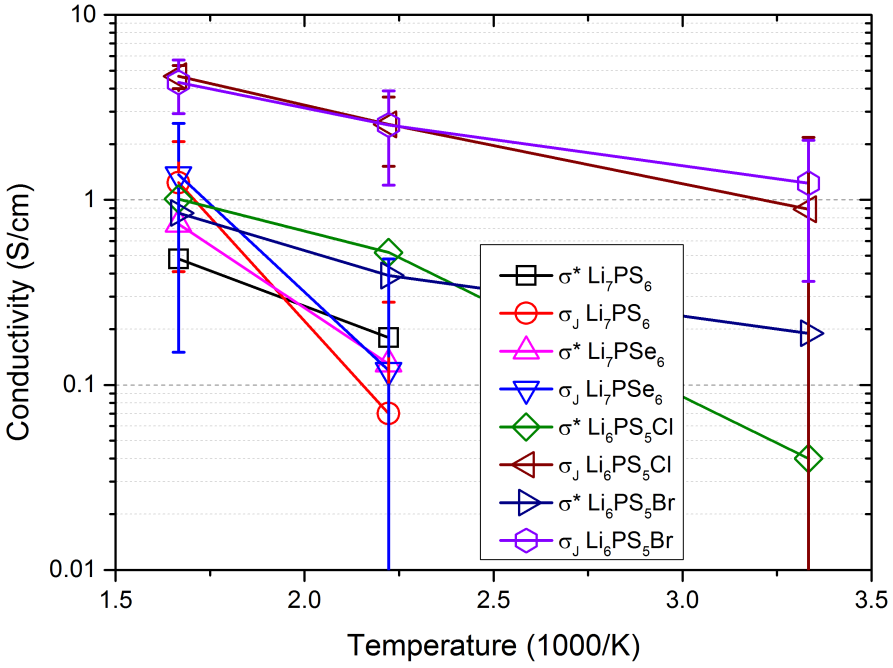

Figure 5.2: Arrhenius plot of the conductivities from MD-simulations based on the intercage jump frequency, σ_J, and the MSD, σ^*.

conductivity, followed by Li_7PS_6 and Li_7PSe_6, and finally Li_6PS_5I, consistent with experiments [11]. The Li-ion conductivities predicted by the MD-simulations are several orders of magnitude larger compared to that measured by impedance spectroscopy. For Li_7PS_6 and Li_7PSe_6 this is caused by the fact that the MD-simulations were performed on the HT-phase, while experiments have been performed on the LT-phase of these compounds [8, 14]. The large differences for Li_6PS_5Cl and Li_6PS_5Br may be explained by the influence of grain boundaries on impedance spectroscopy results, which probes charge transport over tens of nanometres, and since grain boundaries appear to limit the macroscopic conductivity [18], impedance spectroscopy effectively measures the lower limit for Li-ion conductivity in argyrodites. Whereas in the MD-simulations a perfectly crystalline structure is assumed, effectively giving an upper limit for the Li-ion conductivity.

Direct measurement of the local Li-ion mobility inside Li-argyrodite crystals with ^{7}Li NMR relaxation measurements [18, 23] results in conductivities having the same order of magnitude as the present MD-simulations, validating the use of DFT MD-simulations to predict the Li-ion dynamics in the argyrodite structures. The difference between the values of σ_J and σ^* from the MD-simulations is caused by 'back and forth' jumps, which contribute to σ_J, but cancel each other in σ^*. As a consequence the conductivity based on the jump rates should be larger than that based on the MSD, and hence the correlation factor $f = \frac{D^*}{D_J}$ [31] is smaller than 1.

For Li_6PS_5Br and Li_6PS_5Cl the correlation factor is below 0.2 for all the simulated temperatures, indicating that a significant amount of back and forth jumps occur in these compounds. In Li_7PS_6 and Li_7PSe_6 the correlation factor strongly changes with temperature, probably caused by the small number of jumps per Li-ion, which is reflected in the large error bars for σ_J. The small number of jumps per Li-ion makes it unlikely that a Li-ion will perform multiple jumps, thus back and forth jumps are not very likely to occur. To obtain a reliable value for the correlation factor in these compositions more jumps per Li-ion must be sampled, however, this would require much longer simulation times which is outside the scope of this study.

It has been reported that increasing the lattice volume of solid electrolytes, by introducing atoms with larger ionic radii, can significantly influence the Li-ion conductivity [2]. In argyrodites the larger ionic radius of bromide compared to chloride leads to an increase in the cubic lattice parameter, amounting to 0.13 Ångstrom [11], and replacing S by Se leads to an increase by 0.48 Ångstrom [15].

Comparison of the conductivities from the MD-simulations of Li_7PS_6 with Li_7PSe_6 and Li_6PS_5Cl with Li_6PS_5Br does not suggest a significant effect of the ionic radius on the conductivity in the argyrodite structure. However, large differences in the doublet and intracage jump rates are observed for the different compositions (see Tables 5.1, 5.2, and 5.3 in the Supporting Information), hence the ionic radius of the ions appears to affect the Li-ion dynamics. However, the intercage jump rates, which determine the macroscopic conductivity, in Li_7PSe_6 and Li_6PS_5Br are similar to those in Li_7PS_6 and Li_6PS_5Cl, respectively. Therefore the lattice volume per Li-ion does not have a significant influence on the macroscopic Li-ion conductivity in argyrodites.

To understand what causes the differences in Li-ion conductivity between the Li-argyrodites, the Li-density during MD-simulations is shown for Li_7PS_6, Li_6PS_5Cl,

Li_6PS_5I, Li_7PSe_6 and Li_6PS_5Br in Figure 5.3. The Li-densities of Li_7PSe_6 and Li_6PS_5Br are very similar to those of Li_7PS_6 and Li_6PS_5Cl, respectively. The Li-ion densities in Figures 5.3 and 5.3 all show the four cage-like structures in which the Li-ions reside surrounding the 4c-sites. For Li_6PS_5I the Li-density clearly shows why this is a poor Li-ion conductor. The high Li-ion density regions reflect high mobility between pairs of 48h-sites, the doublet jumps, which are also observed by XRD [4] and NMR experiments [30]. However, no diffusion paths between the pairs of 48h-sites are visible, and the Li-ions in Li_6PS_5I thus only display local mobility, explaining its low macroscopic Li-ion diffusion.

In the other compositions the regions with high Li-ion densities are connected to neighbouring high density regions within a cage, although connections between different cages are not clearly visible. However, there are subtle differences between the Li-ion densities in Li_7PS_6 and Li_6PS_5Cl. In Figure 5.3 the Li-ions in Li_7PS_6 appear to be more localized, as observed by the larger maxima in the Li-ion density. In Li_6PS_5Cl the maxima are smaller, and the Li-ion density is more spread out over the Li-ion positions, indicating that the Li-ions are moving around more rapidly inside the cages. In Figure 5.3 similar behaviour is visible in Li_7PSe_6 and Li_6PS_5Br.

The origin of the large differences in macroscopic conductivity in Figure 5.3 are easier to analyse by the jump statistics schematically shown for Li_7PS_6, Li_6PS_5Cl, Li_6PS_5I, Li_7PSe_6 and Li_6PS_5Br in Figure 5.4. In Li_6PS_5I doublet jumps occur very frequently, as already visible in the Li-ion density in Figure 5.3. Furthermore, only a few intracage jumps occur, and not a single intercage jump takes place during the MD-simulation, thus unambiguously revealing why Li_6PS_5I is a poor Li-ion conductor. In all other compositions the frequent doublet and intracage jumps clearly reveal the cage structure formed by the diffusing Li-ions around the 4c-sites. But only in Li_6PS_5Cl and Li_6PS_5Br a significant number of intercage jumps occurs, making macroscopic Li-ion diffusion possible. For Li_6PS_5Cl ^7Li NMR relaxation experiments have measured jump rates of approximately $1 * 10^9$ sec^{-1} at 350 K [18].

The predicted jump rates at 300 K are an order of magnitude larger than the results from the NMR experiments, but there is a large uncertainty in the jump rates at 300 K due to the limited amount of jumps occurring during the simulation time. However, extrapolating the jump rate conductivities of Li_6PS_5Cl at 450 and 600 K towards 350 K, using the activation energies predicted by the MD-simulations, does show good agreement with the NMR results [18]. Using impedance spectroscopy activation energies between 0.16 and 0.56 eV have been reported for Li_6PS_5X (X = Cl, Br or I) [11, 14, 19], strongly depending on the synthesis [19] and measurement procedure [14]. NMR experiments report activation energies of 0.08 and 0.09 eV for short range and 0.20 and 0.29 eV for long range diffusion in Li_6PS_5Br [23] and Li_6PS_5Cl [18], respectively.

Using Equation 5.2, with a typical attempt frequency [31] of $1*10^{13}$, the MD-simulations predict activation energies in Li_6PS_5Cl and Li_6PS_5Br of 0.10 to 0.14 eV for doublet- and intracage-jumps, and 0.20 to 0.25 eV for intercage jumps, comparable to the experimental results from NMR. The energy barriers for short range jumps resulting from the present MD-simulations are similar to those from bond-valence calculations [11, 19], which report activation barriers between 0.10 and 0.20 eV. For intercage jumps

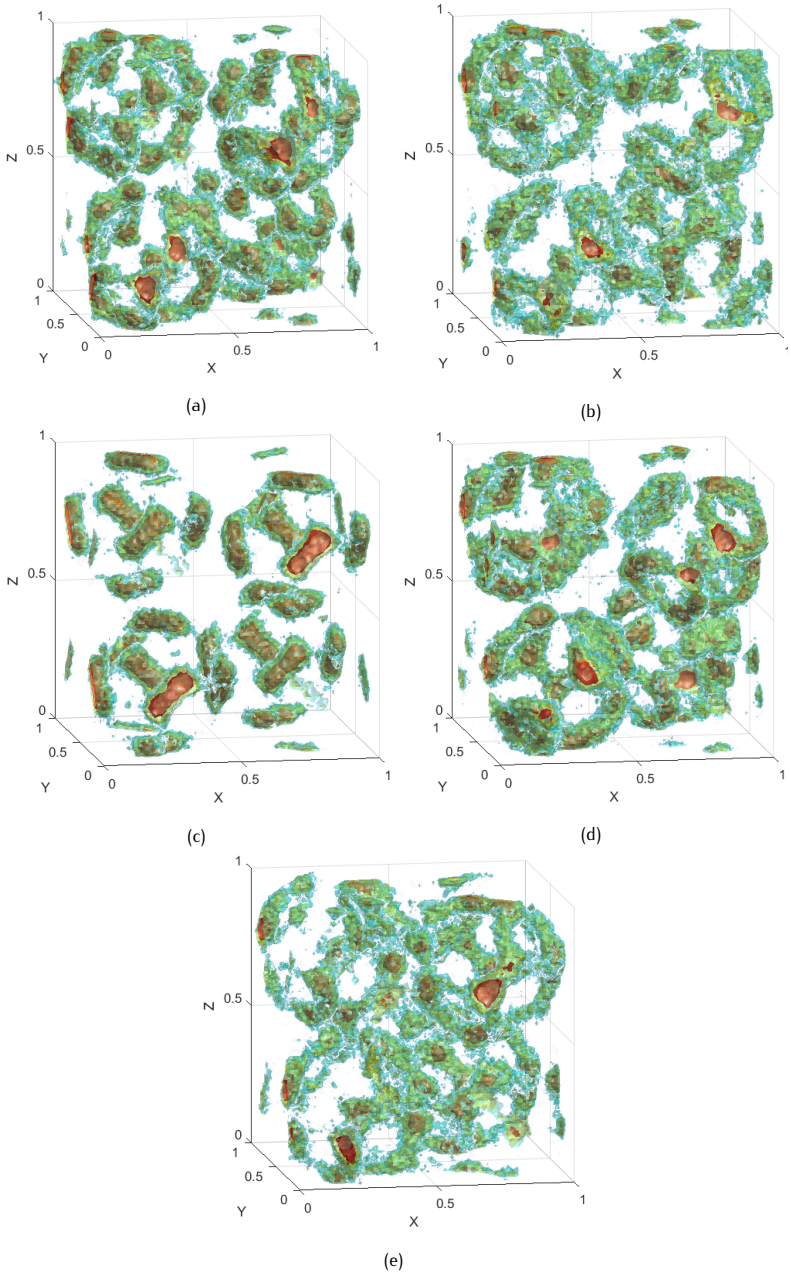

Figure 5.3: Li-ion density in the argyrodite unit cell during MD-simulations at 450 K of (a) Li_7PS_6, (b) Li_6PS_5Cl, (c) Li_6PS_5I, (d) Li_7PSe_6 and (e) Li_6PS_5Br. Red indicates high Li-ion density, followed by yellow, green, and blue representing lower densities.

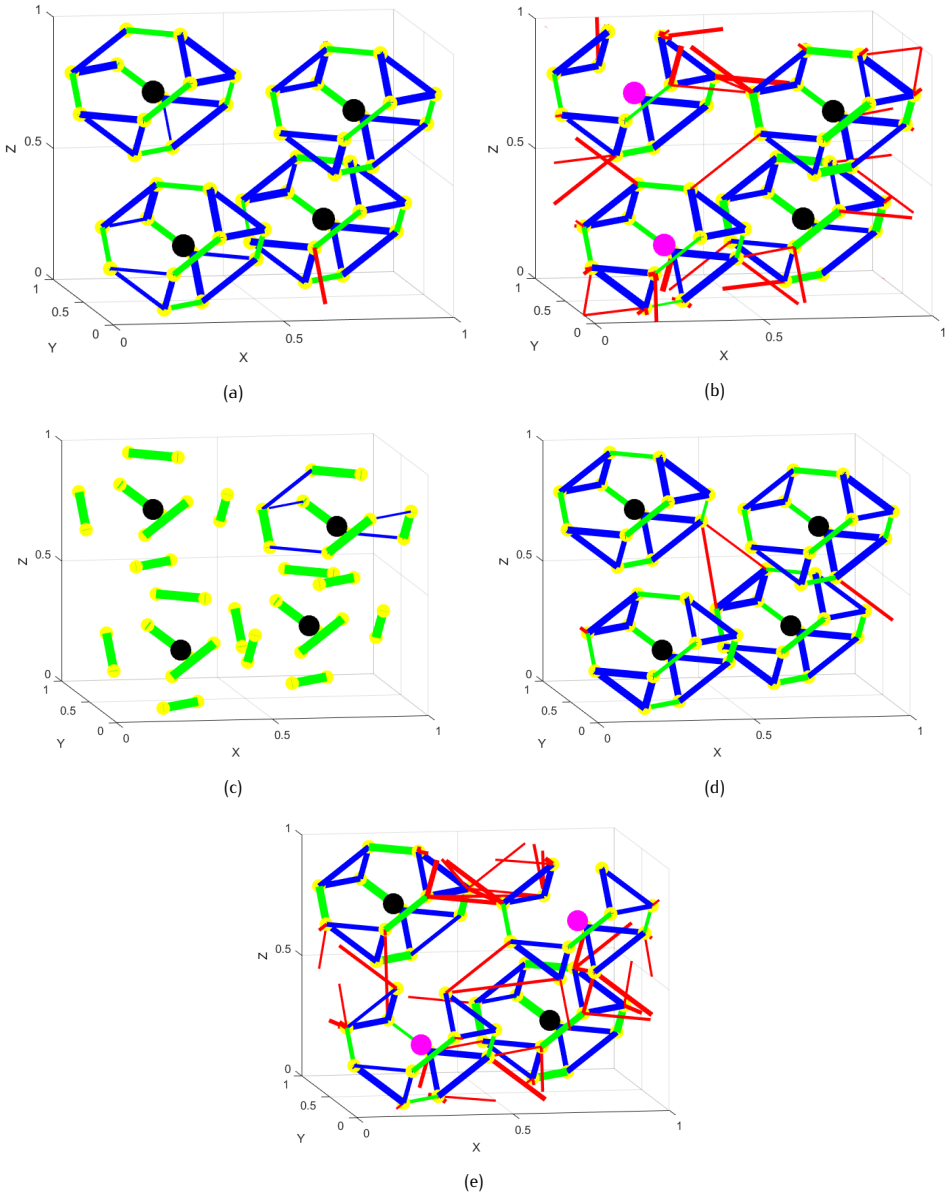

Figure 5.4: Jump statistics plots from MD-simulations at 450 K of (a) Li_7PS_6, (b) Li_6PS_5Cl, (c) Li_6PS_5I, (d) Li_7PSe_6 and (e) Li_6PS_5Br. The lines represent the three different types of jumps; green: doublet, blue: intracage, red: intercage, thicker lines represent larger jump rates. The coloured spheres indicate; black: S/Se at 4c, pink: Cl/Br at 4c, yellow: Li-ion sites (48h).

bond valence calculations report activation energies between 0.30 and 0.35 eV, slightly above the results from the current MD-simulations and NMR measurements.
Comparing the jump rates and activation energies of the different types of jumps clearly shows that the intercage jumps are rate limiting, and hence determine the macroscopic Li-ion conductivity in the argyrodite Li-ion electrolytes. In all the experimentally reported argyrodite compositions the intercage jump rate is at least 5 times smaller than the jump rates of the other jump types during the MD-simulations. Although all three types of jumps are necessary for macroscopic diffusion, this shows that to achieve higher Li-ion conductivities in argyrodites the intercage jump rate should be increased in the first place.

5.3.2. Vacancies

The differences in the intercage jump rates illustrates why the Li-ion conductivity in Li_6PS_5Cl is much higher than in Li_7PS_6, but does not explain the origin of the larger intercage jump rate. The most obvious explanation is that replacing S^{2-} by Cl^{1-} results in charge compensating Li-ion vacancies that induce the larger Li-ion conductivity.
To test this explanation simulations were performed on the artificial Li_6PS_6 and Li_7PS_5Cl compositions, the results of which are shown in Figure 5.5. If only the Li-ion vacancies in Li_6PS_5Cl are responsible for the high conductivity the Li_6PS_6 composition should result in a high Li-ion conductivity by frequent intercage jumps, whereas in Li_7PS_5Cl the decreased amount of vacancies should result in significantly less intercage jumps.
However, in Figure 5.5 similar behaviour is visible for the Li_6PS_6 and Li_7PS_5Cl com-

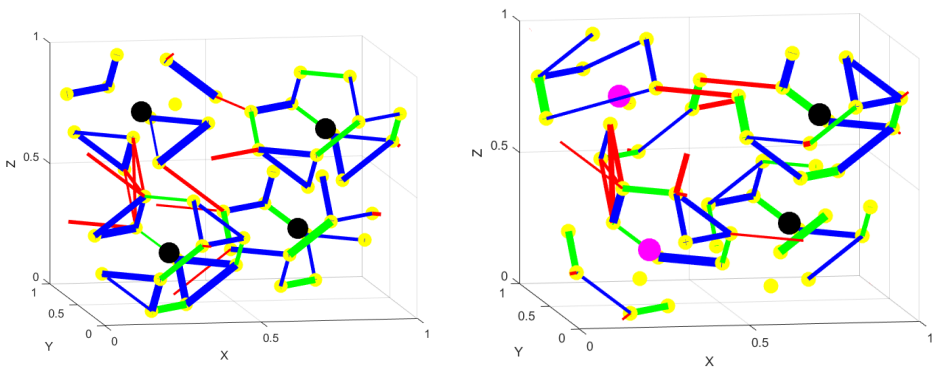

Figure 5.5: Jump statistics plots from MD-simulations at 450 K of (a) Li_6PS_6, and (b) Li_7PS_5Cl. The lines represent the three different types of jumps; green: doublet, blue: intracage, red: intercage, thicker lines represent larger jump rates. The coloured spheres indicate; black: S at 4c, pink: Cl at 4c, yellow: Li-ion sites (48h).

positions. Around the 4c-sites cages are visible in which the Li-ions diffuse, which are interconnected by intercage jumps. Although Li_6PS_6 and Li_7PS_5Cl show significant differences in the intracage and doublet jump rates, the rate limiting intercage jump rates are similar. These results indicate that Li-ion vacancies and substituting S with

Cl changes the jump rates significantly, and both are responsible for increasing the Li-ion conductivity in Li_6PS_5Cl.
It is obvious that increasing the amount of vacancies, to a certain degree, will enhance the Li-ion diffusivity, but understanding the impact of Cl-doping requires a more detailed analysis. The question is what change in local environment, caused by replacing S with Cl, is responsible for the improved conductivity. To bring forward the difference in the local environment of Cl- and S-ions the radial distribution functions (RDF's) around the atoms located on the 4c- and 4a-sites were determined. The RDF's in Figure 5.6 reflect the Li-ion density as a function of distance with respect to the S- or Cl-ion on the 4a- and 4c-sites, clearly reflecting the Li-ion density due to the Li-ions in the cage by a peak around 2.5 Ångstrom.

In Figure 5.6 a significant difference in Li-ion density is observed when comparing

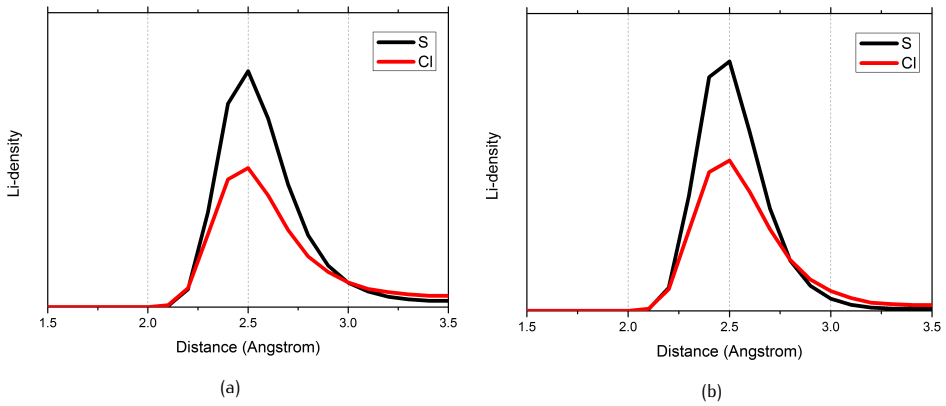

Figure 5.6: Radial distribution functions representing the Li-density as a function of distance around the Cl- and S-ions in Li_6PS_5Cl during the MD-simulation at 450 K at the (a) 4a-sites and (b) 4c-sites.

the RDF's around the Cl- and S-ions at 4a- and 4c-sites. Although the peak width and position are equal for Cl and S, the Li-density around the S-ions is significantly larger. Integrating the Li-density upto 3.5 Ångstrom shows that on average there are 5 Li-ions in the cage surrounding the Cl-ions and 7 Li-ions surround the S-ions. Therefore, (on average) there is always an empty doublet of 48h-sites near the Cl-ions, facilitating intercage jumps. This can be explained by the lower ionic charge of the Cl-ions compared to S-ions, which is charge compensated by the extra vacancies on the Li-sites near Cl-ions.
At all the simulated temperatures a similar Li-distribution is seen in Li_6PS_5Cl and Li_6PS_5Br, indicating that a 5-7 Li-distribution over the cages is more stable than a 6-6 Li-distribution when halogens are present. These results also suggest that the calculated stability of the argyrodites [6] may be strongly influenced by the Li-ion distribution (induced by the halogens). Given the large configurational space on the Li-ion sub-lattice it is beyond the scope of this chapter to consider the stability dependence on the Li-ion configuration.

5.3.3. Halogen disorder

The impact of vacancies on the Li-ion jumps does not explain the orders of magnitude difference in conductivity between Li_6PS_5Cl and Li_6PS_5I. It has been proposed that the difference in conductivity is caused by the fact that I-ions only occupy the 4a-sites, whereas Cl-ions show disorder, being distributed over the 4a- and 4c-sites [11]. The 4a- and 4c-sites represent Cl-ions located outside and inside the cages, respectively. Furthermore, experiments have shown that increasing the Cl-occupancy of 4c-sites can significantly increase the Li-ion conductivity in Li_6PS_5Cl [19]. To validate whether the disorder of halogen-ions over the 4a- and 4c-site is responsible for the high conductivity in Li_6PS_5Cl and Li_6PS_5Br in comparison to Li_6PS_5I, simulations were performed with different distributions of Cl-ions over the 4a- and 4c-sites in a unit cell of Li_6PS_5Cl.

Figure 5.7 shows that the position of the Cl-ions has a profound impact on the jump

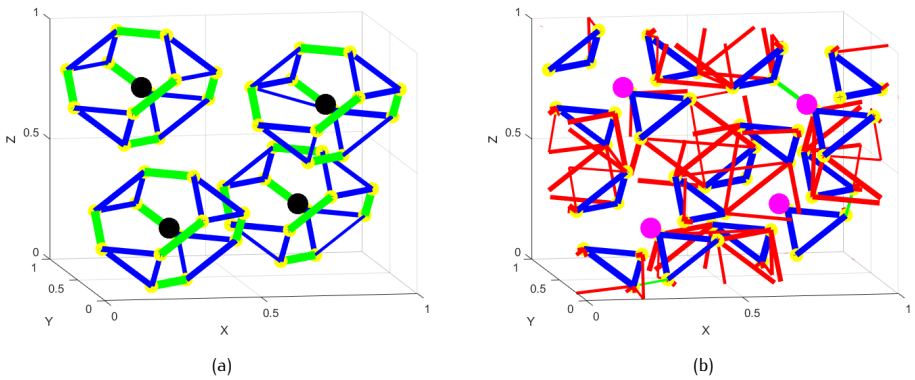

Figure 5.7: Jump statistics plots from MD-simulations at 450 K of Li_6PS_5Cl with all chloride (a) on 4a (outside the cages) and (b) on 4c (inside the cages). The lines represent the three different types of jumps; green: doublet, blue: intracage, red: intercage, thicker lines represent larger jump rates. The coloured spheres indicate; black: S at 4c, pink: Cl at 4c, yellow: Li-ion sites (48h).

rates, and thus on the conductivity. When all the Cl-ions are located at 4a-sites (similar to I-ions in Li_6PS_5I) no intercage jumps occur during the MD-simulation. Placing all the Cl-ions at the 4c-sites also leads to a low Li-diffusivity, however, not because of the intercage jump rate. In contrast, the Cl-ions on the 4c-sites induce a very high intercage jump rate, but the doublet jump rate decreases drastically and becomes rate limiting, thereby causing the intercage jumps to become a local motional process. In this case the Li-ion mobility is limited by the doublet jumps, which thus determines the macroscopic Li-ion conductivity in this structure.

These simulations demonstrate that distributing the halogens over the 4a- and 4c-sites, referred to as halogen disorder, is essential for inducing high macroscopic Li-ion diffusion. It also explains why crystalline Li_6PS_5I, in which all I-ions occupy 4a-sites, shows a Li-ion diffusivity orders of magnitude smaller than crystalline Li_6PS_5Cl [11]. In Figure 5.8 the jump rates of the different jump processes are plotted as a function of Cl-occupancy of the 4c-sites, showing a clear relation between the jump rates and

the Cl-distribution.

The doublet jump rate decreases with increasing Cl-occupancy of the 4c-sites, while

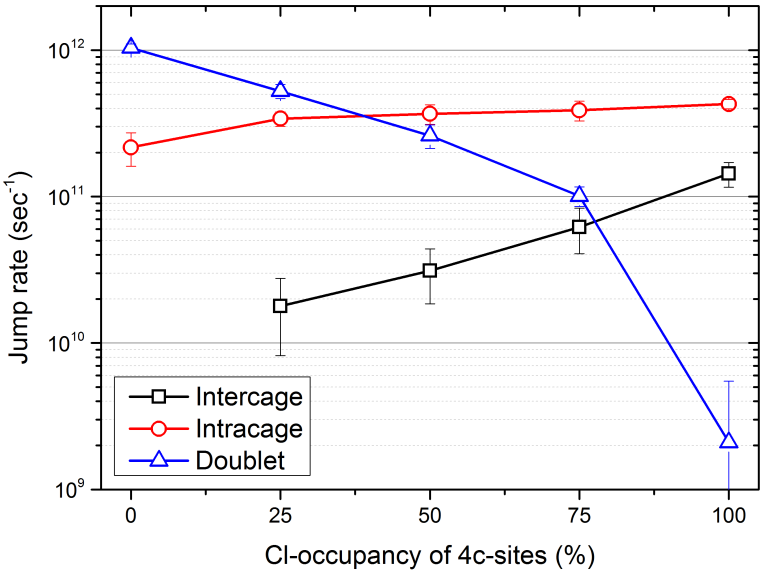

Figure 5.8: Jump rates versus Cl-occupancy of 4c-sites in Li_6PS_5Cl from MD-simulations at 450 K.

the intercage jump rate increases, and the intracage jump rate is nearly constant. To obtain the highest possible Li-ion conductivity the limiting jump rate should be as high as possible, which in Li_6PS_5Cl can be the doublet or intercage jumps, depending on the Cl-ordering over 4a- and 4c-sites. The results in Figure 5.8 indicate that the highest Li-ion conductivity can be obtained when $\frac{3}{4}$ of the 4c-sites (and $\frac{1}{4}$ of the 4a-sites) are occupied by Cl-ions. At this distribution the lowest jumps frequency is maximised, showing a limiting jump rate two times larger compared to when the Cl-ions are evenly distributed over 4a- and 4c-sites.

It has been shown that the disorder of Cl in argyrodites can be tailored by heat treatment [19], therefore optimising the synthesis conditions to obtain a 1:3 Cl-distribution over 4a- and 4c-sites, is at present predicted to double the Li-ion conductivity in Li_6PS_5Cl. Note that the different halogens influence the rate of each jump type differently (see Tables 5.1, 5.2, and 5.3), and therefore the 4a-4c distribution for Li_6PS_5Br and Li_6PS_5I which maximises the Li-ion conductivity will probably differ from the optimal 4a-4c distribution of Li_6PS_5Cl.

5.3.4. $Li_5PS_4X_2$

The results of the MD-simulations indicate that introducing halogens in the argyrodite structure increases the Li-ion conductivity, under the condition that the halogen ions are distributed over the 4a- and 4c-sites. A logical step to increase the conductivity

further would be to introduce a larger amount of halogens, and consequently also more Li-vacancies, giving the composition $Li_5PS_4X_2$ (X = Cl, Br or I).
The similar stability of Li_6PS_5X and $Li_5PS_4X_2$ compounds [6] suggests that synthesis of these compounds should be possible. The larger amount of Li-vacancies would make Li-diffusion easier, although the jump rates in Figure 5.8 suggest that Cl-ion occupying all of the 4a- and 4c-sites might hinder intercage and doublet jumps. To determine whether introducing more halogens is beneficial for the Li-ion conductivity simulations were performed on $Li_5PS_4Cl_2$, $Li_5PS_4Br_2$, and $Li_5PS_4I_2$, the results of which are shown in Figure 5.9.

During the MD-simulations macroscopic Li-ion conductivity is observed in all the

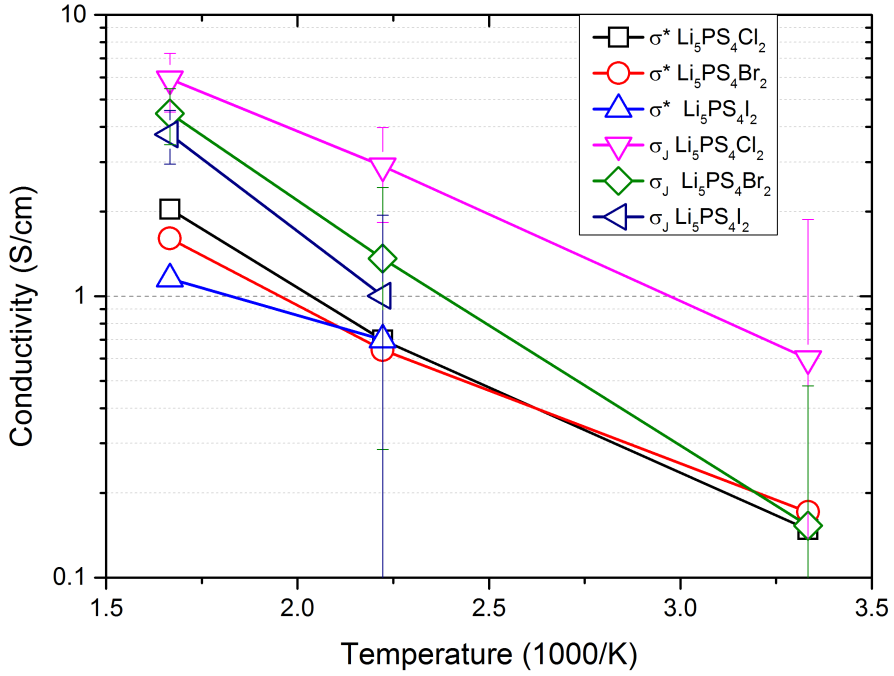

Figure 5.9: Arrhenius plot of the conductivities of $Li_5PS_4X_2$ compounds from MD-simulations based on the intercage jump frequency, σ_J, and the MSD, σ^*.

$Li_5PS_4X_2$ compositions, except for $Li_5PS_4I_2$ at 300 K. While simulations of Li_6PS_5Cl in which the 4a- or 4c-sites are completely occupied display low limiting jump rates, as shown in Figure 5.8, the combination of completely occupied 4a- and 4c-sites in $Li_5PS_4Cl_2$ performs well. Apparently the complete Cl-occupancy of 4a- and 4c-sites does not hinder the jump rates, but the 4a- or 4c-sites being unoccupied by Cl-ions seems to decrease certain jump rates in Li_6PS_5Cl.
This is an additional proof that the combination of occupied 4a- and 4c-sites is essential for macroscopic conductivity in Li-argyrodites. With iodine occupying 4a- and 4c-sites at 450 and 600 K $Li_5PS_4I_2$ shows a conductivity comparable to $Li_5PS_4Cl_2$

and $Li_5PS_4Br_2$, whereas Li_6PS_5I does not show any macroscopic diffusion at these temperatures. Therefore, to improve the Li-ion conductivity in $Li_{7-x}PS_{6-x}I_x$ a fraction of the I-ions should occupy the 4c-sites. Increasing the I-content above $x = 1$ implies that some of the I-ions will occupy the 4c-sites, which is suggested to be a promising strategy to increase the Li-ion conductivity in $Li_{7-x}PS_{6-x}I_x$.
For $Li_5PS_4Cl_2$ and $Li_5PS_4Br_2$ the conductivities are similar to those of Li_6PS_5Cl and Li_6PS_5Br. Although increasing the halogen composition does not significantly alter the Li-ion conductivity, $Li_5PS_4Cl_2$ and $Li_5PS_4Br_2$ may be interesting as solid state electrolytes because other properties of these compositions might be more favourable than those of Li_6PS_4Cl and Li_6PS_4Br. For instance, it is not unlikely that replacing the non-bonded S^{2-} by Cl^- or Br^- will increase the stability versus oxygen and moisture of the argyrodite crystals, making these halogen rich compositions potentially more suitable for application as a solid state electrolyte.

5.4. Conclusions

Using DFT MD-simulations the origin of the Li-ion conductivity in argyrodite solid electrolytes is investigated. Although halogen replacement of sulphur introduces Li-vacancies by charge compensation, the distribution of the halogens over the available sites is equally important. The halogen distribution determines the distribution of Li-vacancies, which is decisive in how the higher local Li-ion diffusivity translates into a higher macroscopic Li-ion conductivity.
Halogen substitution on each of the two possible sulphur sites induces a higher jump frequency of a different Li-ion jump process, whereas all three distinct jump processes are required for macroscopic conductivity. This explains why a distribution of the halogens over the two available sites is required for high Li-ion conductivities.
The simulations suggest that the Li-ion conductivity can be increased by optimising the halogen distribution over the 4a- and 4c-sites, and by increasing the halogen content in Li-argyrodites, where the latter may have the additional advantage of being more stable versus air and moisture.

References

[1] E.P. Roth and C.J. Orendorff. How electrolytes influence battery safety. *Electrochem. Soc. Interface*, 21(2):45–49, 2012.

[2] J.C. Bachman, S. Muy, A. Grimaud, H.H. Chang, N. Pour, S.F. Lux, O. Paschos, F. Maglia, S. Lupart, P. Lamp, L. Giordano, and Y. Shao-Horn. Inorganic solid-state electrolytes for lithium batteries: mechanisms and properties governing ion conduction. *Chem. Rev.*, 116(1):140–162, 2016. doi: 10.1021/acs.chemrev.5b00563.

[3] K. Takada. Progress and prospective of solid-state lithium batteries. *Acta Mater.*, 61(3):759–770, 2013. doi: 10.1016/j.actamat.2012.10.034.

[4] S.T. Kong, H.J. Deiseroth, C. Reiner, O. Gun, E. Neumann, C. Ritter, and D. Zahn. Lithium argyrodites with phosphorus and arsenic: order and disorder of lithium

atoms, crystal chemistry, and phase transitions. *Chemistry*, 16(7):2198–2206, 2010. doi: 10.1002/chem.200902470.

[5] R.P. Rao and S. Adams. Studies of lithium argyrodite solid electrolytes for all-solid-state batteries. *Phys. Status Solidi A*, 208(8):1804–1807, 2011. doi: 10.1002/pssa.201001117.

[6] H.M. Chen, M. Chen, and S. Adams. Stability and ionic mobility in argyrodite-related lithium-ion solid electrolytes. *Phys. Chem. Chem. Phys.*, 17(25):16494–16506, 2015. doi: 10.1039/c5cp01841b.

[7] S.T. Kong, H.J. Deiseroth, J. Maier, V. Nickel, K. Weichert, and C. Reiner. Li_6PO_5Br and Li_6PO_5Cl: the first lithium-oxide-argyrodites. *Z. Anorg. Allg. Chem.*, 636(11):1920–1924, 2010. doi: 10.1002/zaac.201000121.

[8] V. Epp, O. Gun, H.J. Deiseroth, and M. Wilkening. Long-range Li^+ dynamics in the lithium argyrodite Li_7PSe_6 as probed by rotating-frame spin-lattice relaxation NMR. *Phys. Chem. Chem. Phys.*, 15(19):7123–7132, 2013. doi: 10.1039/c3cp44379e.

[9] H.J. Deiseroth, S.T. Kong, H. Eckert, J. Vannahme, C. Reiner, T. Zaiss, and M. Schlosser. Li_6PS_5X: a class of crystalline Li-rich solids with an unusually high Li^+ mobility. *Angew. Chem. Int. Ed.*, 47(4):755–758, 2008. doi: 10.1002/anie.200703900.

[10] S. Boulineau, M. Courty, J.M. Tarascon, and V. Viallet. Mechanochemical synthesis of Li-argyrodite Li_6PS_5X (X=Cl, Br, I) as sulfur-based solid electrolytes for all solid state batteries application. *Solid State Ionics*, 221:1–5, 2012. doi: 10.1016/j.ssi.2012.06.008.

[11] P.R. Rayavarapu, N. Sharma, V.K. Peterson, and S. Adams. Variation in structure and Li^+-ion migration in argyrodite-type Li_6PS_5X (X = Cl, Br, I) solid electrolytes. *J. Solid State Electrochem.*, 16(5):1807–1813, 2011. doi: 10.1007/s10008-011-1572-8.

[12] C. Yu, L. van Eijck, S. Ganapathy, and M. Wagemaker. Synthesis, structure and electrochemical performance of the argyrodite Li_6PS_5Cl solid electrolyte for Li-ion solid state batteries. *Electrochim. Acta*, 215:93–99, 2016. doi: 10.1016/j.electacta.2016.08.081.

[13] F. Stadler and C. Fietzek. Crystalline halide substituted Li-argyrodites as solid electrolytes for lithium secondary batteries. *ECS Transactions*, 25(36):177–183, 2010. doi: 10.1149/1.3393854.

[14] H.J. Deiseroth, J. Maier, K. Weichert, V. Nickel, S.T. Kong, and C. Reiner. Li_7PS_6 and Li_6PS_5X (X: Cl, Br, I): possible three-dimensional diffusion pathways for lithium ions and temperature dependence of the ionic conductivity by impedance measurements. *Z. Anorg. Allg. Chem.*, 637(10):1287–1294, 2011. doi: 10.1002/zaac.201100158.

[15] S.T. Kong, O. Gun, B. Koch, H.J. Deiseroth, H. Eckert, and C. Reiner. Structural characterisation of the Li argyrodites Li_7PS_6 and Li_7PSe_6 and their solid solutions: quantification of site preferences by MAS-NMR spectroscopy. *Chemistry*, 16(17):5138–5147, 2010. doi: 10.1002/chem.200903023.

[16] S. Yubuchi, S. Teragawa, K. Aso, K. Tadanaga, A. Hayashi, and M. Tatsumisago. Preparation of high lithium-ion conducting Li_6PS_5Cl solid electrolyte from ethanol solution for all-solid-state lithium batteries. *J. Power Sources*, 293:941–945, 2015. doi: 10.1016/j.jpowsour.2015.05.093.

[17] S. Boulineau, J.M. Tarascon, J.B. Leriche, and V. Viallet. Electrochemical properties of all-solid-state lithium secondary batteries using Li-argyrodite Li_6PS_5Cl as solid electrolyte. *Solid State Ionics*, 242:45–48, 2013. doi: 10.1016/j.ssi.2013.04.012.

[18] C. Yu, S. Ganapathy, N.J.J. de Klerk, I. Rosłoń, E.R.H. van Eck, A.P. Kentgens, and M. Wagemaker. Unravelling Li-ion transport from picoseconds to seconds: bulk versus interfaces in an argyrodite Li_6PS_5Cl-Li_2S all-solid-state Li-ion battery. *J. Am. Chem. Soc.*, 138(35):11192–11201, 2016. doi: 10.1021/jacs.6b05066.

[19] R.P. Rao, N. Sharma, V.K. Peterson, and S. Adams. Formation and conductivity studies of lithium argyrodite solid electrolytes using *in situ* neutron diffraction. *Solid State Ionics*, 230:72–76, 2013. doi: 10.1016/j.ssi.2012.09.014.

[20] M. Chen and S. Adams. High performance all-solid-state lithium/sulfur batteries using lithium argyrodite electrolyte. *J. Solid State Electrochem.*, 19(3):697–702, 2014. doi: 10.1007/s10008-014-2654-1.

[21] M. Chen, R. Prasada Rao, and S. Adams. The unusual role of Li_6PS_5Br in all-solid-state CuS/Li_6PS_5Br/In-Li batteries. *Solid State Ionics*, 268:300–304, 2014. doi: 10.1016/j.ssi.2014.05.004.

[22] M. Chen, X. Yin, M.V. Reddy, and S. Adams. All-solid-state MoS_2/Li_6PS_5Br/In-Li batteries as a novel type of Li/S battery. *J. Mater. Chem. A*, 3(20):10698–10702, 2015. doi: 10.1039/c5ta02372f.

[23] V. Epp, Ö. Gün, H.J. Deiseroth, and M. Wilkening. Highly mobile ions: low-temperature NMR directly probes extremely fast Li^+ hopping in argyrodite-type Li_6PS_5Br. *J. Phys. Chem. Lett.*, 4(13):2118–2123, 2013. doi: 10.1021/jz401003a.

[24] G. Kresse and J. Hafner. Ab initio molecular dynamics for liquid metals. *Phys. Rev. B*, 47(1):558–561, 1993. doi: 10.1103/PhysRevB.47.558.

[25] J.P. Perdew, K. Burke, and M. Ernzerhof. Generalized gradient approximation made simple. *Phys. Rev. Lett.*, 77(18):3865–3868, 1996. doi: 10.1103/PhysRevLett.77.3865.

[26] P.E. Blöchl. Projector augmented-wave method. *Phys. Rev. B*, 50(24):17953–17979, 1994. doi: 10.1103/PhysRevB.50.17953.

[27] N.J.J. de Klerk and M. Wagemaker. Diffusion mechanism of the sodium-ion solid electrolyte Na_3PS_4 and potential improvements of halogen doping. *Chem. Mater.*, 28(9):3122–3130, 2016. doi: 10.1021/acs.chemmater.6b00698.

[28] G.H. Vineyard. Frequency factors and isotope effects in solid state rate processes. *J. Phys. Chem. Solids*, 3(1-2):121–127, 1957. doi: 10.1016/0022-3697(57)90059-8.

[29] R.J. Friauf. Correlation effects for diffusion in ionic crystals. *J. Appl. Phys.*, 33(1):494–505, 1962. doi: 10.1063/1.1777148.

[30] O. Pecher, S.T. Kong, T. Goebel, V. Nickel, K. Weichert, C. Reiner, H.J. Deiseroth, J. Maier, F. Haarmann, and D. Zahn. Atomistic characterisation of Li^+ mobility and conductivity in $Li_{7-x}PS_{6-x}I_x$ argyrodites from molecular dynamics simulations, solid-state NMR, and impedance spectroscopy. *Chemistry*, 16(28):8347–8354, 2010. doi: 10.1002/chem.201000501.

[31] A. Van der Ven, G. Ceder, M. Asta, and P.D. Tepesch. First-principles theory of ionic diffusion with nondilute carriers. *Phys. Rev. B*, 64(18):184307, 2001. doi: 10.1103/PhysRevB.64.184307.

Supporting Information

Note that in the Tables the uncertainty for jump rates below 10^{10} sec^{-1} is quite large, this is because rates smaller as this correspond to less than 1 jump per Li-ion (on average) in the simulated time.

Table 5.1: Conductivities, jump rates and activation energies from MD-simulations at 300 K, the value in brackets is the standard deviation.

Material	Conductivity		Intercage		Intracage		Doublet	
	MSD (S/cm)	Jump (S/cm)	Jump rate (*10^{10} Hz)	E_{act} (eV)	Jump rate (*10^{10} Hz)	E_{act} (eV)	Jump rate (*10^{10} Hz)	E_{act} (eV)
Li_7PS_6	0.04	-	-	-	16.56(1.37)	0.11(0.01)	0.73(0.63)	0.18(0.01)
Li_7PSe_6	0.06	-	-	-	27.58(4.25)	0.09(0.01)	2.64(2.26)	0.15(0.02)
Li_6PS_5Cl (50% Cl@4c)	0.04	0.89(1.29)	0.73(1.05)	0.18(0.02)	17.78(3.20)	0.10(0.01)	21.58(3.82)	0.10(0.01)
Li_6PS_5Br	0.19	1.23(0.87)	1.03(0.72)	0.18(0.02)	13.97(5.31)	0.11(0.01)	18.85(6.33)	0.10(0.01)
Li_6PS_5I	0.02	-	-	-	-	-	145.26(9.68)	0.05(0.01)
Li_6PS_6	0.06	0.49(0.83)	0.38(0.65)	0.19(0.02)	18.76(4.99)	0.10(0.01)	5.51(2.73)	0.13(0.01)
Li_7PS_5Cl	0.04	0.76(0.56)	0.55(0.41)	0.19(0.01)	3.99(3.23)	0.15(0.02)	13.26(2.43)	0.11(0.01)
$Li_5PS_4Cl_2$	0.15	0.60(1.28)	0.56(1.20)	0.18(0.02)	24.21(14.31)	0.10(0.01)	2.46(3.14)	0.15(0.02)
$Li_5PS_4Br_2$	0.17	0.15(0.33)	0.15(0.33)	0.23(-[a])	9.13(3.50)	0.12(0.01)	10.05(3.37)	0.12(0.01)
$Li_5PS_4I_2$	0.06	-	-	-	1.33(1.40)	0.16(0.01)	31.90(6.36)	0.09(0.01)
Li_6PS_5Cl (0% Cl@4c)	0.29	0.05(0.16)	0.04(0.13)	0.26(-[a])	8.12(5.34)	0.13(0.02)	74.36(6.62)	0.07(0.01)
Li_6PS_5Cl (25% Cl@4c)	0.26	0.91(1.04)	0.73(0.83)	0.19(-[a])	19.32(4.10)	0.10(0.01)	39.83(5.65)	0.08(0.01)
Li_6PS_5Cl (75% Cl@4c)	0.14	1.59(0.79)	1.28(0.63)	0.17(0.01)	20.94(2.55)	0.10(0.01)	6.09(2.01)	0.13(0.01)
Li_6PS_5Cl (100% Cl@4c)	0.29	-	5.34(1.47)	0.14(0.01)	17.82(3.89)	0.10(0.01)	-	-

[a] Standard deviation in the jump rate too large to determine the standard deviation of the activation energy.

Table 5.2: Conductivities, jump rates and activation energies from MD-simulations at 450 K, the value in brackets is the standard deviation.

Material	Conductivity		Intercage		Intracage		Doublet	
	MSD (S/cm)	Jump (S/cm)	Jump rate (*10^{10} Hz)	E_{act} (eV)	Jump rate (*10^{10} Hz)	E_{act} (eV)	Jump rate (*10^{10} Hz)	E_{act} (eV)
Li_7PS_6	0.18	0.07(0.21)	0.07(0.21)	0.37(-[a])	30.99(9.37)	0.14(0.02)	7.55(2.38)	0.19(0.01)
Li_7PSe_6	0.13	0.12(0.36)	0.15(0.44)	0.34(-[a])	47.77(3.75)	0.12(0.01)	7.62(3.41)	0.19(0.02)
Li_6PS_5Cl (50% Cl@4c)	0.52	2.56(1.04)	3.12(1.27)	0.27(0.02)	36.75(5.54)	0.13(0.01)	26.11(4.73)	0.14(0.01)
Li_6PS_5Br	0.39	2.54(1.34)	3.16(1.67)	0.22(0.02)	26.54(4.70)	0.14(0.01)	36.03(4.23)	0.13(0.01)
Li_6PS_5I	0.05	-	-	-	0.26(0.55)	0.32(-[a])	203.25(7.26)	0.06(0.01)
Li_6PS_6	0.10	0.62(0.40)	0.73(0.47)	0.27(0.02)	41.80(11.71)	0.12(0.01)	10.85(4.43)	0.18(0.02)
Li_7PS_5Cl	0.18	1.62(0.85)	1.76(0.92)	0.25(0.02)	19.01(3.24)	0.15(0.01)	21.25(4.46)	0.15(0.01)
$Li_5PS_4Cl_2$	0.70	2.90(1.08)	4.10(1.52)	0.22(0.01)	32.77(6.89)	0.13(0.01)	13.08(5.55)	0.17(0.02)
$Li_5PS_4Br_2$	0.64	1.36(1.07)	2.05(1.62)	0.24(0.02)	16.21(4.05)	0.16(0.01)	31.95(6.29)	0.13(0.01)
$Li_5PS_4I_2$	0.70	1.00(0.94)	1.64(1.54)	0.24(0.03)	9.03(2.98)	0.18(0.01)	55.90(8.93)	0.11(0.01)
Li_6PS_5Cl (0% Cl@4c)	0.18	-	-	-	21.67(5.54)	0.15(0.01)	103.68(6.64)	0.09(0.01)
Li_6PS_5Cl (25% Cl@4c)	0.62	1.50(0.81)	1.79(0.97)	0.25(0.02)	34.10(3.85)	0.13(0.01)	52.44(5.82)	0.11(0.01)
Li_6PS_5Cl (75% Cl@4c)	0.60	5.12(1.76)	6.20(2.13)	0.20(0.01)	38.89(5.97)	0.13(0.01)	10.09(1.54)	0.18(0.01)
Li_6PS_5Cl (100% Cl@4c)	0.25	0.18(0.28)	14.36(2.75)	0.17(0.01)	42.91(3.11)	0.12(0.01)	0.21(0.34)	0.33(-[a])

[a] Standard deviation in the jump rate too large to determine the standard deviation of the activation energy.

Table 5.3: Conductivities, jump rates and activation energies from MD-simulations at 600 K, the value in brackets is the standard deviation.

Material	Conductivity		Intercage		Intracage		Doublet	
	MSD (S/cm)	Jump (S/cm)	Jump rate (*10^{10} Hz)	E_{act} (eV)	Jump rate (*10^{10} Hz)	E_{act} (eV)	Jump rate (*10^{10} Hz)	E_{act} (eV)
Li_7PS_6	0.48	1.24(0.83)	1.72(1.15)	0.33(0.03)	54.84(7.70)	0.15(0.01)	16.96(4.20)	0.21(0.01)
Li_7PSe_6	0.74	1.37(1.22)	2.23(1.98)	0.32(0.04)	66.37(5.70)	0.14(0.01)	15.31(4.32)	0.22(0.02)
Li_6PS_5Cl (50% Cl@4c)	1.01	4.66(0.66)	7.56(1.06)	0.25(0.01)	56.88(5.21)	0.15(0.01)	37.48(6.51)	0.17(0.01)
Li_6PS_5Br	0.85	4.32(1.39)	7.18(2.31)	0.26(0.02)	40.47(4.93)	0.17(0.01)	41.07(4.78)	0.17(0.01)
Li_6PS_5I	0.08	-	-	-	3.08(2.45)	0.30(0.03)	243.89(10.51)	0.07(0.01)
Li_6PS_6	0.55	4.36(1.57)	6.79(2.44)	0.26(0.03)	64.49(7.78)	0.14(0.01)	8.42(1.94)	0.25(0.01)
Li_7PS_5Cl	1.18	3.63(1.14)	5.27(1.65)	0.27(0.02)	31.54(4.27)	0.18(0.01)	14.21(5.55)	0.22(0.02)
$Li_5PS_4Cl_2$	2.04	5.91(1.40)	11.13(2.64)	0.23(0.01)	52.41(7.00)	0.15(0.01)	35.33(5.78)	0.17(0.01)
$Li_5PS_4Br_2$	1.61	4.47(1.01)	8.97(2.03)	0.25(0.01)	31.90(3.57)	0.18(0.01)	42.87(4.86)	0.16(0.01)
$Li_5PS_4I_2$	1.15	3.76(0.81)	8.21(1.78)	0.25(0.01)	18.10(2.99)	0.21(0.01)	78.56(7.77)	0.13(0.01)
Li_6PS_5Cl (0% Cl@4c)	0.18	-	-	-	45.21(7.79)	0.16(0.01)	120.90(4.78)	0.11(0.01)
Li_6PS_5Cl (25% Cl@4c)	0.82	1.82(0.65)	2.91(1.04)	0.31(0.02)	52.26(6.09)	0.15(0.01)	66.24(5.29)	0.14(0.01)
Li_6PS_5Cl (75% Cl@4c)	0.91	7.40(1.50)	11.92(2.42)	0.23(0.01)	57.35(4.59)	0.15(0.01)	14.10(2.85)	0.22(0.01)
Li_6PS_5Cl (100% Cl@4c)	0.47	0.82(0.66)	24.15(3.04)	0.19(0.01)	57.78(4.75)	0.15(0.01)	1.32(1.07)	0.34(0.03)

6

Analysis of diffusion in solid-state electrolytes through MD simulations, improvement of the Li-ion conductivity in β-Li_3PS_4 as an example

This chapter has been published as: Niek J.J. de Klerk, Eveline van der Maas and Marnix Wagemaker, Analysis of diffusion in solid state electrolytes through MD-simulations, improvement of the Li-ion conductivity in β-Li_3PS_4 as an example; ACS Applied Energy Materials **1** (7), 3230-3242 (2018), doi: 10.1021/acsaem.8b00457

Molecular dynamics simulations are a powerful tool to study diffusion processes in battery electrolyte and electrode materials. From molecular dynamics simulations many properties relevant to diffusion can be obtained, including the diffusion path, amplitude of vibrations, jump rates, radial distribution functions, and collective diffusion processes. Here it is shown how the activation energies of different jumps and the attempt frequency can be obtained from a single molecular dynamics simulation. These detailed diffusion properties provide a thorough understanding of diffusion in solid electrolytes, and provide direction for the design of improved solid electrolyte materials. The presently developed analysis methodology is applied to DFT MD simulations of Li-ion diffusion in β-Li_3PS_4. The methodology presented is generally applicable to diffusion in crystalline materials and facilitates the analysis of molecular dynamics simulations. The code used for the analysis is freely available at: https://bitbucket.org/niekdeklerk/md-analysis-with-matlab.
The results on β-Li_3PS_4 demonstrate that jumps between bc-planes limit the conductivity of this important class of solid electrolyte materials. The simulations indicate that the rate limiting jump process can be accelerated significantly by adding Li-interstitials or Li-vacancies, promoting three dimensional diffusion, which results in increased macroscopic Li-ion diffusivity. Li-vacancies can be introduced through Br-doping, which is predicted to result in an order of magnitude larger Li-ion conductivity in β-Li_3PS_4. Furthermore, the present simulations rationalise the improved Li-ion diffusivity upon O-doping through the change in Li-distribution in the crystal.
Thus it is demonstrated how a thorough understanding of diffusion, based on thorough analysis of MD simulations, helps to gain insight and develop strategies to improve the ionic conductivity of solid electrolytes.

6.1. Introduction

To prevent further global warming by greenhouse gas emissions it is necessary to move from fossil fuels towards renewable energy sources. For transport applications other energy carriers, such as hydrogen and batteries, are considered. Of the current technologies which can replace fossil fuels in vehicles, batteries result in the lowest greenhouse gas emissions [1], especially if renewable sources are used for the energy production.
However, safety concerns and the limited range of current battery electric vehicles are slowing down their implementation. Solid state batteries are a promising technology [2, 3] based on the much lower flammability risks, the higher energy density on the cell level, and lower self-discharge rate.
One of the prerequisites towards the realisation of solid state batteries is the development of highly conductive solid electrolytes. In recent years several materials have been discovered which show conductivities comparable to liquid electrolytes. Room temperature ionic conductivities in the order of 10^{-3} S/cm have been reported in a range of lithium containing compounds such as: [2] LLTO ($Li_{3x}La_{\frac{2}{3}-x}TiO_3$), argyrodites, LGPS ($Li_{10}GeP_2S_{12}$), and LATP ($Li_{1+x}Al_xTi_{2-x}(PO)_4$). Fewer sodium containing compounds with such high conductivities are known, most likely the result of less intensive research in this area, but several have been established, including β-alumina [4] and Na_3PS_4 [5]. Recently it has been shown that there is a relation between phonons, high

ionic mobility and low electrochemical stability in lithium ion conductors [6]. Which shows that the combination of high ionic conductivity and large electrochemical stability is challenging [2, 7], although electrochemical stability does not have very strict requirements. A solid electrolyte can be successful if its decomposition products are stable, have a reasonable ionic conductivity and low electronic conductivity [7], similar to the functioning of solid-electrolyte interface (SEI) layers at electrodes in liquid electrolytes. The complex demands on solid electrolytes necessitates fundamental research towards solid electrolyte properties and new solid electrolyte materials.
Computer simulations are playing an important role in understanding and directing materials design towards improved battery performance. For example, calculations have shown that the electrochemical stability of solid electrolytes is enhanced by passivating decomposition products [7], that strain can enhance diffusion [8], how Li-ion diffusion can be increased in anti-perovskites [9] and Na_3PS_4 [5, 10], and why bond frustration is beneficial for Li-ion diffusion [11].
In solid state electrolytes the high concentration of diffusing atoms, 31 mol/L in β-Li_3PS_4, can lead to complex interactions and diffusion behaviour. Diffusion can involve collective jumps [12] and lattice vibrations [10, 13], which are all included in molecular dynamics (MD) simulations by taking into account all possible motions of ions and their interactions. Furthermore, MD simulations can show unanticipated diffusion behaviour [14], whereas static calculations (e.g. nudged elastic band) are limited by the imagination of the researcher. To understand diffusion in solid state electrolytes MD simulations are thus a powerful tool, allowing the dynamic diffusion processes to be studied in detail.
Although MD simulations have been shown to provide understanding of complicated diffusion processes, however, typically the only property that is extracted is the tracer diffusivity, from which the activation energy is calculated by assuming Arrhenius behaviour. A thorough analysis of MD simulations is able to give much more detailed results, potentially providing more understanding and concrete direction towards the design of improved conductivities [10, 15, 16]. In order to make such thorough analysis of MD simulations more easily available, we present an approach, here demonstrated for β-Li_3PS_4, that allows to extract the detailed diffusional properties based on a MD simulation and the crystalline structure of the studied material. The approach determines jump rates, activation energies of different jumps, attempt frequency, vibrational amplitude, radial distribution functions, possible collective motions, site occupancies, tracer diffusivity, and the correlation factor.
The first part of this chapter describes the approach that is followed to obtain the diffusional properties from a single MD simulation. In the second part MD simulations on β-Li_3PS_4 are analysed, exemplifying how the developed approach helps in understanding diffusion in solid state electrolytes, and how this provides direction to design new and improved solid electrolyte materials. The Matlab code used for the analysis of MD simulations is freely available on-line [17].

6.2. Information from MD simulations

After performing a MD simulation the position of all the atoms at every time step is known. Typically, this result is used to determine the tracer diffusivity (D^*) via the

mean squared displacement [18–21]:

$$D^* = \frac{1}{2dNt} \sum_{i=1}^{N} ([r_i(t+t_0)] - [r_i(t_0)])^2 \tag{6.1}$$

where $r_i(t+t_0)$ is the displacement of a single atom with respect to the starting position ($r_i(t_0)$), t the simulated time, N the number of diffusing atoms, and d the number of diffusion dimensions. Provided that the atomic displacement is significantly larger than the vibration amplitude this gives reliable values for the tracer diffusion, although the tracer diffusivity is only an approximation of the ionic diffusion, and taking ion correlations and the displacement of the centre of mass into account leads to more precise results [22].
Using the diffusivity and the Nernst-Einstein relation, assuming that the Haven ratio is equal to one [22], the conductivity (σ) can be approximated [18, 22] by:

$$\sigma = \frac{ne^2z^2}{k_BT} D^* \tag{6.2}$$

where n is the diffusing particle density, e the elementary electron charge, z the ionic charge, k_B Boltzmann's constant, and T the temperature in Kelvin. The ionic conductivity determined in this way gives a good indication whether the material has an ionic conductivity which makes it suitable as a solid electrolyte.
However, to get a thorough understanding of the ionic diffusion in the material much more properties related to the diffusion process can be obtained from a single MD simulation, including:

- Amplitude of vibrations
- Attempt frequency
- Site occupations
- Jump rates
- Correlation factor
- Activation energies
- Collective jumps
- Radial Distribution Functions

6.2.1. Amplitude of vibrations

Atomic vibrations in a crystal are the 'back and forth' movement of an atom around a (meta)stable position. From a MD simulation the position of all atoms is known at any time, hence the absolute displacement can be obtained per time step. The atomic vibrations can be determined by monitoring the derivative of the absolute displacement, a change in the direction of movement gives a change in sign of this derivative, and atomic vibrations can thus be monitored. The vibrational amplitudes (A) are obtained

by determining the change in absolute displacement (r_i) of each atom (i) while the derivative of the displacement keeps the same sign (between time steps t_a and t_b):

$$A = r_i(t_b) - r_i(t_a) \tag{6.3}$$

Doing this for all the atoms of interest throughout the MD-simulation gives a distribution of vibrational amplitudes, an example of which is shown in Fig. 6.1. By fitting

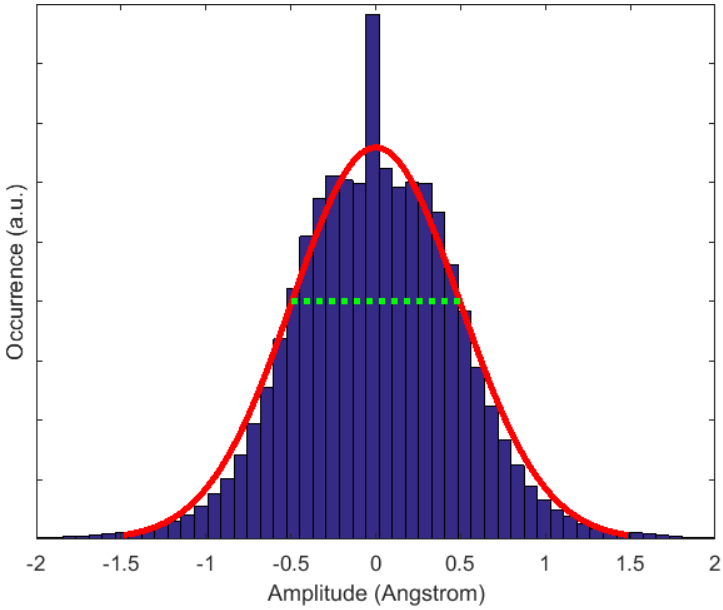

Figure 6.1: Histogram showing the vibrational amplitude of Li-ions in β-Li_3PS_4 at 600 K, with the fitted Gaussian (solid red line) and the standard deviation (± 0.495 Å, dotted green line)

a Gaussian function to the obtained distribution the standard deviation in vibrational displacement can be obtained, providing an estimate of the average amplitude of vibrations in the crystal. Since the 3-D distribution is known, anisotropic vibrational amplitudes can also be determined from a MD simulation in this way.
As shown in Figure 6.1 there are some vibrations with amplitudes above 1 Å, which are probably caused by ionic jumps between different crystallographic sites. However, these large amplitude vibrations are only a small percentage of the total number of vibrations, and will not significantly influence the Gaussian fit.

6.2.2. Attempt frequency

The derivative of the absolute displacement can also be used to determine the vibration time of an atom or, via a Fourier transformation, the vibration frequency. The vibrational spectrum is obtained by determining the derivative of the absolute displacement (Δr_i) per atom (i) at every time-step (t):

$$\Delta r_i(t) = r_i(t) - r_i(t-1) \tag{6.4}$$

which is transformed to a frequency spectrum via a Fourier transformation. The frequency spectrum of each (diffusing) atom is then combined to obtain the vibrational spectrum, as shown for Li-ions in β-Li_3PS_4 in Fig. 6.2. From the frequency spectrum

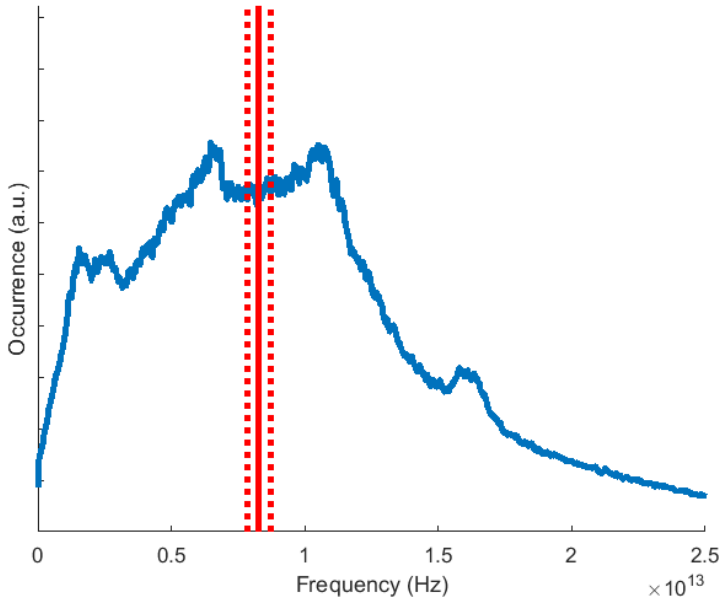

Figure 6.2: Vibration frequency spectrum of Li-ions in β-Li_3PS_4 at 600 K, the average frequency of 8.29 (± 0.46)*10^{12} Hz is shown by the solid (± dotted) red line.

the attempt frequency can be obtained if we consider every vibration of a diffusing atom as an attempt. Thus we define the average vibration frequency as the attempt frequency (ν^*), which is necessary to determine the relation between jump rates and activation energies.
A high attempt frequency does not necessarily lead to a high diffusivity, as high attempt frequencies are often related to a high activation energy [23], a phenomenon which is known as the Meyer-Neldel rule [24]. Note that the presented approach determines a frequency spectrum based on the vibrations of single atoms. The obtained spectrum thus differs from a phonon spectrum, which depends on the collective vibrations of the atoms. To test the robustness of the presented approach the attempt frequency has also been determined with a high and a low cut-off frequency. The high cut-off frequency removes short vibrations which might be caused by numerical errors, while a low cut-off frequency removes long-range atomic motions. For the high cut-off a frequency of 5*10^{13} Hz was used, which equals 10 time-steps in the current MD-simulations, the low cut-off frequency was 1*10^{12} Hz.
From the MD simulation of β-Li_3PS_4 at 600 K an attempt frequency of 8.27*10^{12} Hz was obtained with the high cut-off frequency, while the low cut-off frequency lead to an attempt frequency of 8.39*10^{12} Hz. Both of these values are well within the stan-

dard deviation of the attempt frequency obtained without a cut-off frequency (8.29 (± 0.46) $*10^{12}$ Hz). Extracting the attempt frequency without a cut-off is thus shown to be robust.
The approach of obtaining the attempt frequency presented here is very different from the usual approaches. Several definitions of the attempt frequency exist [25], all of which require the determination of the transition state and calculation of the phonon spectrum for the stable and the transition state [26]. However, often these calculations are not performed, and a 'standard value' of $1*10^{13}$ Hz is used [25, 27].
In comparison to other methods the method presented here is straightforward, by only using the information that is already present in a MD simulation. Furthermore, since the attempt frequency is obtained from a single MD simulation the influence of temperature, structural parameters, etc., on the attempt frequency are included and can be investigated.

6.2.3. Site occupancy

In crystalline ionic conductors diffusion occurs through transitions between relatively stable sites. Typically these crystallographic sites are known from diffraction experiments, but if these are not known the sites can be extracted from a MD simulation through data mining [28]. The condition used for site occupancy is that the distance of the ion to the centre of the crystallographic site is smaller than the site-radius. At present the site-radius is defined as twice the vibrational amplitude.
A defined site-radius can lead to atoms that are not at a defined site, but by using the system and temperature dependent vibrational amplitude as a measure of site-radius this effect is minimised. Instead, this can be used to determine what happens while an atom jumps between sites, which can be used to obtain information about the transition state. Furthermore, an 'undefined' region between sites prevents the counting of small movements at site-borders as jumps between sites, thus giving more reliable jump-rates.
The site-radius can also lead to overlapping sites, but this is accounted for in the analysis code. If two sites show overlap the site-radius (of all sites) is reduced to half the distance between the two sites, thus preventing overlapping sites.

6.2.4. Jump rates

When the crystallographic sites are known, detecting the transitions between sites that occur in a MD simulation is straightforward. Counting the number of jumps (J_i) between (types of) sites provides the mean jump rate (Γ_i) using:

$$\Gamma_i = \frac{J_i}{Nt} \tag{6.5}$$

where N is the number of diffusing atoms, the subscript i defines a type of jump, and t is the simulation time. To get an estimate of the uncertainty in the jump rate the MD-simulation is divided into ten different parts. By assuming that the correlation between consecutive parts is negligible, the differing jump rates in each part allow for the calculation of the standard deviation.
As demonstrated recently [15] determination of the different jump rates in a crystal

provides direct insight in which jump process is rate-limiting for diffusion. This information can be used to design crystal structures with larger atomic diffusivity. Because NMR relaxation experiments can directly probe the jump rates, comparison with the jump rates from MD simulations can be used to validate the MD simulations [29], or to better understand the complex results from NMR experiments [30].
Using the Einstein-Smulochowski relation the jump rates are related to the jump rate diffusivity (D_J):

$$D_J = \sum_i \frac{\Gamma_i a_i^2}{2d} \tag{6.6}$$

where i are the different types of jumps, a_i is the jump distance of jump type i, and d the number of diffusion dimensions. The sum is over all types of jumps, since in most solid electrolytes several different types of jumps contribute to macroscopic diffusion.
In comparison to tracer diffusivity (D^*) the jump rate diffusivity is usually an overestimate. The overestimation is caused by back-and-forth jumps, which cancel each other in the tracer diffusivity but are both counted in the jump diffusivity, and by the angles between consecutive jumps [31], which causes the displacement to be lower than the total jump distance. To get an estimate of how effectively jumps contribute to macroscopic diffusion the correlation factor (f) can be calculated [27, 31]:

$$f = \frac{D^*}{D_J} \tag{6.7}$$

The correlation factor can be used to determine the diffusion mechanism (under certain conditions) [31].

6.2.5. Activation energies

A simple way to describe the temperature dependence of diffusion is the activation energy, which is usually obtained by fitting an Arrhenius equation to diffusion data at various temperatures. This assumes that Arrhenius behaviour is obeyed over the fitted temperature range, which assumes that there is no change in the material properties which determine diffusion over the studied temperature range. However, this is often incorrect [32], especially when the studied temperature range is large.
Non-Arrhenius behaviour usually leads to an underestimate of the activation energies at room temperature if extrapolated values from high temperatures are used. It is hard to say how large the errors are, since this will depend on the material [32] and the temperature range of the extrapolation.
To overcome this problem the activation energy can be calculated at a given temperature, based on which the temperature dependence of the activation energy can be determined via MD-simulations at various temperatures. The activation energy (ΔE_i^A) for a type of jump (i) can be determined by the jump rates in a MD-simulation via [33]:

$$\Delta E_i^A = -k_B T \ln\left(\frac{\Gamma_i^{\text{eff}}}{\nu^*}\right) \tag{6.8}$$

where k_B is Boltzmann's constant, T the temperature in Kelvin, Γ_i^{eff} the effective jump frequency, and ν^* the attempt frequency, which is obtained using the approach described in the Attempt frequency section and assumed to be isotropic.

Entropy effects are naturally included when extracting the activation energy from a MD simulation because the temperature is above zero Kelvin, the obtained activation energy thus includes the activation enthalpy and entropy of the ionic jump, in contrast to activation energies from NEB or bond valence calculations. Since the activation energy is determined by the ratio between the effective jump frequency and attempt frequency, the activation energy can be seen as a measure for the jump probability: if the activation energy is low, the jump probability is high, and vice-versa.

As shown in Figure 6.3 a jump from site A to B can have a different energy barrier

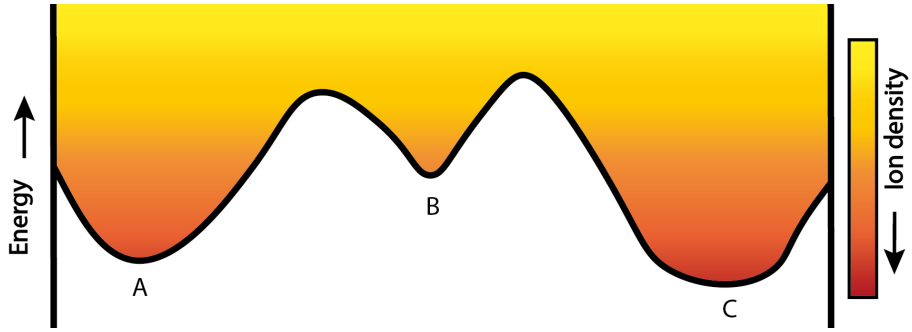

Figure 6.3: Energy landscape and the corresponding ion density, with sites A, B, and C

as the reverse jump due to the difference in site energy, even though the number of A-B and B-A jumps will be the same in equilibrium. Because the number of jumps is equal, simply using Equation 6.5 to determine the jump frequency would give the same activation energy for A-B and B-A jumps, which is clearly incorrect.

The exponential term in equation 6.8 means that the activation energy is determined by the amount of successful jumps divided by the number of attempted jumps. Thus, the amount of time an atom spends at a certain site should be taken into account to correctly determine the activation energy. The effective jump rate, Γ_i^{eff}, thus differs from the jump rate in equation 6.5 by taking into account the fraction of time that the diffusing atoms occupy a type of site (o_j):

$$\Gamma_i^{\text{eff}} = \frac{J_i}{tNo_j} \tag{6.9}$$

where t is the total simulated time, and N the number of diffusing atoms. By incorporating site-occupancy the sites with lower occupancy will have lower activation energies, correctly representing the difference in activation energy between A-B and B-A jumps in Figure 6.3. Furthermore, the difference in activation energy between back and forth jumps provides the energy difference between two sites, which can be used to predict changing site-occupancies with temperature. Since jump and attempt frequencies are temperature dependent the activation energy may also be a function of temperature. Such non-Arrhenius behaviour can be investigated by performing MD simulations at different temperatures.

6.2.6. Collective jumps

The large concentration of diffusing atoms in solid electrolytes, 31 mol/L in β-Li_3PS_4, is likely to result in interactions between the diffusing Li-atoms. This potentially causes collective jump processes [12], which may have a severe impact on macroscopic diffusion [34, 35].

Due to the high ion concentration and rapid movement of ions in a solid electrolyte the energy landscape experienced by an ion changes continuously [36, 37], due to its own movements and the movements of neighbouring ions. As shown schematically in Figure 6.4 the Coulombic repulsion of neighbouring atoms can make energy barriers disappear, or new local energy minima can be created. In this way the movement of one ion can cause the movement of a second ion, thus causing collective jumps.

MD simulations are a powerful tool for investigating complicated collective jump

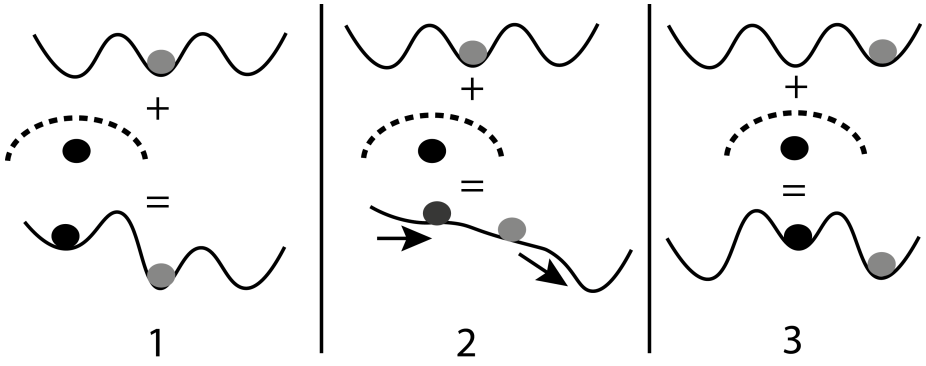

Figure 6.4: Schematic pictures of the energy landscape due to the crystal lattice (top) and the Coulomb repulsion of another Li-ion (middle) during a collective jump, giving the energy landscape experienced by the gray Li-ion (bottom). Step 1: situation before a collective jump. Step 2: the other ion moves to the right and makes the barrier between the gray ion and the next site disappear. Step 3: situation after the collective jump.

processes [1]. Knowing the position and time of jumps allows to determine if jumps are correlated in time and space, although determining the atomic process behind a correlated jump will require further study.

At present the spatial condition for correlated motion is assumed to be slightly larger than the largest jump distance between Li-sites in the crystal. For β-Li_3PS_4 this is 4.5 Å , in which 4 Å between the bc-planes is the largest jump distance.

For collective motions to occur atoms should move in the same direction within a certain time. Since atoms change their direction after a vibration, it is unlikely that atoms still show collective behaviour after a large number of vibrations. The time scale for collective motions should thus be on the order of an average atomic vibration, which is equal to the period of the attempt frequency ($\frac{1}{\nu^*}$ seconds).

A minimal condition for collective motion thus is that two jumps occur within the time

[1] The process which we call 'collective' jumps is also referred to as 'correlated' or 'concerted' jumps in the literature.

required for a single vibration, and therefore we use a time of $\frac{1}{\nu^*}$ seconds. This time condition thus gives a lower limit of the number of collective jumps, but this is enough for the present purpose of determining whether collective motions are of importance for diffusion. Clearly, the conditions that define transitions as collective are debatable and should be chosen carefully for each material.

6.2.7. Radial Distribution Functions

The atomic environment determines the forces and energy barriers that govern the behaviour of diffusing atoms. The Radial Distribution Function (RDF) can be used to reveal the density (g) of an element versus distance (r) with respect to another element during the MD-simulation:

$$g(r) = \frac{1}{n_{tot} A} \sum_{x=1}^{A} \sum_{y=1}^{B} \sum_{n=1}^{n_{tot}} g(r_{xy}(n)) \tag{6.10}$$

where A is the number of atoms of the element at the centre of the RDF, B the number of atoms of the other element, n_{tot} the total amount of simulation steps, and $r_{xy}(n)$ the distance between atom x and y at time step n.
Since the position of all atoms is available at all time steps of a MD simulation, RDF's can be readily obtained for any site, atom or element. For example, this has shown to be useful for Na_3PS_4, where the RDF's from MD simulations suggested that Na-vacancies are essential for increased Na-diffusion [10].

6.2.8. Summary

Summarising, if the crystallographic sites are known, detailed diffusion properties can be extracted from MD simulations. In principle a single MD simulation, in which each type of jump occurs a significant number of times, already provides detailed insight into diffusion, including the diffusion path, attempt frequency, jump rates, activation energies, collective motions, atomic environments, and the correlation factor.
For a thorough understanding MD simulations at several temperatures might be necessary, for instance in the case of non-Arrhenius behaviour, or to investigate the reliability of the results over a range of temperatures. Extracting the described information is beneficial for understanding of the diffusion process, allowing for a targeted approach to design and prepare new materials with enhanced properties, as will be demonstrated in this chapter for the Li-ion conductor β-Li_3PS_4.

6.3. Example: β-Li_3PS_4

Li_3PS_4 has been a well-known Li-ion conductor since the 1980's [38], but interest grew after experiments with nano-sized crystals showed a Li-ion conductivity of $1.6*10^{-4}$ S/cm [39], approaching the value that is required for solid state Li-ion batteries. Three polymorphs of Li_3PS_4 have been reported [40], the low-temperature γ-phase, the β-phase at intermediate temperatures, and the high temperature α-phase. The β-phase shows the highest room temperature conductivity of the three polymorphs [39], and is thus most interesting for application as a solid electrolyte. A beneficial property of β-Li_3PS_4 is its apparent stability against Li-metal [39], although DFT-calculations

report otherwise [7, 41]. Li_3PS_4 can be prepared via a solvent route [42, 43], resulting in a conductivity of $3.3^{*}10^{-4}$ S/cm [42], enabling coating of cathode materials. In this way no additional solid electrolyte material needs to be added in the cathodic mixture [43], resulting in a larger effective energy density in combination with a small interface resistance.
The β-phase of Li_3PS_4 is reported to crystallise in the Pnma space-group (no. 62) [38, 40, 44] in which Li-ions occupy 4b-, 4c- and 8d-positions. Studies [38, 40, 44] investigating the structure of β-Li_3PS_4 report significantly different Li-ion positions and occupancies. Neutron diffraction [44] indicates that the coordinates of the Li-ion 4c position strongly depend on temperature, potentially explaining the differences between X-ray diffraction studies [38, 40].
Based on the larger sensitivity to Li-ions of neutrons compared to X-rays, the Li-positions determined from neutron diffraction [44] at 413 K are used for the analysis of the present MD simulations on β-Li_3PS_4.

6.3.1. Effect of Li-vacancies and Li-interstitials

The introduction of Li-vacancies has been suggested to be beneficial for Li-ion conductivity in β-Li_3PS_4 [13], whereas the high ionic conductivity of the isostructural [45] compound $Li_{10}GeP_2S_{12}$ (= $Li_{3.33}Ge_{0.33}P_{0.67}S_4$) suggests that introducing extra Li-ions in β-Li_3PS_4 can also lead to an increased Li-ion conductivity. To study the effect of both Li-vacancies and Li-interstitials on the diffusion mechanism DFT MD simulations were performed for β-Li_3PS_4, β-$Li_{2.75}PS_4$, and β-$Li_{3.25}PS_4$ at 450, 600 and 750 K.
The compositions of β-$Li_{2.75}PS_4$ and β-$Li_{3.25}PS_4$ were chosen because this leads to two Li-vacancies/interstitials in the super cell. The two Li-vacancies/interstitials were divided over the two bc-planes present in the used super cell, in which the Li-ions show fast diffusion.
The introduction of Li-interstitials leads to a significant increase in the occupancy of 4c-sites, as shown in Figure 6.5 and reported by Lepley et al. [46].

Li-ion diffusion

The diffusion paths from simulations at 600 K, shown in Figure 6.7, demonstrate that diffusion takes place along the b-axis via 4b-4c jumps, via intraplane jumps along the c-axis through 4b-8d and 4c-8d jumps, and 8d-8d jumps in the a-direction are responsible for interplane jumps. As shown in Figure 6.7b in stoichiometric β-Li_3PS_4 the most jumps occur along the b-axis, followed by jumps in the bc-planes, and relatively few transitions occur between the bc-planes. This indicates that Li-ion diffusion occurs primarily within the bc-planes. The MSD for diffusion in the a-, b-, and c-direction shown in Figure 6.6 shows a different picture, with the b-direction having the largest MSD, followed by the c- and a-direction. This indicates that the correlation factor (equation 6.7) is lower for faster diffusion directions, similar to the results of Marcolongo et al. [22] in LGPS.
When Li-vacancies or Li-interstitials are introduced the Li-ion diffusion within the bc-plane remains similar to the stoichiometric composition β-Li_3PS_4, while the amount of interplane jumps increases significantly, resulting in three-dimensional diffusion.
The beneficial effect of the three-dimensional diffusion is reflected in the tracer diffu-

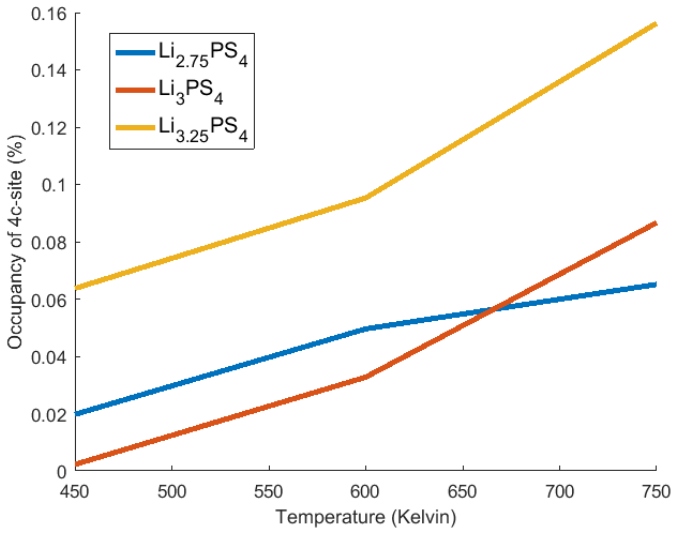

Figure 6.5: Occupancy of the 4c-site for the different simulated compositions and temperatures.

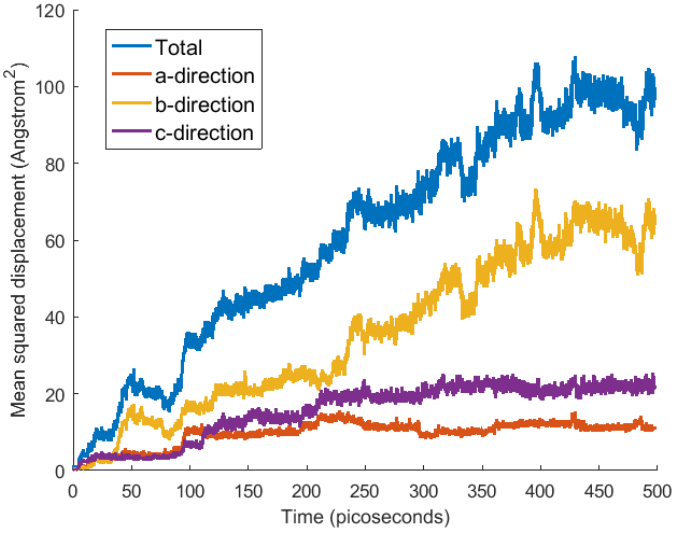

Figure 6.6: Mean squared displacement of Li-ions in β-Li_3PS_4 during the MD-simulation at 600 K in the a-, b-, and c-direction and the total MSD.

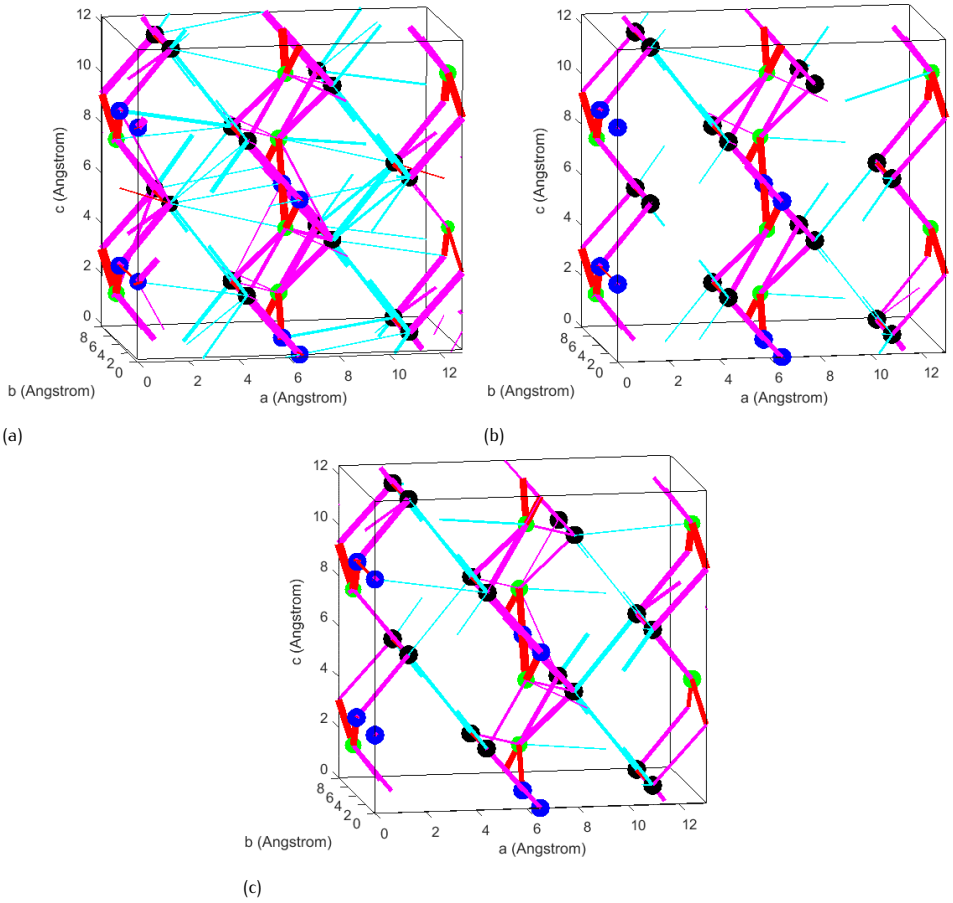

Figure 6.7: Jump diffusion paths at 600 K for (a) β-$Li_{2.75}PS_4$, (b) β-Li_3PS_4, and (c) β-$Li_{3.25}PS_4$. Li-ion sites are shown by: 4b = blue, 4c = green, and 8d = black. The jump types are shown by: 4b-4c = red, intralayer = pink, and interlayer = cyan, thicker lines correspond to larger jump rates.

sivity, shown in Figure 6.8. The Li-ion diffusivity in β-$Li_{2.75}PS_4$ is almost an order of magnitude larger than in β-Li_3PS_4. Introducing Li-interstitials by creating β-$Li_{3.25}PS_4$ also results in a larger diffusivity, especially at the lowest simulated temperature.
Based on the tracer diffusivity the conductivity of β-Li_3PS_4 is 10^{-2} S/cm at 450 K, comparable to impedance experiments [42] at the same temperature. Extrapolating the Li-ion diffusivity of β-Li_3PS_4 to 110 °C results in a Li-ion diffusivity of $1*10^{-8}$ cm^2/sec, close to the values reported by NMR experiments: $3.0*10^{-8}$ cm^2/sec at 100 °C [47] and between 10^{-6} and 10^{-8} cm^2/sec at 120 °C [48].
The results from the current MD simulations on β-Li_3PS_4 are comparable to the val-

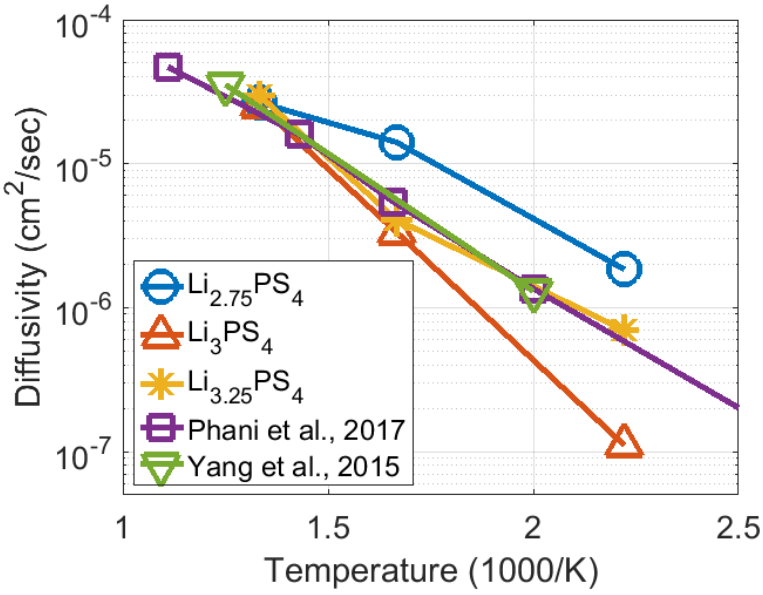

Figure 6.8: Tracer diffusivity from the current MD simulations, Phani et al. [13] and Yang et al. [49]

ues reported previously [13, 49], except at 450 K. This anomaly is most likely caused by the shorter simulation times of the previous studies, which can lead to an overestimation of the tracer diffusion [21], especially at low temperatures. At 750 K all the MD simulations show a similar value for the diffusivity, which can be explained by the melted lithium sub-lattice [13] at this temperature. After melting the lithium ordering over the different crystallographic sites disappears, which seems to have a larger impact than the deviating stoichiometries investigated here. The detrimental effect of Li-ordering has also been reported for the solid electrolyte $Li_7La_3Zr_2O_{12}$, in which Li-ordering can reduce the Li-conductivity by several orders of magnitude [50].

Jump rates

The differences in tracer diffusivities between the three compositions can be explained by the rate-limiting jump mechanism. The most frequent jump process is the 4b-4c transition, the rate of which is comparable between the three compositions, as shown

in Figure 6.9. However, to obtain three-dimensional diffusion paths in β-Li_3PS_4 interplane jumps are necessary, the rate of which is significantly different for the three compositions, also shown in Figure 6.9. With lower temperature these differences increase, and in β-Li_3PS_4 at 450 K no interplane jumps occurred.
Because two-dimensional diffusion processes have a smaller correlation factor compared to three-dimensional processes [18, 31, 51] the tracer diffusivity in β-Li_3PS_4 is significantly lower, even though the jump rate of the fastest diffusion process is similar.

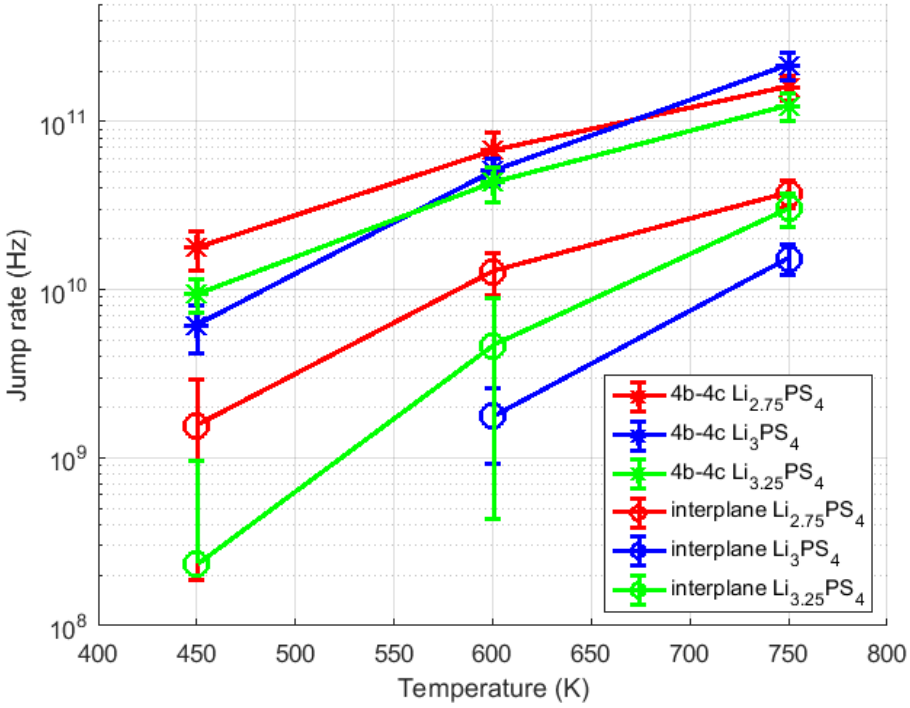

Figure 6.9: Jump rates for the 4b-4c and interplane jumps

Activation energies

The activation barriers for 4b-4c and intraplane jumps obtained from the MD simulations are shown in Figure 6.10. At 600 K the interplane 8d-8d jumps show activation energies of 0.40±0.02 eV for β-Li_3PS_4, 0.31±0.06 eV for β-$Li_{3.25}PS_4$, and 0.29±0.02 eV for β-$Li_{2.75}PS_4$. It should be noted that other jump processes also occur in the simulations, however, their significantly larger activation energy indicates that these will not contribute significantly to Li-ion diffusion and are therefore left out of the current analysis.
Over the simulated temperature range some activation energies remain constant, while others show significant changes, as shown in Figures 6.11 and 6.12.

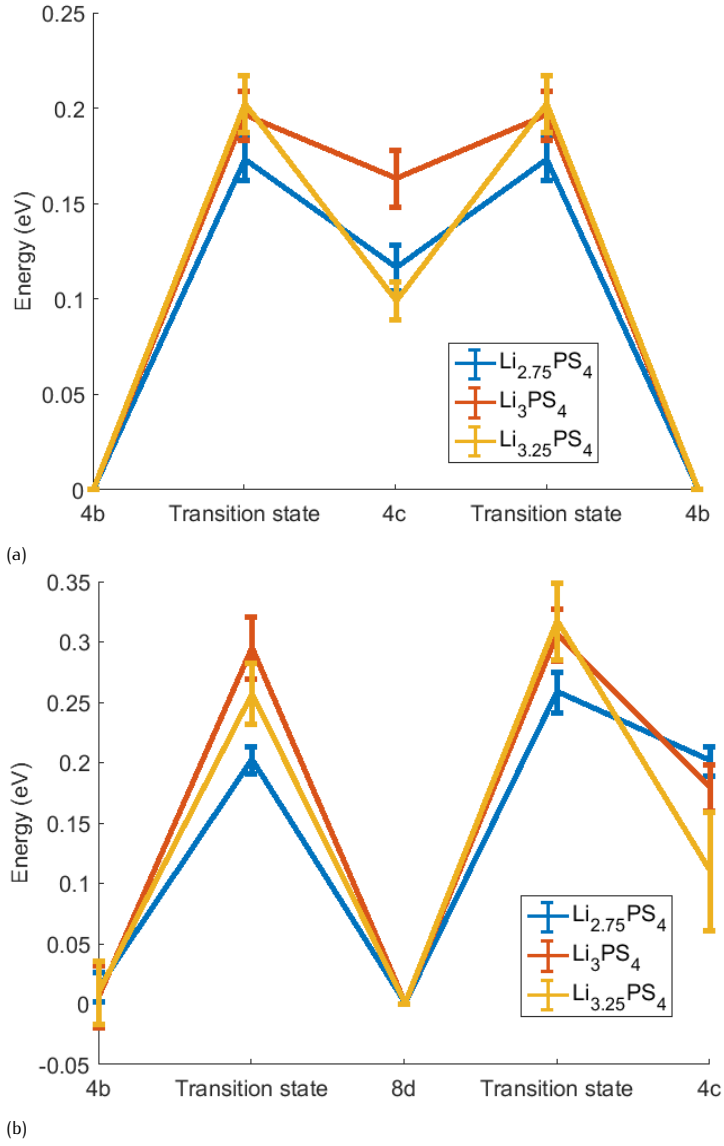

Figure 6.10: Activation energy at 600 K for (a) 4b-4c, and (b) intraplane jumps.

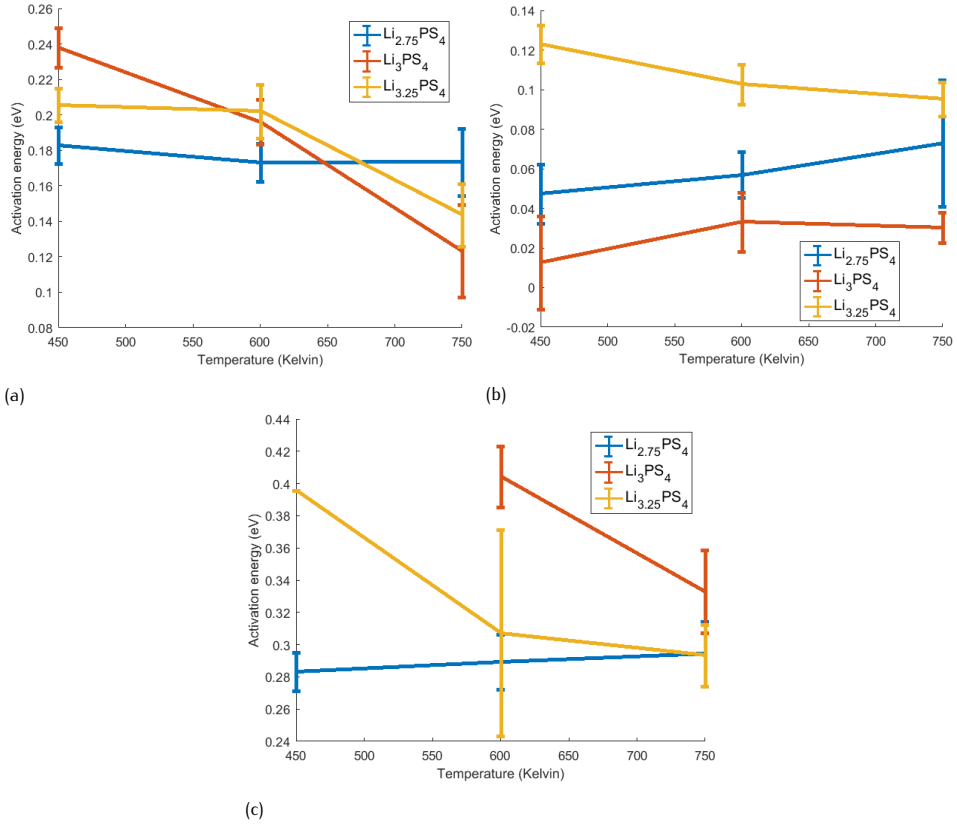

Figure 6.11: Activation energies over the simulated temperature range for the b-axis jumps: (a) 4b-4c, (b) 4c-4b, and (c) interplane 8d-8d. The missing point for the 8d-8d jump in Li_3PS_4 at 450 K is because this jump did not occur in the MD simulation.

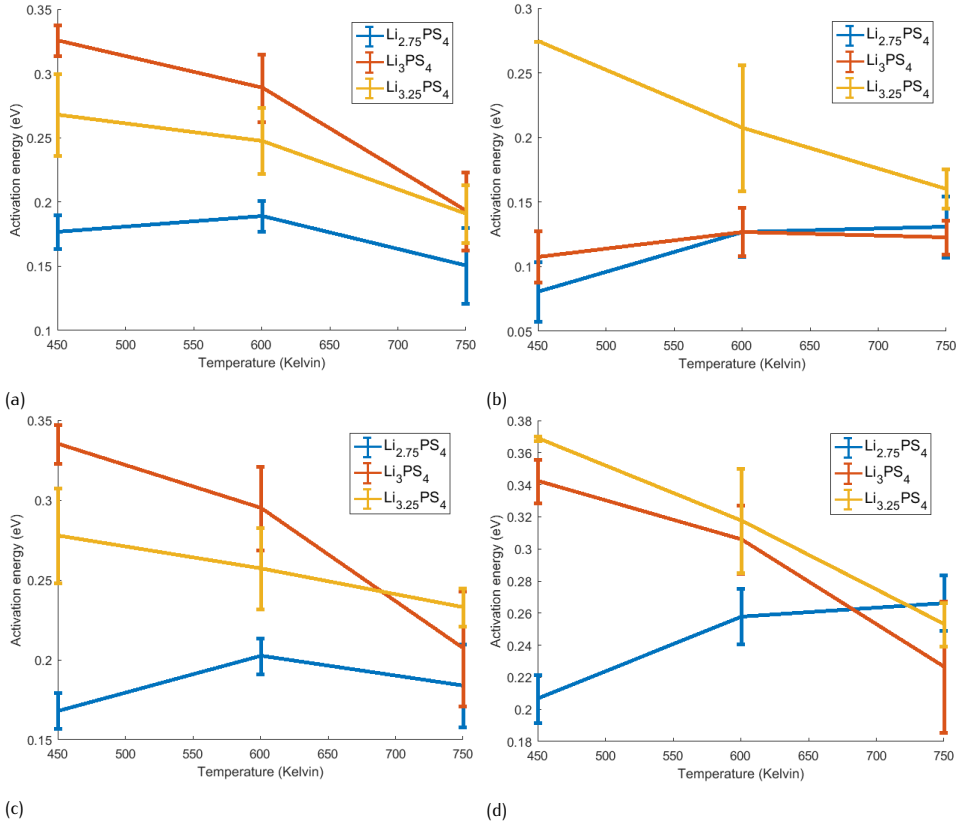

Figure 6.12: Activation energies over the simulated temperature range for the c-axis jumps: (a) 4b-8d,(b) 4c-8d, (c) 8d-4b, and (d) 8d-4c.

The changes in activation energies could be caused by non-Arrhenius behaviour of some types of jumps, but the loss of Li-ordering at 750 K might also be a reason for the changing activation energies. Furthermore, the different compositions sometimes show differing behaviour for the same type of jump. To say something about the (non-)Arrhenius behaviour of β-Li_3PS_4 further study is required.
To validate the activation energies from MD simulations, comparison with experimental values is important, however, a wide distribution in values is reported based on electrochemical experiments: 0.16 [40], 0.32 [42], 0.36 [39], and 0.47 [43] eV. NMR experiments resulted in activation energies of 0.40 eV for macroscopic diffusion and 0.09 eV for local jumps [48]. Given this wide distribution of values a comparison of experimental activation energies with the present simulations seems unreasonable.
Simulations also report a wide range of activation energies. NEB calculations on β-Li_3PS_4 report activation energies of 0.3 eV along the a-axis and 0.2 eV along the b- and c-axis [46, 52], while other NEB calculations [53] report 0.26 eV along the a- and b-axis and 0.08 eV for collective Li-ion jumps in the b-direction, bond-valence calculations report values of 1.0 eV along the a-axis and 0.8 eV in the bc-plane [54], and an Arrhenius fit to MD-simulations [13] gives an activation energy of 0.35 eV . The results from NEB calculations and MD simulations are comparable, while bond-valence calculations appear to overestimate the activation energy. The activation energies from the present MD simulations indicate that diffusion along the b-axis is most facile, followed by diffusion along the c-axis, and along the a-axis diffusion is most difficult, in agreement with results from neutron diffraction [44].

Collective jump processes

Given the large lithium concentration of 31 mol/L in β-Li_3PS_4 Li-ions can be expected to interact strongly with each other. Yang et al. [53] reported the presence of collective jumps in β-Li_3PS_4 by showing that the activation energy for diffusion along the b-axis is just 0.08 eV for two Li-ions moving collectively, while it is 0.26 eV for a single Li-ion.
To determine the importance of collective jumps in the present MD simulations the amount of collective jumps has been determined as described in the Collective jumps section. Comparison of the collective jumps with the total amount of jumps reveals that the percentage of collective jumps strongly depends on the temperature and Li-concentration, as shown in Figure 6.13. The percentage of collective jumps displays a strong increase with temperature, with 65 to 80 % of the jumps occurring collectively at 750 K. Although at 450 K the simulations show less collective jumps, still 24 % of the jumps is collective in $Li_{2.75}PS_4$.
Surprisingly, the lower Li-concentration in $Li_{2.75}PS_4$ leads to a higher percentage of collective jumps. As shown in Figure 6.9 the jump rate is similar in all three compositions, indicating that collective jumps occur more frequently when there are more Li-vacancies, but the mechanism behind this effect is unclear.
To study the effect of the time condition on the determination of collective jumps the time condition was varied between 0.25 and 5 times the attempt frequency, the results of which are shown in Figure 6.14. This shows that the amount of collective jumps determined using the presented method strongly depends on the specified time condition. If the collective jumps would purely be due to coincidences a linear relationship between the number of collective jumps and the time condition is expected, but this is

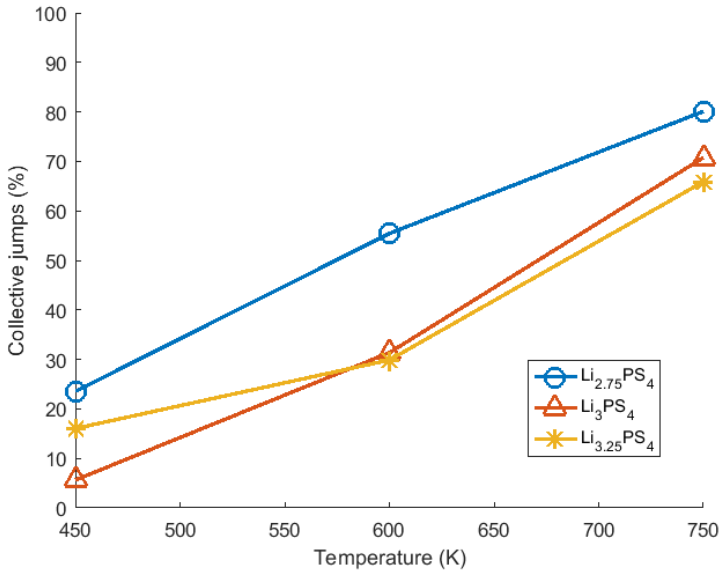

Figure 6.13: Percentage of collective jumps in the MD simulations

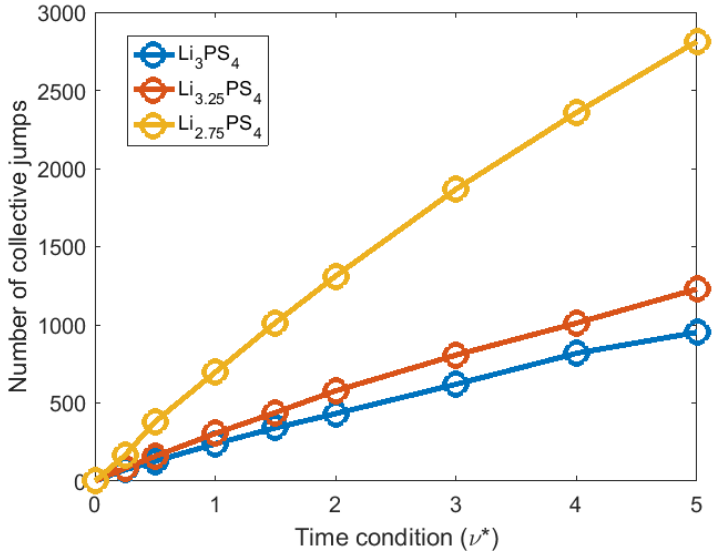

Figure 6.14: Number of collective jumps versus the time condition (in units of the attempt frequency).

not observed in Figure 6.14. When using a shorter time condition the number of collective jumps increases more rapidly as when using longer time conditions, indicating that collective jumps are occurring. However, the strong dependence of this analysis on the time condition specified for collective jumps shows that quantifying the amount of collective jumps will require a more thorough understanding of collective behaviour before conclusions can be drawn. However, the large percentage of collective jumps indicates that collective jump processes may have a significant effect on the Li-ion diffusion in β-Li_3PS_4, especially at elevated temperatures. Although the larger amount of collective jumps is also caused by the higher amount of jumps at elevated temperatures, the movements of a Li-ion will be influenced by jumps of other Li-ions nearby, and increasing the temperature thus increases the amount of collective motion.
In Figure 6.15 the number of collective jumps are shown per combination of jump type during the MD simulation at 600 K for the different compositions. This shows that in β-Li_3PS_4 the collective jumps are primarily simultaneous 4c-4b jumps and simultaneous 4b-4c jumps. In $Li_{3.25}PS_4$ collective 4b-4c and 4c-4b jumps also occur most frequently, but additionally 4b-8d jumps collective with 4b-4c jumps occur and collective interplane jumps are predicted. In the simulations of $Li_{2.75}PS_4$ different collective behaviour is observed, with the combination of 4b-8d jumps and 4b-4c jumps occurring most frequently. Collective 4b-4c jumps also occur frequently, but significantly less compared to the other compositions.
Collective jumps involving more than two Li-ions also occur in the current MD simulations, in some cases involving up to 5 atoms. The collective movement of multiple atoms is complex and difficult to analyse. However, it should be anticipated that collective motion of several ions induces large ionic conductivities, as observed in $Li_{10}GeP_2S_{12}$ [35], making this an interesting and relevant research area.

Attempt frequency

The attempt frequencies obtained from the MD simulations are shown in Figure 6.16a. Using the presented method of obtaining attempt frequencies results in values between $7.6*10^{12}$ and $9.3*10^{12}$ Hz, comparable to reported attempt frequencies, between 10^{12} and 10^{13} Hz, for other materials by experiments [23, 55] and DFT calculations [25, 26]. This consistency indicates that the presented method of determining the attempt frequency from MD-simulations, by a straightforward Fourier transformation of the ionic velocity, can be used to determine the attempt frequency.
Figure 6.16a demonstrates that the attempt frequency decreases with increasing temperature, this decrease with increasing temperature can be understood by the change in the vibrational amplitude, shown in Figure 6.16b. For $Li_{3.25}PS_4$ and Li_3PS_4 the vibrational amplitude increases by approximately 35% between 450 and 750 K, while the speed of the atoms increases by just 29% (based on: $E = \frac{1}{2}mv^2$). The average vibration time therefore increases, leading to a decreasing attempt frequency. Furthermore, as shown in Figure 6.16 the attempt frequency and vibration amplitude in $Li_{2.75}PS_4$ differ by approximately 10% from the other two compositions. This effect can be explained by the lower Li-concentration, which leads to less repulsive interactions between Li-ions, thus allowing for bigger vibrations and a lower attempt frequency.
This example demonstrates that there can be a significant temperature dependence on the attempt frequency and that relatively small changes in the crystal structure can

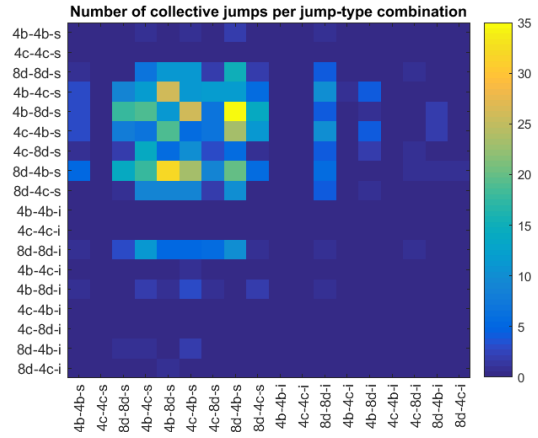

(a) β-Li2.75PS_4

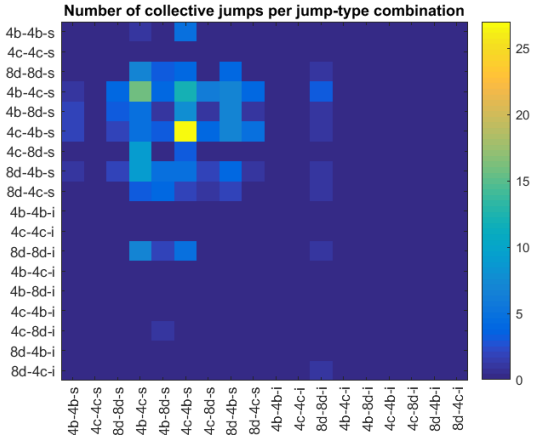

(b) β-Li3PS_4

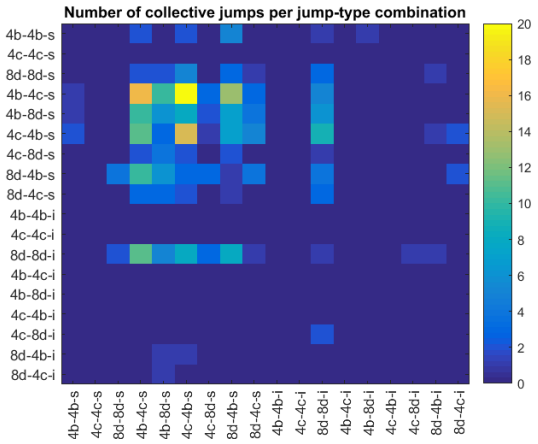

(c) β-Li3.25PS_4

Figure 6.15: Amount of collective jumps for all the jump combinations from MD simulations at 600 K in (a) β-Li2.75PS_4, (b) β-Li3PS_4, and (c) β-Li3.25PS_4. '-s' means that a jump is within the same layer, '-i' means an interlayer jump. Please note that the color bars are different for the different compositions

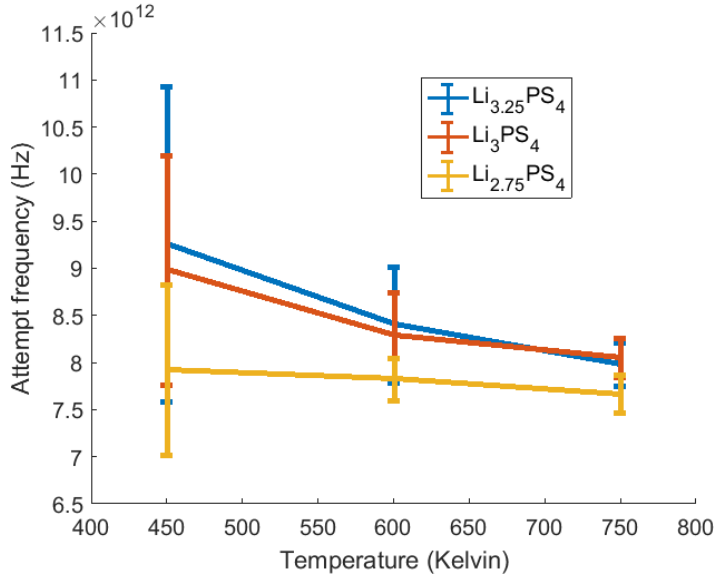

(a)

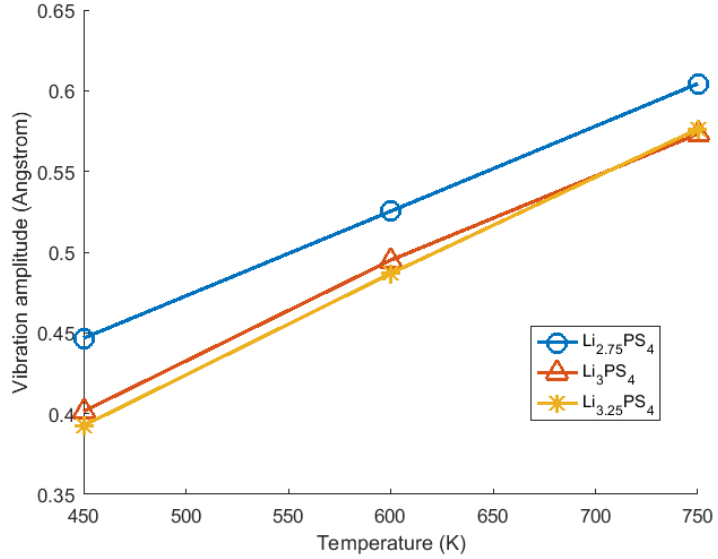

(b)

Figure 6.16: (a) Attempt frequencies and (b) vibration amplitudes from the MD-simulations.

have a significant effect on the attempt frequency. Thereby the presented analysis indicates that consideration of the attempt frequency and its dependence on structure and temperature is of significant importance in quantifying and understanding ionic diffusion.

6.3.2. Effects of doping

The MD simulations on β-$Li_{3.25}PS_4$ show that creating Li-interstitials in β-Li_3PS_4 significantly increases three dimensional diffusion, raising the macroscopic Li-ion conductivity, in line with experimental work [45]. Li-vacancies also increase three dimensional diffusion, and the MD simulations indicate significantly larger Li-ion conductivity compared to the introduction of Li-interstitials. However, we are unaware of work which has explored the impact of introducing Li-vacancies, through doping, on the Li-ion diffusion in β-Li_3PS_4. To determine the impact of introducing Li-vacancies by doping MD simulations were performed on β-$Li_{2.75}PS_{3.75}Br_{0.25}$.

Additionally, the impact of oxygen doping is investigated, since this is also reported as a strategy to improve the Li-ion diffusivity [47, 52, 54]. However, O-doping does not change the Li-content. It has been proposed that the smaller radius of O^{2-} in comparison to S^{2-} opens up a diffusion path along the a-axis, but the mechanism of the oxygen induced larger Li-ion diffusivity remains unclear. To gain further understanding of how oxygen doping increases the Li-ion diffusivity MD simulations on β-$Li_3PS_{3.75}O_{0.25}$ were performed.

The structures with dopants were created by replacing two S-atoms by Br- and O-atoms, respectively. The dopants were placed at the maximum possible distance apart from each other in the supercell, to minimise the interaction between dopant-atoms. The introduction of the dopant atoms causes only minor changes in the lattice parameters, less than 2% in both cases. The dopants only cause local distortions in the crystal, as shown in Figure 6.17, which is consistent with previous calculations on O-doped β-Li_3PS_4 [52].

At small distances the RDF's for the S-atoms are overlapping each other in the sulphur and phosphor distributions, and remain very similar at larger distances. And even though the Br- and O-atoms occupy the same crystallographic positions as the S-atoms, their RDF's differ significantly, especially in the first coordination shell. The lithium distribution shows small differences in the case of Br-doping, but this can be explained by the lower Li-concentration in this structure.

Predicting the stability of solid electrolytes is hard, as shown by the varying decomposition voltages and decomposition products between papers which calculated the stabilities of various solid state electrolytes [7, 41], and it becomes even more complicated when including dopants. In this chapter we focus on which diffusion properties can be determined from MD-simulations on solid electrolytes, and determination of the stability of the doped structures is thus beyond the scope of this chapter.

However, for the O-doped β-Li_3PS_4 it has been shown that the addition of oxygen is beneficial for the stability [52]. And the Na-analogue (Na_3PS_4) of Li_3PS_4 with halogen-doping has been made experimentally [5] and is thus shown to be (meta)stable, and we expect that β-Li_4PS_4 with Br-doping is also (meta)stable.

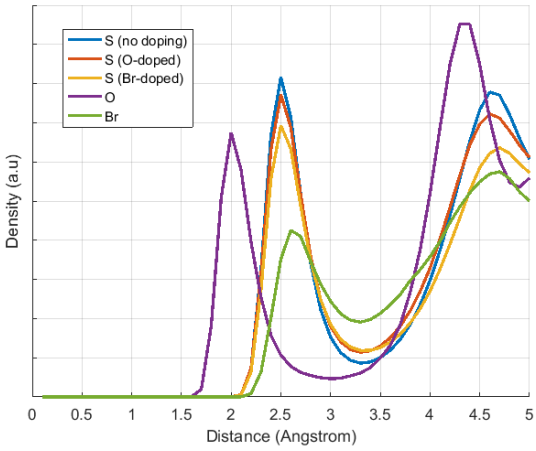

(a)

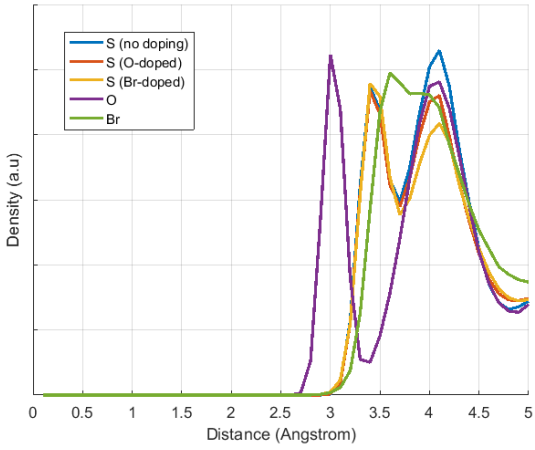

(b)

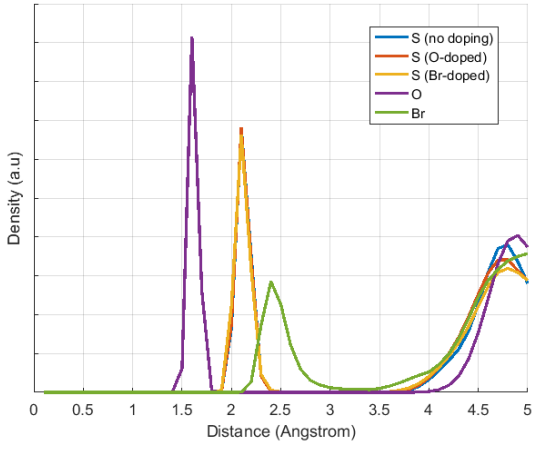

(c)

Figure 6.17: Radial distribution functions of β-Li_3PS_4, β-$Li_3PS_{3.75}O_{0.25}$ and β-$Li_{2.75}PS_{3.75}Br_{0.25}$ at 600 K around (a) Lithium, (b) Sulphur, and (c) Phosphor.

Br-doping

The jump diffusion path from the MD-simulation of β-$Li_{2.75}PS_{3.75}Br_{0.25}$ is shown in Figure 6.18a. As should be anticipated from the simulations of β-$Li_{2.75}PS_4$, Figure 6.18a shows that Br-doping significantly increases the amount of three-dimensional diffusion. In β-$Li_{2.75}PS_{3.75}Br_{0.25}$ the tracer diffusivity results in $1.56*10^{-6}$, $1.01*10^{-5}$, and $3.71*10^{-5}$ cm^2/sec at 450, 600 and 750 K, respectively, comparable to the diffusivities of β-$Li_{2.75}PS_4$. The activation energies for diffusion along the bc-plane in the Br-doped composition at 600 K, shown in Figure 6.19, differ by just 0.02 eV from the MD simulation with Li-vacancies. The activation energy for interplane jumps is 0.29±0.03 eV in β-$Li_{2.75}PS_{3.75}Br_{0.25}$ and 0.29±0.02 eV in β-$Li_{2.75}PS_4$.
The similar activation energies in β-$Li_{2.75}PS_4$ and β-$Li_{2.75}PS_{3.75}Br_{0.25}$ indicates that the primary cause of the high Li-ion diffusivity in Br-doped β-Li_3PS_4 are the Li-vacancies. For other dopants that introduce Li-vacancies similar results are thus expected, suggesting that there are various ways to increase the Li-ion diffusivity in β-Li_3PS_4.

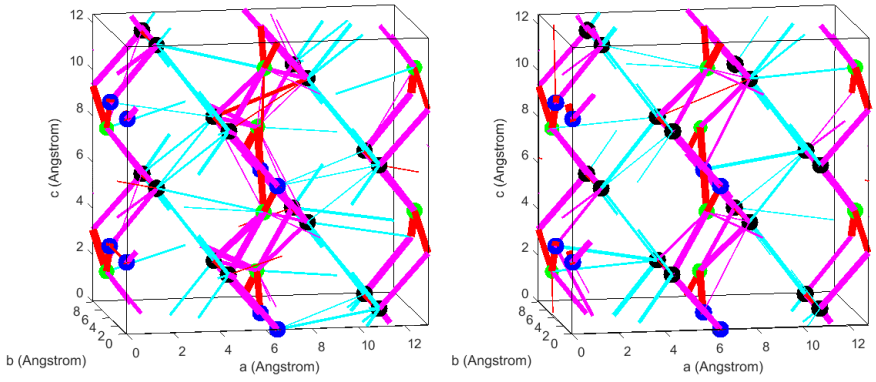

(a) (b)

Figure 6.18: Jump diffusion paths at 600 K for (a) β-$Li_{2.75}PS_{3.75}Br_{0.25}$ and (b) β-$Li_3PS_{3.75}O_{0.25}$. Li-ion sites are shown by: 4b = blue, 4c = green, and 8d = black. The jump types are shown by: 4b-4c = red, intralayer = pink, and interlayer = cyan, thicker lines correspond to larger jump rates.

O-doping

The jump diffusion paths from the present MD-simulations on β-$Li_3PS_{3.75}O_{0.25}$, shown in Figure 6.18b, demonstrate that O-doping also increases three-dimensional diffusion, as was predicted [52, 54]. Compared to β-Li_3PS_4 doping with oxygen leads to a larger Li-ion diffusivity, and tracer diffusivities of $6.96*10^{-7}$, $7.59*10^{-6}$, and $2.52*10^{-5}$ cm^2/sec at 450, 600 and 750 K, respectively. The introduction of oxygen results in smaller activation energies compared to β-Li_3PS_4, as shown in Figure 6.19. The biggest impact is observed for the interplane jumps, which have an activation energy of just 0.31±0.03 eV in β-$Li_3PS_{3.75}O_{0.25}$. NEB calculations on β-Li_3PS_4 with O-doping [52] show activation energies of approximately 0.2 eV in the b- and c-direction, which is comparable to the results presented in Figure 6.19. In the a-direction the activation

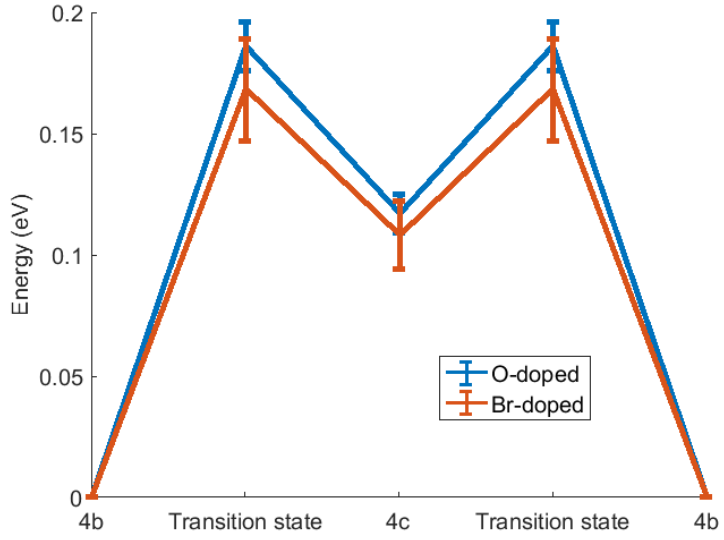

(a)

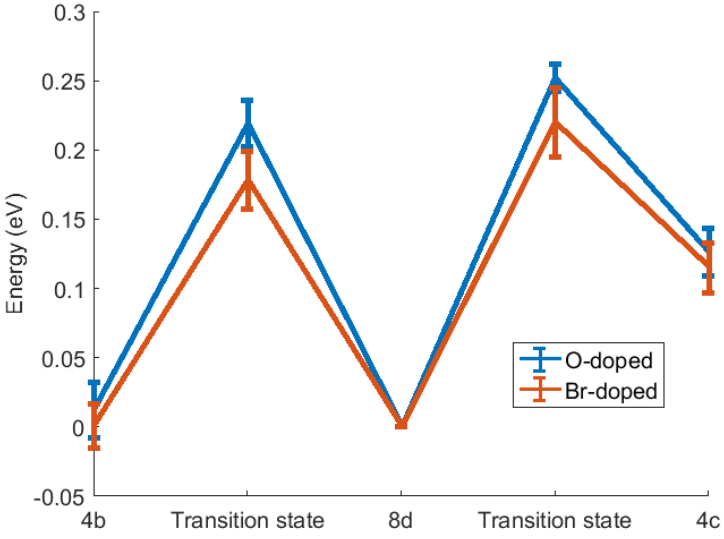

(b)

Figure 6.19: Activation energies at 600 K in Br- and O-doped β-Li_3PS_4 for (a) 4b-4c, and (b) intraplane jumps.

energy is 0.2 eV close to the O-dopant, and 0.3 eV far away from the O-dopant. From the MD simulations no distinction is made between jumps in the a-direction close or far from the O-dopant, but the 0.31±0.03 eV is close to the value reported by the NEB calculations.

It is surprising that the activation energies for the O-doped structure are comparable to the Li-rich β-$Li_{3.25}PS_4$, even though the introduction of oxygen does not affect the Li-concentration. To investigate this the radial distribution functions (RDF's) for oxygen and sulphur in β-$Li_3PS_{3.75}O_{0.25}$ are calculated using Equation 6.10 and shown in Figure 6.20. The smaller ionic radius of oxygen [56] results in a smaller O-Li distance compared to the S-Li distance. However, the Li-density of the first coordination shell in the RDF is significantly lower around the O-atoms. Integrating the Li-density up to 3.5 Å shows that (on average) there are 2.9 Li-atoms in the first coordination shell of O-atoms, and 3.5 Li-atoms in the first coordination shell of S-atoms.

This implies that it is unfavourable for Li-ions to be near the O-atoms in β-$Li_3PS_{3.75}O_{0.25}$, and these Li-ions must be accommodated elsewhere within the crystal structure. Oxygen-doping thus changes the distribution of Li-ions in the crystal, which is shown to be beneficial for the Li-ion diffusivity in β-Li_3PS_4.

It is usually assumed that a higher polarisability leads to higher diffusivity [57] via lower activation energies caused by lattice softening [23]. In the case of β-$Li_3PS_{3.75}O_{0.25}$ the higher diffusivity caused by O-atoms, which have lower polarisability compared to S-atoms, demonstrating that the opposite can also occur. Integrating the RDF's in Figure 6.20 shows that there are less Li-ions near the O-atoms as near the S-atoms, which indicates that the site-energy near the O-atoms is higher. If the transitions state energy stays the same this lowers the activation energy. In this case the less polarisable O-atoms are thus beneficial for Li-ion diffusion.

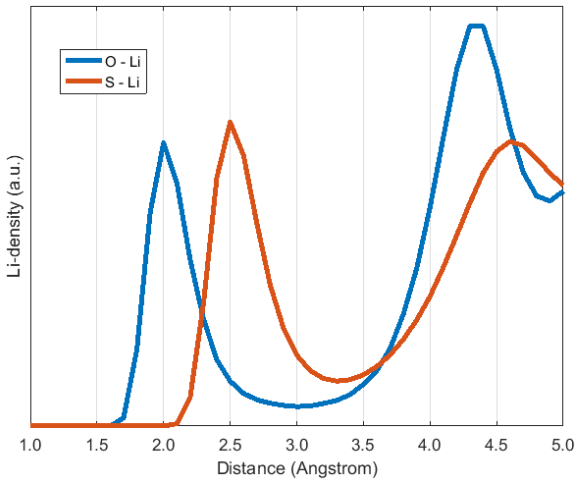

Figure 6.20: O-Li and S-Li distribution in β-$Li_3PS_{3.75}O_{0.25}$ at 600 K, calculated using Equation 6.10.

6.4. Conclusions

The present approach demonstrates that from a single MD simulation key properties for ionic diffusion can be obtained, through which a thorough understanding of diffusion can be developed. The thorough analysis of MD simulations presented is a general approach that can be applied to all crystalline ionic conductors, which can help to build understanding of diffusional processes in solid state electrolytes, and provide direction to the design of new and improved solid electrolyte materials. The Matlab-code developed for the analysis of MD simulations is freely available on-line [17]. The example of DFT MD simulations on β-Li_3PS_4 indicates that Li-ion jumps between bc-layers limit the macroscopic conductivity. Adding Li-interstitials or Li-vacancies significantly promotes these transitions, increasing macroscopic Li-ion diffusion. Li-vacancies can be introduced through Br-doping at the sulphur sites, which is predicted to result in an order of magnitude larger Li-ion conductivity in β-Li_3PS_4. Furthermore, it is shown that oxygen-doping at the sulphur site changes the Li-distribution in the crystal, rationalizing the increased Li-ion diffusivity that has been reported.

6.5. DFT calculations

The DFT simulations were performed using VASP [58], using the GGA approximation [59] and the PAW-PBE basis set [60]. A cut-off energy of 400 eV was used for simulations containing oxygen, and 280 eV for the other simulations. The β-Li_3PS_4-phase crystallises in the orthorhombic space-group Pnma (no. 62), with lattice parameters of a = 12.82, b = 8.22, and c = 6.12 Å at 637 K [40]. The crystal structure as measured by Homma et al. [40] was used as a starting point for the structure minimisations. A 1x1x2 super cell was used in the calculations, testing of finite size effects was not done due to computational limitations. The fractional site-occupancies reported experimentally were approximated as much as possible in the super cell, while maximising the Li-Li distances. After minimisation without symmetry restrictions the lattice angles were close to 90° in all cases, and the lattice parameters changed by less than 2%, with the a- and c-parameters showing a small increase, while the b-parameter decreased slightly. During the minimisations a k-point mesh of 4x6x4 was used, which was reduced to a k-point mesh of 1x2x1 for the MD simulations. The total simulation time of the MD simulations was 500 picoseconds., with time-steps of 2 femtoseconds. The first 2.5 picoseconds were used as equilibration time and were thus not used for the analysis. Simulations were performed in the NVT ensemble, with temperature scaling after every 50 time-steps.

References

[1] C. Bauer, J. Hofer, H.J. Althaus, A. Del Duce, and A. Simons. The environmental performance of current and future passenger vehicles: life cycle assessment based on a novel scenario analysis framework. *Appl. Energy*, 157:871–883, 2015. doi: 10.1016/j.apenergy.2015.01.019.

[2] B.V. Lotsch and J. Maier. Relevance of solid electrolytes for lithium-based

batteries: a realistic view. *J. Electroceram.*, 38(2-4):128–141, 2017. doi: 10.1007/s10832-017-0091-0.

[3] T. Placke, R. Kloepsch, S. Dühnen, and M. Winter. Lithium ion, lithium metal, and alternative rechargeable battery technologies: the odyssey for high energy density. *J. Solid State Electrochem.*, 21(7):1939–1964, 2017. doi: 10.1007/s10008-017-3610-7.

[4] X.C. Lu, G.G. Xia, J.P. Lemmon, and Z.G. Yang. Advanced materials for sodium-beta alumina batteries: status, challenges and perspectives. *J. Power Sources*, 195(9): 2431–2442, 2010. doi: 10.1016/j.jpowsour.2009.11.120.

[5] I.H. Chu, C.S. Kompella, H. Nguyen, Z. Zhu, S. Hy, Z. Deng, Y.S. Meng, and S.P. Ong. Room-temperature all-solid-state rechargeable sodium-ion batteries with a Cl-doped Na_3PS_4 superionic conductor. *Sci. Rep.*, 6:33733, 2016. doi: 10.1038/srep33733.

[6] S. Muy, J.C. Bachman, L. Giordano, H.H. Chang, D.L. Abernathy, D. Bansal, O. Delaire, S. Hori, R. Kanno, F. Maglia, S. Lupart, P. Lamp, and Y. Shao-Horn. Tuning mobility and stability of lithium ion conductors based on lattice dynamics. *Energy Environ. Sci.*, 11(4):850–859, 2018. doi: 10.1039/c7ee03364h.

[7] Y. Zhu, X. He, and Y. Mo. Origin of outstanding stability in the lithium solid electrolyte materials: Insights from thermodynamic analyses based on first-principles calculations. *ACS Appl. Mater. Interfaces*, 7(42):23685–23693, 2015. doi: 10.1021/acsami.5b07517.

[8] C. Tealdi, J. Heath, and M.S. Islam. Feeling the strain: enhancing ionic transport in olivine phosphate cathodes for Li- and Na-ion batteries through strain effects. *J. Mater. Chem. A*, 4(18):6998–7004, 2016. doi: 10.1039/c5ta09418f.

[9] Z. Deng, B. Radhakrishnan, and S.P. Ong. Rational composition optimization of the lithium-rich $Li_3OCl_{1-x}Br_x$ anti-perovskite superionic conductors. *Chem. Mater.*, 27(10):3749–3755, 2015. doi: 10.1021/acs.chemmater.5b00988.

[10] N.J.J. de Klerk and M. Wagemaker. Diffusion mechanism of the sodium-ion solid electrolyte Na_3PS_4 and potential improvements of halogen doping. *Chem. Mater.*, 28(9):3122–3130, 2016. doi: 10.1021/acs.chemmater.6b00698.

[11] N. Adelstein and B.C. Wood. Role of dynamically frustrated bond disorder in a Li^+ superionic solid electrolyte. *Chem. Mater.*, 28(20):7218–7231, 2016. doi: 10.1021/acs.chemmater.6b00790.

[12] A. Vasileiadis and M. Wagemaker. Thermodynamics and kinetics of Na-ion insertion into hollandite-TiO_2 and O3-layered $NaTiO_2$: an unexpected link between two promising anode materials for Na-ion batteries. *Chem. Mater.*, 29(3):1076–1088, 2017. doi: 10.1021/acs.chemmater.6b03928.

[13] G.K. Phani Dathar, J. Balachandran, P.R.C. Kent, A.J. Rondinone, and P. Ganesh. Li-ion site disorder driven superionic conductivity in solid electrolytes: a first-principles investigation of β-Li_3PS_4. *J. Mater. Chem. A*, 5(3):1153–1159, 2017. doi: 10.1039/c6ta07713g.

[14] J. Yang and J.S. Tse. Li ion diffusion mechanisms in $LiFePO_4$: an ab initio molecular dynamics study. *J. Phys. Chem. A*, 115(45):13045–13049, 2011. doi: 10.1021/jp205057d.

[15] N.J.J. de Klerk, I. Rosłoń, and M. Wagemaker. Diffusion mechanism of Li argyrodite solid electrolytes for Li-ion batteries and prediction of optimized halogen doping: the effect of Li vacancies, halogens, and halogen disorder. *Chem. Mater.*, 28(21): 7955–7963, 2016. doi: 10.1021/acs.chemmater.6b03630.

[16] S. Ganapathy, A. Vasileiadis, J.R. Heringa, and M. Wagemaker. The fine line between a two-phase and solid-solution phase transformation and highly mobile phase interfaces in spinel $Li_{4+x}Ti_5O_{12}$. *Adv. Energy Mater.*, page 1601781, 2016. doi: 10.1002/aenm.201601781.

[17] N.J.J. de Klerk. MD analysis with Matlab, 2018. URL https://bitbucket.org/niekdeklerk/md-analysis-with-matlab.

[18] R.J. Friauf. Correlation effects for diffusion in ionic crystals. *J. Appl. Phys.*, 33(1): 494–505, 1962. doi: 10.1063/1.1777148.

[19] S.P. Ong, Y. Mo, W.D. Richards, L. Miara, H.S. Lee, and G. Ceder. Phase stability, electrochemical stability and ionic conductivity of the $Li_{10\pm1}MP_2X_{12}$(M = Ge, Si, Sn, Al or P, and X = O, S or Se) family of superionic conductors. *Energy Environ. Sci.*, 6(1):148–156, 2013. doi: 10.1039/c2ee23355j.

[20] A. Urban, D.H. Seo, and G. Ceder. Computational understanding of Li-ion batteries. *npj Comp. Mater.*, 2:16002, 2016. doi: 10.1038/npjcompumats.2016.2.

[21] X. He, Y. Zhu, A. Epstein, and Y. Mo. Statistical variances of diffusional properties from ab initio molecular dynamics simulations. *npj Comp. Mater.*, 4(1):18, 2018. doi: 10.1038/s41524-018-0074-y.

[22] A. Marcolongo and N. Marzari. Ionic correlations and failure of Nernst-Einstein relation in solid-state electrolytes. *Phys. Rev. Mater.*, 1(2):025402, 2017. doi: 10.1103/PhysRevMaterials.1.025402.

[23] M.A. Kraft, S.P. Culver, M. Calderon, F. Bocher, T. Krauskopf, A. Senyshyn, C. Dietrich, A. Zevalkink, J. Janek, and W.G. Zeier. Influence of lattice polarizability on the ionic conductivity in the lithium superionic argyrodites Li_6PS_5X (X = Cl, Br, I). *J. Am. Chem. Soc.*, 139(31):10909–10918, 2017. doi: 10.1021/jacs.7b06327.

[24] K. Shimakawa and M. Aniya. Dynamics of atomic diffusion in condensed matter: origin of the Meyer-Neldel compensation law. *Monatsh. Chem.*, 144(1):67–71, 2012. doi: 10.1007/s00706-012-0835-0.

[25] J. Koettgen, T. Zacherle, S. Grieshammer, and M. Martin. Ab initio calculation of the attempt frequency of oxygen diffusion in pure and samarium doped ceria. *Phys. Chem. Chem. Phys.*, 19(15):9957–9973, 2017. doi: 10.1039/c6cp04802a.

[26] C.D. Versteylen, N.H. van Dijk, and M.H.F. Sluiter. First-principles analysis of solute diffusion in dilute bcc Fe-X alloys. *Phys. Rev. B*, 96(9):094105, 2017. doi: 10.1103/PhysRevB.96.094105.

[27] A. Van der Ven, G. Ceder, M. Asta, and P.D. Tepesch. First-principles theory of ionic diffusion with nondilute carriers. *Phys. Rev. B*, 64(18):184307, 2001. doi: 10.1103/PhysRevB.64.184307.

[28] C. Chen, Z. Lu, and F. Ciucci. Data mining of molecular dynamics data reveals Li diffusion characteristics in garnet $Li_7La_3Zr_2O_{12}$. *Sci. Rep.*, 7:40769, 2017. doi: 10.1038/srep40769.

[29] C. Yu, S. Ganapathy, N.J.J. de Klerk, E.R.H. van Eck, and M. Wagemaker. Na-ion dynamics in tetragonal and cubic Na_3PS_4, a Na-ion conductor for solid state Na-ion batteries. *J. Mater. Chem. A*, 4(39):15095–15105, 2016. doi: 10.1039/c6ta05896e.

[30] C. Yu, S. Ganapathy, N.J.J. de Klerk, I. Rosłoń, E.R.H. van Eck, A.P. Kentgens, and M. Wagemaker. Unravelling Li-ion transport from picoseconds to seconds: bulk versus interfaces in an argyrodite Li_6PS_5Cl-Li_2S all-solid-state Li-ion battery. *J. Am. Chem. Soc.*, 138(35):11192–11201, 2016. doi: 10.1021/jacs.6b05066.

[31] G. Murch. The Haven ratio in fast ionic conductors. *Solid State Ionics*, 7(3): 177–198, 1982. doi: 10.1016/0167-2738(82)90050-9.

[32] Y. Okada, M. Ikeda, and M. Aniya. Non-Arrhenius ionic conductivity in solid electrolytes: a theoretical model and its relation with the bonding nature. *Solid State Ionics*, 281:43–48, 2015. doi: 10.1016/j.ssi.2015.08.020.

[33] G.H. Vineyard. Frequency factors and isotope effects in solid state rate processes. *J. Phys. Chem. Solids*, 3(1-2):121–127, 1957. doi: 10.1016/0022-3697(57)90059-8.

[34] X. He, Y. Zhu, and Y. Mo. Origin of fast ion diffusion in super-ionic conductors. *Nat. Commun.*, 8:15893, 2017. doi: 10.1038/ncomms15893.

[35] M. Xu, J. Ding, and E. Ma. One-dimensional stringlike cooperative migration of lithium ions in an ultrafast ionic conductor. *Appl. Phys. Lett.*, 101(3):031901, 2012. doi: 10.1063/1.4737397.

[36] K. Funke. Jump relaxation in solid ionic conductors. *Solid State Ionics*, 28-30: 100–107, 1988. doi: 10.1016/s0167-2738(88)80015-8.

[37] K. Funke, R.D. Banhatti, and C. Cramer. Correlated ionic hopping processes in crystalline and glassy electrolytes resulting in MIGRATION-type and nearly-constant-loss-type conductivities. *Phys. Chem. Chem. Phys.*, 7(1):157–165, 2005. doi: 10.1039/b414160c.

[38] R. Mercier, J.P. Malugani, B. Fahys, G. Robert, and J. Douglade. Structure du tetrathiophosphate de lithium. *Acta Crystallogr., Sect. B*, 38(7):1887–1890, 1982. doi: 10.1107/s0567740882007535.

[39] Z. Liu, W. Fu, E.A. Payzant, X. Yu, Z. Wu, N.J. Dudney, J. Kiggans, K. Hong, A.J. Rondinone, and C. Liang. Anomalous high ionic conductivity of nanoporous β-Li_3PS_4. *J. Am. Chem. Soc.*, 135(3):975–978, 2013. doi: 10.1021/ja3110895.

[40] K. Homma, M. Yonemura, T. Kobayashi, M. Nagao, M. Hirayama, and R. Kanno. Crystal structure and phase transitions of the lithium ionic conductor Li_3PS_4. *Solid State Ionics*, 182(1):53–58, 2011. doi: 10.1016/j.ssi.2010.10.001.

[41] W.D. Richards, L.J. Miara, Y. Wang, J.C. Kim, and G. Ceder. Interface stability in solid-state batteries. *Chem. Mater.*, 28(1):266–273, 2016. doi: 10.1021/acs.chemmater.5b04082.

[42] N.H.H. Phuc, M. Totani, K. Morikawa, H. Muto, and A. Matsuda. Preparation of Li_3PS_4 solid electrolyte using ethyl acetate as synthetic medium. *Solid State Ionics*, 288:240–243, 2016. doi: 10.1016/j.ssi.2015.11.032.

[43] S. Teragawa, K. Aso, K. Tadanaga, A. Hayashi, and M. Tatsumisago. Liquid-phase synthesis of a Li_3PS_4 solid electrolyte using N-methylformamide for all-solid-state lithium batteries. *J. Mater. Chem. A*, 2(14):5095–5099, 2014. doi: 10.1039/c3ta15090a.

[44] Y. Chen, L. Cai, Z. Liu, C.R. dela Cruz, C. Liang, and K. An. Correlation of anisotropy and directional conduction in β-Li_3PS_4 fast Li^+ conductor. *Appl. Phys. Lett.*, 107(1):013904, 2015. doi: 10.1063/1.4926725.

[45] S. Nishino, T. Fujiwara, and H. Yamasaki. Nanosecond quantum molecular dynamics simulations of the lithium superionic conductor $Li_{4-x}Ge_{1-x}P_xS_4$. *Phys. Rev. B*, 90(2):024303, 2014. doi: 10.1103/PhysRevB.90.024303.

[46] N.D. Lepley, N.A.W. Holzwarth, and Y.A. Du. Structures, Li^+ mobilities, and interfacial properties of solid electrolytes Li_3PS_4 and Li_3PO_4 from first principles. *Phys. Rev. B*, 88(10):104103, 2013. doi: 10.1103/PhysRevB.88.104103.

[47] M. Gobet, S. Greenbaum, G. Sahu, and C. Liang. Structural evolution and Li dynamics in nanophase Li_3PS_4 by solid-state and pulsed-field gradient NMR. *Chem. Mater.*, 26(11):3558–3564, 2014. doi: 10.1021/cm5012058.

[48] K. Hayamizu, Y. Aihara, T. Watanabe, T. Yamada, S. Ito, and N. Machida. NMR studies on lithium ion migration in sulfide-based conductors, amorphous and crystalline Li_3PS_4. *Solid State Ionics*, 285:51–58, 2016. doi: 10.1016/j.ssi.2015.06.016.

[49] J. Yang and J.S. Tse. First-principles molecular simulations of Li diffusion in solid electrolytes Li_3PS_4. *Comput. Mater. Sci.*, 107:134–138, 2015. doi: 10.1016/j.commatsci.2015.05.022.

[50] B. Kozinsky, S.A. Akhade, P. Hirel, A. Hashibon, C. Elsasser, P. Mehta, A. Logeat, and U. Eisele. Effects of sublattice symmetry and frustration on ionic transport in garnet solid electrolytes. *Phys. Rev. Lett.*, 116(5):055901, 2016. doi: 10.1103/PhysRevLett.116.055901.

[51] H. Mehrer. *Diffusion in Solids: Fundamentals, Methods, Materials, Diffusion-Controlled Processes*, volume 155. Springer Science & Business Media, 2007.

[52] X. Wang, R. Xiao, H. Li, and L. Chen. Oxygen-driven transition from two-dimensional to three-dimensional transport behaviour in beta-Li_3PS_4 electrolyte. *Phys. Chem. Chem. Phys.*, 18(31):21269–21277, 2016. doi: 10.1039/c6cp03179j.

[53] Y. Yang, Q. Wu, Y. Cui, Y. Chen, S. Shi, R.Z. Wang, and H. Yan. Elastic properties, defect thermodynamics, electrochemical window, phase stability, and Li^+ mobility of Li_3PS_4: insights from first-principles calculations. *ACS Appl. Mater. Interfaces*, 8(38):25229–25242, 2016. doi: 10.1021/acsami.6b06754.

[54] R. Xiao, H. Li, and L. Chen. High-throughput design and optimization of fast lithium ion conductors by the combination of bond-valence method and density functional theory. *Sci. Rep.*, 5:14227, 2015. doi: 10.1038/srep14227.

[55] T. Krauskopf, C. Pompe, M.A. Kraft, and W.G. Zeier. Influence of lattice dynamics on Na^+ transport in the solid electrolyte $Na_3PS_{4-x}Se_x$. *Chem. Mater.*, 29(20): 8859–8869, 2017. doi: 10.1021/acs.chemmater.7b03474.

[56] R.D. Shannon. Revised effective ionic radii and systematic studies of interatomic distances in halides and chalcogenides. *Acta Crystallogr. Sect. A*, 32(5):751–767, 1976. doi: 10.1107/s0567739476001551.

[57] J.C. Bachman, S. Muy, A. Grimaud, H.H. Chang, N. Pour, S.F. Lux, O. Paschos, F. Maglia, S. Lupart, P. Lamp, L. Giordano, and Y. Shao-Horn. Inorganic solid-state electrolytes for lithium batteries: mechanisms and properties governing ion conduction. *Chem. Rev.*, 116(1):140–162, 2016. doi: 10.1021/acs.chemrev.5b00563.

[58] G. Kresse and J. Hafner. Ab initio molecular dynamics for liquid metals. *Phys. Rev. B*, 47(1):558–561, 1993. doi: 10.1103/PhysRevB.47.558.

[59] J.P. Perdew, K. Burke, and M. Ernzerhof. Generalized gradient approximation made simple. *Phys. Rev. Lett.*, 77(18):3865–3868, 1996. doi: 10.1103/PhysRevLett.77.3865.

[60] P.E. Blöchl. Projector augmented-wave method. *Phys. Rev. B*, 50(24):17953–17979, 1994. doi: 10.1103/PhysRevB.50.17953.

Summary

Batteries have found widespread use, especially in mobile devices. With the inevitable energy transition the demand for batteries will rise further. Batteries for large-scale storage, transport applications and mobile devices all have different demands, requiring the development of a range of battery types for the storage of electrical energy. For these developments a better understanding of the fundamental aspects of materials and energy is necessary.

In Chapter 2 a thermodynamic model is made to study the lithium-insertion in TiO_2-anatase. The presented phase-field model explains many experimentally observed phenomena, including the effects of Li-ion diffusivity, particle size, C-rate, and surface area. The model shows that slow Li-ion diffusion in the Li_1TiO_2 phase limits the performance of TiO_2-anatase electrodes. Improving TiO_2-anatase electrodes thus requires the prevention of Li_1TiO_2 layers, or raising the Li-ion diffusivity in this phase. The good qualitative agreement of the model, which is obtained using parameters from literature only, demonstrates the sound physical basis of phase-field modelling. Using phase-field modelling to gain understanding of the behaviour of electrode materials thus shows promise for improving battery designs.

Many battery types are currently under development, one of which is the all-solid state battery. The main promises of all-solid state batteries are the increased safety and higher volumetric energy density in comparison to conventional Li-ion batteries. To make all-solid state batteries commercially available, solid electrolytes with ionic conductivities comparable to liquid electrolytes are necessary. Although such solid electrolytes are known nowadays, fast charging and discharging of all-solid-state batteries remains challenging. This is generally attributed to poor kinetics over the interface of the electrode and the solid electrolyte, either due to poorly conducting decomposition products, small contact areas, or space-charge layers.
In Chapter 3 a thermodynamic model is developed to better understand and quantify the role of space-charge layers in all-solid-state batteries. For several combinations of solid electrolytes and electrode materials at different voltages the space-charge layers and its effects are calculated. The model indicates that the space-charge layers are approximately a nanometre in thickness. The resistance for Li-ion transport through the space-charge layer is below 1 Ω cm^2 in most cases, indicating that space-charge layers have a negligible impact on the performance of all-solid-state batteries.

To get a better understanding of solid electrolytes and how atomic processes affect ionic conductivity molecular dynamics (MD) simulations using density functional theory (DFT) are an ideal tool. The large amount of control over the atomic structure allows for a detailed study on how the atomic structure influences macroscopic properties, thus increasing the understanding of ionic conductors.

In Chapter 4 DFT MD-simulations on the cubic and tetragonal phases of the solid

electrolyte Na_3PS_4 are presented. These show that the Na-ion conductivity in the two phases is similar, indicating that the experimentally observed differences between them are most likely caused by differing synthesis procedures. A large increase in Na-ion conductivity is observed when Na-ion vacancies are introduced. With the introduction of just 2% Na-vacancies an order of magnitude increase in ionic conductivity is observed, which rises further with increasing Na-vacancy concentration. To determine whether introducing Na-vacancies is a practical route towards improvement, MD-simulations of halogen doped cubic Na_3PS_4 are performed, which show promising results. Through a detailed investigation of the Na-ion transitions the importance of free volume for enabling Na-ion diffusion is revealed, showing the importance of phonons for ionic conduction in this material.

In Chapter 5 the origin of the large differences in Li-ion conductivity between the argyrodite solid electrolytes is investigated using DFT MD-simulations. It is shown that the position of the halogen atoms in the crystal structure is of crucial importance for the ionic conductivity, explaining why Li_6PS_5I is a poor ionic conductor. By altering the Cl-distribution over the 4a- and 4c-sites the DFT-MD simulations predict that the ideal Cl-distribution over the 4a- and 4c-sites is 1:3, which increases the ionic conductivity by a factor of two in comparison to the currently prepared materials. Li-ion vacancies are also shown to play a role in the ionic conductivity, based on which simulations were performed on $Li_5PS_4X_2$ (X = Cl, Br or I). These materials show Li-ion conductivities similar to Li_6PS_5Cl and Li_6PS_5Br, but are expected to have a higher electrochemical stability, suggesting that the $Li_5PS_4X_2$ compounds are interesting new solid state electrolytes.

As shown in Chapters 4 and 5 molecular dynamics simulations are a powerful tool to study diffusion processes in solid electrolyte materials. The analysis developed in these chapters is further expanded upon in chapter 6, in which it is shown how many properties relevant to diffusion can be obtained from MD simulations. These properties include the diffusion path, amplitude of vibrations, jump rates, radial distribution functions, and collective diffusion processes. Furthermore, for the first time it is shown that the activation energies of different jumps and the attempt frequency can be obtained from a single molecular dynamics simulation. The analysis developed in this chapter is applied to DFT MD simulations of β-Li_3PS_4, for which it rationalises the beneficial effect of O-doping on the Li-ion diffusivity, and indicates that introducing Li-vacancies through Br-doping can be beneficial. This example shows how knowledge of the detailed diffusion properties can give a thorough understanding of diffusion in solid electrolytes, and that ways to improve solid electrolyte materials can be obtained using this knowledge.

Summarising, in this thesis several models are used to increase the understanding of batteries, space-charge layers, and solid electrolyte materials. With the knowledge gained from modelling promising routes for improving batteries and battery materials are revealed, helping the further development of batteries.

Samenvatting

Batterijen worden tegenwoordig door bijna iedereen dagelijks gebruikt in mobiele telefoons, afstandsbedieningen, laptops, etc. Met de overstap naar duurzame energie zullen er steeds meer elektrische voertuigen komen, waarin batterijen een belangrijke rol spelen. Daarnaast zal het nodig zijn om duurzaam opgewekte elektrische energie op te slaan om de fluctuaties in de opwekking en het gebruik van energie op te vangen, waarvoor grootschalige batterijen gebruikt kunnen worden. Het gebruik van batterijen zal in de toekomst dus alleen maar verder toenemen, wat het ontwikkelen van goede en veilige batterijen steeds belangrijker maakt.
Verschillende soorten apparaten en toepassingen stellen allemaal andere eisen aan de gebruikte batterijen. Voor grootschalige toepassingen is de prijs per hoeveelheid energie (kWh/€) een doorslaggevende factor, voor mobiele toepassingen zullen gewicht (kWh/kg) en volume (kWh/L) belangrijker zijn, terwijl ook rekening gehouden moet worden met de veiligheid, duurzaamheid en (ont)laadsnelheid van de batterij. Idealiter zou een batterij klein, goedkoop, duurzaam, etc. zijn, maar een batterij die aan al deze eisen voldoet bestaat waarschijnlijk niet. Dit heeft er toe geleid dat er vele verschillende types batterijen ontwikkeld worden, zoals te zien is in Figuur 1.1. Elk van deze types heeft zijn eigen voor- en nadelen, en zal dus geschikt zijn voor verschillende toepassingen.

Batterijen slaan energie op door elektrische energie om te zetten in chemische energie. Door de elektrochemische reactie om te draaien kan de elektrische energie weer teruggewonnen worden, en gebruikt om stroom te leveren aan elektrische apparaten. Zoals schematisch weergegeven in Figuur 1.2 gebeurt dit door atomen, lithiumatomen in lithium-ionbatterijen, van de anode naar de kathode te transporteren. De verplaatsing van atomen tussen de twee elektrodes wordt veroorzaakt door het verschil in chemische potentiaal van de atomen in de twee materialen. Als deze twee materialen direct contact zouden maken met elkaar zou er kortsluiting ontstaan, en zou er dus geen (nuttige) elektrische energie uit de batterij gehaald kunnen worden. Het is daarom essentieel om er een derde materiaal tussenin te doen: het elektrolyt. Het elektrolyt is een materiaal waar ionen gemakkelijk doorheen kunnen, terwijl elektronen door dit materiaal geblokkeerd worden. De elektronen worden hierdoor gedwongen om via een extern circuit te gaan, en hun energie kan zo nuttig gebruikt worden in de vorm van elektriciteit.
Het gebruik van (minstens) drie verschillende materialen, de ionen en elektronen die door de batterij bewegen en alle processen die daarmee samenhangen maken van een batterij een complex systeem. Om het nog ingewikkelder te maken kunnen de verschillende materialen en processen allerlei interacties met elkaar hebben, waardoor een bepaald experimenteel geobserveerd effect verschillende oorzaken kan hebben. Om te onderzoeken hoe bepaalde eigenschappen van een batterij(materiaal) de prestaties van een batterij beïnvloeden zijn modellen ideaal. In een model is het namelijk

zeer gemakkelijk om een bepaalde eigenschap te veranderen om het effect hiervan te bepalen. In dit proefschrift wordt daarom getracht om met behulp van verschillende modellen een beter begrip te verkrijgen van batterijen en batterijmaterialen. Hierdoor wordt een dieper inzicht in de fundamentele aspecten van materialen en energie en een beter begrip van de opslag van elektrochemische energie mogelijk, wat bijdraagt aan de verdere ontwikkeling van batterijen.

Het gedrag van een batterij kan beschreven worden door een set van thermodynamische vergelijkingen, wat impliceert dat door het meten van alle relevante materiaaleigenschappen een batterij gesimuleerd kan worden. In batterijmodellen in de literatuur wordt meestal echter gebruik gemaakt van parameters die gefit zijn op experimenten, wat het toepassen van deze modellen twijfelachtig maakt als de omstandigheden niet lijken op die van de gefitte experimenten.
Om te bepalen of het mogelijk is om een batterijmodel te maken zonder gefitte variabelen is in hoofdstuk 2 is een faseveldmodel gemaakt voor anataaselektrodes waarvoor alleen parameterwaardes uit de literatuur gebruikt zijn. De sterke overeenkomsten tussen experimentele resultaten en het faseveldmodel laat zien dat het mogelijk is om een batterijmodel te maken uitgaande van fysische principes. Dit houdt de belofte in zich dat een grondig begrip van materiaaleigenschappen en hun interacties in batterijen mogelijk is, wat op zijn beurt verbeteringen in het ontwerp van elektrodes mogelijk maakt.
Voor anataaselektrodes laat het faseveldmodel zien dat de beperkende factor voor een hoge (ont)laadsnelheid de langzame Li-diffusie in de Li_1TiO_2-fase is. Tijdens de lithiatie van de anataaselektrode zal eerst de $Li_{0.5}TiO_2$-fase gevormd worden, waarna op het oppervlak de formatie van de Li_1TiO_2-fase begint. Zodra er een laag van enkele nanometers Li_1TiO_2 is gevormd wordt de Li-diffusie zo erg verlaagd dat verdere lithiatie van de anataasdeeltjes (praktisch) onmogelijk is. Om batterijen met anataaselektrodes te verbeteren zal hiervoor een oplossing gevonden moeten worden, door de vorming van de Li_1TiO_2-fase te voorkomen of via een verhoging van de Li-ion diffusie in de Li_1TiO_2-fase.

Zoals eerder genoemd worden er vele verschillende types batterijen ontwikkeld, waaronder de vaste-stofbatterij, die een grotere veiligheid en energiedichtheid beloofd. Om dit type batterij te maken moet het (nu gebruikte) vloeibare elektrolyt vervangen worden door een vaste-stofelektrolyt. Een van de belangrijkste eisen om een vaste-stofbatterij te laten werken is dat het vaste-stofelektrolyt een ionische geleiding heeft die vergelijkbaar is met die in vloeibare elektrolyten.
Hoewel er in de afgelopen jaren verscheidene materialen zijn ontdekt die aan deze eis voldoen blijft het lastig om vaste-stofbatterijen goed te laten werken bij hoge (ont)laadsnelheden. De oorzaak van deze teleurstellende resultaten wordt gezocht bij de slechte kinetische eigenschappen op de grensvlakken tussen het elektrode- en elektrolytmateriaal. De slechte kinetiek kan veroorzaakt worden doordat de combinatie van elektrode en elektrolyt onstabiel is, er weinig contactoppervlak is en/of doordat ruimteladingslagen de overgang van ionen tussen de materialen bemoeilijken. Doordat deze processen optreden op het grensvlak van verschillende materialen is het moeilijk om ze te bestuderen, en het tegelijkertijd optreden van deze effecten maakt het lastig om de gevolgen van de verschillende processen van elkaar te onderscheiden.

Er wordt veel onderzoek gedaan naar de stabiliteit van materialen en het vergroten van het contactoppervlak, maar over de rol van ruimteladingslagen in vaste-stofbatterijen is nog weinig bekend. Dit heeft ertoe geleid dat sommige auteurs zeggen dat de ruimteladingslagen meerdere micrometers dik zijn, wat een zeer grote grensvlakweerstand zou veroorzaken. Anderen zeggen echter dat de dikte van de ruimteladingslagen slechts enkele nanometers is, wat een verwaarloosbare grensvlakweerstand zou geven. Om te bepalen of ruimteladingslagen een significante invloed hebben op de prestaties van vaste-stofbatterijen is er in hoofdstuk 3 een thermodynamisch model gemaakt om de dikte, weerstand en capaciteit van de ruimteladingslaag op het grensvlak van elektrode en vaste-stofelektrolyt te berekenen.
Voor meerdere combinaties van vaste-stofelektrolyten en elektrodematerialen zijn de eigenschappen en effecten van de ruimteladingslaag berekend. Deze berekeningen laten zien dat de ruimteladingslaag over het algemeen minder dan een nanometer dik is, en dat de weerstand die hierdoor veroorzaakt wordt minder dan 1 Ω cm^2 is. Deze resultaten wijzen erop dat ruimteladingslagen een verwaarloosbare invloed hebben op de prestaties van vaste-stofbatterijen, wat goed nieuws is voor hun verdere ontwikkeling.
Zoals in Figuur 1.5 te zien is zijn er tegenwoordig meerdere klassen vaste-stofelektrolyten bekend die een ionische geleiding hebben die vergelijkbaar is met die van vloeibare elektrolyten. Maar vaste-stofelektrolyten moeten ook aan andere eisen voldoen, en het 'perfecte' vaste-stofelektrolyt is dan ook nog niet gevonden. Om dit 'perfecte' elektrolyt te vinden is het belangrijk om de eigenschappen die hoge ionengeleiding veroorzaken te begrijpen. Veel verschillende eigenschappen zijn geopperd als veroorzaker van hoge ionische geleiding in vaste-stofelektrolyten, zoals lage-energie fononen, de polariseerbaarheid van het kristalrooster, het percentage lege Li-posities, en vele anderen. Hoewel veel van deze eigenschappen een correlatie hebben met ionengeleiding zijn ze geen van alle perfecte voorspellers voor hoge ionische geleiding.
Aangezien ionische geleiding veroorzaakt wordt door processen op de atomaire schaal zijn simulaties op atomair niveau nodig om een beter begrip te krijgen van deze materialen. Hiervoor zijn moleculaire dynamica (MD) studies in combinatie met dichtheidsfunctionaaltheorie (DFT) ideaal. In DFT-MD simulaties is een grote controle over de atomaire structuur van een kristal mogelijk, kunnen atomaire processen tot in detail bestudeerd worden, en kan de kristalstructuur gemakkelijk gevarieerd worden. Dit maakt het bestuderen van een reeks materialen met DFT-MD simulaties gemakkelijker dan via experimenten, en hypotheses over hoe een materiaal te verbeteren kunnen ook sneller getest worden.

In hoofdstuk 4 worden DFT-MD simulaties toegepast op de Na-ionengeleider Na_3PS_4, waarvan zowel de tetragonale als de kubische structuur bestudeerd wordt. De simulaties laten zien dat het stoichiometrische materiaal praktisch geen geleiding vertoond, maar door het introduceren van slechts 2% Na-vacatures gaat de geleiding met een orde van grootte omhoog, en het stijgt verder bij grotere vacatureconcentraties.
De DFT-MD simulaties laten slechts geringe verschillen in Na-geleiding zien tussen de tetragonale en kubische structuur, wat erop wijst dat de experimenteel waargenomen verschillen komen door variatie in de synthesecondities. Om te bepalen of Na-

vacatures een praktische manier zijn om de ionengeleiding te verhogen zijn simulaties gedaan aan de kubische fase waarin zwavelatomen zijn vervangen door verschillende halogeenatomen, wat hoopgevende resultaten geeft. Daarnaast wordt door een gedetailleerde analyse van de overgangen van Na-ionen het belang getoond van vrij volume voor diffusie, wat impliceert dat fononen een essentiële rol spelen in de snelle Na-geleiding door dit materiaal.
In hoofdstuk 5 wordt de oorzaak van de grote verschillen in Li-ionengeleiding binnen de Li-argyrodieten onderzocht met behulp van DFT-MD simulaties. Er wordt getoond dat de verdeling van halogeenatomen over de 4a- en 4c-posities in de kristalstructuur een grote invloed heeft op de diffusie van Li-ionen binnen deze klasse van materialen. Dit verklaard waarom experimenten een hoge ionengeleiding meten in Li_6PS_5Cl en Li_6PS_5Br, terwijl dit in Li_6PS_5I ordes van grootte lager is. Door de verdeling van Cl-atomen over de 4a- en 4c-posities systematisch te variëren wordt voorspeld dat een 1:3 verdeling over de 4a- en 4c-posities een verdubbeling van de ionengeleiding kan veroorzaken ten opzichte van de huidige gesynthetiseerde Li-argyrodieten.
Daarnaast wordt aangetoond dat ook Li-vacatures een rol spelen in de ionengeleiding. Om de invloed van een hogere concentratie Li-vacatures te bepalen zijn voor $Li_5PS_4X_2$ (X = Cl, Br of I) DFT-MD simulaties gedaan. Deze materialen laten vergelijkbare ionengeleiding zien als Li_6PS_5Cl en Li_6PS_5Br, maar door het vervangen van zwavelatomen door halogeenatomen wordt verwacht dat deze materialen een hogere elektrochemische stabiliteit hebben, wat suggereert dat de $Li_5PS_4X_2$-materialen interessante nieuwe vaste-stofelektrolyten kunnen zijn.
De analysemethode om de diffusie in vaste-stofelektrolyten te bestuderen met behulp van DFT-MD simulaties die is ontwikkeld in hoofdstuk 4 en 5 wordt in hoofdstuk 6 verder uitgebreid. Er wordt getoond hoe vele eigenschappen die relevant zijn voor de beschrijving van diffusie uit MD-simulaties bepaald kunnen worden. Deze eigenschappen zijn onder andere het diffusiepad, de vibratie-amplitude, sprongfrequenties, radiale distributiefuncties en collectieve diffusieprocessen. Bovendien wordt voor het eerst gedemonstreerd dat het mogelijk is om uit een enkele MD simulatie de activeringsenergie van verschillende sprongen en de pogingsfrequentie te bepalen.
Door deze analyse toe te passen op β-Li_3PS_4 wordt getoond hoe de kennis over deze eigenschappen een beter begrip geeft van diffusie in vaste-stofelektrolyten. Voor β-Li_3PS_4 leidt dit tot het inzicht dat 3D-diffusiepaden de Li-diffusie significant verhogen, en dat zo'n 3D-pad verkregen kan worden door Li-vacatures te introduceren, of door het materiaal te doteren met zuurstof. De gepresenteerde analysemethode is algemeen bruikbaar voor diffusie in kristallijne materialen en helpt om nieuwe manieren te vinden om vaste-stofelektrolyten verder te verbeteren.

Samenvattend, in dit proefschrift zijn verschillende modellen gebruikt om de eigenschappen van batterijen en batterijmaterialen beter te begrijpen, en om inzicht te krijgen in de knelpunten die de prestaties van een batterij beperken. Door deze kennis is een gerichte aanpak mogelijk om batterijen en batterijmaterialen te verbeteren, wat hopelijk zal bijdragen aan de verdere ontwikkeling van batterijen.

Dankwoord

Marnix, bedankt voor alle vrijheid die je me in de afgelopen vier jaar gaf om mijn eigen weg te zoeken, terwijl tegelijkertijd je deur altijd open stond om advies te geven. Het knapste vind ik dat je mijn ideeën nooit afwees, maar ze toch altijd zo wist te sturen dat ze nuttig werden, ik weet zeker dat dit mij vele uren nutteloos werk heeft bespaard. En nu je hier vier jaar lang op bent blijven aandringen, beloof ik je dat ik nooit meer uit het oog zal verliezen hoe mijn werk toegepast kan worden.
Ekkes, al spraken we elkaar niet zo vaak, het was indrukwekkend dat je me altijd weer op scherp wist te zetten met je kritische vragen. Dit heeft mij veel geholpen in het altijd kritisch blijven kijken naar resultaten, vooral die van mijn eigen werk.

When I started I didn't know a lot about batteries, and practically nothing about solid state electrolytes. Swapna and Chuang Yu, thanks a lot for helping me with this when I started my research. I always enjoyed our trips to Nijmegen for NMR experiments, even though they meant hard work and long days.
Alexandros, thanks to you I will always be able to order a salad in Greek, this means a lot to me. But even more important, you were always happy to discuss about MD simulations or phase-fields, and our discussions helped me a lot to gain a better understanding of both.

Voor mijn vragen over batterijen ging ik de afgelopen vier jaar altijd naar PP en Tomas toe. Heren, veel dank voor het altijd geduldig beantwoorden van mijn soms domme, soms makkelijke en soms verbazend moeilijke vragen.
Mijn studenten, Irek, Jasper, Jorino, Eveline, Tammo en Loic, van het beantwoorden van jullie vragen heb ik misschien wel even veel heb geleerd als jullie. Zonder julie zou dit proefschrift er dan ook heel anders uit hebben gezien, en niet op een goede manier.

Om mij te laten werken moeten er vele dingen werken, waarvoor ik veel dank verschuldigd ben: aan Jouke voor het fixen van computer gerelateerde dingen waar ik zelf niet uit kwam, aan Ilse en Nicole voor het regelen van allerlei administratieve zaken, en aan Kees en Yevgeni voor de heerlijke koffie.
Gedurende mijn laatste jaar heb veel te danken aan Hylke (en de TCM groep) voor het beschikbaar stellen van een werkplek in Nijmegen, en veel plezier beleeft aan het logeren bij al mijn gastvrije collega's uit Delft.

Michi, Casper, Violetta, Hylke, Remco, Yaolin, Martijn, Zhaolong, Carla, Swapna, Chandra, PP, Tomas, Alex, ik kon het altijd erg waarderen om met jullie een kopje koffie of een biertje te drinken en te babbelen over werk en vele andere dingen. Daarnaast natuurlijk alle anderen op de afdeling FAME/SEE/NPM2, waar iedereen klaar staat om elkaar te helpen en altijd een goede sfeer hangt.

Verder ook mijn ouders, familie en vrienden, die ervoor zorgen dat er ook nog een leven is buiten het werk, zonder jullie zou ik soms gek zijn geworden.

En natuurlijk Anne, zonder wie mijn leven veel minder leuk zou zijn, die altijd voor me klaar staat om me op te beuren, maar gelukkig nog vaker om iets te vieren.

Bedankt allemaal,

Niek

Curriculum Vitæ

Op 7 januari 1990 is Niek geboren te State College, Pennsylvania in de Verenigde Staten van Amerika. Na enkele maanden werd hij door zijn ouders mee terug genomen naar Nederland, waar hij opgroeide in Wageningen. Hier ging hij eerst naar de Sint Jozefschool, waarna hij op het Pantarijn begon aan het VWO, wat hij in 2008 afrondde met de profielen N&T en N&G.

Hij besloot hierna om Scheikunde te gaan studeren in Nijmegen. In 2012 haalde hij zijn bachelor, en in 2012 zijn Master Scheikunde met een minor Filosofie en afstudeeronderzoek bij de afdeling Vaste Stofchemie. Zijn afstudeeronderzoek vondt hij zo leuk dat hij besloot om hier verder mee te gaan. Marnix Wagemaker gaf hem de kans om promotieonderzoek te doen met een focus op simulaties van vaste-stofbatterijen, de titel van het hieruit voortgekomen proefschrift is 'Simulations of electrode and solid electrolyte materials'.

Niek hoopt nog vele jaren gelukkig te leven met Anne, om op zijn 93e te sterven op een van de manen van Pluto.

List of Publications

- **Niek J.J. de Klerk & Marnix Wagemaker**, *Space-charge Layers in All-Solid-State Batteries; Important or Negligible?*, ACS Applied Energy Materials, **1** (7), 5609-5618 (2018).

- **Alexandros Vasileiadis, Brian Carlsen, Niek J.J. de Klerk & Marnix Wagemaker**, *Ab Initio Study of Sodium Insertion in the λ-Mn_2O_4 and Dis/Ordered λ-$Mn_{1.5}Ni_{0.5}O_4$ Spinels*, Chemistry of Materials, **30** (19), 6646-6659 (2018)

- **Niek J.J. de Klerk, Eveline van der Maas & Marnix Wagemaker**, *Analysis of Diffusion in Solid-State Electrolytes through MD Simulations, Improvement of the Li-Ion Conductivity in β-Li_3PS_4 as an Example*, ACS Applied Energy Materials, **1** (7), 3230-3242 (2018).

- **Alexandros Vasileiadis, Niek J.J. de Klerk, Raymond B. Smith, Swapna Ganapathy, Peter-Paul R.M.L. Harks, Martin Z. Bazant & Marnix Wagemaker**, *Toward Optimal Performance and In-Depth Understanding of Spinel $Li_4Ti_5O_{12}$ Electrodes through Phase Field Modeling*, Advanced Functional Materials **28** (16), 1705992 (2018).

- **Niek J.J. de Klerk, Alexandros Vasileiadis, Raymond B. Smith, Martin Z. Bazant & Marnix Wagemaker**, *Explaining Key Properties of Lithiation in TiO_2-anatase Li-ion Battery Electrodes using Phase-Field Modeling*, Physical Review Materials **1** (2), 025404 (2017).

- **Niek J.J. de Klerk, Irek Rosłoń & Marnix Wagemaker**, *Diffusion Mechanism of Li Argyrodite Solid Electrolytes for Li-Ion Batteries and Prediction of Optimized Halogen Doping: The Effect of Li Vacancies, Halogens, and Halogen Disorder*, Chemistry of Materials **28** (21), 7955-7963 (2016).

- **Niek J.J. de Klerk & Marnix Wagemaker**, *Diffusion Mechanism of the Sodium-Ion Solid Electrolyte Na_3PS_4 and Potential Improvements of Halogen Doping*, Chemistry of Materials **28** (9), 3122-3130 (2016).

- **Chuang Yu, Swapna Ganapathy, Niek J.J. de Klerk, Irek Rosłoń, Ernst R. van Eck, Arno P. Kentgens & Marnix Wagemaker**, *Unravelling Li-Ion Transport from Picoseconds to Seconds: Bulk versus Interfaces in an Argyrodite Li_6PS_5Cl-Li_2S All-Solid-State Li-Ion Battery*, Journal of the American Chemical Society **138** (35), 11192-11201 (2016).

- **Chuang Yu, Swapna Ganapathy, Niek J.J. de Klerk, Irek Rosłoń, Ernst R. van Eck & Marnix Wagemaker**, *Na-Ion Dynamics in Tetragonal and Cubic Na_3PS_4, a Na-Ion Conductor for Solid State Na-Ion Batteries*, Journal of Materials Chemistry A **4** (39), 15095-15105 (2016).

- **Niek J.J. de Klerk, Joost A. van den Ende, Rita Bylsma, Peter Grančič, Gilles A. de Wijs, Herma Cuppen & Hugo Meekes**, *q-GRID: A New Method To Calculate Lattice and Interaction Energies for Molecular Crystals from Electron Densities*, Crystal Growth & Design **16** (2), 662-671 (2016).

- **A.M. Reilly, R. Cooper, ..., N.J.J. de Klerk, ..., and C.R. Groom** *Report on the Sixth Blind Test of Organic Crystal Structure Prediction Methods*, Acta Crystallographica Section B, **72** (4), 439-59 (2016).